UNIVERSITY OF SOUTHAMPTON

FACULTY OF ENGINEERING, SCIENCE AND MATHEMATICS

School of Mathematics

The Mathematical Modelling of Microstructured Optical Fibres

by

Christopher Jonathan Voyce

Thesis for the degree of Doctor of Philosophy

November 2005

UNIVERSITY OF SOUTHAMPTON

ABSTRACT

FACULTY OF ENGINEERING, SCIENCE AND MATHEMATICS

SCHOOL OF MATHEMATICS

Doctor of Philosophy

THE MATHEMATICAL MODELLING OF MICROSTRUCTURED OPTICAL FIBRES

by Christopher Jonathan Voyce

The work presented in this thesis is concerned with modelling the manufacture of microstructured optical fibres. Though the manufacture of microstructured fibres is comprised of (i) preform manufacture and (ii) fibre manufacture, this thesis focuses on fibre manufacture.

Microstructured optical fibres contain a large number of holes in a transverse cross–section This thesis models the drawing of a capillary tube, taking advantage of the aspect-ratio of the geometry, producing both analytic and numerical solutions of the systems of PDEs resulting from the Navier-Stokes equations. The effects of spinning a fibre preform as it is passed into the drawing furnace and the subsequent geometrical effects on the fibre are considered. Theoretical predictions compare favourably with the results of experimental trials.

An insight into the spinning of microstructured optical fibres is gained in certain asymptotic limits, and the model of capillary drawing used to determine methodologies for minimizing Polarization Mode Dispersion for different classes of fibre.

The drawing of particular types of fibre are modelled, and analytical tools developed to describe the particular fluid–flows that occur in a cross-section of the fibres. Once again, theoretical predictions are compared to experimental results and a hitherto unexplained phenomenon is understood.

A two-phase flow model is developed to address the full microstructured–fibre problem, based on the model for a capillary tube. The two–phase flow model is an intermediate step between modelling the drawing of capillary tubes and that of holey fibres. The resulting equations are solved asymptotically and numerically, and the results interpreted in a wholly practical manner. The restrictions of the two-phase flow model are then removed and a model that describes the manufacture of arbitrary holes fibres is derived. The equations are solved to produce analytic solutions for simple geometries.

Contents

List of Tables

List of Figures

Acknowledgements

I should like to thank my supervisors Professor Alistair Fitt and Professor Tanya Monro for their enthusiastic help throughout. I should also like to thank Professor Colin Please for his insight, help and enthusiasm, and Doctor Christopher Howls for his support. Doctor Peter Howell of the University of Oxford provided useful modelling ideas, and Mr John Hayes of the Optoelectronics Research Centre conducted most of the experiments required to obtain results for this thesis: my thanks to you both. Finally, particular thanks to Mark and Rachel for their support.

Chapter 1

Introduction

1.1 Overview

A definition of some of the technical terminology used in this introduction may be found in the glossary in Appendix E.

This thesis is concerned with the mathematical modelling of a variety of problems related to the manufacture of optical glass fibres that contain holes. Whilst the thesis concentrates specifically on the modelling of this process in direct relation to optical fibres, it is likely to be relevant to a variety of other industries and problems, including the manufacture of textiles, the blowing of glass bottles and other such containers.

The manufacture of optical fibres is a costly and often unpredictable process (described fully in Chapter 2) when new types of fibre are being fabricated and their manufacture optimized (once established though, industry has a good knowledge of how to vary fibre geometry precisely by altering draw parameters). Experimentalists achieve the required optical properties of the resultant fibres by varying the parameters available in the manufacture process. Consequently, fibres with different

optical and mechanical properties may often be made from a single initial structure. Experimentalists continually seek ways of making fibre in a less expensive and more consistent way, whilst trying to manufacture new types of fibre that have completely different mechanical and optical properties. These new fibres often behave differently in the various stages of manufacture to be described later.

The manufacture of optical fibres for high–performance applications requires a precise control of the refractive index and diameter variations in order to minimize fluctuation in the optical properties of the fibre along its length. It is therefore crucial to develop an understanding of the fluid-flow processes involved in such manufacture, in order that we may give experimentalists more than engineering "rules-of-thumb" to rely on, thence greatly reducing the cost and time of the manufacturing process and perhaps allowing previously unachievable fibres to be produced consistently and economically.

The first holey fibre was made in 1996 [1]. Holey fibres (or microstructured optical fibres) contain an array of air holes that run throughout the length of the fibre (see Figure 1.1). Light is guided in the fibres by one of two rather different mechanisms.

(i) Index–guiding fibres. These fibres guide light by making use of the principle of total internal reflection. These are known as holey fibres. Light exhibits wave–like behaviour in glass, and its interactions with the material are determined by geometrical considerations and the physical properties of the glass. The refractive index of glass is inversely proportional to the wave speed and arises due to absorptive resonances at specific wavelengths. This causes the refractive index to be wavelength dependent, giving rise to material dispersion where different wavelengths of light travel at different speeds.

Index–guiding fibres do not rely on having a periodic lattice of air holes, though often the holes are arranged on a hexagonal lattice. For this reason the fibres are sometimes referred to as photonic crystal fibres.

Holey fibres are of particular interest to experimentalists for several reasons and therefore the mathematical modelling of the process of the manufacture of such fibres is necessary. Unlike conventional optical fibres, holey fibres may be manufactured from a single material (see later description of manufacturing process), which is often chosen to be silica. It is possible to arrange the structure of the holes in a transverse cross–section of the preform in such a way that the effective refractive–index contrast is a strong function of the wavelength of light being guided along the fibre. It is therefore possible to design fibres with unique optical properties not possible in conventional (solid) optical fibres. Holey fibres can, for example, be endlessly single–mode fibres that transmit only one mode regardless of the wavelength of light used. They may have mode areas that range over as much as three orders of magnitude. Large mode-area fibres allow high optical power to be transmitted with few nonlinear effects, ideal for long–range data transmission. Conversely, small mode–area fibres allow nonlinear effects to be exploited at low optical power, which may be used in optical switching devices for example. The unique dispersion properties of holey fibres, discussed later, allow the possibility of soliton formation in the visible wavelength–band: something not currently possible in single–mode fibres. Soliton formation is advantageous since solitons have been shown to avoid broadening by dispersion and retain their temporal shape [2]. For further applications and discussion of the optical properties and potential applications for holey fibres see [3], [4] [5], [6], [7], [8], [9], [10] and [11].

The dispersion and polarization properties of a holey fibre may be particularly strongly influenced by the cladding configuration, especially when the distance between the holes is small. The control of chromatic dispersion in optical fibres is a very important problem for communication systems, both in the linear and nonlinear regimes. Systems that support ultra–short soliton dispersion tend to have their transmission features largely destroyed by third–order dispersion. In wavelength–division multiplexing systems chromatic dispersion control is required to maintain a uniform response in different wavelength channels. In all of the above cases and ubiquitously, the degree of optical efficiency of the system depends heavily on the shape (in fact

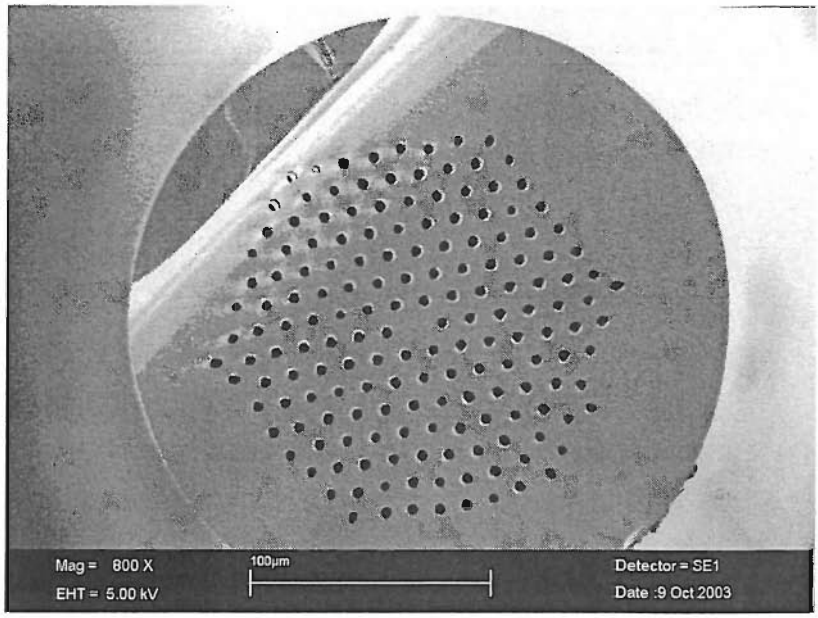

Figure 1.1: A close-up picture of a typical holey fibre core.

the flatness) of the optical fibre dispersion profile. Achromatic behaviour in fibres such as photonic crystal fibres and 'W' fibres may be designed to generate a flattened behaviour in the wavelengths of importance, removing or reducing these problems. Photonic crystal fibres may be made to generate such flat dispersion profiles over a range of wavelength windows.

(ii) Photonic bandgap fibres. If the air holes that define the cladding region are arranged on a strict periodic lattice, the structures can exhibit photonic bandgaps, meaning that frequencies located within the bandgap cannot propagate through the cladding (see [8] and [12]).

Photonic bandgap fibres, whose structure is visually similar to that of holey fibres, have a large, highly controllable periodic variation of refractive index, and it is this that opens up exciting opportunities for the control of the passage of light in optical devices and fibres. For example, a hexagonal arrangement of holes with a large air fraction is able to guide light using the formation of a full two–dimensional photonic bandgap. In a photonic bandgap fibre, light is guided due to the photonic bandgap effect, which is analogous to an electronic bandgap for electrons in semiconductors. If

the air holes that define the cladding region are arranged as a strict periodic lattice, the structures prohibit the propagation of certain wavelengths of light through the cladding. By breaking the periodicity of the cladding, for example by adding or removing a hole, it is possible to introduce a localized mode. Such a defect as this may act as the core of the fibre. For this reason photonic bandgap guidance fibres can have a core that is made either from glass or air, the modes being confined to that region. The surrounding structure looks much the same as a regular holey fibre, though the positioning of the holes in the surrounding structure is crucial to exploit the photonic bandgap effect. The fibres may be designed to have transmission windows at near–infrared wavelengths, and are of particular interest for studying interactions between light and gas, and in the transport of high–intensity optical fields.

It is clear that holey fibre technology offers great promise for fibre devices. Indeed, kilometres of robustly coated holey fibre may be produced with losses that approach the losses of conventional (solid) optical fibre. The fibre can be processed and spliced, making it possible to readily integrate it with low loss to conventional fibre systems. The manufacture process is compatible with a broad range of glasses, dramatically enhancing the potential scope for device manufacture and the applications that may be considered.

1.1.1 Mathematical modelling

Extrusion is used to manufacture glass preforms (preforms made from other materials may also be manufactured) but to date little work has been done on the mathematical modelling of glass extrusion except in terms of die-swell analysis [13]. Die-swell occurs when the cross-sectional area increases as fluid exits the die. Its occurrence results from the non-uniform fluid velocity profile at the die exit. However, the usual no-slip conditions on the surfaces of the die must be carefully considered. It is crucial with glass extrusion to have an accurate picture of the conditions that must be applied

to the inner surfaces of the die, since this will dramatically affect the mechanical pressure in the fluid, the stress at the boundaries, the local temperature, and thus the likelihood of glass crystallisation. If crystals form in the glass its quality is dramatically reduced, thus motivating the need to minimise the extrusion pressure and temperature and the need for mathematical modelling.

During the mathematical modelling of the final stage of fibre manufacture (fibre drawing) we are able to exploit the slender geometry of the glass preforms and their resulting fibres. The glass–air surface is free to move according to the influence of both gravity and the fact that it is being pulled at the winder end and fed in at the top end of the furnace. The boundary conditions are applied at the edges of the fluid domain. The consequence of this is that neither the point-wise fluid velocity nor the resulting fibre geometry is known in advance and must be determined by the model.

Both types of fibre manufacture are discussed at greater length later, but the focus of this thesis will be the manufacture of glass fibres from existing preforms, leaving the detail of preform manufacture postponed to another study.

The fluid concerned is assumed to be incompressible, which in the case of glass is a good approximation to reality. Its viscosity varies significantly with temperature though (see Figure 1.2), and this is sometimes problematic both from a practical and theoretical point of view. Whilst our models apply to an incompressible Newtonian fluid, in principle the mathematical techniques employed may be applied to a more general class of fluids such as incompressible non–Newtonian fluids. Figure 1.2 shows the viscosity and temperature ranges used in both extrusion and fibre drawing. Viscosity curves for two glasses are included.

We include the effects of gravity, as mentioned above, and also those of inertia, viscosity, surface tension and preform rotation. As we shall see though, it is sometimes possible to ignore the effects of one or more of these. The parameters that can be neglected will depend on the relative size of the associated terms in the equations, derived making use of asymptotic perturbations based on the slender geometry of

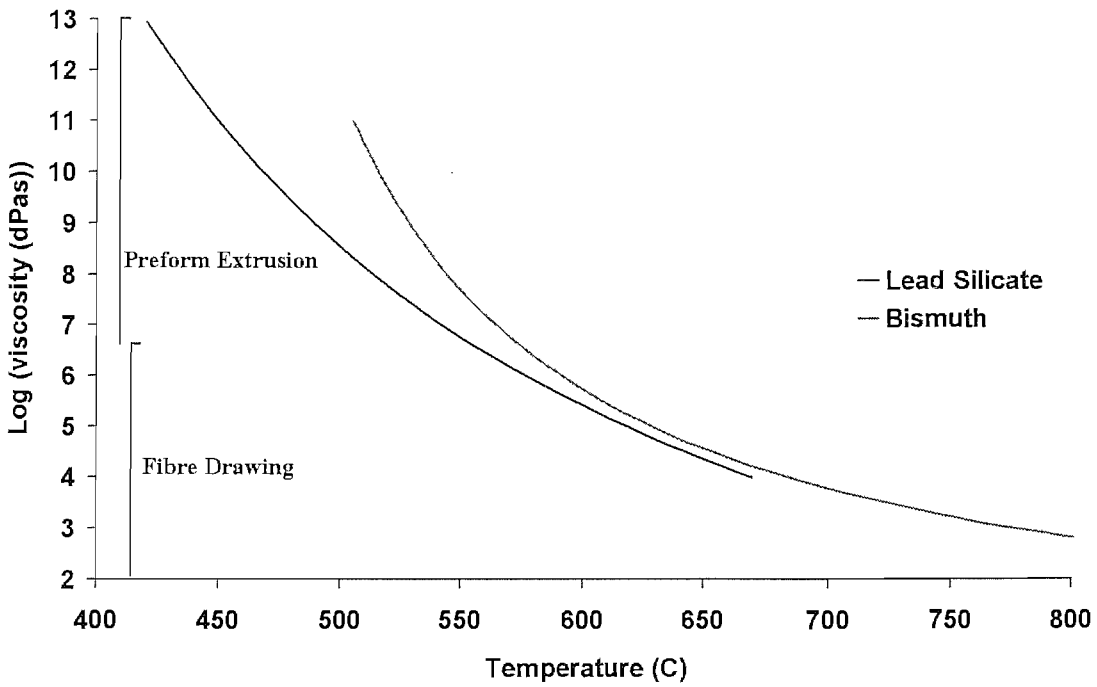

Figure 1.2: Graph to show the viscosity range of the manufacturing processes.

the preform. This allows the problems to be simplified greatly and used to build a comprehensive physical picture for the processes occurring, without becoming prematurely distracted by lengthy numerical analysis.

For the remainder of this section we will briefly describe the content of each chapter and finally give a concise review some of the work completed in this area to date.

1.2 Chapter review

It is not intended that this thesis be read as a whole and the reader is referred to §1.2.1. Each chapter is written with the aim of being relatively self-contained whilst still being progressive in the context of the aims of the thesis, so some of the descriptive text may be repeated briefly within each chapter. It is hoped that this

will increase the ease with which this work may be extended.

Chapter 2 briefly describes the methods by which both solid and holey fibres are produced experimentally.

Chapter 3 describes the mathematical modelling of the drawing of capillary tubes that are being rotated as they enter the fibre drawing furnace. It is an extension of the work carried out in [14] and [15], and may be regarded as a first step towards the ultimate goal of modelling the multiple–hole problem. We consider a variety of interesting and indeed essential asymptotic limits of the resulting Navier–Stokes equations in order to both gain a feel for the physics involved in the problem and also to simplify the equations in a way that allows us to work more intimately with analytic solutions.

Chapter 4 uses the model developed in Chapter 3 to understand and quantify methods for controlling the geometry of practical microstructured optical fibres. The effects of preform rotation are included to examine methods for reducing fibre birefringence. Asymptotic and numerical solutions are obtained and applied to two typical microstructured fibres, and a number of practical suggestions are made for achieving sub–mm spin pitches without damaging the microstructure within such fibres.

Chapter 5 is concerned with the stability of drawing capillary tubes, since it is a well known fact, reported extensively in the literature and experimentally observed, that a critical draw–ratio exists. This corresponds to the fact that when the resulting fibres are pulled more rapidly than a certain multiple of the feed speed, the fibres exhibit an instability that eventually leads to the fibre breaking and the drawing process needing to be reset. This is unsatisfactory when a fibre of constant geometry along its length is required, as is often but not always the case in realistic fibre–pulls. We construct a model that agrees well with previous calculations for solid fibres, and make predictions for the case of the stability of the drawing of a capillary tube.

Chapter 6 comprises a full numerical analysis of the equations obtained for the drawing of capillary tubes in Chapter 3, and considers the effects of changes in each of the available parameters of the drawing process on the final fibre–geometry. Numerical examples focus on the effects of preform rotation.

Chapter 7 details the numerical analysis conducted on the drawing of such fibres with the correct temperature dependent viscosity (fitted from measurements taken experimentally) and realistic drawing parameters, and makes comparisons with experiments performed at the Optoelectronics Research Centre, University of Southampton, UK (henceforth Optoelectronics Research Centre).

Chapter 8 discusses a somewhat separate problem of the manufacture of a particular type of fibre whose initial preform looks like a cup handle. The most pressing problem in the consistent manufacture of such fibres is that it is necessary to be able to control and predict the shape of the core region of the fibre. Furthermore, the struts in such a fibre typically thicken as they reach the core and outer–wall of the fibre, and are at their most thin at the central point in the strut. This affects the light propagation modes of the fibre and is highly undesirable. Ideally, experimentalists would like to consistently produce a fibre whose struts are uniformly shaped and whose core is more circular than those observed experimentally. Additionally, it is desirable to vary the geometry of the fibres by using the results of mathematical modelling to inform the structural design of the preform.

We make use of a previous study by Howell [16] to describe the problem asymptotically and solve it numerically. Experimental data is used for comparison, and suggestions are made for an improvement of the mathematical model and also to the preforms used to make such fibres, in order to remove some of the frequently encountered problems.

Chapter 9 discusses the problem of pressurizing a capillary tube by sealing one end of the tube. If pressurization and rotation are used simultaneously, directly applying an overpressure to a capillary tube during drawing is problematic. It is shown that whilst

this procedure may be used to counteract the effects of surface tension in the same way as directly applying an overpressure to a capillary tube, a steady–state draw no longer results. Predictions of the pressure–time and radius–time relationships are made and compared with results obtained experimentally.

Chapter 10 develops a two–phase flow model that allows predictions to be made of the size and distribution of bubbles in the cross–section of a holey fibre preform, and includes effects such as space–varying viscosity. Numerical simulations are performed for a variety of physically interesting cases and the physics of the results explained. The model serves as a first step to a consideration of the more general holey fibre problem.

Chapter 11 sets out the full holey fibre problem and details attempts made to solve the problem for the simplified cases of a solid fibre and a capillary tube.

Chapter 12 draws conclusions and summarizes the results obtained in this thesis. Suggestions are made for future work and the increasing importance of glass extrusion and its modelling is discussed.

1.2.1 Road–map

Since this thesis reports on extremely collaborative work, the mathematical reader and the experimentalist may wish to focus on certain Chapters only.

The mathematical reader might read Chapters 2, 3, 5, 6, 8, 9, 10, 11 and 12. SI units are used throughout unless otherwise specified.

The experimentalist might read Chapters 4, 5, 6, 7, and 12. SI units are used throughout unless otherwise specified.

Additionally, key experimental results are listed briefly at the end of conclusions

sections within most Chapters. Specifically, see §3.8.1, §4.6.1, §5.4.1, §6.5.1, §7.4.1, §8.4.1 and §10.6.1.

1.3 Literature review

The bulk of this thesis is concerned with glass structures that contain air holes, whose potential range of application in the physical sciences is vast. Small mode–area fibres, highly nonlinear fibres for nonlinear devices [5], large mode–area fibres for high–powered devices [3], [17], and atom–guiding fibres [18] are just a few of such applications. Further applications are discussed in more detail in [4], [19], [20].

The photonic bandgap fibre, which makes use of the photonic bandgap occurring in such periodic structures found in holey fibres, is one growth area of particular interest. See [21], [22] and [23] for more detail.

The textile industry has developed a wealth of literature on the spinning of thread-lines [24], [25], [26], [27]. This work was then adapted to glass industry problems in order to study the steady–state drawing of optical fibres [28], [29], [30], in which the flow is assumed to be axisymmetric, Newtonian and inertia–free. Most often the steady–state problem alone is considered, with time dependence being considered only when the stability of solutions to the governing equations is of concern. We will largely follow this approach since only steady–state processes are of practical interest. The reason for this is that when optical fibre is produced in large quantities, uniform (optical and thus geometrical) properties are required, indicating a steady–state process.

A weak stability–analysis of the drawing process was completed in [31]. Draw resonance is the instability observed when fibres are drawn with the ratio of draw speed to feed speed larger than a critical value that depends on draw parameters. It is considered for solid fibres in [27], [32], [33], [34], [35], [36] and [37]. The results from

these studies are used as to test the model developed in this thesis for the stability of drawing capillary tubes (with inner radius set to zero).

The strong temperature dependence of glass viscosity and the difficulty in measuring it directly at the high temperatures used in fibre manufacture has motivated several studies on the effects of heat transfer [38]. Surface tension effects [39] and those of inertia have also been considered [26]. Gravity and inertia were considered together in [40] for the case of a slender geometry and a fibre with an arbitrary transverse cross–section. Fibre breakage was investigated using an asymptotic model in [41].

All of the aforementioned studies considered only solid fibre manufacture, though, and the study of fibres that contain holes seems only to have been reported in [14], [15], [42], [43] and [44]. Thin–walled viscous capillaries were modelled in [27] and [45].

The complexity of equations that describe fibre drawing means that full numerical calculations are required to solve the equations fully, such as those reported in [25], [46] and [47]. It is hoped that we may gain more physical insight into the drawing of microstructured optical fibres without resorting to full numerical simulation.

Chapter 2

The Manufacturing Process

Holey fibres are made directly from a glass preform, whose detailed manufacture and geometric form are discussed at a later point. The glass is usually undoped silica glass, and the preform is essentially 'stretched out' into fibre form after having been heated past its melting point in a furnace. The furnace is designed so that as the fibre is pulled, it leaves the furnace and passes through a diameter gauge used to ensure that a constant fibre geometry is obtained. It then passes through a series of pulleys and onto a rotation drum where the fibre is stored. The feed speed is controlled electronically and determines the speed at which the metal insert in the top of the glass preform is lowered into the furnace. Similarly the draw speed sets the rate at which the drawing wheels are rotated.

The experimental set–up of the draw–down process is shown later (Figure 3.2) in Chapter 3. A photograph of one of the drawing towers at the Optoelectronics Research Centre, is shown in Figure 2.1. An overhead view of a fibre drawing furnace in operation is shown in Figure 2.2.

Optical glass fibres traditionally consist of solid fibres made from two concentric glass cylinders, the outer of which is hollow. In this thesis we will consider both solid fibres and the more complex 'holey' fibre. The cross-section of a typical holey fibre is

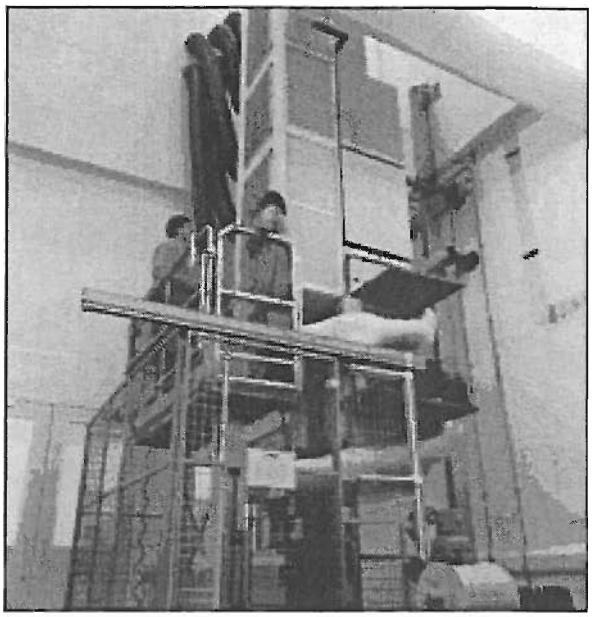

Figure 2.1: A fibre drawing tower at the Optoelectronics Research Centre.

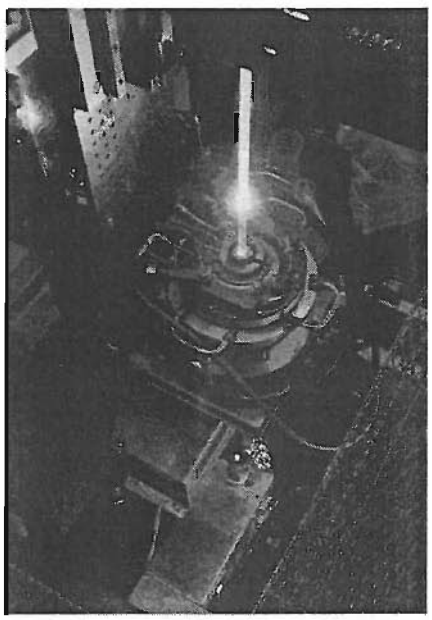

Figure 2.2: An overhead view of a typical fibre drawing furnace.

shown in Figure 1.1. Holey fibres have a range of interesting and important optical properties, but they are currently difficult to manufacture to required specifications. The specifications vary from one fibre to another since the geometric properties are determined by the optical properties required by the experimenter or industry. Consistent manufacture is also difficult as a result of complications arising from the presence of air holes in the preform cross–section.

Holey fibres were first successfully made by the Optoelectronics Research Centre, but since this time several spin–off companies have been established and numerous Universities world–wide include groups that are conducting research on fibres of this type.

Total internal reflection occurs when light is incident at glancing angles at an interface where the refractive index medium is higher than that of the medium past the interface. Optical fibres are dielectric waveguides often formed from two solid transparent materials usually made from glass. The glass preforms used to make such fibres are typically cylindrical, and are drawn into fibre form in a fibre drawing furnace. They guide light by the mechanism of total internal reflection. The final (solid) fibre normally has a core region and a cladding region, and the fibre is coated with a soft coating or buffer. This coating has both optical and mechanical properties. It protects the surface of the fibre, preventing it from being weakened by microscopic scratches. Optically, it is roughly index–matched to the silica cladding, but absorbing so that it absorbs and suppresses undesirable cladding modes.

The presence of air holes in the cross–section of a microstructured fibre lowers the effective refractive–index of the cladding in holey fibres. The difference between the refractive index of the core and the effective refractive–index of the air–glass cladding is a strong function of the wavelength of light. This is because at longer wavelengths the mode extends further into the holes, thus reducing the effective refractive–index of the cladding region.

Some of the industrial consequences of this are the possibility of single–mode oper-

ation over a broad range of wavelengths, and unusual dispersion characteristics that can be exploited, as described above.

We shall now describe the process of the manufacture of optical fibres in two parts. The first part will discuss the manufacture of solid optical fibres and the second part the manufacture of microstructured optical fibres, or holey fibres as they are more commonly known. Within each section a variety of techniques will be described, depending on the type of fibre being considered.

2.1 The manufacture of solid fibres

The overall principle for the manufacture of optical fibre is the same, irrespective of the particular type of fibre being manufactured. That is one of heating a macroscopic piece of structured glass, shaped as a glass rod (the preform), until it becomes fluid enough for it to be stretched out into a long, thin fibre. There are therefore two sub–processes that must be considered: the manufacture of the preform and the manufacture of the fibre.

In the manufacture of solid glass fibres two or more different glasses must somehow be made into one structure so as to provide a core glass and a cladding glass. In general these glasses possess quite different mechanical properties and optical properties. However, the two glasses are chosen so as to minimize the differences in mechanical properties to avoid unwanted effects, including heat–induced stress fracture and viscosities that vary wildly from glass to glass.

Given a suitable choice of core and cladding glass, a macroscopic preform that has one glass wrapped around the other as shown in Figure 2.7 must be produced. This is achievable in several ways, each of which will be described here. One way is to use the double crucible method of preform manufacture, though this method is no longer used. It involves an experimental set–up such as the one shown in Figure 2.4, where

the cladding glass is poured into an outer crucible and the core glass into an inner crucible. The two glasses exit the crucibles at the bottom forming a final preform, and are immediately drawn down into a fibre by the action of rotating wheels in the usual way. The double crucible method may only be used for soft glasses, for the reasons discussed below for the case of glass extrusion.

Second, there is the "rod–in–tube" method in which core glass is inserted into the hole in a capillary tube made from cladding glass. The glasses are then heated until the two materials fuse, at which point the preform is allowed to cool and solidify. The fibre is then drawn from the preform in the usual way. This method is no longer used in practice because of the quality of the surfaces on the inner wall of the capillary tube and the outer wall of the core rod. An advantage of this method is that it is possible with both soft glasses and silica glass, which has a high softening temperature.

When the glass used, such as silica, has a high softening temperature a method known as Modified Chemical Vapour Deposition (MCVD) may be employed. With this technique, a rotating glass tube is passed over a lathe, as shown in Figure 2.3. Chemicals are passed into the tube during this process and extremely fine particles of germanosilicate or phosphosilicate are deposited on the inside of the tube. As the tube passes over the lathe a chemical reaction occurs and the deposited material is fused to the inside wall of the tube. The preform is deposited layer–by–layer, starting first with the cladding layers and then followed by the core layers. Varying the mixture of chemicals alters the refractive index gradient in the resulting preform. When the deposition is complete, the tube is collapsed (drawn down in a fibre drawing furnace as one would the final preform) at approximately 2000C, into a preform of the purest silica with a core of a different composition and hence refractive index, creating the final preform in the usual manner. It may be the case that a variety of different layers are built up on the inner–wall of the capillary tube by varying the chemicals used, before the tube is collapsed into a solid preform rod. Finally, the solid preform is placed in a drawing furnace and drawn down into the final fibre

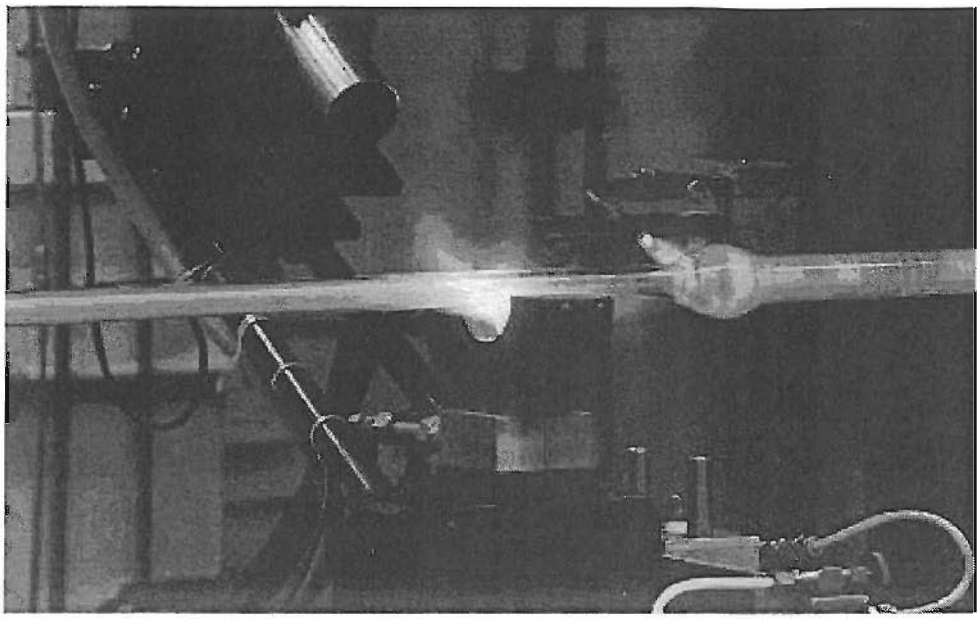

Figure 2.3: A glass capillary tube being rotated and passed over a lathe.

form.

In the event that the glasses are soft (and have a softening temperature much less than that of steel, for example, $T_s < 1000$C) the method of glass extrusion may be used for the manufacture of the preform as it is possible to heat the glass until it is fluid without melting the material of the extrusion die. The method is used both to produce glass preforms of the solid type with a core and cladding glass, and also in the production of holey fibre preforms, in which case only one glass is used. The more general two–glass method will now be described.

Preform manufacture by extrusion is achieved by placing two circular glass disks, typically a few centimetres in diameter and about a centimetre thick, on top of one another inside a die. The die is essentially a highly–engineered metal funnel. A large pressure is applied to the upper glass disk (see Figure 2.8), often called a glass blank, through the depression of a piston. This forces the glasses through the opening at the bottom of the die and results in one glass flowing 'into the other' (see Figures 2.8 and 2.9). In this way the structured preform alluded to above and shown in Figure 2.7 is manufactured.

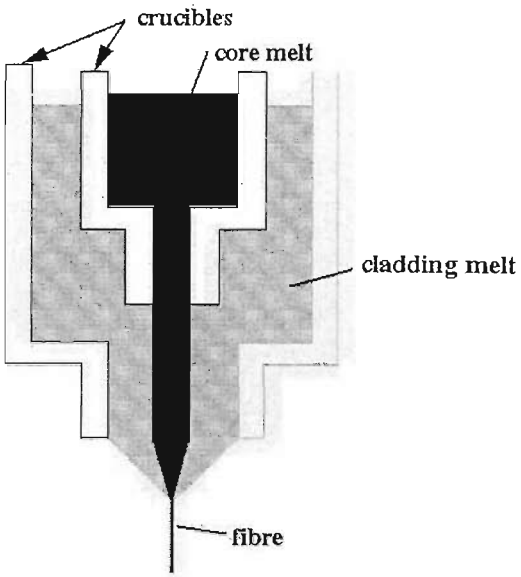

Figure 2.4: The crucible method for preform production.

After this stage is complete the resulting preform is placed into a fibre drawing tower such as the one shown in Figure 2.1, and has its dimensions reduced to those of the final fibre. As mentioned, this preform may take the form of a holey fibre preform made from a single glass that has been pushed through a shaped die to give the preform the necessary 'holey' geometry, or else be in the form of a solid fibre made from two or more distinct glasses. Figures 2.5 and 2.6 show a schematic diagram of the glass extrusion process and a picture of a typical die used to produce a holey fibre preform, respectively.

2.2 The manufacture of microstructured fibres

In the manufacture of conventional optical fibres, a preform is constructed (whose diameter is typically a few centimetres) and drawn down to the final dimensions desired (typically about 125μm).

The process of holey fibre manufacture is rather different to the process for conventional optical fibres. Because both the dimensions of the required fibre are so

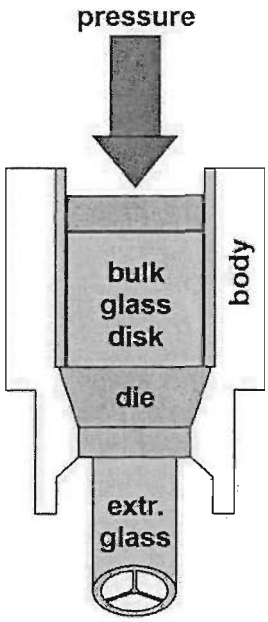

Figure 2.5: Schematic diagram showing the extrusion process.

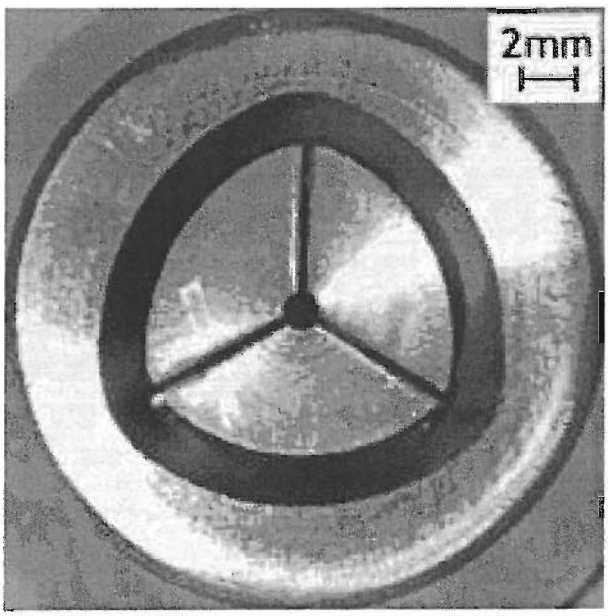

Figure 2.6: An extrusion die used to manufacture holey fibre preforms.

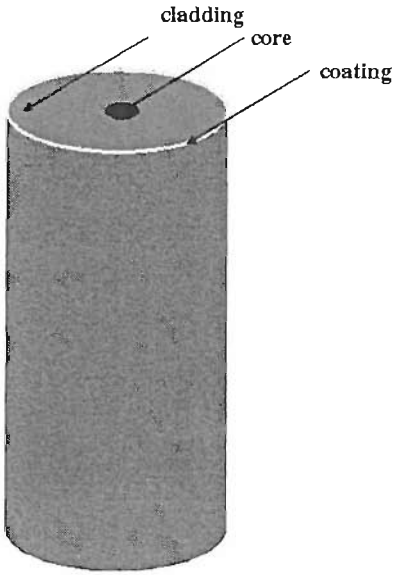

Figure 2.7: Schematic diagram of a conventional optical fibre transverse cross–section.

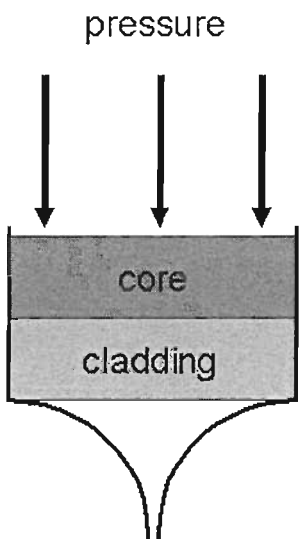

Figure 2.8: Schematic diagram of a die containing core and cladding glass for extrusion.

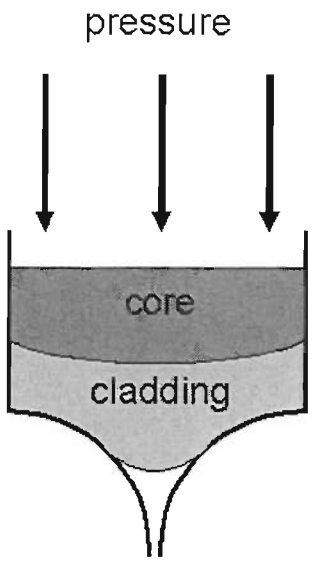

Figure 2.9: Schematic diagram of a die containing core and cladding glass as the extrusion process commences and one glass begins to flow into the other.

small relative to those of the initial preform, and because some practically useful fibres contain such a large density of holes – perhaps several hundred – the draw is often completed in two separate stages. The first stage consists of stacking numerous capillary tubes inside a larger capillary tube (whose diameter is typically a few centimetres) and then drawing this tube and its contents down to a 'cane'.

The second stage of production of the preform involves attaching the drawn–down sections to the inside wall of a large capillary tube (typically a few centimetres in diameter) and drawing the new preform down to the required dimensions (typically 125μm in diameter, as before). This method is the one employed for holey fibres as they are usually made from silica glass. It is not always necessary to employ a two–stage manufacture process (for example, large mode area fibres are made in a single step, i.e. without caning), but when small–scale features are required in the final fibre, a two stage process is used.

Non–silica based holey fibres may also be manufactured and the preforms may be constructed in two main ways. First, the same method as used for silica glass,

that of stacking, may be used. Additionally, the method of glass extrusion may be employed, since it is possible to create a die whose geometry directly gives rise to a 'holey' structure in the resultant flow without the need for stacking the preform. The use of materials with lower melting points than silica glass allows for new preform production techniques, including glass extrusion, to be utilized.

Two other types of fibre not specifically discussed above deserve mention. The first are solid microstructured optical fibres (structures are similar to holey fibres but the "holes" are made from a different glass to the bulk of the fibre, rather than air). Solid holey fibres have potentially wide–ranging applications, particularly for the use in highly–nonlinear devices, due to the high nonlinear index of the materials and the small mode–area of the holey fibre as described in [48]. Indeed, the authors of [48] successfully fabricated such a fibre made from a borosilicate glass containing a high concentration of lead–oxide as a background glass, and potassium fluoride glass as the glass to fill the structure. The preform was manufactured using the rod–in–tube method described above and the fibre was drawn down in the usual way.

The second type of fibres that have not yet been discussed are polymer fibres. Polymer fibres are made by drawing down a fibre from a preform in the usual way, though the methods of manufacture of the preform are wide–ranging. The double crucible method may be used, as may the method of glass extrusion, the stacking method (as for silica holey fibres), the method of polymerization in a mould, or the method of drilling injection–moulding. Thus polymer fibres may have preform structures not restricted to hexagonal or square close–packing resulting from capillary stacking techniques, giving them an advantage over glass holey fibres. Recently these restrictions have been removed for glass holey fibres since it is possible to construct preforms of many varied forms with glass, as has been demonstrated by the Optoelectronics Research Centre. The interested reader may find further details on the fabrication of polymer holey fibres in [12].

Chapter 3

The Rotation of Capillary Tubes

3.1 Abstract

Understanding the drawing process for microstructured optical fibres in order to obtain better control of the final fibre geometry and identify practically useful regimes is of paramount importance, not least of all due to the high cost of the manufacturing process. A fluid mechanics model first developed by Fitt *et al.* [14], [15] based on the small aspect ratio of the capillary tube is extended here, with particular reference made to the spinning of such fibres as they enter the top of the drawing furnace. Predictions are made concerning preform rotation, and a variety of asymptotic limits are examined in order to gain a feel for the physics involved, as well as to identify the aforementioned useful drawing regimes.

3.2 Introduction

Microstructured optical fibres or 'holey fibres' have become an area of increased interest. These fibres consist of a lattice of air–filled holes centred on a solid core,

such as the one pictured in Figure 3.1, and are made by heating a macroscopic preform and drawing it into fibre form. The holes are either open to the atmosphere at the ends of the preform, pressurized with gas by sealing the bottom end of the preform and filling the holes with a pressurized gas from the top, or sealed at one end and then drawn (during the early stages of the draw the other end is automatically sealed and thereafter the preform maintains an overpressure that depends on time. See Chapter 9 for details).

The work started by Fitt *et al.* [14], [15] is developed here by modelling the drawing of optical fibres that contain holes. Extensional flow modelling for fibre drawing was considered by Howell [49] and a number of other sources. The study of Fitt *et al.* [14] proposed equations to determine the behaviour of a drawn capillary tube given only its initial geometry, mechanical properties such as surface tension and viscosity and the speed at which it both enters and leaves the drawing furnace. We extend the work to allow for a rotation of the preform. Though rotation of a solid fibre was considered briefly by Howell [49], to our knowledge the current study is the first theoretical attempt to characterize the effects of rotation on a capillary tube.

Holey fibres are of particular interest and we first consider the case of a single axisymmetric capillary tube. The ideas and techniques developed here may then be extrapolated and used to inform the full holey fibre problem. Additionally, we may also use this simple model to gain some physical and mathematical insight into the full problem. Therefore, the implicit assumption hereafter is that what we learn here may be directly related to the behaviour of a full holey fibre.

The fluid mechanics model constructed gives rise to leading–order equations describing the resulting flow. These equations may be solved numerically in order to make predictions of the final fibre geometry. In addition, physically motivated asymptotic limits of these equations may be analysed both to give physical insight into the process of holey fibre drawing and also to make practically useful predictions; for example by determining whether or not it is possible to stave off surface tension

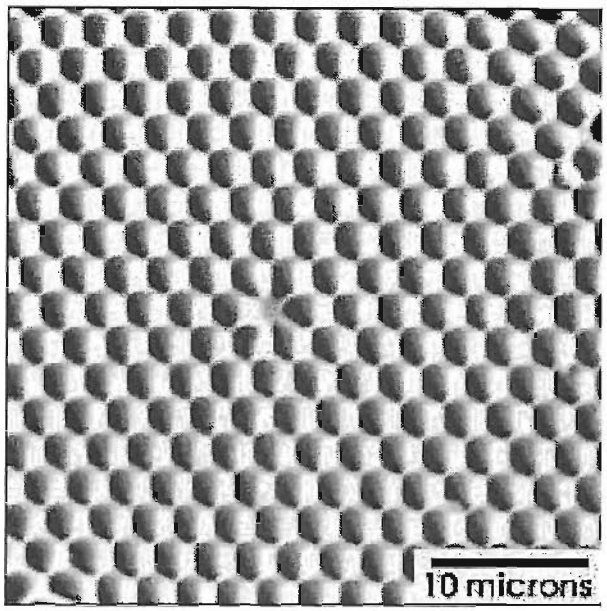

Figure 3.1: A close-up picture of a typical holey fibre core.

induced hole collapse through the act of rotating the preform as it enters the furnace. We show also that the act of imparting angular momentum to a capillary tube as it passes through the furnace affects the final fibre geometry. We not only predict the effects of fibre rotation, but also, for example, calculate the distance between successive twists, i.e. the twist periodicity (commonly known as the 'pitch') in a final drawn fibre. These predictions agree perfectly with experimental data (see later Chapters). For a brief overview of the following model see [50] and for a summary see [51].

3.3 Background

It transpires that holey fibre fabrication is extremely sensitive to the draw parameters used. An exact understanding of the relative effects of changes in one or more of these parameters is required in order to be able to tailor the geometry of the fibre from a single given preform by way of varying these parameters. Additionally, fibre birefringence in holey fibres is often large and is sometimes undesirable. By rotating

the fibre as it enters the furnace we are able to reduce this effect, as will later be explained.

Experimentalists would like to be able to predict more precisely the exact draw–down ratio that will result when pulling an optical fibre, and to gain at least a qualitative understanding of the physical effects that the rotating of holey fibre preforms as they enter the furnace will have on the final fibre geometry.

The presence of air holes within the transverse cross–section of a microstructured fibre presents both challenges and opportunities for the fabrication of these fibres. Competition between viscosity and surface tension effects typically changes the size and shape of the holes during the fibre drawing process, and in extreme cases, hole closure may occur. It is clear that this technology would be greatly aided by the development of accurate tools for predicting the changes that occur during fibre drawing.

Although the fabrication of structured preforms is one of the most labour intensive parts of the manufacturing process it is often possible to produce a number of different fibre profiles from a single preform by changing the conditions under which the fibre is drawn. Such a model would allow this approach to be effective in practice and this work represents the first step towards developing a model for the drawing of microstructured optical fibres whose preforms are spun as they are passed into the furnace.

3.4 The rotation of holey fibres

In a perfectly symmetric waveguide, the two orthogonal polarizations of light (each composed of electric and magnetic fields) travel along the wave–guide with the same velocity. In the case of holey fibres, however, because there are different refractive indices depending on the direction in which the fields are travelling, these two

polarizations travel with different velocities. This is known as fibre birefringence (see [10] and [52]) and is often a pronounced effect in holey fibres. There are three main reasons for its marked presence. First, the small structure scale of the holes; second, the significant refractive index contrast between the core and the effective refractive–index of the cladding; and third, asymmetries introduced by the manufacturing process itself, either intentionally or not. The asymmetries introduced might include the locking–in of some asymmetric stress distribution within the fibre [53].

The effect of this is that the degeneracy of the orthogonal polarization modes is broken, causing the different polarization modes to change their phase and group velocities. In some devices and in sensor applications, for example, it is desirable to maintain polarization and thus increase waveguide asymmetry in order to maximize the mode splitting and thus improve the isolation between the various modes. At the same time, some devices render it imperative to reduce these mode–splitting effects in the fibre.

Because the components travel at different rates, there is interference between the two fields, causing the signal to 'beat', with a characteristic beat–length. Some holey fibres are geometrically symmetric and others are not. In a fibre that has a perfect symmetry, no birefringence is exhibited, but any small deviation from this perfect symmetry may lead to significant birefringence. It is for this reason that birefringence is often present in manufactured fibres.

Introducing a twist into the resulting fibre by rotating the preform as it enters the furnace reduces the birefringence for both solid and microstructured fibres, so long as the twists are on a scale equal to or less than that of the beat length. When this criteria is met, light is coupled between the two polarizations modes. The coupling averages out the effects of the refractive index–differences as the two orthogonal components of light travel the length of the fibre. Thus the resulting fibre has a significantly reduced birefringence.

As explained above, it is sometimes desirable to make use of fibre birefringence

and not remove or reduce it by invoking this method of preform rotation, since birefringent optical fibres are used as polarizers, single polarization transmission lines for coherent systems, sensors and single polarization couplers.

If the removal or reduction of fibre birefringence is required, the glass preform may either be rotated as it enters the furnace, leaving it with an overall twist along its length, or the fibre may be rotated directly as it leaves the furnace. The preferred method is to to rotate the preform as it enters the furnace by attaching an electric drill to the top of the perform and passing the resulting fibre onto a rotating drum (see for example, [54], [55] and [56]). Since nothing significant acts to impede the rotation of the preform, a constant angular frequency may be assumed throughout the drawing process.

As already stated, the reduction of fibre birefringence is achieved by rotating holey fibre preforms as they enter the furnace and setting the rotation rate to zero at the furnace exit. It is later shown that the act of imparting a non–zero angular momentum to the preform as it traverses the furnace affects the final fibre geometry. The distance apart of each successive twist in the final fibre, the twist periodicity, is also established.

As mentioned above, it is also possible to spin the fibre as it leaves the furnace. This has the disadvantage of causing the fibre to exhibit circular birefringence [54], which is often undesirable. The birefringence arises because as the glass cools and solidifies, its large viscosity causes stress to become locked into the fibre. This stress gives rise to further unwanted (circular) birefringence. If the "twist" is taken up as the preform enters the furnace and not when it leaves, these effects can be minimized, thus explaining why in practice preforms are rotated as they enter the furnace [54], [56], [57].

Unlike holey fibres, conventional optical fibres with a sold core and cladding region are routinely rotated. The presence of air holes raises questions as to how such fibres will behave once rotated, thus further motivating this study. The Optoelectronics

Research Centre has been successful in recent experimental trials that rotate holey fibres. See [58] and Chapter 4 for a discussion of this.

Polarization Mode Dispersion (PMD) is a phenomenon of great importance in modern optical communications, since it imposes limitations on both analogue and digital optical systems. It arises from the fact that in optical fibres there exists a small level of birefringence for the reasons stated above. Birefringence causes pulse spreading due to the slight difference between the propagation velocities of the two orthogonal polarization states that constitute the light signal. As a result of fibre movement, temperature variations and other environmental variations, these two polarization states couple strongly. This causes PMD to be both wavelength dependent and strongly affected by the environment. It is therefore desirable to rotate the fibres in order to remove or reduce birefringence, for this additional reason. More detail may be found in [58].

For the remainder of this thesis preform rotation will be described of in terms of its effect on the reduction of fibre birefringence. The effect of PMD reduction will not be discussed in detail.

It should be pointed out that throughout this thesis the starting product of manufacture is termed the preform, the end product is termed fibre, and during the transition from one to the other (whilst the glass is present in the furnace and in the process of being drawn down), the terms preform and fibre are used interchangeably.

3.5 Mathematical modelling

To develop a mathematical model for the process of capillary drawing that is capable of including the effects of internal hole pressurization, surface tension, gravity and inertia as well as including spin, we begin with the Navier-Stokes and convection-diffusion equations, respectively, using cylindrical coordinates. The governing equa-

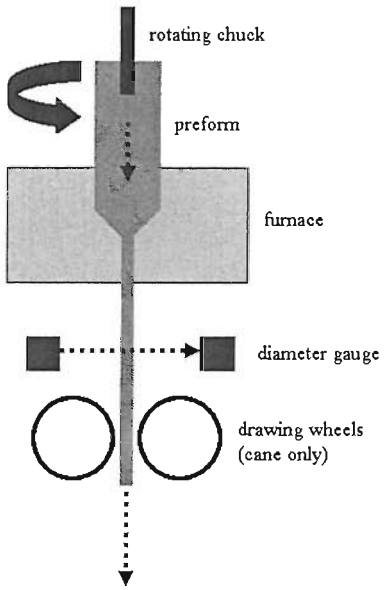

Figure 3.2: Experimental set-up.

tions are (see [59])

$$\rho(w_t + uw_r + ww_z) = -p_z + \frac{1}{r}(\mu r w_r)_r + (2\mu w_z)_z + \frac{1}{r}(\mu r u_z)_r + \rho g, \quad (3.1)$$

$$\rho\left(u_t + uu_r + wu_z - \frac{v^2}{r}\right) = -p_r + \mu\left(\frac{1}{r}(ru)_r\right)_r + (\mu u_z)_z + \mu_z w_r, \quad (3.2)$$

$$\rho\left(v_t + wv_z + uv_r + \frac{uv}{r}\right) = \mu\left(\frac{1}{r}(rv)_r\right)_r + (\mu v_z)_z, \quad (3.3)$$

$$\frac{1}{r}(ru)_r + w_z = 0, \quad (3.4)$$

$$\rho c_p(T_t + uT_z + wT_r) = (kT_z)_z + \frac{1}{r}(krT_r)_r + \sigma\alpha(T_a^4 - T^4). \quad (3.5)$$

In (3.1)–(3.5), t denotes time, z measures the distance along the axis of a capillary, and r denotes distance normal to it. The flow has been assumed to be axisymmetric, and therefore independent of the azimuthal angle θ, although a velocity is permitted to exist in that direction. All t, z and r subscripts denote differentiation and the velocity $\boldsymbol{q}$ of the molten glass is denoted by $\boldsymbol{q} = w\boldsymbol{e}_z + u\boldsymbol{e}_r + v\boldsymbol{e}_\theta$, where $\boldsymbol{e}_z$, $\boldsymbol{e}_r$ and $\boldsymbol{e}_\theta$ are unit vectors in the z, r and θ directions respectively.

A schematic diagram of the geometry of the capillary is shown in Figure 3.3, where v is related to the angular frequency of the preform, and is derived later. The viscosity

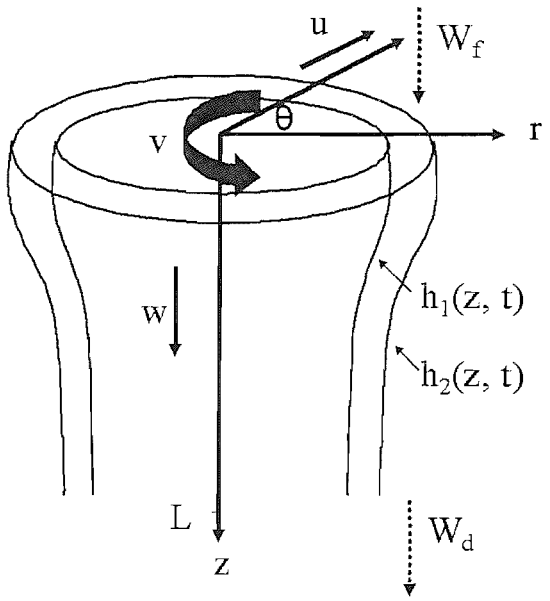

Figure 3.3: Problem geometry.

is assumed to be a function of both z and r for the sake of obtaining the final equations, though later this generalisation will often be dropped and the viscosity assumed to be constant.

The pressure is denoted by p, g is the acceleration due to gravity, and density, dynamic viscosity, surface tension, thermal conductivity and specific heat are denoted by ρ, μ, γ,k and c_p respectively. The glass temperature is denoted by T, the ambient temperature in the furnace by T_a, σ is the Stefan-Boltzmann constant and α is a material constant that involves the emissivity of the fibre.

As shown in Figure 3.3, we denote the inner and outer radii of the capillary by $r = h_1(z,t)$ and $r = h_2(z,t)$ respectively. The equations (3.1)–(3.4) thus apply in the region $0 \leq z \leq L$, $h_1 \leq r \leq h_2$, for $0 \leq t \leq \infty$, and must be solved subject to suitable boundary and initial conditions, which will be considered presently. The feed and draw speeds are denoted by W_f and W_d respectively, the ambient pressure in the air surrounding the fibre is denoted by p_a and the pressure of the air in the hole $r \leq h_1(z,t)$ by p_H.

It is now appropriate to non–dimensionalize (3.1)–(3.5) to take advantage of the small parameters that are present in the problem, henceforth allowing dominant terms to become evident. To non–dimensionalize we set

$$z = L\bar{z}, \quad r = h\bar{r},$$

$$t = (L/W)\bar{t}, \quad h_1 = h\bar{h}_1,$$

$$h_2 = h\bar{h}_2, \quad \mu = \mu_0\bar{\mu},$$

$$p = (\mu_0 W/L)\bar{p}, \quad w = W\bar{w},$$

$$u = (hW/L)\bar{u}, \quad v = \Omega L\bar{v},$$

$$\theta = \bar{\theta}, \quad T_a = T_R\bar{T}_a,$$

and

$$T = T_R\bar{T},$$

where an overbar denotes a non–dimensional quantity and L denotes a typical hot–zone length in the fibre drawing furnace: we only need model the region encompassed by the hot–zone of the drawing furnace, since the fluid solidifies rapidly and is therefore everywhere else assumed to be solid. Here h denotes a typical drawn capillary size, W denotes a typical draw speed and μ_0 and T_R denote a typical glass viscosity and fibre reference–temperature respectively. The constant Ω is a measure of the angular frequency of the fibre.

Upon application of these non–dimensionalizations the equations become

$$\epsilon^2 Re\,(\bar{w}_{\bar{t}} + \bar{u}\bar{w}_{\bar{r}} + \bar{w}\bar{w}_{\bar{z}}) = -\epsilon^2\bar{p}_{\bar{z}} + \frac{1}{\bar{r}}(\bar{\mu}\bar{r}\bar{w}_{\bar{r}})_{\bar{r}} + \epsilon^2(2\bar{\mu}\bar{w}_{\bar{z}})_{\bar{z}} + \frac{\epsilon^2}{\bar{r}}(\bar{\mu}\bar{r}\bar{u}_{\bar{z}})_{\bar{r}} + \frac{\epsilon^2 Re}{Fr}, \quad (3.6)$$

$$\epsilon^2 Re\left(\bar{u}_{\bar{t}} + \bar{u}\bar{u}_{\bar{r}} + \bar{w}\bar{u}_{\bar{z}} - \frac{S^2\bar{v}^2}{\epsilon^2\bar{r}}\right) = -\bar{p}_{\bar{r}} + \bar{\mu}\left(\frac{1}{\bar{r}}(\bar{r}\bar{u})_{\bar{r}}\right)_{\bar{r}} + \epsilon^2(\bar{\mu}\bar{u}_{\bar{z}})_{\bar{z}} + \bar{\mu}_{\bar{z}}\bar{w}_{\bar{r}}, \quad (3.7)$$

$$Re\left(\bar{v}_{\bar{t}} + \bar{w}\bar{v}_{\bar{z}} + \bar{u}\bar{u}_{\bar{r}} + \frac{\bar{u}\bar{v}}{\bar{r}}\right) = \bar{\mu}\frac{1}{\epsilon^2}\left(\frac{1}{\bar{r}}(\bar{r}\bar{v})_{\bar{r}}\right)_{\bar{r}} + (\bar{\mu}\bar{v}_{\bar{z}})_{\bar{z}}, \quad (3.8)$$

$$\frac{1}{\bar{r}}(\bar{r}\bar{u})_{\bar{r}} + \bar{w}_{\bar{z}} = 0, \quad (3.9)$$

$$\bar{T}_{\bar{t}} + \bar{u}\bar{T}_{\bar{z}} + \bar{w}\bar{T}_{\bar{r}} = \frac{1}{PrRe}(\bar{T}_{\bar{z}})_{\bar{z}} + \frac{1}{\bar{r}\epsilon^2 PrRe}(\bar{r}\bar{T}_{\bar{r}})_{\bar{r}} + \gamma(\bar{T}_a^4 - \bar{T}^4), \quad (3.10)$$

where the key non–dimensional parameters in the problem are given by

$$\epsilon = \frac{h}{L}, \quad Re = \frac{LW\rho}{\mu_0}, \quad Fr = \frac{W^2}{gL}, \quad St = \frac{L^2\rho g}{\mu_0 W},$$

and

$$Pr = \frac{\mu_0 c_p}{k}, \quad S = \frac{\Omega L}{W}, \quad \Gamma = \frac{L\sigma\alpha T_R^3}{\rho c_p W}.$$

We note at this stage that in all cases of interest $h \ll L$ (the largest values of ϵ tend to occur for capillaries, where L is of order cm and h of order mm. For optical fibres ϵ is smaller still). We shall therefore assume henceforth that the small parameter in the problem is ϵ, where $\epsilon \ll 1$. Typically $Re < 1$ and $Fr = O(1)$. The leading–order equations in ϵ are now naively satisfied by the obvious *ansätze*

$$\begin{aligned}
\bar{w} &= \bar{w}_0(\bar{z},\bar{t}) + \epsilon^2\bar{w}_1(\bar{z},\bar{r},\bar{t}) + ...,\\
\bar{u} &= \bar{u}_0(\bar{z},\bar{r},\bar{t}) + \epsilon^2\bar{u}_1(\bar{z},\bar{r},\bar{t}) + ...,\\
\bar{v} &= \bar{v}_0(\bar{z},\bar{r},\bar{t}) + \epsilon^2\bar{v}_1(\bar{z},\bar{r},\bar{t}) + ...,\\
\bar{p} &= \frac{\bar{p}_a}{\epsilon^2} + \bar{P}(\bar{z},\bar{r},\bar{t}) + ...,\\
\bar{T} &= \bar{T}_0(\bar{z},\bar{t}) + \epsilon^2\bar{T}_1(\bar{z},\bar{r},\bar{t}) + ...,
\end{aligned}$$

where $\bar{p}_a$ denotes the non–dimensional ambient pressure, defined in the obvious way by

$$p_a = (\mu_0 W/L)\bar{p}_a.$$

From the continuity equation we have

$$\bar{u}_0 = -\frac{\bar{r}\bar{w}_{0\bar{z}}}{2} + \frac{\bar{A}}{\bar{r}}, \tag{3.11}$$

where the function $\bar{A}(\bar{z},\bar{t})$ is to be determined. Since from our *ansätze* $\bar{T}$, (and thus the viscosity) is independent of $\bar{r}$ to leading order, it follows that, by equating like powers of ϵ, to leading order, the $\bar{z}$-momentum equation (3.6) becomes

$$Re\,(\bar{w}_{0\bar{t}} + \bar{w}_0\bar{w}_{0\bar{z}}) + \bar{P}_{\bar{z}} - \frac{Re}{Fr} - 2(\bar{\mu}\bar{w}_{0\bar{z}})_{\bar{z}} + \bar{\mu}\bar{w}_{0\bar{z}\bar{z}} = \frac{1}{\bar{r}}(\bar{\mu}\bar{r}\bar{w}_{1\bar{r}})_{\bar{r}}. \tag{3.12}$$

To leading order, the $\bar{\theta}$-momentum equation (3.8) becomes

$$\bar{v}_{0\bar{r}\bar{r}} + \frac{\bar{v}_{0\bar{r}}}{\bar{r}} - \frac{\bar{v}_0}{\bar{r}^2} = 0, \tag{3.13}$$

and the $\bar{r}$-momentum (3.7) yields, using (3.11),

$$\bar{P}_{\bar{r}} = \frac{ReS^2\bar{v}_0^2}{\bar{r}}.$$

The energy equation (3.10) gives

$$\bar{T}_{0\bar{t}} + \bar{u}_0\bar{T}_{0\bar{z}} - \frac{1}{RePr}(\bar{T}_{0\bar{z}})_{\bar{z}} - \gamma(\bar{T}_a^4 - \bar{T}_0^4) = \frac{1}{\bar{r}RePr}(\bar{r}\bar{T}_{1\bar{r}})_{\bar{r}}, \tag{3.14}$$

and to close the problem it is now necessary to specify the relevant kinematic conditions, normal and tangential stress conditions, and temperature conditions on the free boundaries $\bar{h}_1$ and $\bar{h}_2$. The kinematic boundary conditions are

$$\bar{u}_0 = \bar{h}_{1\bar{t}} + \bar{w}_0\bar{h}_{1\bar{z}} \quad \text{at} \quad \bar{r} = \bar{h}_1, \tag{3.15}$$

$$\bar{u}_0 = \bar{h}_{2\bar{t}} + \bar{w}_0\bar{h}_{2\bar{z}} \quad \text{at} \quad \bar{r} = \bar{h}_2. \tag{3.16}$$

As mentioned above, we wish to allow for the possibility of controlling hole size by internal hole pressurization. The normal stress boundary conditions will thus include both the surface tension coefficient γ and the fibre hole pressure p_H. If we define the non–dimensional fibre hole pressure by $p_H = (\mu_0 W/L)\bar{p}_H$, it is clear that we must further write

$$\bar{p}_H = \frac{\bar{p}_a}{\epsilon^2} + \bar{p}_o, \tag{3.17}$$

where $\bar{p}_o$ is the non–dimensional hole overpressure. This scaling reflects the fact that, unless the fibre hole pressure is within $O(\epsilon^2)$ of the ambient pressure, the capillary will either collapse immediately or "explode" [14]. The equation (3.17) therefore already gives a useful estimate of the size of hole inflation pressure that is required to prevent collapse.

The normal stress boundary conditions may now be applied. The stress tensor $\mathcal{T}$ written in terms of non–dimensional quantities is given by

$$\mathcal{T} = \begin{pmatrix} (\frac{\mu_0 W}{L})(-\bar{p} + 2\bar{\mu}\bar{w}_{\bar{z}}) & (\mu_0\Omega\bar{\mu}\bar{v}_{\bar{z}}) & (\frac{\mu_0 W}{L})(\bar{\mu}\epsilon\bar{u}_{\bar{z}} + \frac{\bar{\mu}\bar{w}_{\bar{r}}}{\epsilon}) \\ (\mu_0\Omega\bar{\mu}\bar{v}_{\bar{z}}) & (\frac{\mu_0 W}{L})(-\bar{p} + 2\bar{\mu}\bar{r}\bar{v}_{\bar{\theta}}) & (\frac{\mu_0\Omega\bar{\mu}}{\epsilon})(-\frac{\bar{v}}{\bar{r}} + \bar{v}_{\bar{r}}) \\ (\frac{\mu_0 W}{L})(\bar{\mu}\epsilon\bar{u}_{\bar{z}} + \frac{\bar{\mu}\bar{w}_{\bar{r}}}{\epsilon}) & (\frac{\mu_0\Omega\bar{\mu}}{\epsilon})(-\frac{\bar{v}}{\bar{r}} + \bar{v}_{\bar{r}}) & (\frac{\mu_0 W}{L})(-\bar{p} + 2\bar{\mu}\bar{u}_{\bar{r}}) \end{pmatrix}.$$

If we now denote the dimensionless unit outward-pointing normal to $\bar{r} = \bar{h}_i$ (where $i = 1, 2$) by $\hat{\boldsymbol{n}}_i$, then the normal stress conditions are

$$-\hat{\boldsymbol{n}}_1^T \mathcal{T} \hat{\boldsymbol{n}}_1 + \frac{\bar{\gamma}\mu_0 W}{\bar{h}_1 L} = \frac{\bar{p}_H \mu_0 W}{L} \text{ at } \bar{r} = \bar{h}_1, \tag{3.18}$$

$$-\hat{\boldsymbol{n}}_2^T \mathcal{T} \hat{\boldsymbol{n}}_2 - \frac{\bar{\gamma}\mu_0 W}{\bar{h}_2 L} = \frac{\bar{p}_a \mu_0 W}{L\epsilon^2} \text{ at } \bar{r} = \bar{h}_2. \tag{3.19}$$

Here, a non-dimensional surface tension coefficient $\bar{\gamma}$ has been defined by $\gamma = \mu_0 W \epsilon \bar{\gamma}$, thus immediately giving an estimate of the order of magnitude that the size of surface tension of the molten glass has to be to influence the final shape of the fibre.

We now assume that the tangential stress on both of the fibre boundaries is zero (for all realistic rotation rates this is realistic). For $i = 1, 2$, we therefore have

$$\hat{\boldsymbol{t}}_i^T \mathcal{T} \hat{\boldsymbol{n}}_i = 0,$$

where $\hat{\boldsymbol{t}}_i$ is the relevant unit tangent vector normal to the z–direction.

To complete the specification of the boundary conditions, we assume that, because the thermal conductivity of air is much lower than the thermal conductivity of glass, the fibre is essentially insulated on its inner surface. We also assume that the fibre loses heat to the surrounding air in the furnace by Newton-type cooling at its outer surface. Thus (in dimensional variables)

$$T_r = 0 \quad \text{at } r = h_1,$$

$$kT_r = N(T_a - T) \quad \text{at } r = h_2,$$

where N is a heat transfer coefficient that we assume for simplicity is constant and known from standard engineering correlations.

The normal and tangential stress conditions and thermal boundary conditions may now be expanded according to the *ansätze* for $\bar{w}$, $\bar{u}$ and $\bar{p}$. With

$$\hat{\boldsymbol{n}}_i^T = \frac{(-1)^{i+1}}{\sqrt{1+\epsilon^2 \bar{h}_{i\bar{z}}^2}}(\epsilon \bar{h}_{i\bar{z}}, 0, -1), \quad \hat{\boldsymbol{t}}_i^T = \frac{(-1)^{i+1}}{\sqrt{1+\epsilon^2 \bar{h}_{i\bar{z}}^2}}(1, 0, \epsilon \bar{h}_{i\bar{z}}),$$

we find that

$$\begin{aligned}
-\frac{\bar{\gamma}}{\bar{h}_1} - \bar{P}_1 + 2\bar{\mu}\bar{u}_{0\bar{r}} + \bar{p}_o &= 0 \quad \text{at } \bar{r} = \bar{h}_1, \\
\frac{\bar{\gamma}}{\bar{h}_2} - \bar{P}_2 + 2\bar{\mu}\bar{u}_{0\bar{r}} &= 0 \quad \text{at } \bar{r} = \bar{h}_2, \\
2\bar{h}_{1\bar{z}}(\bar{w}_{0\bar{z}} - \bar{u}_{0\bar{r}}) - \bar{u}_{0\bar{z}} &= \bar{w}_{1\bar{r}} \quad \text{at } \bar{r} = \bar{h}_1, \\
2\bar{h}_{2\bar{z}}(\bar{w}_{0\bar{z}} - \bar{u}_{0\bar{r}}) - \bar{u}_{0\bar{z}} &= \bar{w}_{1\bar{r}} \quad \text{at } \bar{r} = \bar{h}_2.
\end{aligned}$$

An additional stress boundary condition is that of the tangential stress being zero, and with the same normal vector, but with the tangential vector now becoming

$$\hat{\boldsymbol{t}}_i^T = (0, 1, 0),$$

for $i = 1,2$.

This leads us to the following additional boundary conditions. To leading order

$$\frac{\bar{v}_0}{\bar{h}_1} = \bar{v}_{0\bar{r}} \quad \text{at } \bar{r} = \bar{h}_1, \tag{3.20}$$

$$\frac{\bar{v}_0}{\bar{h}_2} = \bar{v}_{0\bar{r}} \quad \text{at } \bar{r} = \bar{h}_2. \tag{3.21}$$

To $O(\epsilon^2)$ these boundary conditions become

$$\bar{v}_{1\bar{r}} - \bar{h}_{1\bar{z}}\bar{v}_{0\bar{z}} - \frac{\bar{v}_1}{\bar{r}} = 0 \quad \text{at } \bar{r} = \bar{h}_1, \tag{3.22}$$

and

$$\bar{v}_{1\bar{r}} - \bar{h}_{2\bar{z}}\bar{v}_{0\bar{z}} - \frac{\bar{v}_1}{\bar{r}} = 0 \quad \text{at } \bar{r} = \bar{h}_2. \tag{3.23}$$

Expanded in non–dimensional variables, the thermal boundary conditions become

$$\bar{T}_{1\bar{r}} = 0 \quad \text{at } \bar{r} = \bar{h}_1, \tag{3.24}$$

$$\bar{T}_{1\bar{r}} = \bar{N}(\bar{T}_a - \bar{T}_0) \quad \text{at } \bar{r} = \bar{h}_2, \tag{3.25}$$

where $\bar{N} = LN/(\epsilon k)$ determines the relative importance of the Newton cooling, so that for small values of $\bar{N}$ the heat transfer is negligible, but for large $\bar{N}$ the condition is essentially $T = T_a$.

It is now possible to derive a closed system of leading–order equations for annular fibre drawing. We first integrate the $\bar{r}$-momentum equation having solved the leading–order $\bar{\theta}$-momentum equation to give

$$\bar{v}_0 = \bar{B}(\bar{z},\bar{t})\bar{r}, \tag{3.26}$$

where we have ignored a term $\frac{D(\bar{z},\bar{t})}{\bar{r}}$ as a result of the fact that substituting the result for $\bar{v}_0$ into the leading–order boundary conditions (3.20)–(3.21) gives $D(\bar{z},\bar{t}) = 0$, leading us to the fact that the pressure is given by

$$\bar{P} = \frac{ReS^2\bar{B}(\bar{z},\bar{t})^2\bar{r}^2}{2} + \bar{C}(\bar{z},\bar{t}). \tag{3.27}$$

$\bar{B}(\bar{z},\bar{t})$ may be considered an angular frequency, although it is not the total angular frequency. The reason for this is that

$$\bar{v} = \bar{v}_0(\bar{z},\bar{r},\bar{t}) + \epsilon^2\bar{v}_1(\bar{z},\bar{r},\bar{t}) + ...,$$

meaning that $\frac{\bar{v}}{\bar{r}}$ rather than $\frac{\bar{v}_0}{\bar{r}}$ is the correct expression for the angular frequency. It is interesting to note that we in no way specified the form of the $\bar{r}$–dependence that $\bar{v}_0$ should have, and we find that to leading order it is in the familiar '$\bar{v} = \bar{r}\bar{\omega}$' form, with $\bar{\omega}$ as the angular frequency. We would expect that higher order terms in the expansion of $\bar{v}$ would bring in other less simple dependencies on the fibre radius, $\bar{r}$. Both $\bar{B}(\bar{z},\bar{t})$ and $\bar{C}(\bar{z},\bar{t})$ are unknown functions of integration that will later be determined.

The result (3.27) for $\bar{P}$ may now be substituted into the $\bar{z}$-momentum equation (3.12), which is multiplied by $\bar{r}$ and integrated from $\bar{r} = \bar{h}_1$ to $\bar{r} = \bar{h}_2$. This replaces the $\bar{r}$–dependence with expressions for the free surfaces $\bar{h}_1$ and $\bar{h}_2$ giving

$$\frac{(\bar{h}_2^2 - \bar{h}_1^2)}{2}\left(Re(\bar{w}_{0\bar{t}} + \bar{w}_0\bar{w}_{0\bar{z}}) + \bar{C}_{\bar{z}} - \frac{Re}{Fr} - 2(\bar{\mu}\bar{w}_{0\bar{z}})_{\bar{z}} + \bar{\mu}\bar{w}_{0\bar{z}\bar{z}}\right) =$$
$$-\frac{ReS^2(\bar{B}^2)_{\bar{z}}}{8}(\bar{h}_2^4 - \bar{h}_1^4) + (\bar{\mu}\bar{h}_2\bar{w}_{1\bar{r}})\,|_{\bar{h}_2} - (\bar{\mu}\bar{h}_1\bar{w}_{1\bar{r}})\,|_{\bar{h}_1}\,. \tag{3.28}$$

Next, the energy equation (3.14) is multiplied through by $\bar{r}$ and integrated from $\bar{r} = \bar{h}_1$ to $\bar{r} = \bar{h}_2$ to yield

$$\left(\frac{\bar{h}_2^2 - \bar{h}_1^2}{2}\right)\left(\bar{T}_{0\bar{t}} + \bar{w}_0\bar{T}_{0\bar{z}} - \frac{1}{RePr}(\bar{T}_{0\bar{z}})_{\bar{z}} - \Gamma(\bar{T}_a^4 - \bar{T}_0^4)\right) =$$

$$\frac{1}{RePr}(\bar{h}_2\bar{T}_{1\bar{r}}\,|_{\bar{h}_2} - \bar{h}_1\bar{T}_{1\bar{r}}\,|_{\bar{h}_1}).$$

The kinematic boundary conditions (3.15) and (3.16) now give

$$(\bar{h}_1^2)_{\bar{t}} + (\bar{h}_1^2\bar{w}_0)_{\bar{z}} = 2\bar{A}(\bar{z},\bar{t}), \tag{3.29}$$

$$(\bar{h}_2^2)_{\bar{t}} + (\bar{h}_2^2\bar{w}_0)_{\bar{z}} = 2\bar{A}(\bar{z},\bar{t}), \tag{3.30}$$

and the normal and tangential stress boundary conditions, when applied at $\bar{r} = \bar{h}_1$ and $\bar{r} = \bar{h}_2$ respectively, give

$$0 = -\frac{\bar{\gamma}}{\bar{h}_1} - \bar{P}_1 + \bar{p}_o + \bar{\mu}\left(-\bar{w}_{0\bar{z}} - \frac{2\bar{A}}{\bar{h}_1^2}\right), \tag{3.31}$$

$$0 = \frac{\bar{\gamma}}{\bar{h}_2} - \bar{P}_2 + \bar{\mu}\left(-\bar{w}_{0\bar{z}} - \frac{2\bar{A}}{\bar{h}_2^2}\right), \tag{3.32}$$

$$\bar{w}_{1\bar{r}}\,|_{\bar{r}=\bar{h}_1} = 2\bar{h}_{1\bar{z}}\left(\frac{3\bar{w}_{0\bar{z}}}{2} + \frac{\bar{A}}{\bar{h}_1^2}\right) - \frac{\bar{A}_{\bar{z}}}{\bar{h}_1} + \frac{\bar{h}_1\bar{w}_{0\bar{z}\bar{z}}}{2}, \tag{3.33}$$

$$\bar{w}_{1\bar{r}}\,|_{\bar{r}=\bar{h}_2} = 2\bar{h}_{2\bar{z}}\left(\frac{3\bar{w}_{0\bar{z}}}{2} + \frac{\bar{A}}{\bar{h}_2^2}\right) - \frac{\bar{A}_{\bar{z}}}{\bar{h}_2} + \frac{\bar{h}_2\bar{w}_{0\bar{z}\bar{z}}}{2}, \tag{3.34}$$

while the relevant temperature boundary conditions are (3.24) and (3.25).

The $\bar{\theta}$-momentum equation (3.8) correct to $O(\epsilon^2)$ gives

$$Re\left(\bar{v}_{0\bar{t}} + \bar{v}_0\bar{v}_{0\bar{r}} + \bar{w}_0\bar{v}_{0\bar{z}} + \frac{\bar{u}_0\bar{v}_0}{\bar{r}}\right) = \bar{\mu}\left(\bar{v}_{1\bar{r}\bar{r}} + \frac{\bar{v}_{1\bar{r}}}{\bar{r}} - \frac{\bar{v}_1}{\bar{r}^2}\right) + (\mu\bar{v}_{0\bar{z}})_{\bar{z}}. \tag{3.35}$$

On multiplying through by $\bar{r}^2$, making use of relations for $\bar{v}_0$ and the continuity equation, and integrating from $\bar{r} = \bar{h}_1$ to $\bar{r} = \bar{h}_2$, we learn that, upon application of the relevant boundary conditions (3.22)–(3.23), (3.35) becomes

$$Re\bar{B}_{\bar{t}}(\bar{h}_2^4 - \bar{h}_1^4) - Re\bar{B}\bar{w}_{0\bar{z}}(\bar{h}_2^4 - \bar{h}_1^4) + 4Re\bar{A}\bar{B}(\bar{h}_2^2 - \bar{h}_1^2)$$
$$+Re\bar{B}_{\bar{z}}\bar{w}_0(\bar{h}_2^4 - \bar{h}_1^4) = \left(\bar{\mu}\bar{B}_{\bar{z}}(\bar{h}_2^4 - \bar{h}_1^4)\right)_{\bar{z}}. \tag{3.36}$$

3.5.1 Summary of equations and boundary conditions

For completeness, the leading–order equations are

$$\frac{(\bar{h}_2^2 - \bar{h}_1^2)}{2}\left(Re(\bar{w}_{0\bar{t}} + \bar{w}_0\bar{w}_{0\bar{z}}) + \bar{C}_{\bar{z}} - \frac{Re}{Fr} - 2(\bar{\mu}\bar{w}_{0\bar{z}})_{\bar{z}} + \bar{\mu}\bar{w}_{0\bar{z}\bar{z}}\right) =$$

$$-\frac{ReS^2(\bar{B}^2)_{\bar{z}}}{8}(\bar{h}_2^4-\bar{h}_1^4)+(\bar{\mu}\bar{h}_2\bar{w}_{1\bar{r}})\mid_{\bar{h}_2}-(\bar{\mu}\bar{h}_1\bar{w}_{1\bar{r}})\mid_{\bar{h}_1}, \tag{3.37}$$

and

$$Re\bar{B}_{\bar{t}}(\bar{h}_2^4-\bar{h}_1^4)-ReB\bar{w}_{0\bar{z}}(\bar{h}_2^4-\bar{h}_1^4)+4Re\bar{A}\bar{B}(\bar{h}_2^2-\bar{h}_1^2)$$
$$+Re\bar{B}_{\bar{z}}\bar{w}_0(\bar{h}_2^4-\bar{h}_1^4)=\left(\bar{\mu}\bar{B}_{\bar{z}}(\bar{h}_2^4-\bar{h}_1^4)\right)_{\bar{z}}, \tag{3.38}$$

with boundary conditions given by

$$(\bar{h}_1^2)_{\bar{t}}+(\bar{h}_1^2\bar{w}_0)_{\bar{z}}=2\bar{A}(\bar{z},\bar{t}), \tag{3.39}$$

$$(\bar{h}_2^2)_{\bar{t}}+(\bar{h}_2^2\bar{w}_0)_{\bar{z}}=2\bar{A}(\bar{z},\bar{t}), \tag{3.40}$$

$$0=-\frac{\bar{\gamma}}{\bar{h}_1}-\bar{P}_1+\bar{p}_o+\bar{\mu}\left(-\bar{w}_{0\bar{z}}-\frac{2\bar{A}}{\bar{h}_1^2}\right), \tag{3.41}$$

$$0=\frac{\bar{\gamma}}{\bar{h}_2}-\bar{P}_2+\bar{\mu}\left(-\bar{w}_{0\bar{z}}-\frac{2\bar{A}}{\bar{h}_2^2}\right), \tag{3.42}$$

$$\bar{w}_{1\bar{r}}\mid_{\bar{r}=\bar{h}_1}=2\bar{h}_{1\bar{z}}\left(\frac{3\bar{w}_{0\bar{z}}}{2}+\frac{\bar{A}}{\bar{h}_1^2}\right)-\frac{\bar{A}_{\bar{z}}}{\bar{h}_1}+\frac{\bar{h}_1\bar{w}_{0\bar{z}\bar{z}}}{2}, \tag{3.43}$$

$$\bar{w}_{1\bar{r}}\mid_{\bar{r}=\bar{h}_2}=2\bar{h}_{2\bar{z}}\left(\frac{3\bar{w}_{0\bar{z}}}{2}+\frac{\bar{A}}{\bar{h}_2^2}\right)-\frac{\bar{A}_{\bar{z}}}{\bar{h}_2}+\frac{\bar{h}_2\bar{w}_{0\bar{z}\bar{z}}}{2}, \tag{3.44}$$

and

$$\bar{P}=\frac{ReS^2\bar{B}(\bar{z},\bar{t})^2\bar{r}^2}{2}+\bar{C}(\bar{z},\bar{t}), \tag{3.45}$$

where $\bar{P}$ is to be specified on $\bar{r}=\bar{h}_1$ and $\bar{r}=\bar{h}_2$.

The equations (3.37), (3.39), (3.40), (3.41)-(3.44) and (3.38), together with the equations for $\bar{P}$ at $\bar{r}=\bar{h}_1$ and $\bar{r}=\bar{h}_2$ respectively (obtained using (3.45)), now constitute a system of ten equations in ten unknowns for the quantities $\bar{h}_1$, $\bar{h}_2$, $\bar{w}_0$, $\bar{P}_1$, $\bar{P}_2$, $\bar{C}_{\bar{z}}$ (through $\bar{C}$), $\bar{B}$, $\bar{A}$, $\bar{w}_{1r}\mid_{\bar{r}=\bar{h}_1}$ and $\bar{w}_{1r}\mid_{\bar{r}=\bar{h}_2}$. These equations may now be greatly simplified. If we regard (3.41) and (3.42) as linear equations for $\bar{A}$ and $\bar{C}$, we find, after the appropriate substitutions that

$$\bar{A}=\frac{\bar{h}_1\bar{h}_2(2\bar{p}_o\bar{h}_1\bar{h}_2-2\bar{\gamma}(\bar{h}_1+\bar{h}_2)-ReS^2\bar{B}^2(\bar{h}_2\bar{h}_1^3-\bar{h}_1\bar{h}_2^3))}{4\bar{\mu}(\bar{h}_2^2-\bar{h}_1^2)}, \tag{3.46}$$

$$\bar{C}=\frac{2\gamma(\bar{h}_1+\bar{h}_2)+2\bar{\mu}\bar{w}_{0\bar{z}}(\bar{h}_1^2-\bar{h}_2^2)-2\bar{p}_o\bar{h}_1^2+ReS^2\bar{B}^2(\bar{h}_1^4-\bar{h}_2^4)}{2(\bar{h}_2^2-\bar{h}_1^2)}. \tag{3.47}$$

Using (3.43) and (3.44) in (3.37), a great deal of cancellation occurs, and the final equations that govern the drawing of a capillary become

$$Re\left((\bar{h}_2^2-\bar{h}_1^2)\left(\bar{w}_{0\bar{t}}+\bar{w}_0\bar{w}_{0\bar{z}}-\frac{1}{Fr}\right)\right)=(3\bar{\mu}(\bar{h}_2^2-\bar{h}_1^2)\bar{w}_{0\bar{z}}$$

$$+\bar{\gamma}(\bar{h}_1+\bar{h}_2)+\frac{1}{4}ReS^2(\bar{h}_2^4-\bar{h}_1^4)\bar{B}^2)_{\bar{z}}, \tag{3.48}$$

$$(\bar{h}_1^2)_{\bar{t}}+(\bar{h}_1^2\bar{w}_0)_{\bar{z}}=\frac{\bar{h}_1\bar{h}_2(2\bar{p}_o\bar{h}_1\bar{h}_2-2\bar{\gamma}(\bar{h}_1+\bar{h}_2)+ReS^2\bar{B}^2\bar{h}_1\bar{h}_2(\bar{h}_2^2-\bar{h}_1^2))}{2\bar{\mu}(\bar{h}_2^2-\bar{h}_1^2)}, \tag{3.49}$$

$$(\bar{h}_2^2)_{\bar{t}}+(\bar{h}_2^2\bar{w}_0)_{\bar{z}}=\frac{\bar{h}_1\bar{h}_2(2\bar{p}_o\bar{h}_1\bar{h}_2-2\bar{\gamma}(\bar{h}_1+\bar{h}_2)+ReS^2\bar{B}^2\bar{h}_1\bar{h}_2(\bar{h}_2^2-\bar{h}_1^2))}{2\bar{\mu}(\bar{h}_2^2-\bar{h}_1^2)}, \tag{3.50}$$

$$Re\left(\bar{h}_2^2(\bar{h}_2^2\bar{B})_{\bar{t}}-\bar{h}_1^2(\bar{h}_1^2\bar{B})_{\bar{t}}\right)+Re\bar{w}_0(\bar{h}_2^2(\bar{h}_2^2\bar{B})_{\bar{z}}-\bar{h}_1^2(\bar{h}_1^2\bar{B})_{\bar{z}})+\frac{Re\bar{p}_o}{\bar{\mu}}\bar{B}\bar{h}_1^2\bar{h}_2^2$$

$$-\frac{Re\bar{\gamma}\bar{B}\bar{h}_1\bar{h}_2}{\bar{\mu}}(\bar{h}_1+\bar{h}_2)+\frac{Re^2S^2\bar{B}^3\bar{h}_1^2\bar{h}_2^2(\bar{h}_2^2-\bar{h}_1^2)}{2\bar{\mu}}=\left(\bar{\mu}(\bar{h}_2^4-\bar{h}_1^4)\bar{B}_{\bar{z}}\right)_{\bar{z}}, \tag{3.51}$$

$$\frac{(h_2^2-h_1^2)}{2}[\rho c_p(T_{0t}+u_0T_{0z})-k(T_{0z})_z-\sigma\alpha(T_a^4-T_0^4)]=h_2N(T_a-T_0). \tag{3.52}$$

To fully close the problem (3.48)–(3.51) it is necessary to specify appropriate boundary and initial conditions. It is simplest to assume that $\bar{h}_1$, $\bar{h}_2$, $\bar{w}_0$, $\bar{B}$ and T_0 are all known as functions of $\bar{z}$ at time $\bar{t}=0$; for the majority of this study, however, we will be interested primarily in steady-state fibre manufacture. As far as boundary conditions are concerned, the preform geometry is invariably known, the feed speed is normally prescribed and the temperatures at the start ($\bar{z}=0$) and end of the draw ($\bar{z}=1$) are assumed to be given. At the furnace exit different boundary conditions may be appropriate for different regimes of fibre manufacture. For "caning" (the drawing of relatively large capillaries with outer diameters (ODs) of order mm), the capillaries are normally pulled by counter-rotating wheels that travel at a constant speed: see Figure 3.2. These capillaries are then stacked together to create a new preform and drawn into the fibre that is often pulled again onto a rotating drum. Some slip may occur between the drawn capillary and the wheels, although if at all, this is thought to be minimal. Once drawn, these capillaries may later be stacked together to create a preform. Holey fibres are drawn from a preform of this type, and the finished product is normally pulled onto a rotating drum. It may therefore not be quite clear whether the draw speed or the draw force is the appropriate condition to

prescribe, or whether a combination of the two is more true to reality. In the absence of any firm indications to the contrary, we shall proceed under the assumption that the draw speed is prescribed. We shall also assume that the fibre is rotated at $\bar{z} = 0$ and held fixed (no rotation) at $\bar{z} = 1$. This is because the fibre is attached to the drawing wheels downstream, by which point it has solidified. The rotation rate at $z = 0$ is assumed constant, though in practice a more complex "spinning profile" is sometimes used, where for example, the rotation rate at $z = 0$ oscillates (changes direction rapidly) [60], [61].

3.5.2 The dimensional form of the final equations

Before a further discussion and analysis of these equations we dimensionalize the equations using the additional scaling $B = \frac{\Omega}{\epsilon}\bar{B}$, which results from (3.26).

The equations (3.48)–(3.51) then become

$$\rho(h_2^2 - h_1^2)(w_{0t} + w_0 w_{0z} - g) = \left(3\mu(h_2^2 - h_1^2)w_{0z} + \gamma(h_1 + h_2) + \frac{\rho}{4}(h_2^4 - h_1^4)B^2\right)_z, \tag{3.53}$$

$$(h_1^2)_t + (h_1^2 w_0)_z = \frac{h_1 h_2(2p_0 h_1 h_2 - 2\gamma(h_1 + h_2) + \rho h_1 h_2 B^2(h_2^2 - h_1^2))}{2\mu(h_2^2 - h_1^2)}, \tag{3.54}$$

$$(h_2^2)_t + (h_2^2 w_0)_z = \frac{h_1 h_2(2p_0 h_1 h_2 - 2\gamma(h_1 + h_2) + \rho h_1 h_2 B^2(h_2^2 - h_1^2))}{2\mu(h_2^2 - h_1^2)}, \tag{3.55}$$

$$\rho\left(h_2^2(h_2^2 B)_t - h_1^2(h_1^2 B)_t\right) + \rho w_0\left(h_2^2(h_2^2 B)_z - h_1^2(h_1^2 B)_z\right) + \frac{\rho}{\mu}p_0 B h_1^2 h_2^2$$
$$- \frac{\rho\gamma B h_1 h_2}{\mu}(h_1 + h_2) + \frac{\rho^2 B^3 h_1^2 h_2^2}{2\mu}(h_2^2 - h_1^2) = \mu\left((h_2^4 - h_1^4)B_z\right)_z. \tag{3.56}$$

with

$$\frac{(h_2^2 - h_1^2)}{2}[\rho c_p(T_{0t} + u_0 T_{0z}) - k(T_{0z})_z - \sigma\alpha(T_a^4 - T_0^4)] = h_2 N(T_a - T_0). \tag{3.57}$$

For definiteness, we shall assume that, unless otherwise stated, the boundary conditions for (3.57), and (3.53)–(3.56) are that the initial geometry of the capillary

preform is known, that the feed and draw speeds are prescribed at $z = 0$ and $z = L$ respectively, and the fibre is rotated at $z = 0$ and held with $B = 0$ at $z = L$. Thus

$$h_1(0) = h_{10}, \quad h_2(0) = h_{20}, \quad w_0(0) = W_f, \quad w_0(L) = W_d,$$

$$B(0) = B_0, \quad B(L) = 0, \quad T_0(0) = T_f, \quad T_0(L) = T_d, \tag{3.58}$$

where subscripts f and d denote feed and draw conditions respectively; for the unsteady problem suitable initial conditions must also be prescribed.

It is worth pointing out that these should be regarded as lowest order boundary conditions appropriate to our leading–order model, and that the full Navier-Stokes problem described by (3.1)–(3.4) would require additional boundary data to be fully specified.

The model outlined above and some key results are discussed by Voyce *et al.* in [51].

3.5.3 Non-constant hole overpressure

Experiments undertaken at the Optoelectronics Research Centre demonstrate that when the ends of capillary tubes are sealed before the tube is drawn into fibre form, it is possible to retain an open hole past the point at which surface tension would be expected to close it.

As a sealed capillary tube enters the furnace it heats up and the pressure of the gas inside increases. It is observed that it is possible to draw slender geometries (for example, $h_{10} = 50\mu$m, $h_{20} = 70\mu$m) as explained above, but if the effects of surface tension were counteracted by having a large hole overpressure, then the capillary tube would be expected to bulge or "explode" somewhere close to $z = 0$ where the effects of surface tension are reduced. This is not observed and it is therefore suggested that a pressure *gradient* exists inside the preform during the drawing process.

In order to be able to include a pressure gradient in the model we revise equations

(3.53)–(3.56) in both non–dimensional and dimensional forms, allowing p_0 in (3.17) to be a function of z. Following the same procedure as before we find that the final equations are modified by the including a p_{0z} term in the momentum equation (3.48).

In non–dimensional form equations (3.53)–(3.56) become

$$Re(\bar{h}_2^2 - \bar{h}_1^2)(\bar{w}_{0\bar{t}} + \bar{w}_0\bar{w}_{0\bar{z}} - \frac{1}{Fr}) = [3\bar{\mu}((\bar{h}_2^2 - \bar{h}_1^2)\bar{w}_{0\bar{z}})$$

$$+\bar{\gamma}(\bar{h}_1 + \bar{h}_2) + \frac{1}{4}ReS^2((\bar{h}_2^4 - \bar{h}_1^4)\bar{B}^2)]_{\bar{z}} + \bar{p}_{0\bar{z}}\bar{h}_1^2, \tag{3.59}$$

$$(\bar{h}_1^2)_{\bar{t}} + (\bar{h}_1^2\bar{w}_0)_{\bar{z}} = \frac{\bar{h}_1\bar{h}_2(2\bar{p}_o\bar{h}_1\bar{h}_2 - 2\bar{\gamma}(\bar{h}_1 + \bar{h}_2) + ReS^2\bar{B}^2\bar{h}_1\bar{h}_2(\bar{h}_2^2 - \bar{h}_1^2))}{2\bar{\mu}(\bar{h}_2^2 - \bar{h}_1^2)}, \tag{3.60}$$

$$(\bar{h}_2^2)_{\bar{t}} + (\bar{h}_2^2\bar{w}_0)_{\bar{z}} = \frac{\bar{h}_1\bar{h}_2(2\bar{p}_o\bar{h}_1\bar{h}_2 - 2\bar{\gamma}(\bar{h}_1 + \bar{h}_2) + ReS^2\bar{B}^2\bar{h}_1\bar{h}_2(\bar{h}_2^2 - \bar{h}_1^2))}{2\bar{\mu}(\bar{h}_2^2 - \bar{h}_1^2)}, \tag{3.61}$$

$$Re\left(\bar{h}_2^2(\bar{h}_2^2\bar{B})_{\bar{t}} - \bar{h}_1^2(\bar{h}_1^2\bar{B})_{\bar{t}}\right) + Re\bar{w}_0\left(\bar{h}_2^2(\bar{h}_2^2\bar{B})_{\bar{z}} - \bar{h}_1^2(\bar{h}_1^2\bar{B})_{\bar{z}}\right) + \frac{Re\bar{p}_o}{\bar{\mu}}\bar{B}\bar{h}_1^2\bar{h}_2^2$$

$$-\frac{Re\bar{\gamma}\bar{B}\bar{h}_1\bar{h}_2}{\bar{\mu}}(\bar{h}_1 + \bar{h}_2) + \frac{Re^2S^2\bar{B}^3\bar{h}_1^2\bar{h}_2^2(\bar{h}_2^2 - \bar{h}_1^2)}{2\bar{\mu}} = \left(\bar{\mu}((\bar{h}_2^4\bar{B}_{\bar{z}}) - (\bar{h}_1^4\bar{B}_{\bar{z}}))\right)_{\bar{z}}. \tag{3.62}$$

In dimensional form equations (3.59)–(3.62) are

$$\rho(h_2^2 - h_1^2)(w_{0t} + w_0w_{0z} - g) = [3\mu(h_2^2 - h_1^2)w_{0z}$$

$$+\gamma(h_1 + h_2) + \frac{\rho}{4}(h_2^4 - h_1^4)B^2]_z + p_{0z}h_1^2, \tag{3.63}$$

$$(h_1^2)_t + (h_1^2w_0)_z = \frac{h_1h_2(2p_0h_1h_2 - 2\gamma(h_1 + h_2) + \rho h_1h_2B^2(h_2^2 - h_1^2))}{2\mu(h_2^2 - h_1^2)}, \tag{3.64}$$

$$(h_2^2)_t + (h_2^2w_0)_z = \frac{h_1h_2(2p_0h_1h_2 - 2\gamma(h_1 + h_2) + \rho h_1h_2B^2(h_2^2 - h_1^2))}{2\mu(h_2^2 - h_1^2)}, \tag{3.65}$$

$$\rho\left(h_2^2(h_2^2B)_t - h_1^2(h_1^2B)_t\right) + \rho w_0\left(h_2^2(h_2^2B)_z - h_1^2(h_1^2B)_z\right) + \frac{\rho}{\mu}p_0Bh_1^2h_2^2$$

$$-\frac{\rho\gamma Bh_1h_2}{\mu}(h_1 + h_2) + \frac{\rho^2B^3h_1^2h_2^2}{2\mu}(h_2^2 - h_1^2) = \left(\mu(h_2^4 - h_1^4)B_z\right)_z, \tag{3.66}$$

with (3.52) as before. These equations will later be referred to as the leading–order capillary drawing equations.

In order that we may estimate the form and magnitude of the pressure gradient it is necessary to establish a mechanism that might give rise to the pressure gradient.

The obvious way of generating the pressure gradient is by using standard lubrication theory on the gas flow inside the hole in the capillary tube. Conducting this lubrication theory shows that a pressure gradient large enough to have an effect on the geometry is not obtained unless the pressure is scaled such that it does not enter (3.64)–(3.66) to leading order. It is therefore not possible to generate a pressure gradient through the above mechanism.

It remains unclear if a significant pressure gradient exists during the drawing of a sealed capillary tube. However, if such a gradient exists then equations (3.63)–(3.66) may be used to predict the effects. Chapter 9 considers another possible explanation for the effects observed when drawing sealed capillary tubes.

3.6 A numerical analysis for the rotation of capillary tubes

In the sections to come we will analyse the non–dimensional equations (3.48)–(3.51), using asymptotic analysis. However, to motivate this mathematical study it is necessary to first confirm that the act of imparting a rotation to a capillary has noticeable consequences for its geometry. As noted above, rotation is essential to reduce birefringence. If the fibre geometry alters as a result of this rotation, then the possibility arises of using preform rotation as an additional control parameter in the drawing process.

To confirm that geometry changes do indeed occur, the full leading–order dimensional steady-state equations (3.48)–(3.51) may be solved using standard numerical library routines.

To give a flavour of the sort of effect that rotation may have, we show graphs of the numerical calculations whose results demonstrate the effects of preform rotation

on both a thin– and a thick–walled capillary. We assumed that the glass involved was silica Suprasil F300, commonly used in the production of low-loss optical fibres. The physical properties used for the computations were taken from [15]. F300 has a density of 2200kg/m^3. Based on the calculations in [15], we assumed a surface tension of 0.3N/m and a viscosity that depends on the temperature as shown below, where temperature is measured in Celsius and viscosity in Poise. Unless otherwise stated we shall henceforth take the furnace temperature to be constant along its length, thus removing the z dependence from the viscosity, which is now simply related to the constant furnace temperature. It should be pointed out that this viscosity model is not known to be correct, and since the viscosity depends exponentially on the temperature of the fluid, this is unlikely to be accurate: in later Chapters more consideration is given to the choice of viscosity law. Needless to say, both the model and the method are applicable to general fluids. In the limit that the number of holes in a microstructured optical fibre is large, one might expect the geometry of the resulting fibre to act more in accordance with a capillary tube than a solid glass fibre, motivating this section. The glass viscosity will be taken as

$$\mu = 0.1 \times 10^{-6.24+26900/(T+273)},$$

where the temperature T is measured in Celsius and the viscosity in Poise.

The results in Figure 3.4, where the dashed line represents the outer radius profile before rotation, and the solid line represents the outer radius profile after rotation, demonstrate that rotation causes the outer fibre radii to increase, predominantly at the top of the furnace.

It may be confirmed that the general effect of rotating the preform as it enters the furnace is to increase both the inner and outer radii of the fibre along the entirety of the draw length, implying that the final fibre dimensions are larger than if the fibre were not rotated. In the case of the thin–walled tube the dimensions at $z = L$ were increased by 20%, and for the thick–walled tube they were increased by 11%. Preform rotation may thus be used as an additional control in the drawing process, since it is the fibre dimensions at the end of the furnace that primarily concern us.

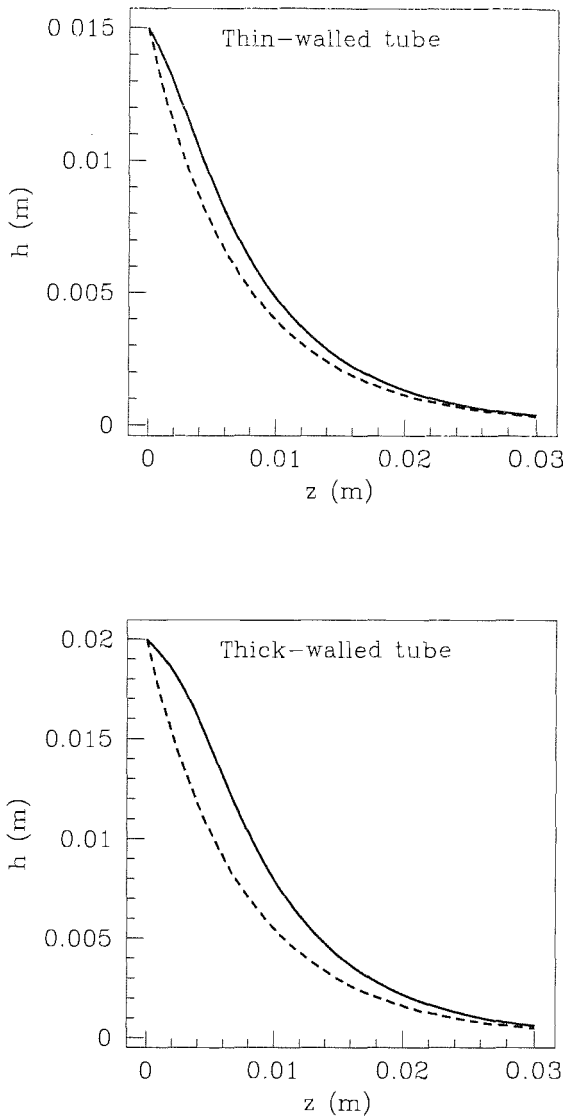

Figure 3.4: Numerical calculation of the effects of preform rotation on an outer capillary radius. (Draw length $L = 0.03$m, temperature $T = 2200$C, draw speed $W_d = 25$m/min, feed speed $W_d = 15$mm/min, rotation rate $\Omega/\epsilon = 35$rad/s.) Each diagram shows the outer tube radius h_2 for fibre pulls with and without rotation. (Upper diagram: thin–walled tube with $h_1(0) = 0.01$m, $h_2(0) = 0.015$m. Lower diagram: thick–walled tube with $h_1(0) = 0.01$m, $h_2(0) = 0.02$m). In both cases, the lower (broken) of the two curves is the case with no rotation. The upper curves both show a 'bulge' resulting from the effect of preform rotation.

We also note that rotation appears to act on the fibre in a way that counteracts the effects of surface tension, which otherwise tends to close air holes in the fibre. As well as reducing birefringence, rotation may thus, for example, allow fibres to be drawn at increased temperatures; this is advantageous from a manufacturing point of view as fibres drawn at high temperatures are often less vulnerable to breakage during drawing [62].

It is also clear from Figure 3.4 that the thick–walled tube experiences a much greater deformation than the thin–; this is largely because the initial outer radius of the thick-walled capillary is larger than that of the thin-walled capillary, and partly because of mass conservation conditions imposed. To gain more insight into the results, we have compared the magnitudes of respective changes in fibre radii as a result of spinning the different fibre types (see results in Chapters 6 and 7 for details). This reveals that, for both thin– and thick–walled tubes, the inner radius increases more than the outer. The fluid near to the outer edges of the fibre rotates faster and therefore experiences more of an effect due to the rotation than the fluid near to the central hole. The displacement of the outer edge of the fibre, coupled with mass conservation requirements, require that the inner portions of the fibre must undergo larger changes in radial position. Whilst it is clear that the effects of preform rotation on capillary tubes will be similar to the effects of preform rotation on microstructured preforms with many holes or a large air filling fraction, it is not clear how thick the walls of the capillary should be - a necessary requirement for concrete predictions of the final geometry of microstructured fibres to be made, as demonstrated above by the difference in behaviour of thick– and thin–walled tubes.

From the above numerical analysis, it is already clear that we are justified in further investigating the effects of the preform rotation on the fibre geometry more closely. An analysis will be undertaken in part in the proceeding sections.

3.7 Asymptotic limits of the model

We shall here recap the definition of the various constants and variables involved, and discuss where relevant their physical meaning, since this will be of utmost importance in the limiting analyses that shortly follow. Table 3.1 defines the notation used in this section. We previously defined

$$\epsilon = \frac{h}{L}, \quad Re = \frac{LW\rho}{\mu_0}, \quad Fr = \frac{W^2}{gL}, \quad S = \frac{\Omega L}{W}.$$

Later we speak of Re being $\ll 1$. Whilst this may be achieved in a large variety of ways (e.g. $\rho \ll 1$), this is normally realized through having a large viscosity and hence low temperature. Conversely, $Re = O(1)$ implies a small viscosity and thus a high temperature. Typical furnace temperatures correspond to $Re \ll 1$.

Since Ω scales the angular frequency B $\left(B = \frac{\Omega}{\epsilon}\bar{B}\right)$, and S is proportional to Ω, it is clear that S may be considered a measure of the rotation rate of the preform as it enters the fibre drawing furnace. $S \ll 1$ therefore means that the amount of rotation is small. $S = O(1)$ corresponds to a large rotation rate: rotating the fibre at $\approx$ 1000rpm, a rate that may be achieved in practice: this is because the rotation rate $\approx \frac{\Omega}{\epsilon} = \frac{SW}{L\epsilon} \approx \frac{1\times10^{-1}}{10^{-2}\times10^{-2}} = 1000$rpm when $S = O(1)$. This, however, is close to the current practical upper limit. Beyond about $\approx$ 2000rpm the alignment of the preform in the furnace becomes critical. Any perturbation in its alignment then develops into radial oscillations [55]. Interestingly, it is found experimentally that these die out at higher angular frequencies.

When the effects of gravity are ignored, $\frac{1}{Fr}$ is zero. The inertial force term is Rew_0w_{0z}. This is set equal to zero when 'inertia is neglected', as it often is. It is easily shown numerically that this limit is realistic since the Reynolds number of the flow is frequently small.

Overbars represent non–dimensional quantities throughout, and for the most part we shall only be interested in steady–state solutions to this model. This is because

Table 3.1: Key.

Quantity (S.I. Units)	Description
SV	Smallest Value used
LV	Largest Value used
TV	Typical Value used
$\bar{h}_1$	Inner fibre radius
$\bar{h}_2$	Outer fibre radius
$\bar{w}$	Downstream fluid velocity
$\bar{B}$	Angular frequency of fluid
$\bar{v}$	Azimuthal fluid velocity
$\bar{\mu}$	Viscosity: one when $T(z) = T_R$
h	Typical fibre radius
W	Typical downstream fluid velocity
Ω/ϵ	Typical angular frequency 0-100
L	Draw length (hot zone length of furnace), typical value 0.03
μ_0	Typical viscosity $10 - 10^5$
ρ	Fluid density = 2200 (Suprasil F300)
g	Acceleration induced by gravitation, 9.81
$h_1(0) = h_{10}$	Initial inner radius, $10^{-4} - 10^{-1}$
$h_2(0) = h_{20}$	Initial outer radius, $10^{-4} - 10^{-2}$
$w_0(0) = W_d$	Feed speed, $10^{-5} - 10^{-4}$
$w_0(L) = W_d$	Draw speed, $10^{-1} - 1$
$B(0) = B_0$	Initial angular frequency = Ω/ϵ
$B(L) = B_L$	Final angular frequency, 0

experimentalists do not have problems reaching steady–state drawing conditions unless they use large rotation rates, when the alignment of the fibre in the furnace is critical to avoid growing oscillations. Chapter 5 considers the transient equations in a stability analysis. For notational simplicity we set $\bar{\mu} = 1$ (assume no z variation of viscosity) and vary μ_0. We also define $\bar{w}_0 = \bar{w}$ unless otherwise stated.

We notice that the rotation equation (3.51) decouples from the momentum equation (3.48) when the rotation rate is small. To obtain an estimate of the amount of rotation necessary for the geometry to be affected we may consider the steady–state case for solid fibres, when inertia, surface tension, gravity and hole overpressure are neglected. The z-momentum equation (3.48) then becomes

$$3\bar{\mu}(\bar{h}_2^2\bar{w}_{0\bar{z}})_{\bar{z}} = -\frac{1}{4}ReS^2(\bar{h}_2^4\bar{B}^2)_{\bar{z}},$$

and so the rotation starts to affect fibre geometry when

$$S \approx \sqrt{\frac{12\bar{\mu}}{Re}}$$

or

$$\frac{\Omega}{\epsilon} \approx \frac{2}{\bar{h}}\sqrt{\frac{3\bar{\mu}\mu_0 W}{L\rho}}. \tag{3.67}$$

Increasing the viscosity suggests that one would have to rotate the fibre more rapidly to effect a geometry change. This agrees with the form of the expression above.

We assign a viscosity and other parameters that are realistic but that give rise to the earliest onset of geometry change, and use (3.67) to show that this occurs when $\frac{\Omega}{\epsilon} \approx 2900$rpm. This may be verified by solving (3.53)–(3.56) numerically. Whilst it is possible to rotate preforms at such a rate [63], vibrations and instabilities are often encountered in practice. Additionally, these drawing parameters were chosen specifically to create geometry change at low rotation rates, and in typically much larger rotation rates (100,000rpm) will be possible with no effect on fibre geometry. Although the point at which microstructured fibre geometry is modified may be somewhat different, (3.67) provides a useful first approximation. Needless to say, we

do not expect the point which rotation affects geometry for holey fibres that contain a large number of holes, or whose air–filling fraction is large, to be characterized by (3.67).

Even though the geometry of a solid fibre and thus to a first approximation holey fibre geometry, is not expected to be modified by the presence of practical rotation rates < 2900rpm, one must consider the fact that holes remaining circular in unspun holey fibres may now be distorted by the effects of the preform rotation. This is because one should expect (3.67) to be good in the limit of few holes. However, as the hole density increases and the air–glass mix behaves more as a homogenized medium, one should expect the effects of rotation to occur at lower rotation rates. Equation (3.67) may therefore be regarded as an upper limit on the point at which rotation affects the geometry of holey fibres. This reasoning follows from the fact that air has a much lower viscosity than glass.

To obtain an estimate of the extent to which hole distortion will occur, as a function of distance from the preform centreline, we plot the leading–order mechanical pressure (3.27) obtained by solving (3.48), (3.50) and (3.51) for a solid fibre being spun at 500–1000 rpm (the exact value depends on the value of W_d chosen), $Re = 0.1$ and $\gamma = 0$. Figure 3.5 shows that, as one might expect, the non–dimensionalized mechanical pressure is lowest at the core of the fibre and increases with increasing r, where it takes a value necessary to allow the radial stress at the boundary of the preform to equal the atmospheric pressure. (Note: the reason that the values of pressure are negative is that this pressure is scaled to represent the pressure over atmospheric pressure.)

The intuitive effect of rotation on the shape of off–centre holes is to transform them into ellipses. A possible way to counteract this effect is to construct a preform whose holes are elliptical, but whose major axis runs perpendicular to the radial vector. Figure 3.5 suggests that increasing the eccentricity of the holes at the centre of the preform and decreasing it for holes closer to the edge of the preform might be most

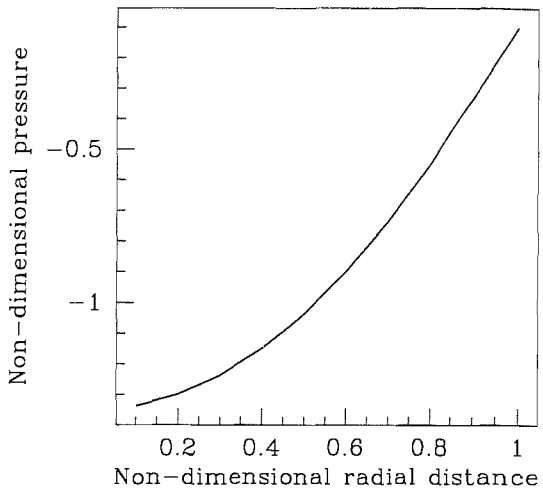

Figure 3.5: The non–dimensionalized mechanical pressure at $\bar{z} = 0$ as a function of distance from the centre of the fibre.

effective. This results from the way one might expect a deformable matrix of glass and air to respond to a pressure gradient similar to the one shown. Indeed, it has already been observed experimentally that this distortion occurs. Figure 3.6 shows a holey fibre whose corresponding holes in the preform were initially circular, drawn at 2000C and rotated at an unknown rate . It is clear both that the holes are elliptical and that the eccentricity of the holes increases as one moves closer to the outer–wall of the fibre, in agreement with the above discussion.

The above description is an over simplification of the interaction between surface tension, lattice distortion resulting from radial flow induced by gradients in stress and distortion in hole shape resulting from such stress gradients, and should be treated cautiously. A full holey fibre model is required to determine more precisely the behaviour of holes in rotating molten preforms.

Whilst it is not possible to make more exact predictions at this stage, some general guidance may be given regarding how to vary the ellipticity of the holes as a function of radial position, depending on the rotation rate, the diameter of the initial preform

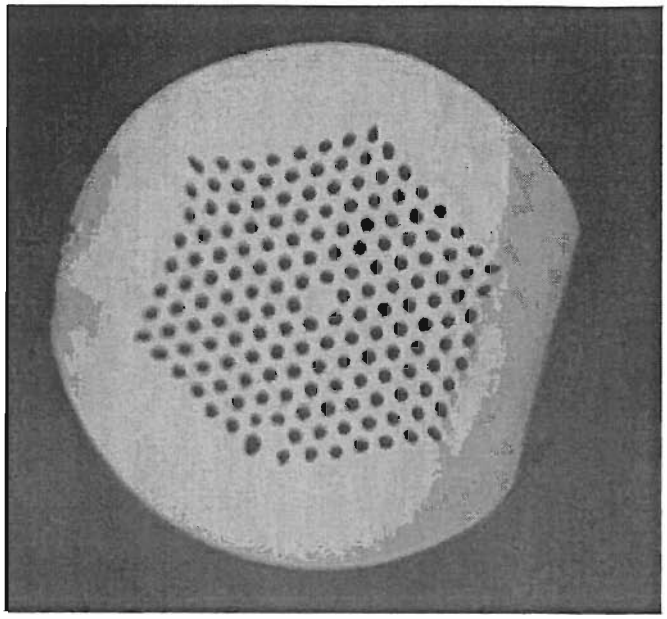

Figure 3.6: The transverse cross–section of a holey fibre to show the effects of preform rotation on the shape of the holes.

and also the fraction of air in a cross–section.

Since the ability of an air–glass matrix to deform is expected to be directly related to the size of the air–fraction in a cross–section of the preform it is suggested that both the rate at which the eccentricity increases as a function of radial distance, and the eccentricity at any one point, should depend on the initial air–fraction of the preform. For example, if one starts with a large air–fraction in the preform and requires circular holes in the final fibre, holes with a large eccentricity at any radius should be present in the initial preform and the rate at which this eccentricity increases with radius should also be large.

The more rapidly one rotates the preform, the greater the effect of the rotation will be on the fibre geometry and thus the shape and distribution of holes within. Therefore, if the preform is rotated rapidly, holes with a large eccentricity will be required and should have an eccentricity that dramatically increases with radius. This is also the case for preforms with a large outer diameter, since diameter is a parameter that increases the sensitivity of fibre geometry to spinning.

3.7.1 The solid fibre limit

Equations (3.48), (3.50) and (3.51) cannot be solved in closed form, though progress may be made by considering the case of the solid fibre limit, where $\bar{h}_1 = 0$ and $\bar{h}_2 = \bar{h}$. We consider the steady–versions of these equations and neglect inertial force terms (no matter the size of Re), with no gravity, hole overpressure and surface tension. The motivation for considering this limit is that it will provide an insight into the physics of the problem whilst the equations remain relatively simple and are more likely to possess closed–form solutions. Once satisfied that the model behaves as one might expect this imposed simplification will be removed.

Under these assumptions, the equations governing drawing (3.48), (3.50) and (3.51), become

$$3\bar{\mu}(\bar{h}^2\bar{w}_{\bar{z}})_{\bar{z}} + \frac{ReS^2}{4}(\bar{h}^4\bar{B}^2)_{\bar{z}} = 0, \tag{3.68}$$

$$(\bar{h}^2\bar{w})_{\bar{z}} = 0, \tag{3.69}$$

$$Re\bar{w}\bar{h}^2(\bar{h}^2\bar{B})_{\bar{z}} = \bar{\mu}(\bar{h}^4\bar{B}_{\bar{z}})_{\bar{z}}. \tag{3.70}$$

Taking Re is $O(1)$ and $S^2 \ll 1$ corresponds to the regime where rotation and viscosity are extremely small, and thus the draw temperature large. Alternatively it corresponds to a limit where both feed and draw speeds are extremely small. Unfortunately neither of these two limits are practical, since realistic viscosities are not small enough to give $Re = 1$. However, under these conditions the equations may be solved in closed–form with boundary conditions $\bar{h}(0) = \bar{h}_0$, $\bar{w}(0) = \bar{W}_f$, $\bar{w}(1) = \bar{W}_d$, $\bar{B}(0) = \bar{B}_0$ and $\bar{B}(1) = \bar{B}_L$ to yield

$$\bar{h} = \bar{h}_0 e^{\frac{-\beta\bar{z}}{2}}, \quad \bar{w} = \bar{W}_f e^{\beta\bar{z}}, \tag{3.71}$$

and

$$\bar{B} = Ce^{\left(\frac{Re\bar{W}_f e^{\beta\bar{z}}}{\bar{\mu}\beta}\right)} + D(Re\bar{W}_f e^{\beta\bar{z}} + \bar{\mu}\beta). \tag{3.72}$$

Here $\beta = \ln(\frac{W_d}{W_d})$ and

$$C = \frac{Re(\bar{W}_f\bar{B}_L - \bar{W}_d\bar{B}_0) + \bar{\mu}\beta(\bar{B}_L - \bar{B}_0)}{Re(\bar{W}_f\bar{H}_d - \bar{W}_d\bar{H}_f) + \bar{\mu}\beta(\bar{H}_d - \bar{H}_f)},$$

and

$$D = \frac{\bar{B}_0\bar{H}_d - \bar{B}_L\bar{H}_f}{Re(\bar{W}_f\bar{H}_d - \bar{W}_d\bar{H}_f) + \bar{\mu}\beta(\bar{H}_d - \bar{H}_f)},$$

where C and D are the constants of integrations defined above and

$$\bar{H}_f = \exp\left(\frac{Re\bar{W}_f}{\bar{\mu}\beta}\right),$$

$$\bar{H}_d = \exp\left(\frac{Re\bar{W}_d}{\bar{\mu}\beta}\right).$$

When S^2 is $O(1)$ and $Re \ll 1$ (so that both the rotation and the viscosity are large), the equations may once again be solved directly to give

$$\bar{h} = \bar{h}_0 e^{\frac{-\beta\bar{z}}{2}}, \quad \bar{w} = \bar{W}_f e^{\beta\bar{z}}, \tag{3.73}$$

and

$$\bar{B} = \frac{1}{e^{2\beta} - 1}((\bar{B}_L - \bar{B}_0)e^{2\beta\bar{z}} - \bar{B}_L + \bar{B}_0 e^{2\beta}). \tag{3.74}$$

This is as required, as in both limits the downstream–momentum equation decouples from the angular–frequency equation, leaving the usual exponential solutions for $\bar{h}$ and $\bar{w}$ [14], and a separate equation for $\bar{B}$.

A physical interpretation of this is that when the rotation is small (S is small) or the viscosity is large (Re is small), the momentum equation (3.48) decouples from the rotation equation (3.51). This occurs because when the rotation is small, viscous effects dominate geometry changes. Matters are then considerably simplified since (3.48)–(3.50) may be solved separately to (3.51), and the solutions substituted into (3.51), leaving an equation in $\bar{B}$ that can also be solved in closed–form.

Some interesting conclusions can be drawn from these cases. It may easily be shown that (3.72) predicts, somewhat surprisingly, that the rotation rate may not always

be monotonic, for $\bar{B}$ attains a maximum at

$$\bar{z} = \frac{1}{\beta} \log \left[\frac{\bar{\mu}\beta}{\bar{W}_f Re} \log \left(\frac{-D\beta\bar{\mu}}{C} \right) \right].$$

For example, with $\bar{\mu} = 1$, $Re = 1$, $\bar{W}_f = 1/100$, $\bar{W}_d = 1$, $\bar{B}_0 = 1$, and $\bar{B}_L = 0$ the maximum in the rotation rate occurs at $\bar{z} \simeq 0.489$.

In contrast, the rotation rate given by (3.74), (where the effects of preform rotation dominate those due to viscosity) is evidently monotonic. For most practical fibre draws the ratio β is large. Under these circumstances (3.74) shows that $\bar{B} \sim \bar{B}_0$ for most of the draw, changing to assume the value $\bar{B}_L$ at $\bar{z} = 1$ only in a boundary layer near to the end of the draw (see §3.7.1.3 for details).

Integrating and combining equations (3.68)–(3.70) allows an expression for $\bar{B}$ as a function of $\bar{w}$ to be found, which might have allowed a contour plot for $\bar{B}$ and $\bar{w}$ identifying any singular points. However, numerical simulations demonstrate that the sign of $\bar{w}_{\bar{z}}$ is non–unique, and this prevents the contour plot. Similarly, when equations (3.68)–(3.70) are used to determine an expression for $\bar{B}$ in terms of $\bar{h}$, we find that the constants therein are non–unique in sign, once again preventing a particularly useful contour plot from being constructed.

3.7.1.1 The twist periodicity

Since fibre birefringence is often an undesirable feature in both holey fibres and solid glass optical fibres, it would be useful to have an estimate of how rapidly one must rotate the preform as it enters the furnace to remove or reduce this effect. The length scale of the pitch required in the final fibre will depend on the wavelength window of light of interest to end–user of the fibre and the consequent beat length of the interference between the two components of light as they travel along the length of the fibre. We set about obtaining such an estimate below.

In the physically realistic case where S^2 is $O(1)$ and $Re \ll 1$ (rotation rate of

approximately 1000rpm and typical preform geometry, etc.) we ask how to determine the distance between two successive 2π rotations in the fibre, evaluated at $z = L$, hereafter called the twist periodicity. It might be expected that the twist periodicity depends on the functional form of the solutions to the governing equations, and therefore be non–trivial.

To establish whether or not this is the case we define the angle θ to be the number of radians that a fluid element has rotated through as it traverses the z-axis (moved from the furnace inlet to its outlet). If we know the rate at which θ changes with time then from this we may directly calculate the twist periodicity as

$$d(z) = \frac{2\pi w(z)}{\frac{\partial \theta(z,t')}{\partial t'}}, \tag{3.75}$$

where the prime denotes the fact that, considering only steady–state cases, the time variable signifies the transit time for a fluid element to traverse the length of the furnace.

To derive an equation for $\theta(z, t')$ we follow a fluid element along the furnace as the fibre is drawn to obtain

$$\theta_{t'} + w(z)\theta_z = B(z), \tag{3.76}$$

whose initial condition that results from the definition of θ is prescribed to be

$$\theta(0, t') = B(0)t'.$$

This has the general solution

$$\theta(z, t') = B(0)t' + \int_0^z \frac{[B(z) - B(0)]\, dz}{w},$$

where w is the usual downstream fluid velocity.

Substituting this into (3.75) yields

$$d(z) = \frac{2\pi w(z)}{B(0)}, \tag{3.77}$$

so that when $z = L$ and $w = W_d$ the final twist periodicity d is given by

$$d = \frac{2\pi W_d}{B(0)}. \tag{3.78}$$

Thus the twist periodicity depends on z, increasing in value as the increasing downstream fluid velocity has the effect of increasing the distance between two successive twists. As the fibre leaves the furnace and solidifies, the twist periodicity becomes fixed and its value given by equation (3.78).

We note that the twist periodicity is independent of the functional form of the fibre radius, its downstream fluid velocity and the angular frequency of the preform. The details of the draw appear only through the draw speed, W_d, and the initial rotation rate, $B(0)$. This seems reasonable as the twist periodicity should be determined only by the draw speed and the rotation rate at $z = 0$ (assuming zero rotation at $z = L$).

Assuming a steady–state means that the same number of 2π rotations that pass any point along z per unit of time must be a constant equal to the rotation rate at the beginning of the draw length. The twist periodicity should then be determined simply by how rapidly the fibre is being 'stretched out'. At the end of the draw length this speed is the draw speed, thus explaining the form that the expression (3.78) takes. The only things that could prevent d taking this form would be if either or both of B and w were functions of time as well as space. Figure 3.7 shows how d varies with applied rotation rate and with draw speed, where the calculations were made by considering a solid fibre, though a capillary tube could have been used to produce an identical plot.

The expression (3.78) for d is therefore an accurate prediction of the twist periodicity for solid fibres. Since it was in no way necessary to assume that the fibres were solid in the above derivation, (3.78) is true for all fibres, solid or not. One may also use this relation to decide how rapidly the preform must be rotated in order to achieve the necessary twist periodicity in a solid fibre, a capillary tube or more generally in a holey fibre.

When the holes in a holey fibre (both preform and final fibre) sparsely populate the fibre cross–section, we may safely assume that the rotation rate at which rotation starts to affect the geometry of solid fibres is approximately the same as that for

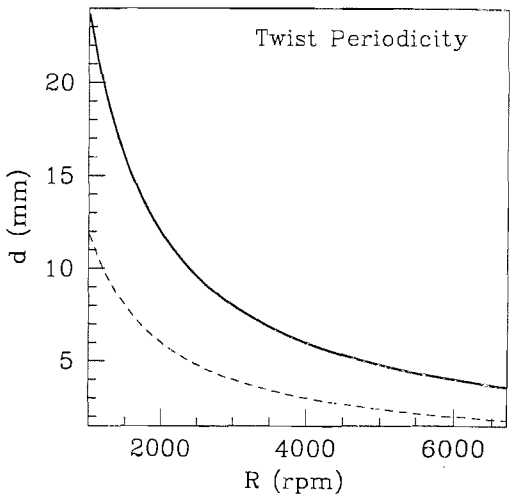

Figure 3.7: The variation in twist periodicity with rotation rate, shown here for two realistic draw speeds in the case of a solid fibre. The upper line corresponds to a draw speed of 48m/min ($\beta = 8.07$), and the bottom line to a draw speed of 24m/min ($\beta = 7.38$). In both cases the feed speed is 15mm/min.

holey fibres. Generally, holey fibres are pulled with a draw speed that varies between 3 and 30m/min, depending on the desired geometry of the fibre given the initial structure of the preform and mechanical properties of the glass. Furthermore, the twist periodicity that one may wish to achieve in a holey fibre, whose order depends on the wavelength of light, will vary between approximately 1 and 20mm.

It is tempting to consider a worst–case scenario, where the glass viscosity is extremely low, the draw speed at its maximum and the spin pitch the minimum required, in order to ask how rapidly one might need to rotate fibres to obtain the desired spin pitch, and then ask if the rotation will affect the geometry. However, in practice the rate of spinning is usually limited to about 3000rpm, above which value instabilities arise and the glass preform starts to oscillate violently in the furnace. Even though large draw speeds are often required to produce a fibre of the correct geometry, the limitations in rotation rate require that desirable fibres are produced by using a preform with reduced dimensions to allow the draw to be performed at a lower

draw speed. The net effect of this is that it is possible to obtain relatively small spin–pitches at low rotation rates whilst still achieving the fibre geometry required by the experimenter.

In consequence of this it can be shown that for a moderate draw speed of 6m/min, the rotation rate needed to produce a spin pitch of between 0.1mm and 3m is between 60000 and 2rpm respectively, as determined by (3.78). Such a small spin–pitch is required when beat lengths are similarly small, which occurs when wavelength–scale features and a high refractive–index contrast are present in a fibre. Selecting a typical glass viscosity of 20,000Pa.s, a draw length of 3cm and a preform diameter of 2cm, (3.67) predicts that resulting fibre will not be significantly modified by such rotation rates as these. Spin pitches of between 0.1mm and 3m were considered as they represent the typical range of birefringent beat–lengths in holey fibres (see [48], [53] and [64]), and the twist introduced into a fibre must be on a scale equal to or less than that of the beat length in order to remove the fibre birefringence. Since it is theoretically possible to reduce birefringence without affecting the final fibre geometry, and PMD reduction occurs as soon as birefringence is reduced from its value in an unspun fibre, spinning preforms at low rotation rates can reduce PMD without affecting the fibre geometry [58].

Whilst these calculations were made by assuming a solid fibre with no holes, they serve as a good first–approximation to what will happen in the event that holey fibres are spun so long as the density of holes is small, as discussed. A more careful study of the effect of rotation on different holey fibres structures is given in Chapter 4.

3.7.1.2 A solid fibre with small surface tension

Further progress may be made in solving equations (3.48), (3.50) and (3.51) analytically by examining what happens when, in addition to ϵ, $\bar{\gamma}$ is a small parameter. We now perform a regular perturbation in $\bar{\gamma}$ for equations (3.68)–(3.70) with surface

tension included. The initial equations become

$$3\bar{\mu}(\bar{h}^2\bar{w}_{\bar{z}})_{\bar{z}} + \bar{\gamma}\bar{h}_{\bar{z}} + \frac{ReS^2}{4}(\bar{h}^4\bar{B}^2)_{\bar{z}} = 0, \tag{3.79}$$

$$(\bar{h}^2\bar{w})_{\bar{z}} = 0, \tag{3.80}$$

$$Re\bar{w}\bar{h}^2(\bar{h}^2\bar{B})_{\bar{z}} = \bar{\mu}(\bar{h}^4\bar{B}_{\bar{z}})_{\bar{z}}. \tag{3.81}$$

Setting

$$\bar{h} = \bar{h}_0 + \bar{\gamma}\bar{h}_{01} + ...,$$

$$\bar{w} = \bar{w}_0 + \bar{\gamma}\bar{w}_1 + ...,$$

$$\bar{B} = \bar{B}_0 + \bar{\gamma}\bar{B}_1 + ...,$$

and taking the limit where $S \leq O(1)$ and $Re \ll 1$ (a large rotation rate and large viscosity, respectively), we solve for $\bar{h}_{01}$, $\bar{w}_1$ and $\bar{B}_1$.

It transpires that $\bar{h}_{01}$, $\bar{w}_1$ and $\bar{B}_1$ are the functions defined below. These allow us to determine whether surface tension acts with or against the rotation through the sign of $\bar{h}_{01}$.

Setting $S \leq O(1)$ we have that, when $\bar{h}_0$, $\bar{w}_0$ and $\bar{B}_0$ are given by (3.73) and (3.74), the perturbations are given by

$$\bar{h}_{01} = \frac{e^{-\frac{\beta\bar{z}}{2}}\left(3F\bar{\mu}\beta\bar{W}_f - e^{-\frac{\beta\bar{z}}{2}} + 3G\bar{\mu}\beta\bar{W}_f\bar{z}\right)}{3\bar{\mu}\beta\bar{W}_f}, \tag{3.82}$$

$$\bar{w}_1 = \frac{e^{\frac{\beta\bar{z}}{2}}\left(3J\bar{\mu}\beta\bar{h}_0e^{\frac{\beta\bar{z}}{2}} - 6G\bar{\mu}\beta\bar{W}_f\bar{z}e^{\frac{\beta\bar{z}}{2}} + 2\right)}{3\bar{\mu}\beta\bar{h}_0} \tag{3.83}$$

and

$$\begin{aligned}\bar{B}_1 = [&36G\bar{B}_L\bar{\mu}\bar{W}_fe^{2\beta\bar{z}} - 72G\bar{B}_L\bar{\mu}\beta\bar{W}_f\bar{z}e^{2\beta\bar{z}} + 32\bar{B}_Le^{\frac{3\beta\bar{z}}{2}} + 72G\bar{B}_0\bar{\mu}\beta\bar{W}_f\bar{z}e^{2\beta\bar{z}} \\ &-36G\bar{B}_0\bar{\mu}\bar{W}_fe^{2\beta\bar{z}} - 32\bar{B}_0e^{\frac{3\beta\bar{z}}{2}} + 9K\bar{\mu}\bar{W}_f\bar{h}_0e^{2\beta(1+\bar{z})} - 9K\bar{\mu}\bar{W}_f\bar{h}_0e^{2\beta\bar{z}} \\ &+18M\bar{\mu}\beta\bar{W}_f\bar{h}_0e^{2\beta} - 18M\bar{\mu}\beta\bar{W}_f\bar{h}_0]/\left(18\bar{\mu}\beta\bar{W}_f\bar{h}_0(e^{2\beta}-1)\right).\end{aligned} \tag{3.84}$$

where F, G, J, K and M are constants defined by

$$F = \frac{1}{3\bar{\mu}\beta\bar{W}_f},$$

$$G = \frac{1 - e^{\frac{\beta}{2}}}{3\bar{\mu}\beta\bar{W}_f e^{\frac{\beta}{2}}},$$

$$J = -\frac{2}{3\bar{\mu}\beta\bar{h}_0},$$

$$K = 4(\bar{B}_0 - \bar{B}_L)\left((6\beta - 3)e^{2\beta} + 8\beta(e^{\frac{3\beta}{2}} + e^{\beta} + e^{\frac{\beta}{2}}) + 3\right)$$
$$/9\bar{\mu}\beta\bar{W}_f\bar{h}_0 e^{\frac{\beta}{2}}\left(e^{\frac{7\beta}{2}} + e^{3\beta} + e^{\frac{5\beta}{2}} + e^{2\beta} - e^{\frac{3\beta}{2}} - e^{\beta} - e^{\frac{\beta}{2}} - 1\right)$$

and

$$M = \frac{4(\bar{B}_0 - \bar{B}_L)e^{\frac{3\beta}{2}}}{9\bar{\mu}\beta\bar{W}_f\bar{h}_0\left(e^{\frac{7\beta}{2}} + e^{3\beta} + e^{5\frac{\beta}{2}} + e^{2\beta} - e^{3\frac{\beta}{2}} - e^{\beta} - e^{\frac{\beta}{2}} - 1\right)}.$$

Whilst this is not a physically realistic situation as by definition $\bar{\gamma}$ is $O(1)$, we conducted this analysis in the hope that completing a regular perturbation in $\bar{\gamma}$ would result in leading–order equations that may be solved in closed–form. These solutions offer an understanding of the effects of surface tension on a solid fibre, even if the exact results cannot be extrapolated from these solutions.

Figure 3.8 plots the solution for h with and without surface tension added ($\bar{\gamma} \ll 1$), and demonstrates that the presence of surface tension acts to push the fibre out along the majority of the draw length except at the very ends of the draw length, where the boundary must remain at a fixed radius to conserve mass. At first this expansion seems counter intuitive, but can be understood through a consideration of the constant velocity boundary conditions, rather than constant force, and their consequent effects on the fibre radius.

When $\bar{h}_1 \neq 0$, as occurs for capillary tubes where closed–form solutions are not available, it may be shown numerically that the surface tension always acts against the rotation to reduce the surface area of the fibre; i.e. $\bar{h}_{01}$ and $\bar{h}_{02}$ are always negative. Given the results for the solid fibre however, this result was not obvious.

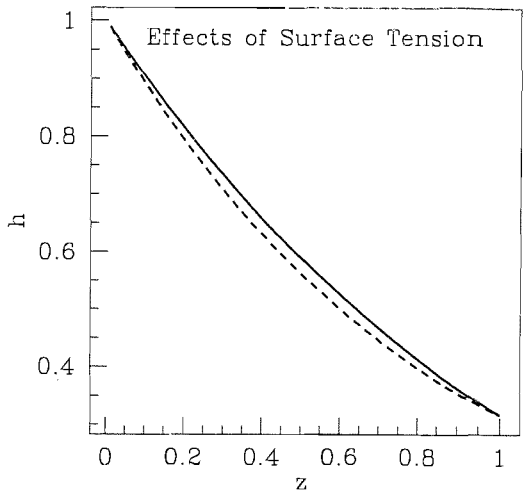

Figure 3.8: The effect of a small surface tension on the radius of a solid fibre, calculated theoretically. The dashed curve shows the fibre radius without surface tension, and the upper curve represents the fibre radius with surface tension added. Both h and z are non–dimensional quantities.

3.7.1.3 The rotation boundary layer

As the draw speed is increased for a constant feed speed, a solid fibre thins rapidly. Since the results for h and w (3.71) display an exponential dependence on the distance along the furnace, further down the furnace fibre thins more rapidly. As the ratio of the draw speed to the feed speed increases, $\beta = \ln\left(\frac{W_d}{Wf}\right)$, which appears in the exponent in the solutions for h and w, will increase. This demonstrates that the preform thins rapidly, causing the rotation to remain at its initial value until further along the draw length, and thereafter to decrease rapidly (towards $\bar{z} = 1$). It is evident that the greater ratio of draw speed to feed speed, the more rapidly the preform thins, and thus through mass conservation the downstream fluid velocity increases.

We may therefore expect to observe the appearance of a sudden change in the angular frequency, close to $\bar{z} = 1$, as the downstream velocity becomes large compared to

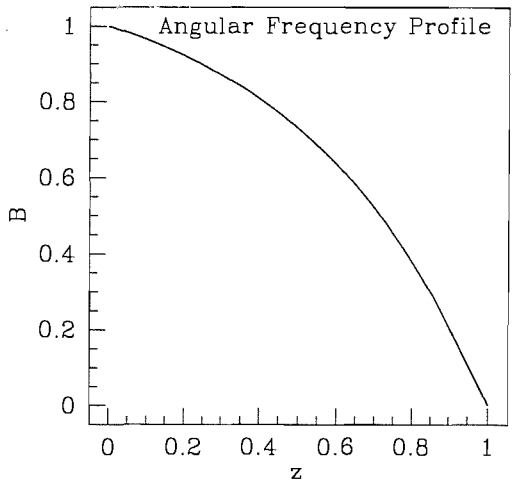

Figure 3.9: The angular frequency profile for $\beta = 1$.

the feed speed. This corresponds to having β large as is always the case in practice. This results in a boundary layer and is investigated below using standard boundary layer theory and techniques.

Numerical simulations of the final dimensional equations confirm that a boundary layer exists in the angular frequency $\bar{B}$. An analysis of the non–dimensional equations at this stage does not make clear the small parameter that we expect to be multiplying a highest derivative term, although from the above discussion it is clear that we expect β to be in some way closely related to the small parameter present. In order to determine the origin of this boundary layer, we recall that in all practical regimes Re is extremely small. Considering the case of $Re \to 0$ and $S = O(1)$ as in the previous section, we found that we could solve the equations in closed–form. The solution for $\bar{B}$, if plotted, shows that the origin of the observed boundary layer comes from β being large: see Figures 3.9–3.11. Setting $Re \to 0$ we solve for $\bar{h}$ and $\bar{w}$ separately and substitute the solutions into the rotation equation.

Ignoring non-steady solutions, fibre inertia, surface tension and gravity the relevant

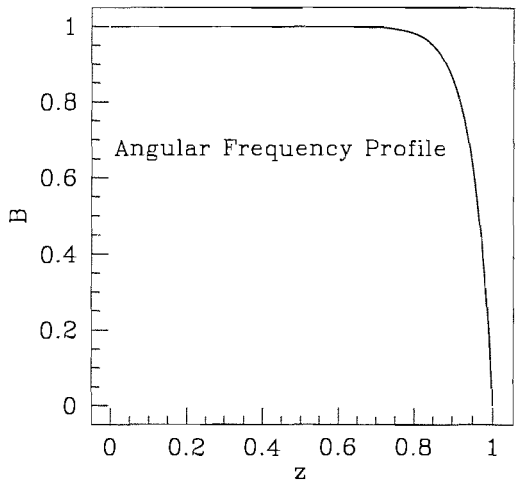

Figure 3.10: The angular frequency profile for $\beta = 10$.

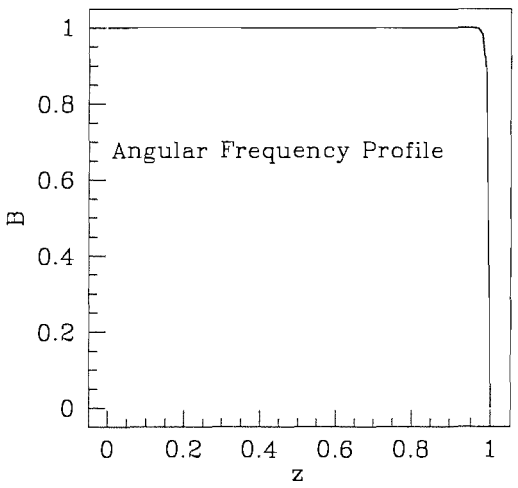

Figure 3.11: The angular frequency profile for $\beta = 100$.

equations are

$$3\bar{\mu}(\bar{h}^2\bar{w}_{\bar{z}})_{\bar{z}} = 0, \tag{3.85}$$

$$(\bar{h}^2\bar{w})_{\bar{z}} = 0, \tag{3.86}$$

and

$$\bar{\mu}(\bar{h}^4\bar{B}_{\bar{z}})_{\bar{z}} = 0, \tag{3.87}$$

with $\bar{\mu} = 1$ as the temperature is assumed to be constant in $\bar{z}$.

From (3.71) in §3.7.1 we know that $\bar{h} = \bar{h}_0 e^{-\frac{\beta\bar{z}}{2}}$ with $\bar{h}_0 = 1$, and $\bar{w} = \bar{W}_f e^{\beta\bar{z}}$ with $\bar{W}_f = 1$.

Substituting this result into (3.87) yields

$$(e^{-2\beta\bar{z}}\bar{B}_{\bar{z}})_{\bar{z}} = 0.$$

Differentiating and rearranging gives

$$2\bar{B}_{\bar{z}} - \phi\bar{B}_{\bar{z}\bar{z}} = 0,$$

with $\phi = 1/\beta$.

We therefore have a small parameter ϕ multiplying the second derivative, giving rise to a boundary layer. Completing the boundary layer analysis in the usual way we obtain a solution for $\bar{z}$ that must behave in the same way as (3.74), which also shows how the boundary layer behaviour ceases when β is not large.

The outer problem

The outer problem is found by neglecting terms $O(\phi)$ or higher giving

$$2\bar{B}_{\bar{z}} = 0,$$

so that $\bar{B} = \bar{B}_0$, a constant in the outer region. $\bar{B}_0$ is chosen because the boundary layer is at the end of the draw length, away from $\bar{z} = 0$ where $\bar{B} = \bar{B}_0$. This outer

region may be seen in Figure 3.11, where $\bar{B}_0$ is constant for large β, for the majority of the draw length.

The inner problem

The inner problem is found by rescaling the $\bar{z}$ variable in order to magnify the region of interest: that near to $\bar{z} = 1$. To do this we set

$$1 - \bar{z} = \delta\psi,$$

with

$$\frac{d}{d\bar{z}} = -\frac{1}{\delta}\frac{d}{d\psi}.$$

Upon substitution,

$$2\bar{B}_\psi + \frac{\phi\bar{B}_{\bar{z}\bar{z}}}{\delta}.$$

Employing a scaling of $\delta = O(\phi)$ and solving with the boundary conditions $\bar{B}(0) = 0$ and $\bar{B}(\infty) = \bar{B}_0$ gives

$$\bar{B} = \bar{B}_0(1 - e^{-2\psi}) = \bar{B}_0(1 - e^{2\beta(\bar{z}-1)}).$$

Combining this with the outer solution to obtain a solution valid for all $\bar{z}$ we have that

$$\bar{B} = \bar{B}_0 + \bar{B}_0(1 - e^{2\beta(\bar{z}-1)}) - \bar{B}_0 = \bar{B}_0(1 - e^{2\beta(\bar{z}-1)}). \tag{3.88}$$

As stated previously, equation (3.88) should be of the same form as the exact solution obtained in §3.7.1 in the limit that $Re \to 0$ and $S = O(1)$ for $\bar{B}$, whose exact form was $\bar{B} = \frac{1}{e^{2\beta}-1}((\bar{B}_L - \bar{B}_0)e^{2\beta\bar{z}} - \bar{B}_L + \bar{B}_0 e^{2\beta})$. In the limit of large β, and setting the rotation at $\bar{z} = 1$, $\bar{B}_L = 0$, (3.88) becomes $\approx \bar{B}_0(1 - e^{2\beta(\bar{z}-1)})$, in exact agreement with the above analysis. This result was effectively used to obtain (3.78), where we assumed a large draw–ratio.

Standard boundary layer theory analyses may also be undertaken for more general forms of the governing equations than (3.85)–(3.87), but these invariably suggest that, for realistic fibre drawing configurations, the rotation boundary layer is ubiquitous.

3.7.2 Thick–walled capillaries (small hole)

When the inner radius is $O(\delta)$ with $\delta \ll 1$, surface tension is expected to close the hole unless the preform rotation rate is large (for example). $\bar{h}_1 = O(\delta)$ corresponds to a thick–walled tube, since the outer radius is defined to be $O(1)$. This is a situation to consider, as it is observed that surface tension often acts to close the hole when it is small. Since this is undesirable and we normally desire for holes to remain, possible ways to counteract hole-closure are examined.

With $\bar{h}_1 = O(\delta)$ and $\bar{h}_2 = O(1)$ and whilst in the steady–state with no hole overpressure, gravity or inertia, to leading order equations (3.48)-(3.51) are

$$3\bar{\mu}(\bar{h}_2^2\bar{w}_{\bar{z}})_{\bar{z}} + \bar{\gamma}\bar{h}_2 + \frac{ReS^2}{4}(\bar{h}_2^4\bar{B}^2)_{\bar{z}} = 0, \tag{3.89}$$

$$\bar{h}_1 = 0, \tag{3.90}$$

$$(\bar{h}_2^2\bar{w})_{\bar{z}} = 0, \tag{3.91}$$

$$Re\bar{w}\bar{h}_2^2(\bar{h}_2^2\bar{B})_{\bar{z}} = \bar{\mu}(\bar{h}_2^4\bar{B}_{\bar{z}})_{\bar{z}}. \tag{3.92}$$

As one might expect, when $\bar{h}_1$ is small but all other parameters are of order one, the equations reduce to those of the solid rod case, as in §(3.7.1). Physically this means that the hole in the capillary tube closes through the effects induced by the presence of surface tension.

The above analysis assumed that $\bar{\gamma}$ is $O(1)$, but because of the scaling of surface tension and the drawing conditions, it is more usually much smaller than one. The above analysis will hold until $\bar{\gamma} \ll \delta$, because then the term $(\bar{h}_1^2\bar{w}_0)_{\bar{z}}$ from the left

hand side of (3.49) will become appreciable in size, whereas otherwise it makes a negligible contribution.

Taking a slightly different approach we consider the case where $\bar{h}_1 = O(\delta)$, where $\delta \ll 1$, taking $\bar{h}_2 = O(1)$, $S = O(1)$, $Re = O(\delta^2)$, $\bar{\gamma} = O(1)$ and $\bar{w} = O(\frac{1}{\delta})$ (corresponding to a large draw–ratio). The steady–state leading–order equations (3.48) and (3.50) in the absence of inertia and gravity give

$$\bar{h}_2 = \bar{h}_{20} e^{-\beta \bar{z}/2}, \tag{3.93}$$

$$\bar{w} = \bar{W}_f e^{\beta \bar{z}} \tag{3.94}$$

and

$$2\bar{w}\bar{h}_{1\bar{z}} + \bar{h}_1 \bar{w}_{\bar{z}} = -\bar{\gamma}, \tag{3.95}$$

so that

$$\bar{h}_1 = \frac{1}{\beta \bar{W}_f}[\bar{\gamma} e^{-\beta \bar{z}} + (\beta \bar{W}_f \bar{h}_{10} - \bar{\gamma}) e^{-\beta \bar{z}/2}]. \tag{3.96}$$

The hole size thus decreases monotonically in $\bar{z}$ (provided $\bar{h}_1$ remains positive), with

$$\bar{h}_1(1) = \frac{e^{-\beta/2}}{\beta \bar{W}_f}[\bar{\gamma}(e^{-\beta/2} - 1) + \beta \bar{W}_f \bar{h}_{10}], \tag{3.97}$$

so that the hole survives whenever

$$\bar{h}_{10} > \frac{\bar{\gamma}}{\beta \bar{W}_f}(1 - e^{-\beta/2}). \tag{3.98}$$

Suppose we now attempt to retain the hole structure by pressurizing the hole. Examining the equations reveals that a pressure $O(1/\delta)$ is required to affect the equation for $\bar{h}_1$, which then becomes

$$2\bar{w}\bar{h}_{1\bar{z}} + \bar{h}_1 \bar{w}_{\bar{z}} = -\bar{\gamma} + \bar{p}_0 \bar{h}_1. \tag{3.99}$$

Since $\bar{h}_2$ and $\bar{w}$ are still given by (3.93)–(3.94), (3.99) may be solved to yield

$$\bar{h}_1 = \exp\left(-\frac{\beta \bar{z}}{2} - \frac{k}{2} e^{-\beta \bar{z}}\right)\left[\bar{h}_{10} e^{-k/2} - \frac{\bar{\gamma}}{2\bar{W}_f} \int_0^{\bar{z}} \exp\left(-\frac{\beta \zeta}{2} + \frac{k}{2} e^{-\beta \zeta}\right) d\zeta\right], \tag{3.100}$$

where $k = \bar{p}_0/(\beta \bar{W}_f)$. Now consider the specific case where $\bar{W}_f = w_f$, $\bar{W}_d = w_d/\delta$, $\bar{h}_{10} = H_{10}\delta$, $\bar{p}_0 = P/\delta$, and $V = w_d/w_f$. Then $\beta = \log(V/\delta)$ and $k = P/(w_f \delta \log(V/\delta))$. We now find that

$$I(\bar{z}) = \int_0^{\bar{z}} \exp\left(-\frac{\beta\zeta}{2} + \frac{k}{2}e^{-\beta\zeta}\right) d\zeta = \frac{1}{\beta}\int_{e^{-\beta\bar{z}}}^{1} \xi^{-1/2} e^{k\xi/2}\, d\xi, \tag{3.101}$$

and thus

$$I(\bar{z}) = \frac{\sqrt{2\pi}}{\beta\sqrt{-k}}\left[\mathrm{erf}\left(\sqrt{-\frac{k}{2}}\right) - \mathrm{erf}\left(\sqrt{-\frac{ke^{-\beta\bar{z}}}{2}}\right)\right], \tag{3.102}$$

where $\sqrt{-\frac{k}{2}} > 0$ and $\sqrt{-\frac{ke^{-\beta\bar{z}}}{2}} > 0$.

For $x \gg 1$ we have

$$\mathrm{erf}(x) \sim 1 + \frac{e^{-x^2}}{\sqrt{\pi}}\left(-\frac{1}{x} + \frac{1}{2x^3} - \frac{3}{4x^5} + O(x^{-7})\right),$$

and we also note that $k \gg 1$ and $ke^{-\beta\bar{z}} \gg 1$ for all $\bar{z} \in [0,1]$ *except* exponentially close to $\bar{z} = 1$. Thus so long as $\bar{z}$ is not near to 1, we have

$$I(\bar{z}) \sim \frac{2}{\beta k}\left[e^{k/2} - \exp\left(\frac{\beta\bar{z}}{2} + \frac{k}{2}e^{-\beta\bar{z}}\right)\right] + \frac{2}{\beta k^2}\left[e^{k/2} - \exp\left(\frac{3\beta\bar{z}}{2} + \frac{k}{2}e^{-\beta\bar{z}}\right)\right] + \ldots\ldots,$$

the one–term approximation yielding good agreement with the exact value for most large values of β. Using this, we find that $\bar{h}_1$ may be approximated by

$$\bar{h}_1 \sim e^{-\frac{\beta\bar{z}}{2} + \frac{k}{2}(1-e^{-\beta\bar{z}})}\left[\delta H_{10} - \frac{\bar{\gamma}}{\beta w_f k}\left(1 - e^{\frac{\beta\bar{z}}{2} + \frac{k}{2}(e^{-\beta\bar{z}}-1)}\right)\right].$$

Let us now examine how $\bar{h}_1$ depends on the pressurization somewhere away from the two ends of the draw. Since $\beta = \log(V/\delta) \gg 1$ and $k = O((\delta \log\delta)^{-1})$, when $\bar{z}$ is close neither to 0 nor 1 we have that

$$\bar{h}_1 \sim \delta e^{k/2}\left[H_{10} - \frac{\bar{\gamma}}{\delta\beta w_f k}\right], \tag{3.103}$$

which is $O(\delta)$ given the scalings for β and k, as required.

Since $k \gg 1$, we see that $\bar{h}_1$ is exponentially sensitive to the amount of pressurization used, so that unless the pressure in the hole is controlled with unerring accuracy, the capillary will "explode" else the hole will close.

Our observations of the dependence of hole diameter on internal–hole pressure suggest that pressure may not be a robust control mechanism to prevent hole closure; but what of rotation? When overpressure is absent but the capillary is rotated, we study the small hole/large draw–ratio case where $\bar{h}_1 = O(\delta)$ where $\delta \ll 1$, $Re = O(\delta^2)$, $S = O(1)$, $\bar{\gamma} = O(1)$, $\bar{h}_2 = O(1)$ and $\bar{w} = O(1/\delta)$. The rotation appears to leading order in the equation for $\bar{h}_1$ when $\bar{B} = O(\delta^{3/2})$, in which case the governing equations (3.48)–(3.51), for constant viscosity, are

$$\left[3\bar{h}_2^2\bar{w}_{\bar{z}} + \frac{1}{4}ReS^2\bar{h}_2^4\bar{B}^2\right]_{\bar{z}} = 0, \tag{3.104}$$

$$(\bar{h}_2^2\bar{w})_{\bar{z}} = 0, \tag{3.105}$$

$$(\bar{h}_2^4\bar{B}_{\bar{z}})_{\bar{z}} = 0, \tag{3.106}$$

$$\frac{\bar{h}_1}{2}\left[ReS^2\bar{B}^2\bar{h}_1\bar{h}_2^2 - 2\bar{\gamma}\right] = (\bar{h}_1^2\bar{w})_{\bar{z}}. \tag{3.107}$$

Further analysis is rendered awkward by the fact that these equations do not possess a closed–form solution, but bearing in mind the ubiquity of the boundary–layer behaviour of $\bar{B}$ previously established, we may simplify the problem by assuming that the angular frequency is constant and equal, say, to $\bar{B}_0$. We now find that (3.48) and (3.50) give

$$\bar{w} = K(1 + Ce^{A\bar{z}})^{1/2}, \tag{3.108}$$

$$\bar{h}_2 = \sqrt{\frac{AK}{2Q^2}}(1 + Ce^{A\bar{z}})^{-1/4}, \tag{3.109}$$

where $Q^2 = ReS^2\bar{B}_0^2/12$, the constants A and K satisfy

$$A = \frac{2Q^2\bar{h}_{20}^2(1+C)}{\bar{W}_f}, \tag{3.110}$$

$$K = \bar{W}_f(1+C)^{-1/2}, \tag{3.111}$$

and the constant C is determined by solving

$$\left(\frac{\bar{W}_d}{\bar{W}_f}\right)^2 - 1 = \frac{C}{1+C}\left[\exp\left(\frac{2Q^2\bar{h}_{20}(1+C)}{\bar{W}_f}\right) - 1\right], \tag{3.112}$$

which may easily be shown to have a unique positive solution for C. The governing equation for $\bar{h}_1$ is now

$$2\bar{h}_{1\bar{z}}\bar{w} = \bar{h}_1\bar{w}_{\bar{z}} - \bar{\gamma} + 6Q^2\bar{h}_2^2\bar{h}_1,$$

and thus

$$\bar{h}_1 = \frac{e^{3A\bar{z}/2}}{(1+Ce^{A\bar{z}})^{7/4}}\left[\bar{h}_{10}(1+C)^{7/4} - \frac{\bar{\gamma}}{2K}\int_0^{\bar{z}} e^{-3A\zeta/2}(1+Ce^{A\zeta})^{5/4}\,d\zeta\right]. \quad (3.113)$$

As before, we now set $\bar{W}_d = w_d/\delta$, $\bar{W}_f = w_f$, $\bar{h}_{10} = H_{10}\delta$, $Re = R\delta^2$ and $\bar{B} = \bar{B}_0/\delta^{3/2}$. We now find that C satisfies

$$\frac{V^2}{\delta^2} - 1 = \frac{C}{1+C}\left(e^{\Lambda(1+C)/6\delta} - 1\right), \quad (3.114)$$

where $V = w_d/w_f$ and $\Lambda = RS^2\bar{B}_0^2\bar{h}_{20}^2/w_f = O(1)$. For $\delta \ll 1$, (3.114) may be solved asymptotically to yield

$$C \sim \frac{V^2}{\delta^2}e^{-\Lambda/6\delta}, \quad (3.115)$$

$$K \sim w_f, \quad (3.116)$$

$$A \sim \frac{\Lambda}{6\delta}. \quad (3.117)$$

For $\Lambda = O(1)$ it is now easy to show that

$$\int_0^{\bar{z}} e^{-\Lambda\zeta/4\delta}\left(1+\frac{V^2}{\delta^2}e^{-\Lambda(1-\zeta)/6\delta}\right)^{5/4} d\zeta \sim \frac{4\delta}{\Lambda}\left[1-e^{-\Lambda\bar{z}/4\delta}\right] \quad (3.118)$$

and thus in this limit

$$\bar{h}_1 = \frac{e^{\Lambda\bar{z}/4\delta}}{\left(1+\frac{V^2}{\delta^2}e^{\Lambda(\bar{z}-1)/6\delta}\right)^{7/4}}\left[\delta H_{10}\left(1+\frac{V^2}{\delta^2}e^{-\Lambda/6\delta}\right)^{7/4} - \frac{2\bar{\gamma}\delta}{w_f\Lambda}\left(1-e^{-\Lambda\bar{z}/4\delta}\right)\right]. \quad (3.119)$$

The exponential dependence of (3.119) on the rotation rate suggests that, as concluded above for pressurization, active control of hole size via rotation is likely to be extremely difficult from a practical point of view. Note, however, that the analysis that led to (3.119) assumed that δ was small enough so that $C \ll 1$. For many practical fibre draws, the small parameter δ may be identified with the quantity $1/\beta$, which, since $\beta = \log(\bar{W}_d/\bar{W}_f)$, is likely to be small but not minute. For example, in many cases $\delta \sim 0.1$. In these cases the quantity $C = (V^2/\delta^2)e^{-\Lambda/6\delta}$ in fact proves to be *large*. What really happens in such cases? Suppose we acknowledge the fact that

C is not small by setting $\Gamma = \Lambda/6\delta$ in the exponential and assuming that $\Gamma = O(1)$. We now find that

$$C \sim -\frac{2}{\Gamma}\log\left(\frac{\delta}{V}\right) - 1 - \frac{1}{2\log\delta} + O\left((\log\delta)^{-2}\right), \tag{3.120}$$

$$A \sim -2\log\left(\frac{\delta}{V}\right) - \frac{\Gamma}{2\log\delta} + O\left((\log\delta)^{-2}\right), \tag{3.121}$$

$$K \sim w_f\sqrt{\frac{\Gamma}{2}}\left(\frac{1}{\sqrt{-\log\delta}} - \frac{\log V}{2(-\log\delta)^{3/2}} + O\left((-\log\delta)^{-5/2}\right)\right), \tag{3.122}$$

and thence, to leading order,

$$\bar{h}_1 \sim \frac{e^{-A\bar{z}/4}}{C^{7/4}}\left[\bar{h}_{10}C^{7/4} - \frac{\bar{\gamma}}{2K}\int_0^{\bar{z}} C^{5/4}e^{-A\zeta/4}\,d\zeta\right]. \tag{3.123}$$

From this we conclude that, in this limit,

$$\bar{h}_1 \sim e^{\bar{z}\log\delta/2}\left[H_{10}\delta - \frac{\bar{\gamma}}{w_f\log\delta}(e^{\bar{z}\log\delta/2} - 1)\right], \tag{3.124}$$

an expression that is *independent* of the rotation rate $\bar{B}_0$, which appears only if one proceeds to the next order. This situation is in marked contrast to the previous exponential dependence and suggests that in practice rotation will prove to be a useful control mechanism and may be used to produce capillaries with extremely small holes.

The various asymptotic limits considered above give good agreement with numerical simulations of the full equations (3.48)–(3.51) (not presented here), and make useful predictions regarding the use of preform rotation to prevent hole collapse under the action of surface tension. They also predict the final twist–periodicity of a given drawing scenario. Together, these predictions allow an experimenter to predetermine the spin rate according to the required pitch, and hence quantify the effect that the prescribed rotation rate will have on the final fibre geometry.

The effects of hole overpressure have been investigated and it has been shown that although this may be a useful control parameter, it is unlikely by itself to allow the overall control of hole closure (that is its prevention): for further details see [14]. Rotation, however, does provide a useful experimental control so long as the draw ratio is not too large. For more discussion of the rotation of holey fibres see [65].

We now ask how we might prevent hole closure whilst still in this same limiting situation of a small inner radius.

3.7.2.1 Thick–walled capillaries with large rotation

Holey fibres are made by drawing a preform from a hot furnace. The aperture of the furnace though, is of limited size, and so in order to obtain a large hole density in the final fibre, as is sometimes desirable, the components of the holey fibre preform, capillary tubes, must be of the smallest possible diameter. Obviously, surface tension effects then become dominant and problems occur with surface tension induced hole collapse.

Numerical simulations show that in general it is possible for a fibre whose hole is starting to close under the action of surface tension to be rotated rapidly enough to prevent the closure. However, if the initial inner radius is decreased further and the simulation performed again, it is not possible to prevent hole collapse whilst remaining within the practical limits on rotation rates.

One must also remember that it is not possible to generalize to the case of holey fibres from capillary tubes. For example, if we establish that it is possible to keep capillary tubes open despite the best efforts of surface tension, it may not be possible to simply scale up the problem and claim that the same is true of holey fibres, because such fibres are a collection of capillary tubes. For example, a holey fibre that is mostly comprised of air would behave more like a large capillary tube when holes are closely spaced. Furthermore and also in the opposite extreme of small widely-spaced holes when it is likely that they do not feel the presence of the other holes, the holes are not being spun around their geometric centres, further complicating matters.

An inspection of (3.48)-(3.51) reveals that unless the rotation rate is large, the surface tension will act to close the hole when the initial radius is small ($O(\epsilon)$). To obtain an estimate for the point at which rotation is able to prevent this closure, we need

to achieve a balance between $2\bar{\gamma}\bar{h}_2$, which is naively of order one, and $ReS^2B^2\bar{h}_1\bar{h}_2^3$. Because of the way in which $\bar{\gamma}$ was non–dimensionalized though, $\bar{\gamma}$ may be $O(\epsilon)$ or smaller, and the necessary balance must take account of the exact size of this term. As in the case of thick–walled capillaries, $(\bar{h}_1^2\bar{w}_0)_{\bar{z}}$ from the left hand side of (3.49) makes a negligible contribution to the solution, and so may be ignored until ϵ becomes at least smaller than any value we would encounter in practice (not below $\approx 10^{-6}$).

In order to make the rotation "large" we increase the size of S, since this is $\propto \Omega$, which in turn scales B. An order of magnitude estimate of the size of the angular frequency needed to prevent hole collapse is, setting $\bar{\gamma} = O(\epsilon)$, therefore

$$R = \frac{\Omega}{\epsilon} \approx \frac{W_d}{L\epsilon}\sqrt{\frac{2}{Re}}. \tag{3.125}$$

We now briefly show that (3.125) produces numerically realistic results for practically reproducible drawing scenarios.

In Table 3.2, PR denotes the predicted rotation rate necessary to prevent hole collapse under the action of surface tension and AR denotes the rate actually necessary in numerical simulations that include the effects of gravity and inertia. The results demonstrate a remarkable agreement with the predictions made, and suggests that this relation is satisfactory as an order of magnitude approximation of the amount of rotation needed to keep any given hole open.

Furthermore, when ϵ is not of the same size of $\bar{\gamma}$ then it becomes apparent that the above balance is no longer true. The above balance holds because in the cases considered $\bar{\gamma}$ was always roughly the same size as ϵ. When this is not the case we need to balance the surface tension term with the rotation term. In the absence of surface tension we know that the hole cannot close, since there is no force in the inward radial direction of a fibre transverse cross–section that allows this to happen. It is therefore this term that the rotation must compete with and balance.

Table 3.2: Table to show comparison between predictions of asymptotics and numerical solutions to equations (3.48)-(3.51).

Quantity (S.I Units)	Case One	Case Two	Case Three
h_{10}	1.00×10^{-10}	5.00×10^{-8}	2.0×10^{-6}
h_{20}	1.73×10^{-5}	3.87×10^{-5}	2.45×10^{-4}
W_d	8.33×10^{-2}	8.33×10^{-2}	8.33×10^{-2}
W_d	2.50×10^{-2}	2.50×10^{-2}	2.50×10^{-2}
T	1400	1700	2000
μ_0	6.91×10^{8}	2.48×10^{6}	3.93×10^{4}
Re	7.97×10^{-9}	2.22×10^{-6}	1.40×10^{-4}
S	2.23×10^{4}	6.26×10^{2}	9.91×10^{1}
ϵ	5.77×10^{-5}	1.29×10^{-3}	8.16×10^{-3}
PR	7.0×10^{8}	2.04×10^{6}	4.07×10^{4}
AR	1×10^{9}	1×10^{6}	6×10^{4}
% Error	43	51	32

In wholly realistic drawing scenarios we often have a smaller viscosity than considered in the above calculation, and certainly have a larger draw–ratio. We already know that in these circumstances a boundary layer starts to form (through the mathematical action of large β on derivative terms), but this does not mean that the requirement of surface tension effects balancing those of rotation to prevent hole closure no longer holds. Conducting a similar analysis reveals that for arbitrary case, the rotational frequency needed to prevent hole collapse is

$$R = \frac{\Omega}{\epsilon} \approx \frac{W_d}{L\epsilon}\sqrt{\frac{2\bar{\gamma}}{\epsilon Re}}, \tag{3.126}$$

which reduces to the previous expression (3.125) when $\bar{\gamma} = O(\epsilon)$ as required.

To confirm the status of (3.126) we once again consider some practical examples, shown in Table 3.3.

The numerical simulations once again show good agreement with the predictions made, confirming that this is a reasonable approximation for all realistic drawing scenarios that one may wish to consider.

3.7.2.2 Thick–walled capillaries with small surface tension

As previously mentioned, it is the action of surface tension on the hole that causes it to close, given that the hole is small and that the surface tension force is $\propto \frac{1}{r}$. It therefore seems reasonable to assume that one other way of stopping the inner radius from shrinking to zero under the action of surface tension is to rescale the surface tension as we have the inner radius (achieved in practice by choosing an appropriate viscosity).

We therefore set $\bar{\gamma} = O(\epsilon)$. If we scaled the surface tension with anything smaller than $O(\epsilon)$, then to leading order it would not appear in the equations and thus have no effect. To leading–order equations (3.48)–(3.51) become

$$(3\bar{h}_2^2\bar{w}_{\bar{z}})_{\bar{z}} = -\frac{ReS^2}{4}(\bar{h}_2^4\bar{B}^2)_{\bar{z}}, \tag{3.127}$$

Table 3.3: Table to show comparison between predictions of asymptotics and numerical solutions to equations (3.48)–(3.51).

Quantity (S.I. Units)	Case One	Case Two
h_{10}	4.00×10^{-6}	6.00×10^{-5}
h_{20}	3.46×10^{-4}	1.34×10^{-3}
W_d	8.33×10^{-2}	8.33×10^{-1}
W_d	2.50×10^{-4}	2.50×10^{-4}
T	1750	1950
μ_0	1.14×10^{6}	7.26×10^{4}
Re	4.80×10^{-6}	7.59×10^{-4}
S	9.95×10^{1}	2.57
ϵ	1.15×10^{-1}	4.47×10^{-2}
$\bar{\gamma}$	2.74×10^{-4}	1.11×10^{-4}
PR	2.9×10^{4}	1.59×10^{3}
AR	2.3×10^{4}	7.9×10^{2}
% Error	21	50

$$(\bar{h}_1^2\bar{w})_{\bar{z}} = \bar{p}_o\bar{h}_1^2 - \bar{\gamma}\bar{h}_1 + \frac{ReS^2}{8}\bar{h}_1^2\bar{h}_2^2\bar{B}^2, \tag{3.128}$$

$$(\bar{h}_2^2\bar{w})_{\bar{z}} = 0, \tag{3.129}$$

$$Re\bar{w}\bar{h}_2^2(\bar{h}_2^2\bar{B})_{\bar{z}} = (\bar{h}_2^4\bar{B}_{\bar{z}})_{\bar{z}}. \tag{3.130}$$

Equations (3.127)–(3.130) resemble those for the solid fibre, but without the presence of surface tension. The mass conservation equation for $\bar{h}_1$ is now a non-trivial differential equation involving other variables. Since $\bar{h}_1$ is not coupled to any other equation, we should be able to solve (3.127), (3.129) and (3.130) for the three variables $\bar{h}_2$, $\bar{w}$ and $\bar{B}$, and then substitute their solutions into (3.128) in order to solve for $\bar{h}_1$. However, §3.7.1 reminds us that only under certain conditions, namely when the momentum equation decouples from the rotation equation, may we solve (3.127), (3.129) and (3.130) in closed–form. Making use of these limits and substituting the consequent solutions into (3.129) leaves us with an equation that must once again be solved numerically unless $p_0 = 0$, which gives (3.73) and (3.74) together with

$$\bar{h}_1 = \left(\bar{h}_{10} + \frac{\bar{\gamma}}{\bar{W}_d\beta}\left(e^{\left(\frac{-\beta\bar{z}}{2}\right)} - 1\right)\right)e^{\left(\frac{-\beta\bar{z}}{2}\right)}.$$

3.7.3 Thin–walled capillaries

We now examine the drawing of thin–walled capillary tubes. Here we set $\bar{h}_2 = \bar{h}_1 + \epsilon\bar{h}_{22}$, with $\bar{h}_1$, $\bar{B}$ and $\bar{w}$ all $O(1)$. Neglecting inertial force, surface tension, hole overpressure, gravity, transient solutions and taking $Re \ll 1$, to leading order equations (3.48)–(3.51) are (writing $w_0 = w$)

$$(\bar{h}_1\bar{h}_{22}\bar{w}_{\bar{z}})_{\bar{z}} = 0, \tag{3.131}$$

$$(\bar{h}_1^2\bar{w})_{\bar{z}} = 0, \tag{3.132}$$

$$(\bar{h}_1\bar{h}_{22}\bar{w})_{\bar{z}} = 0, \tag{3.133}$$

$$(\bar{h}_1^3\bar{h}_{22}\bar{B}_{\bar{z}})_{\bar{z}} = 0, \tag{3.134}$$

whose solution is

$$\bar{h}_1 = \bar{h}_{10}e^{-\frac{\beta\bar{z}}{2}},$$

$$\begin{aligned}
\bar{h}_2 &= (\bar{h}_{10} + \epsilon)e^{-\frac{\beta\bar{z}}{2}}, \\
\bar{w} &= \bar{W}_f e^{\beta\bar{z}}, \\
\bar{B} &= \frac{1}{e^{2\beta} - 1}((\bar{B}_L - \bar{B}_0)e^{2\beta\bar{z}} - \bar{B}_L + \bar{B}_0 e^{2\beta}).
\end{aligned}$$

Physically this result may be interpreted as follows. There is no reason that the solutions to this problem should differ from those to the case where $\bar{h}_2$ is independent of $\bar{h}_1$ (when $\bar{h}_2$ is not a perturbation around $\bar{h}_1$). The reason for this is that when hole overpressure, surface tension, inertial force, etc. are ignored, the fibre geometry is preserved throughout the draw length (simple exponential solutions for $\bar{h}_1$, $\bar{h}_2$ and $\bar{w}$ given by (3.71)). It has been shown that under similar conditions the geometry ratio $\frac{\bar{h}_2}{\bar{h}_1}$ remains constant along the draw length [14]. The same reasoning applies to the solution for $\bar{B}$, where the results are identical to those shown in (3.73)–(3.74).

3.7.3.1 Thin–walled capillaries with surface tension

Setting surface tension to be $O(1)$, an analysis similar to the one above may be conducted to show that the inner radius collapses along the majority of the draw length, and that the outer radius and downstream fluid velocity become constant along the majority of the draw length. The boundary conditions that we must impose imply that boundary layers are present in all of the three variables $\bar{w}$, $\bar{B}$ and $\bar{h}_2$. We note at this stage that the presence of a boundary layer in $\bar{w}$ may have implications for fibre manufacture. In particular, rapid changes in $\bar{w}$ are expected to increase the possibility of fibre breakage.

To examine this further, we consider what happens if we do not impose the usual boundary conditions for $\bar{w}$ at $\bar{z} = 0$ and $\bar{z} = 1$. Instead we shall allow $\bar{h}_2 \to \bar{h}_1$ and note that (3.48) gives $\bar{h}_{2\bar{z}} = 0$. This forces $\bar{h} = \bar{h}_0$ for all $\bar{z}$. We now need to consider the boundary conditions for $\bar{w}$ in order to be able to determine the form of the solution. Our choice is to either impose the usual conditions to impose something different. Imposing the usual conditions the above situation is achieved once more

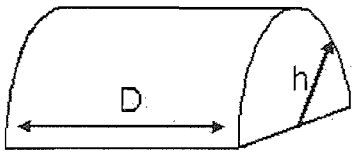

Figure 3.12: Half-cylinder to calculate the overpressure inside a stationary capillary tube necessary to counteract the effect of surface tension.

with boundary layers present as described above. If we do not impose different velocity boundary conditions at $\bar{z} = 0$ and $\bar{z} = 1$, then for a steady–state solution to exist we note that for $\bar{h} \neq 0$, using hole overpressure to prevent hole closure and assuming nothing about the form of $\bar{w}$ other than that its derivatives are $O(1)$, to leading–order (3.49) and (3.50) become

$$\bar{p}_o \bar{h}^2 - 2\bar{\gamma}\bar{h} = 0, \tag{3.135}$$

assuming no preform rotation. Thus the balance between hole overpressure and surface tension must be achieved by setting

$$\bar{p}_o = \frac{2\bar{\gamma}}{\bar{h}}. \tag{3.136}$$

Equation (3.136) may be interpreted as follows. In the case where the fluid is not moving at all, the pressure must balance the surface tension according to (3.136). This is easily confirmed by considering the half–cylinder in Figure 3.12 of length D and radius $\bar{h}$, whose wall is a made from a thin glass film. It is supported by the overpressure $\bar{p}_o$ acting over an area $2\bar{h}D$ that must balance the total surface tension force of $4\bar{\gamma}D$ acting on both the inner– and outer–surface giving once again that

$$\bar{p}_o = \frac{2\bar{\gamma}}{\bar{h}},$$

in agreement with (3.136).

It is interesting to note at this point that, in the event that we do not require $\bar{h}_2 \to \bar{h}_1$ but assume that $\bar{w} \equiv 0$, (3.48) gives

$$\bar{\gamma}(\bar{h}_1 + \bar{h}_2)_{\bar{z}} = 0, \tag{3.137}$$

and (3.49) and (3.50) both give

$$\bar{p}_0 = \bar{\gamma}\left(\frac{1}{\bar{h}_1} + \frac{1}{\bar{h}_2}\right), \tag{3.138}$$

which is the Laplace–Young equation, reducing to (3.136) when $\bar{h}_1 = \bar{h}_2$ as required. Furthermore, since (3.137) and (3.138) constitute one first–order equation in either of the two variables, they may be solved to give

$$\bar{h}_1 = \bar{h}_{10}, \tag{3.139}$$

$$\bar{h}_2 = \frac{\bar{\gamma}\bar{h}_{10}}{\bar{p}_0\bar{h}_{10} - \bar{\gamma}}, \tag{3.140}$$

or

$$\bar{h}_1 = \frac{\bar{\gamma}\bar{h}_{20}}{\bar{p}_0\bar{h}_{20} - \bar{\gamma}}, \tag{3.141}$$

$$\bar{h}_2 = \bar{h}_{20}. \tag{3.142}$$

In practice for fibre drawing we must impose different values for W_f and W_d, in which case pressurizing the hole to prevent hole closure will give rise to boundary–layers in $\bar{h}$ and $\bar{w}$.

3.7.4 An estimate of the maximum hole overpressure that may be applied

In order to obtain an estimate for the amount of hole overpressure that may be applied before the preform "explodes", it is necessary to simplify the equations (3.48)–(3.51) somewhat. We make gross simplifications to the variables in the equations so that we may determine a simple relationship between the balance of surface tension, rotation and hole overpressure.

The most natural choice seems to be to set $\bar{h}_2 = \alpha\bar{h}_1$ and $\bar{h}_1$, $\bar{w}$, and $\bar{B}$ to constant values for all $\bar{z}$. We also set $\alpha > 1$. Using equations (3.48)–(3.51) we see that (3.48) and (3.51) are automatically satisfied, whereas (3.49) and (3.50) both give, with

$\bar{h} = \bar{h}_1$,

$$2\bar{p}_o\bar{h}\alpha - 2\bar{\gamma}(1+\alpha) + ReS^2\bar{B}^2\bar{h}^3\alpha(\alpha^2-1) = 0,$$

and

$$\bar{p}_o\bar{h}\alpha - \bar{\gamma}(1+\bar{\alpha}) + \frac{ReS^2}{2}\bar{B}^2\bar{h}^3\alpha(\alpha^2-1) = 0,$$

which, upon rearrangement gives

$$\bar{B}^2 = 2\frac{\bar{\gamma}(1+\alpha) - \bar{p}_o\bar{h}\alpha}{ReS^2\bar{h}^3\alpha(\alpha^2-1)}. \tag{3.143}$$

Thus for $\bar{B}$ to be real we must have that

$$\bar{p}_o\bar{h}\alpha \leq \bar{\gamma}(1+\alpha), \tag{3.144}$$

which gives us an order of magnitude check for the maximum overpressure that may be applied to the inner hole.

One should expect the pressure predicted by (3.144) to be much smaller than the values of hole overpressure used in realistic experimental draws (which may be as large as a few PSI), because in these experiments the pressure is not only counteracting the force of surface tension, but also and more notably viscous forces. Here, since we have set the fibre radius and therefore downstream velocity, to be constant, we must expect that the only force able to balance with the pressure, in the absence of viscous forces introduced when a geometry change along the length is present, is the surface tension; or else no steady–state solution would exist and either the fibre would collapse or 'explode'.

Redimensionalizing (3.144) and inserting typical parameter values of $h = 1\text{mm}$, $\alpha = 2$ and $\gamma = 0.3\text{N/m}$, we find that

$$p_0 \leq \frac{\gamma(1+\alpha)}{\alpha h}, \tag{3.145}$$

or

$$p_0 \leq 450Pa \approx \epsilon\ \text{PSI},$$

where $\epsilon \approx 0.1$ is a small parameter. This is in agreement with experimental evidence where pressures $O(1)$PSI are routinely used without hole explosion being observed.

3.7.4.1 A note on geometry preservation

In the previous section we chose $\bar{h}_2 = \alpha \bar{h}_1$ where α was a constant > 1. This immediately implies that a geometry–preserving solution is being assumed.

It was shown previously in §3.7.1.2 and [15] that it is not possible to retain a geometry–preserving solution in the presence of surface tension. One might also intuitively think that there is also no reason why rotating the preform should allow a geometry–preserving solution to be found. We can easily verify this here by exhibiting a contradiction.

Assume that $\bar{h}_2 = \alpha \bar{h}_1$ where α is a constant > 1 as before. If we allow $\bar{w}$ to vary along the length of the fibre with the usual velocity boundary conditions at $\bar{z} = 0$ and $\bar{z} = 1$ (and $\bar{W}_d > \bar{W}_f$) then the fibre is being stretched out, as is required by mass–conservation conditions. Given that $\bar{h} = \bar{h}(\bar{z})$, the only way that both (3.49) and (3.50) may be satisfied (save the trivial solution $\alpha = 1$ that we shall ignore) is if the right hand sides of both (3.49) and (3.50) are zero. Solving the right hand side of either (3.49) or (3.50) for p_0 and substituting into the rotation equation (3.51) then requires that either $\bar{h} = 0$ or $\bar{h}_{\bar{z}} = 0$, contradicting the initial assumption. It is therefore as one would imagine: it is not possible to regain the geometry–preserving solutions seen previously and lost with the addition of surface tension, by trying to balance the effects of surface tension with those of preform rotation and/or hole overpressure.

3.8 Conclusions

The various asymptotic limits considered give good agreement with numerical simulations of the full equations, and make useful predictions regarding the use of preform rotation to prevent hole collapse under the action of surface tension. They also predict the final twist periodicity of a given drawing scenario. Together these predictions

allow an experimenter to predetermine the spin rate according to the required pitch, and hence quantify the effect that the necessary rotation will have on the final fibre geometry.

Care must be taken when generalising the rotation of capillary tube physics to the full holey fibre problem. Among other things such as the complex geometry, the fact that holes are not rotated around their centres, and that multiple surfaces are present, must be carefully considered.

The effects of hole overpressure have not been investigated here, although for an introduction to this see [14]. Further details will be presented later in the thesis. For further discussion of the rotation of holey fibres see [50], and for general background on the effect of fibre birefringence see for example [54].

The model is to be seen as a first step that goes some way towards analysing the process of drawing whilst rotating full holey fibres with a non–axisymmetric geometry. The model makes accurate predictions of the maximum hole overpressure that may be applied and of the geometry of final the fibre (see Chapter 7 for details). Under certain circumstances the model for capillary tubes may be used to directly measure the effects of preform rotation on holey fibre geometry, as will be more fully discussed in Chapter 4.

3.8.1 Practical Results

In this Chapter we:

- determine the rotation rate at which rotation affects the geometry of solid fibre preforms (see §3.7);
- determine the rotation rate at which rotation affects the geometry of capillary tubes (see §3.7);

- derive a formula to calculate the twist periodicity in a fibre given the drawing parameters (see §3.7.1.1);
- describe the effects of surface tension on a solid fibre (see §3.7.1.2);
- describe the effects of surface tension on a capillary tube and, potentially, a holey fibre (see §3.7.1.2);
- examine the possibilities for controlling small holes in a capillary tube and, potentially, a holey fibre (see §3.7.2);
- derive an approximate formula to predict the maximum hole overpressure that may be applied to a capillary tube (see §3.7.4).

Chapter 4

Estimating the Effects of Rotation on Holey Fibres

4.1 Introduction

In this Chapter we will categorize two broad classes of holey fibre in order to predict the effects of preform rotation on their macroscopic structure and on their microstructure.

As noted before, conventional (i.e. solid) preforms are routinely rotated to introduce a twist into the final fibre, since this reduces polarization mode dispersion (PMD) [54], [55], [57]. It is not obvious that the same process may be applied to holey fibre preforms without producing adverse macroscopic geometry changes that severely compromise the microstructure within. Notwithstanding this, preservation of the microstructure has recently been demonstrated when rotating large mode–area fibres with a high density of small, dispersed holes, at rates sufficient to dramatically improve PMD [58].

The control of fibre birefringence provides another reason for spinning during the

fibre manufacture process. Its effects may be significant in holey fibres for three main reasons [52]. First, many of holey fibres have wavelength–scale structures. Secondly, a significant refractive index contrast may exist between the core and the effective refractive–index of the cladding. Thirdly, intended or accidental geometrical asymmetries may be introduced in the manufacturing process, which may include the locking in of some asymmetric stress–distribution to the fibre [53]. When such asymmetries are present in holey fibres, exacerbated by the high refractive–index contrast, the two polarizations of light travel at different speeds. This results in fibre birefringence with a characteristic beat–length, caused by the components of light interfering as they travel at different rates, which may be as short as 0.3mm (see §4.3).

In sensor applications the maintenance of polarization is desirable to improve isolation between the modes by maximizing the mode splitting, fibre birefringence is desirable. By contrast, in data transmission and other applications fibre birefringence is unwanted and may be reduced by averaging out the effects of asymmetries along the fibre by introducing a twist [54]. We recall that the periodicity of the twist required depends on the wavelength of light and the details of the fibre profile. Fibre preforms may be rotated as they enter the furnace and held with zero rotation at its exit, leaving the fibre with an overall twist along its length [58]. This stratagem succeeds provided the twist periodicity (spin pitch) does not exceed the beat length. However, there is currently a practical limit of about 2000rpm to the rate at which preforms may be rotated. At rates greater than this, the alignment of the preform in the furnace becomes unstable and the preform begins to vibrate [66].

Evidently holey fibre technology would be greatly aided by the development of accurate tools for predicting the changes that occur during fibre drawing. We now use numerical and analytic results from the model that governs capillary drawing to answer three questions about holey fibres: (i) can we reduce or remove fibre birefringence at realistic rotation rates whilst preserving the microstructure? (ii) can we minimize the spin pitch in fibres by other means whilst remaining within the

rotation limit and preserving the microstructure? (iii) can we use preform spinning as a method for controlling the fibre geometry?

To assist characterization of fibres, we now identify two broad types of fibre. The first type of fibre considered is a large mode–area holey fibre with an approximately uniform distribution of diffuse holes. This will be referred to as a "type–one" holey fibre (see Figure 4.1), and might be useful for transmission, where there is a need to reduce PMD. These are manufactured in a single stage, the preform being assembled and then drawn directly into fibre form. Type–one fibres will be considered solid fibres. Secondly, we consider fibres where a large jacket surrounds a microstructured region with a high density of holes. These fibres have small core–dimensions and outer dimensions that allow the fibre to be handled easily. These will be referred to as "type–two" holey fibres (see Figure 4.1), and are useful for non–linear devices in which the reduction of birefringence is often a critical issue. Type–two fibres are typically manufactured in two stages. A "cane" preform (comprising the microstructured region in the final fibre) is drawn to a cane. The cane is then inserted into a "jacket tube" (capillary tube) and the resulting structure drawn to produce a fibre. In principle these fibres could be manufactured in a single–stage process with a suitable drawing furnace. Type–two fibres are modelled as capillary tubes. Some of the following descriptive text is repeated briefly and the reader may now move to §4.5 if they are already familiar with previous Chapters in this thesis.

We assume throughout that the glass used is Suprasil F300, a silica glass commonly used in the production of high–quality silica optical–fibres. The physical properties used for the computations were taken from [15].

4.2 Mathematical modelling

Details of the derivation of the model used in this Chapter along with an asymptotic analysis may be found in Chapter 3. After appropriate non–dimensionalizations

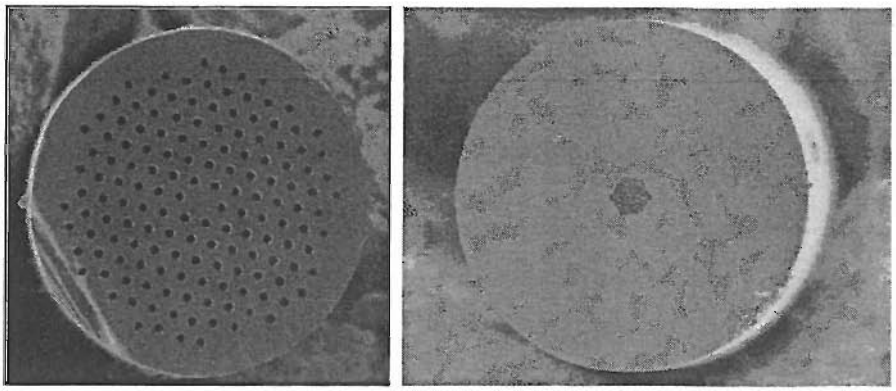

Figure 4.1: (Left) The cross–section of a type–one holey fibre. (Right) The cross–section of a type–two holey fibre.

of the governing equations, an asymptotic analysis based on the small aspect ratio (radius/length) of the preform, eventually leads to the (dimensional) isothermal equations

$$\rho(h_2^2 - h_1^2)(w_{0t} + w_0 w_{0z} - g) = [3\mu(h_2^2 - h_1^2)w_{0z} + \gamma(h_1 + h_2) + \frac{\rho}{4}(h_2^4 - h_1^4)B^2]_z, \quad (4.1)$$

$$(h_1^2)_t + (h_1^2 w_0)_z = \frac{2p_0 h_1^2 h_2^2 - 2\gamma h_1 h_2(h_1 + h_2) + \rho h_1^2 h_2^2 B^2(h_2^2 - h_1^2)}{2\mu(h_2^2 - h_1^2)}, \quad (4.2)$$

$$(h_2^2)_t + (h_2^2 w_0)_z = \frac{2p_0 h_1^2 h_2^2 - 2\gamma h_1 h_2(h_1 + h_2) + \rho h_1^2 h_2^2 B^2(h_2^2 - h_1^2)}{2\mu(h_2^2 - h_1^2)}, \quad (4.3)$$

$$\mu\left((h_2^4 - h_1^4)B_z\right)_z = \rho[h_2^2(h_2^2 B)_t - h_1^2(h_1^2 B)_t] + \rho w_0[h_2^2(h_2^2 B)_z - h_1^2(h_1^2 B)_z]$$
$$-\frac{\rho\gamma B}{\mu}(h_1^2 h_2 + h_2^2 h_1) + \frac{\rho^2 B^3}{2\mu}(h_1^2 h_2^4 - h_2^2 h_1^4) + \frac{\rho}{\mu}p_0 B h_1^2 h_2^2, \quad (4.4)$$

where the boundary conditions for the flow are given by

$$w(0,t) = W_f, \quad w(L,t) = W_d,$$

$$h_1(0,t) = h_{10}, \quad h_2(0,t) = h_{20},$$

and

$$B(0,t) = B_0, \quad B(L,t) = B_L.$$

All notation is defined in §3.5, Chapter 3.

Consistent with [14], the surface tension of silica is henceforth taken in this Chapter to be γ =0.3N/m and a draw length of L = 3cm is assumed throughout. Since an

efficient furnace gives an approximately constant temperature throughout, we ignore the effects of heat transfer in assuming that the temperature of the glass is uniform. The viscosity law used for pure silica glass was taken from [67] and is given by

$$1400\text{C} - 2500\text{C} \qquad \mu = 5.8 \times 10^{-7} \exp\left(515400/(8.3145T + 2271.10567)\right) \text{ Poise.} \tag{4.5}$$

Numerical solutions of equations (4.1)–(4.4) will presently be utilized to quantify the effects of rotation on capillary geometry. First we recall the key properties of "spin pitch" for optical fibres. It was shown in Chapter 3 that we may directly calculate the spin pitch d at a point z using

$$d = \frac{2\pi W_d}{B(0)}. \tag{4.6}$$

4.3 The effect of preform rotation on solid fibres

Though the practice of spinning solid optical fibres to reduce fibre birefringence is well established [54], the spinning of microstructured fibres has only recently been reported in [58], where a significant reduction in PMD was achieved. It would therefore be valuable to know whether it is possible to spin microstructured fibres at a rate necessary to remove fibre birefringence whilst preserving the microstructure. Beat lengths as small as 0.3mm have been measured [48], [53] in fibres with wavelength–scale features and a large refractive–index contrast. Currently, the smallest spin–pitch measured in a spun holey–fibre appears to be 1.23cm [58] and a sub–mm spin pitch is desirable.

We first examine the effects of rotation rate on the geometry of a solid fibre ($h_1 = 0$). When equations (4.1)–(4.4) are presented in non–dimensional form, we recall that equation (4.4) decouples from equation (4.1) when the rotation is less than a certain value. For steady-state fibre drawing, ignoring the complications of inertial forces,

surface tension, hole pressurisation and gravity, we showed in Chapter 3 that

$$3\bar{\mu}(\bar{h}_2^2\bar{w}_{0\bar{z}})_{\bar{z}} \cong -\frac{1}{4}ReS^2(\bar{h}_2^4\bar{B}^2)_{\bar{z}}, \tag{4.7}$$

where overbars denote non–dimensional quantities whose scalings can be found in §3.5. Substituting for the non–dimensional parameters shows that rotation therefore first begins to influence fibre geometry when

$$\frac{\Omega}{\epsilon} \cong \frac{2}{h}\sqrt{\frac{3\bar{\mu}\mu_0 W}{L\rho}}. \tag{4.8}$$

Various realistic drawing–parameters could be chosen and substituted into equation (4.8) to determine the rotation rate at which geometry is affected. As in Chapter 3, equation (4.8) shows that this occurs when $\frac{\Omega}{\epsilon} \approx 2900$ rpm. Full numerical solutions of equations (4.1)–(4.4), including the factors neglected in deriving equation (3.67) corroborate this. Whilst it is possible to rotate preforms at such a rate [63], vibrations and instabilities are often encountered in practice. Additionally, these drawing parameters were chosen specifically to create geometry change at low rotation rates, and in everyday draw scenarios much larger rotation rates will be possible with no effect on fibre geometry. We thus conclude that preform rotation will not generally affect the geometry of solid fibres. Although the point at which geometry of a microstructured fibre is modified may be somewhat different, equation (4.8) provides a useful first approximation in certain limiting cases that will be examined below.

4.4 Numerical results for capillary tubes

A great many asymptotic limits of the equations (4.1)–(4.4) may be considered. These can show whether it is possible to prevent surface–tension induced hole–collapse by rotating the preform, whether preform rotation may act as a useful control of hole size, and be used to investigate other possible control mechanisms. See Chapter 3 for details. We now consider briefly the results of numerical studies

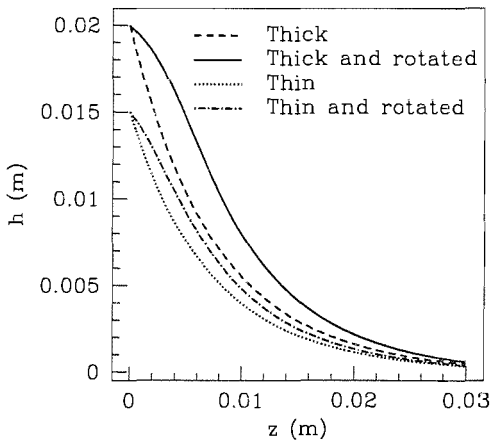

Figure 4.2: The effects of preform rotation on outer capillary radius. The diagram shows the outer radius h_2 for fibre pulls with and without rotation. The thin–walled tube has $h_1(0) = 0.01$m, $h_2(0) = 0.015$m and the thick–walled tube has $h_1(0) = 0.01$m, $h_2(0) = 0.02$m. (Draw length $L = 0.03$m, temperature $T = 2200$C, draw speed $W_d = 25$m/min, feed speed $W_f = 15$mm/min, rotation rate $\Omega = 35$rad/s.)

of the steady version of the equations using standard numerical library routines to solve the boundary value problem.

Figure 4.2 shows numerical results for rotation of both a thin– and a thick–walled capillary. As noted before, the general effect of rotating the preform as it enters the furnace is to increase both the inner and outer radii of the fibre along the entirety of the draw length. Preform rotation may thus be used as an additional control in the drawing process, since it is the fibre dimensions at the end of the furnace that primarily concern us. We also note that rotation appears to act on the fibre in a way that counteracts the effects of surface tension, which otherwise tends to close the air holes in the fibre. As well as reducing birefringence, rotation may thus, for example, allow fibres to be drawn at increased temperatures or reduced tensions. This may be advantageous from a manufacturing viewpoint, as fibres drawn at high temperatures often possess superior strength [62].

It is also clear from Figure 4.2 that the thick–walled capillary experiences a much greater deformation than the thin–walled. This is largely because the initial outer radius of the thick–walled capillary is larger than that of the thin–walled capillary. Comparison of the changes in fibre radii reveals that for both thin– and thick–walled tubes, the inner radius increases more than the outer. This occurs because the outer wall of the preform reacts to the effects of preform rotation (as a result of the 'centrifugal force'). The inner wall is then modified in accordance with mass conservation conditions, which require it to be modified more heavily and thus increase the OD/ID ratio. The implications of this analysis will be discussed in the following section.

4.5 The effects of preform rotation on microstructured fibres

4.5.1 Type–one holey fibres

In the limit that the holes in the microstructured fibre are sparse (large mode–area fibres), we may safely assume that the effects of rotation on the geometry of these type–one microstructured fibres are approximately the same as in the solid–fibre case.

If fibre birefringence is to be significantly reduced or removed, the twists must be on a scale equal to or less than that of the beat length, which is typically between 1 and 20mm. It is tempting to consider the practically–desirable case of the maximum draw speed and the minimum spin–pitch, in order to discover the rate of preform rotation required. We may then consider whether this rotation rate will affect the geometry. However the rate of rotation is usually limited to about 2000rpm and overcoming this rotation rate limit by reducing the drawing speed would provide the desired spin–pitch, but will not produce the required fibre geometry unless the dimensions of the initial preform are accordingly reduced. Equation (4.6) shows that

for a moderately low draw speed of 1m/min, the rotation rate needed to produce a spin pitch of between 1 and 20mm is between 1000rpm and 50rpm respectively. Assuming a typical silica glass viscosity of 2×10^5 Poise, a draw length of 3cm and an initial preform diameter of 2cm, equation (4.8) predicts that the resulting geometry of type–one fibres will not be significantly modified at such rotation rates.

Addressing the questions posed in the introduction, it is clear that starting with a standard preform and pulling at typical draw speeds, practical limits will prevent the preform from being rotated rapidly enough to significantly reduce fibre birefringence. However, a 1mm spin pitch may be obtained by breaking the manufacture into two stages and drawing the final fibre more slowly. The first stage would be used to obtain a preform for the second stage of production, whose size is small enough to allow the production of a small diameter fibre despite the low draw–speed. Finally, our assumption that type–one fibres behave as solid fibres does not allow us to address the question of geometry control since solid fibres have a geometry uniquely determined by the velocity boundary–conditions and the preform dimensions.

4.5.2 Type–two holey fibres

When the microstructured portion of a holey fibre preform is surrounded by a thick jacket–tube and the density of holes in the microstructured region is large, we may approximate the holey fibre preform by a capillary tube. The large air–fraction holey cladding may be represented by the air hole in the centre of the capillary tube and the jacket by the glass region of a capillary tube cross–section. This is tantamount to assuming that the large air–fraction holey cladding has no significant impact on the behaviour of the solid jacket when spun. We can thus determine how the geometry of the fibre varies when spun by treating the whole structure as a capillary tube. The manner in which it is modified will then give an insight into whether the microstructured region will remain intact.

As mentioned previously, it is desirable to obtain a spin pitch in the holey fibre of about 1mm. Equation (4.7) shows that this may be accomplished either by applying a large rotation–rate or a small draw–speed.

Numerical calculations using equations (4.1)–(4.4) show that capillary tubes whose initial outer diameter (OD) is as small as 1cm suffer significant geometry changes to both the inner and outer radii as a result of rotating the capillary tubes at 2000rpm and above. Capillary tubes with larger initial dimensions suffer even more of an effect. This distortion at lower rotation results from the presence of the hole in the capillary tube preform, representing the microstructure. When a one–step drawing process is employed, the initial dimensions of the preforms are too large to prevent rotation affecting the geometry of the final fibre. This is crucial because such changes will modify the microstructure of the fibre. If the geometry of the microstructure (modelled as the hole in the capillary) changes too rapidly at the top of the furnace, the fluid will not have time to react to this change and the structure within will surely be destroyed. However, if such changes take place gradually over the length of the draw it is reasonable to assume that the microstructure will be modified but will remain intact.

Further numerical studies of equations (4.1)–(4.4) show that when a preform is rotated the inner diameter (ID) is increased, compared to the unrotated case, at every point along the furnace. The bulk of this increase occurs at the top of the furnace and in some cases (where a large furnace temperature is simulated, for example) the ID actually increases at the top of the furnace before being decreased by the draw–down process lower in the furnace. This suggests that as the preform enters the furnace it immediately expands as a result of the 'centrifugal force'. This initial expansion will surely have significant consequences for the survival of the microstructure as discussed above. It is less clear what might happen to the microstructure when the rotation steadily modifies the capillary geometry as it moves through the furnace, resulting in a final geometry slightly different from that produced without rotation. However, it may be assumed that the microstructure survives but its internal proper-

ties will be modified. We must therefore search for conditions under which type–two fibres may be drawn with a 1mm spin pitch whilst also attempting to minimize the effect of preform rotation on the fibre geometry, particularly towards the top of the furnace.

The practical implication of this is that the rotation rate must be kept as low as possible, requiring us to draw the fibre slowly to achieve a small spin–pitch. Unfortunately, it is hard to manufacture fibres with a highly consistent geometry along the length of the fibre when the draw speed is extremely low. If we assume a minimum draw speed of 1m/min, a preform rotation rate of 1000rpm is required to achieve a spin pitch of 1mm.

We now examine in detail how we may rotate a type–two preform to achieve a 1mm spin pitch. Equations (4.1)–(4.4) were solved numerically for a variety of drawing scenarios aimed at minimizing the final geometry change. Some examples are now given for a final fibre whose holey fibre cladding is 15–30μm in diameter and whose jacket has diameter 80–300μm. The core dimensions are chosen to be large enough to confine light well but small enough not to be difficult to produce or to weaken the fibre. The jacket dimensions are chosen to make the fibre sufficiently robust.

When the manufacture of these fibres is completed in a single stage, the initial diameter of the preform must be large (typically a few centimetres). A minimum size for the holey cladding in the preform exists because of practical difficulties in stacking canes with OD $\ll$1mm, which in turn sets a minimum diameter for the jacket. If the preform is rotated during drawing, the initial jacket diameter and drawing rate must both be increased to obtain the same fibre geometry as would be produced without rotation. This results from the effects of rotation on the OD/ID ratio, described in §4.4.

Let us therefore consider a preform with a jacket diameter of 15mm and a holey–cladding diameter of 10mm. Whilst these particular diameters would never be chosen to make a commercial fibre, they clearly show the possible effects of rotation on

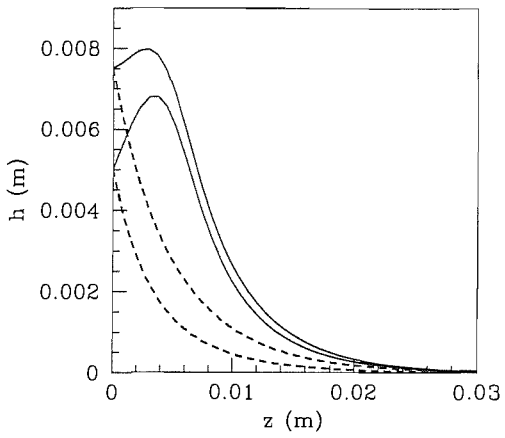

Figure 4.3: The destructive effects of preform rotation on the microstructure of type–two fibres. Dashed lines show holey cladding and jacket radii of preform without rotation and solid lines show the radii with rotation. Compare results with Figure 4.2.

the microstructure. To obtain the fibre geometry required, the feed speed is set to 1mm/min, the draw speed to 40m/min and temperature to 2000C. With no rotation a final holey–cladding diameter of 22.3μm and jacket diameter of 60.2μm is obtained. Rotation at a rate that gives a spin–pitch of 45mm causes the holey–cladding diameter to initially increase by 23%, from 10mm at the beginning of the draw to 12.2mm at $z = L/20$ as shown in Figure 4.3. Such a rate of increase is unlikely to allow the survival of the microstructured region of the fibre.

It is therefore clear that to obtain fibres with a sub–1mm spin pitch one must split the manufacture into two stages, as is often already the case [68]. The second stage of manufacture, where the preform is rotated, may then have an initial geometry much smaller than in the one–stage process. This smaller geometry allows a lower draw speed to obtain the final geometry, which in turn allows lower rotation rates for any given spin–pitch. The combined effect is to reduce significantly the geometric effects of preform rotation allowing the draw to be performed at higher temperatures. This increases the strength of the final product and allows the temperature to be varied

to influence the final OD/ID ratio.

As an example of the effects of preform rotation in such a situation consider a second–stage preform with a jacket diameter of 7mm and holey cladding 1.5mm in diameter. Without rotation, a glass temperature of 1940C, a draw speed of 1m/min and a feed speed of 1.7mm/min, the final fibre has a holey cladding of 8.6μm and a jacket diameter of 282.0μm; outside the desired range described earlier. When preform rotation of 2000rpm is included to give a spin pitch of 0.5mm, these final fibre–dimensions increase to 22.8μm holey–cladding diameter and 282.8μm jacket diameter. The final OD/ID ratio, 65.4 in the absence of rotation, is decreased to 24.8. The rotation causes no initial increase in fibre dimensions towards the top of the furnace (unlike that shown in Figure 4.3), suggesting that the microstructure will remain intact.

Even with the smaller initial geometry, rotation rates may be increased to the point where the holey cladding suffers a initial increase in diameter at the top of the furnace, damaging the microstructure. If the above preform is spun at 3333rpm, corresponding to a slightly smaller spin–pitch of 0.3mm, the holey–cladding diameter increases by 20% from 1.5mm at the beginning of the draw to 1.8mm at $z = L/20$. This large initial expansion of the holey cladding would surely heavily modify the microstructure. This confirms the sensitivity of the holey cladding to spin rates at high temperatures and demonstrates that one must be careful to only apply the rotation necessary to achieve the final spin–pitch, having already minimized the draw speed; even with such small initial dimensions.

A two–stage drawing process allows a freedom in the initial geometry for the second stage. This should be used to choose a feed speed and initial OD/ID ratio that give the desired final OD/ID ratio.

To address the questions posed in the introduction, we first observe that the presence of a hole causes the effects of rotation on the geometry to be seen at much lower spin–rates than for solid fibres. We cannot remove fibre birefringence whilst preserving the microstructure unless a two–stage process is employed, in which case the

initial geometry draw speed must be carefully chosen to prevent destruction of the microstructure. This approach has the benefit of giving an extra degree of freedom in the temperature. Preform rotation may be used to control the fibre geometry within the limits imposed by the required preservation of the microstructure as it passes through the furnace.

4.6 Conclusions

An asymptotic model has been constructed and solved numerically to determine the effects on the fibre dimensions of preform rotation, to allow the reduction or removal of fibre birefringence. It was discovered that a sub–mm spin pitch could be achieved for both fibre–types considered. However, the manufacture of type–one fibres must be broken into two stages and preform rotation may not be used as a method to control the resulting fibre geometry. For type–two fibres, care must be taken to preserve the microstructured region of the fibre, having broken the manufacture into two stages and used the second stage to prescribe the fibre geometry. The two–stage process also allows fibres to be drawn at higher temperatures, producing fibres of superior strength.

The guidelines developed in this Chapter for producing microstructured optical fibres with a twist periodicity small enough to reduce or remove PMD have been successfully implemented experimentally.

4.6.1 Practical Results

In this Chapter we:

- characterized holey fibres into two broad types for the purposes of examining the effects of rotation used to reduce or remove PMD (see §8.1);

- described the effects of rotation on solid fibres and capillary tubes (see §4.3 and §4.4 respectively);
- constructed guidelines for reducing or removing PMD in large mode area fibres (see §4.5.1);
- constructed guidelines for reducing or removing PMD in fibres with a large jacket (see §4.5.2).

Chapter 5

A Stability Analysis for the Drawing of Capillary Tubes

5.1 Introduction

Optical fibres are manufactured from a preform that is typically a few centimetres in diameter. The preforms are drawn down to fibre form, where dimensions are typically 125 microns. Holey fibre preforms may be even larger, and in order to achieve the required dimensions for final fibres, experimenters would ideally pull the fibre more rapidly. However, fibres break if they are pulled too rapidly (relative to the feed speed). This phenomenon is known as draw resonance (though it is noted that fibres may also break when pulled too rapidly as a result of the mechanical properties of the solidifying glass at the furnace exit). An instability exists in fibre drawing, such that for a given feed speed, fibres have a maximum allowed draw speed, beyond which instabilities arise and grow, causing the fibre to break. In this Chapter we will conduct a stability analysis for the drawing of capillary tubes and attempt to understand the effects of changing the various parameters on the maximum ratio of draw to feed speed.

The stability of solid fibres was considered by [14], [25], [33] and [69], and extensive numerical calculations have been undertaken in [32] and [33]. We will use the numerical results in [32] and [33] as a check of the code that must be constructed in order to examine the stability of capillary drawing.

A weak (linear) stability analysis assumes that any growth in perturbations introduced into a system is small. If the perturbations are small then the effect of nonlinear terms is negligible and the resulting equations are simplified. If the perturbations derived from this analysis become large then the analysis breaks down and a weakly-nonlinear analysis must be completed, including the effect of non–linear terms in the governing equations. However, any perturbation that grows in a linear analysis is undesirable for the purposes of fibre manufacture, so this method is satisfactory.

As far as the industrial process of drawing annular fibres is concerned, the stability of the process is obviously a key issue. For instance, is the process sensitive to small changes in the experimental equipment or conditions? More importantly, is the process stable enough to suggest that long lengths of fibre or capillary with uniform structure can be produced? Before considering the stability of capillary drawing, it is helpful to consider first the case of solid fibres.

5.2 Stability for solid fibres

The simplest isothermal stability analysis for a solid fibre is easy to carry out and has been addressed many times before (see [14], [25], [33] and [69]). Here we will briefly repeat the main points of the analysis for the sake of completeness. Neglecting inertial force terms, gravity and surface tension in (3.53) and (3.55), setting $h_1 = 0$, $B = 0$ and writing $A(z,t) = \pi h_2^2(z,t)$, we find that the time–dependent governing equations are

$$A_t + (Aw_0)_z = 0, \qquad (Au_{0z})_z = 0. \tag{5.1}$$

To examine stability we now set

$$w_0 = W_0(z)[1 + w(z)e^{\sigma t}],$$

and

$$A = A_0(z)[1 + a(z)e^{\sigma t}],$$

where $W_0 = W_f \exp(\beta z/L)$, $A_0 = A_f \exp(-\beta z/L)$ are the steady-state solutions, A_f is the initial fibre cross-sectional area and a, w and σ are complex. We therefore seek solutions where σ is not real and positive. We now assume that w and a are small, we find that at first order

$$\sigma a + W_f e^{\beta z/L}(a_z + w_z) = 0, \tag{5.2}$$

and

$$w_{zz} + \left(\frac{\beta}{L}\right)(w_z + a_z) = 0. \tag{5.3}$$

The boundary conditions are that $a(0) = w(0) = w(L) = 0$. We find on elimination of w that a satisfies the equation

$$a_{zz} + \frac{\sigma e^{-\beta z/L}}{W_f} a_z = 0. \tag{5.4}$$

The solution of this equation that satisfies the boundary condition $a(0) = 0$ is

$$a = B\left[-\mathrm{Ei}\left(1, -\frac{\sigma L}{\beta W_f}\right) + \mathrm{Ei}\left(1, -\frac{\sigma L e^{-\beta z/L}}{\beta W_f}\right)\right], \tag{5.5}$$

where B is an arbitrary constant, and the exponential integral function $Ei(n, z)$ is defined in the usual way by

$$\mathrm{Ei}(n, z) = \int_1^\infty \frac{e^{-zt}}{t^n} dt.$$

By integrating (5.3) from 0 to L and evaluating (5.2) at 0 and L we find that a second boundary condition for (5.4) is given by

$$a_z(L) - a_z(0) + a(L)\left[\frac{\sigma}{W_f} e^{-\beta} - \frac{\beta}{L}\right] = 0.$$

Applying this condition to (5.5) (and setting $\xi = \sigma L/(\beta W_f)$) yields the condition

$$e^{\xi e^{-\beta}} - e^{\xi} + [1 - \xi e^{-\beta}][\mathrm{Ei}(1, -\xi) - \mathrm{Ei}(1, -\xi e^{-\beta})] = 0. \tag{5.6}$$

In any given fibre drawing experiment, β, W_f and L are known quantities. The stability problem then consists of establishing the circumstances under which the complex equation (5.6) possesses solutions for ξ with positive real parts. These are the unstable cases. Routine numerical calculations demonstrate that as β increases (from zero), (5.6) has a purely imaginary root when $\beta \sim 3.00651$. This is the "draw resonance" (see, for example, [45]) that for solid fibres occurs when $W_d/W_f \sim 20.21$. This places an absolute restriction on fibre drawing, as draw ratios are usually significantly larger than 20. Whilst this analysis has neglected the effects of gravity, inertia, temperature and surface tension, numerical studies for a solid fibre (see, for example [26], [32], [33] and [38]) show that inertia and gravity stabilise the process, but surface tension is a destabilising factor. However, typically these effects are not significant, and this raises concern as to how fibres may be manufactured with highly supercritical draw ratios (as is often seen in practice). The answer is thought to lie in the fact that, though ostensibly the draw speed is prescribed, in reality the force is controlled as a result of slippage at the exit winder where the fibre is pulled onto a rotating drum. Repeating the same analysis as above but adjusting the boundary conditions to those given by

$$w_0(0) = W_f, \quad A(0) = A_f, \quad A(L)w_{0z}(L) = F_d,$$

gives $W_0 = W_f \exp(\chi z)$ and $A_0 = A_f \exp(-\chi z)$ where $\chi = F_d/A_f W_f$. The previous stability equation (5.4) then becomes

$$a_{zz} + \frac{\sigma e^{-\chi z}}{W_f} a_z = 0,$$

and the solution with $a(0) = 0$ is thus

$$a = B\left[-Ei\left(1, -\frac{\sigma}{\chi W_f}\right) + Ei\left(1, -\frac{\sigma e^{-\chi z}}{\chi W_f}\right)\right].$$

However, since in this case the boundary conditions modified to $w(0) = 0$, $a(0) = 0$ and $w_z(L) + \chi(w(L) + a(L)) = 0$, we may show that $a_z(0) = 0$. Thus the problem is an initial value one and in consequence no unstable modes are present.

5.3 Stability for capillary tubes

We now complete a stability analysis for the drawing of capillary tubes.

5.3.1 Derivation of stability equations

Following the methodology used for the stability analysis of solid fibres we commence by setting

$$w(z,t) = w_0(z)(1 + w_2(z)e^{\sigma t}), \tag{5.7}$$

$$h_1(z,t) = h_1(z)(1 + h_{12}(z)e^{\sigma t}), \tag{5.8}$$

$$h_2(z,t) = h_2(z)(1 + h_{22}(z)e^{\sigma t}), \tag{5.9}$$

where $w_0(z)$, $h_1(z)$ and $h_2(z)$ are the base–state solutions of the equations that govern capillary drawing ((3.53)–(3.55) with $B(z,t) \equiv 0$, shown in Chapter 3 where all notation is defined). In the event that we ignore fibre inertia, gravity, surface tension and hole overpressure, the base–state solutions are simply

$$w_0(z) = W_f e^{\beta z}, \tag{5.10}$$

$$h_1(z) = h_{10} e^{-\frac{\beta z}{2}}, \tag{5.11}$$

$$h_2(z) = h_{20} e^{-\frac{\beta z}{2}}. \tag{5.12}$$

However, we wish to include these effects and as the equations cannot be solved in closed–form, we will obtain numerical solutions for the base-state.

We first recap the form of the time dependent equations that govern fibre drawing, with fibre inertia, surface tension and hole overpressure included. In this Chapter we will work with dimensional equations at all times, even though some dimensionless numbers are introduced in order to compare our results with those of previous studies. As in the case of solid fibre stability, we assume that w_2, h_{12} and h_{22} are "small".

The (dimensional) equations are

$$\mu\left(h_2(z,t)^2 - h_1(z,t)^2\right)\left(h_1(z,t)_t^2 + w(z,t)h_1(z,t)_z^2\right)_z - p_0 h_1(z,t)^2 h_2(z,t)^2 + \gamma h_1(z,t)h_2(z,t)\left(h_1(z,t) + h_2(z,t)\right) = 0, \tag{5.13}$$

$$\mu\left(h_2(z,t)^2 - h_1(z,t)^2\right)\left(h_2(z,t)_t^2 + w(z,t)h_2(z,t)_z^2\right)_z - p_0 h_1(z,t)^2 h_2(z,t)^2 + \gamma h_1(z,t)h_2(z,t)\left(h_1(z,t) + h_2(z,t)\right) = 0 \tag{5.14}$$

and

$$\rho\left(h_2(z,t)^2 - h_1(z,t)^2\right)\left(w(z,t)_t + w(z,t)_z w(z,t) - g\right) - \left(3\mu(h_2(z,t)^2 - h_1(z,t)^2)w(z,t)_z + \gamma(h_1(z,t) + h_2(z,t))\right)_z = 0, \tag{5.15}$$

where the boundary conditions are

$$w_2(0) = 0, \quad w_2(L) = 0, \quad h_{12}(0) = 0 \text{ and } h_{22}(0) = 0.$$

We substitute $w(z,t)$, $h_1(z,t)$ and $h_2(z,t)$ given by (5.7)–(5.9) into the governing equations (5.13)–(5.15), and equate terms of like powers in ϵ. At zeroth order this gives (5.13)–(5.15) and at first-order gives

$$\begin{aligned}
&\gamma h_2(2h_{12}h_1 + h_1h_{22} + h_2h_{12} + 2h_2h_{22}) - 2p_0h_2^2h_1(h_{22} + h_{12}) \\
&+ \mu(h_1h_2^2w_0w_{2z} - h_1^3w_0w_{2z} - 2h_1^3w_0h_{12z} - h_1^3w_{0z}w_2 - 4h_1^3w_{0z}h_{12} \\
&2\sigma h_1^3h_{12} - 8h_1^2w_0h_{1z}h_{12} - 2h_1^2w_0h_{1z}w_2 + 2h_1h_2^2w_0h_{12z} \\
&+ 2\sigma h_1h_2^2h_{12} + 2h_1h_2^2w_{0z}h_{12} + h_1h_2^2w_{0z}w_2 + 2h_1h_2^2h_{22}w_{0z} \\
&+ 2h_2^2w_0h_{1z}w_2 + 4h_2^2w_0h_{1z}h_{12z} + 4h_{2z}^2h_{22}w_0h_1z) = 0,
\end{aligned} \tag{5.16}$$

$$\begin{aligned}
&- 2p_0h_1^2h_2(h_{22} + h_{12}) + \gamma h_1(2h_{12}h_1 + h_1h_{22} + h_2h_{12} + 2h_2h_{22}) \\
&+ \mu\sigma(2h_2^3h_{22} + 4h_2^3w_{0z}h_{22} + h_2^3w_0w_{2z} + 2h_2^3w_0h_{22z} + h_2^3w_{0z}w_2 \\
&+ 8h_2^2w_0h_{2z}h_{22} + 2h_2^2w_0h_{2z}w_2 - 2\sigma h_2h_1^2h_{22} - 2h_2h_1^2w_{0z}h_{22} \\
&- h_2h_1^2w_{0z}w_2 - 2h_2h_1^2w_0h_{22z} - 2h_2h_1^2h_{12}w_{0z} - h_2h_1^2w_0w_{2z} \\
&- 4h_1^2w_0h_{2z}h_{22} - 4h_1^2h_{12}w_0h_{2z} - 2h_1^2w_0h_{2z}w_2) = 0
\end{aligned} \tag{5.17}$$

and

$$\mu(6h_1h_{1z}w_0w_{2z} - 12h_2h_{2z}h_{22}w_{0z} - 6h_2h_{2z}w_{0z}w_2 - 6h_2h_{2z}w_0w_{2z}$$
$$+ 6h_1h_{1z}w_{0z}w_2 + 12h_1h_{1z}h_{12}w_{0z} + 6h_1^2h_{12z}w_{0z} - 6h_2^2w_{0z}w_{2z}$$
$$- 6h_2^2h_{22z}w_{0z} + 6h_1^2w_{0z}w_{2z} - 3h_2^2w_{0zz}w_2 + 3h_1^2w_0w_{2zz} + 6h_1^2h_{12}w_{2zz}$$
$$+ 3h_1^2w_{0zz}w_2 - 6h_2^2h_{22}w_{0zz} - 3h_2^2w_0w_{2zz}) + \mu_z(6h_1^2h_{12}w_{0z} + 3h_1^2w_0w_{2z}$$
$$+ 3h_1^2w_{0z}w_2 - 6h_2^2h_{22}w_{0z} - 3h_2^2w_0w_{2z} - 3h_2^2w_{0z}w_2) + \rho(2h_2^2w_0w_{0z}w_2$$
$$- 2h_1^2h_{12}w_0w_{0z} - 2h_1^2w_0w_{0z}w_2 + 2h_2^2h_{22}w_0w_{0z} + h_2^2w_0^2w_{2z} - h_1^2w_0^2w_{2z}$$
$$+ 2gh_1^2h_{12} - 2gh_2^2h_{22} - \sigma h_1^2w_0w_2 + \sigma h_2^2w_0w_2) = 0. \tag{5.18}$$

Equations (5.16)–(5.18) above are three second–order partial differential equations in the unknowns w_2, h_{12} and h_{22}, with w_0, h_1 and h_2 known. These equations will be solved using standard finite difference schemes.

The stability problem consists of establishing the circumstances under which equations (5.16)–(5.18) possess solutions for σ with positive real parts: these are the unstable cases. Finding the values of σ that satisfy equations (5.16)–(5.18) is an eigenvalue problem, and the methodology used will be identical to the methodology used to solve the example problem given in §5.3.2.

The finite difference scheme of choice uses central differences for derivatives since these have a smaller error associated with them for a given mesh size than either forward or backward schemes. We set

$$\begin{aligned} w_{2z} &= \frac{n(w_2(m+1) - w_2(m-1))}{2L}, \\ h_{12z} &= \frac{n(h_{12}(m+1) - h_{12}(m-1))}{2L}, \\ h_{22z} &= \frac{n(h_{22}(m+1) - h_{22}(m-1))}{2L}, \\ w_{2zz} &= \frac{n^2(w_{22}(m+1) - 2w_{22}(m) + w_{22}(m-1))}{L^2}; \end{aligned} \tag{5.19}$$

where L is the size of the z domain, which is divided into n elements. Thus L/n is the size of each element.

5.3.2 An example eigenvalue problem

To see how to solve equations (5.16)-(5.18) and determine the allowed values of σ, we consider a simple equivalent example. Consider the equation

$$y + \lambda^2 y_{zz} = 0, \tag{5.20}$$

whose (non–trivial) solution we seek given the additional knowledge that $y(0) = 0$ and $y(1) = 0$.

We start by rewriting the equation using a central differencing scheme. Dividing the z domain into N parts each of size $\Delta z/N$ gives

$$N^2\left(y^{n+1} - 2y^n + y^{n-1}\right) + \lambda^2 y^n = 0,$$

where $n = 1, 2, ...N$.

Representing this equation in matrix form with $n = 1, 2, ...4$ (i.e. setting $N = 4$) gives

$$\mathcal{A}\mathbf{y} = \mathbf{0},$$

where

$$\mathcal{A} = \begin{pmatrix} 1 & 0 & 0 & 0 \\ 1 & -2 + \frac{\lambda^2}{N^2} & 1 & 0 \\ 0 & 1 & -2 + \frac{\lambda^2}{N^2} & 1 \\ 0 & 0 & 0 & 1 \end{pmatrix},$$

and the boundary conditions correspond to the first and last row.

This matrix may now be manipulated into the form $\mathcal{A}' - \lambda\mathcal{I} = 0$, where $\mathcal{I}$ is the identity matrix. Remembering that each row may be multiplied by arbitrary constants we set $\lambda' = \lambda^2$, multiply each row by $-N^2$, divide rows 1 and 4 (more generally row 1 and N) by N^2 and multiply them by λ'. We then once again have

$$\mathcal{A}''\mathbf{y} = \mathbf{0},$$

where this time

$$\mathcal{A} = \begin{pmatrix} -\lambda' & 0 & 0 & 0 \\ -N^2 & 2N^2 - \lambda' & -N^2 & 0 \\ 0 & -N^2 & 2N^2 - \lambda' & -N^2 \\ 0 & 0 & 0 & -\lambda' \end{pmatrix}.$$

This matrix takes the form $\mathcal{A}' - \lambda'\mathcal{I} = \mathbf{0}$, where finding eigenvalues of the $\mathcal{A}'$ is equivalent to finding the values of λ^2 that satisfy the original equation. Once $\mathcal{A}'$ is obtained, the eigenvalues are determined by setting $\lambda' = 0$ and finding the eigenvalues of the resulting matrix. The eigenvalues of (5.20) correspond to $\lambda = m\pi$, where m is an integer. To confirm this we write a short code in *Maple*, and see how many elements the square matrix must have to achieve good agreement with the known eigenvalues.

5.3.2.1 Code implemented

Using the simple example above we give detail of the code constructed to find the eigenvalues. The methodology used is identical to that used to solve the full stability problem, shown in Appendix A.

To enable the *eigenvalues* command:

```
restart:
with(linalg):
```

To define the number of elements:

```
N:=5:
```

To construct a square array of the appropriate size:

```
sol:=array(1..N+1,1..N+1):
```

We fill the array with zeros, and then alter those elements that should be non-zero:

```
for m from 1 to N+1 do
for j from 1 to N+1 do
sol[m,j]:=0: od: od:
```

We fill the rest of the matrix as required:

```
for k from 2 to N do
sol[k,k-1]:=1:
sol[k,k]:=-2 + lambda/N^2:
sol[k,k+1]:=1: od:
for j from 1 to N+1 do for ii from 1 to N+1 do
gurk:=coeff(sol[i,ii],lambda,1):
if gurk>0 then for g from 1 to N+1 do sol[i,g]:=-sol[i,g]/gurk: od: end if:
od: od:
```

We multiply the first and last rows by $(-\lambda)$:

```
sol[1,1]:=-lambda:
sol[N+1,N+1]:=-lambda:
```

Since we now have a matrix of the form $\mathcal{A}' - \lambda'\mathcal{I} = 0$, where $\mathcal{I}$ is the identity matrix, we may solve by finding the eigenvalues of the matrix with $\lambda' = 0$:

```
lambda:=0:
sol2:=array(1...12):
sol2:=eigenvalues(sol);
```

Table 5.1: Table to show convergence of eigenvalues.

N	Eigenvalue for $m = 1$	Eigenvalue for $m = 2$
5	3.090169945	5.877852524
10	3.128689310	6.180339894
15	3.135853898	6.237350724
20	3.138363841	6.257378604
30	3.140157374	6.271707796
40	3.140785411	6.276727651
80	3.141391411	6.281570663

5.3.2.2 Results and convergence

Considering only the eigenvalues $m\pi$ where $m = 1, 2$, Table 5.1 shows how altering the size of the matrix, N, affects the determined eigenvalues. The results clearly converge to the eigenvalues π and 2π rapidly with increasing N.

5.3.3 Comparison with previous studies

To determine whether or not any given drawing scenario is stable, one simply looks for the presence of one or more positive eigenvalues of the matrix '*sol*'. The drawing conditions are therefore inserted into the program, a suitable mesh size is defined (typically a 500×500 matrix achieves a good balance between accuracy and computational time), and the program is run and the eigenvalues determined. If one or more positive eigenvalues are found, the draw–ratio is decreased until all eigenvalues have negative real parts. The value of the draw–ratio that corresponds exactly to the

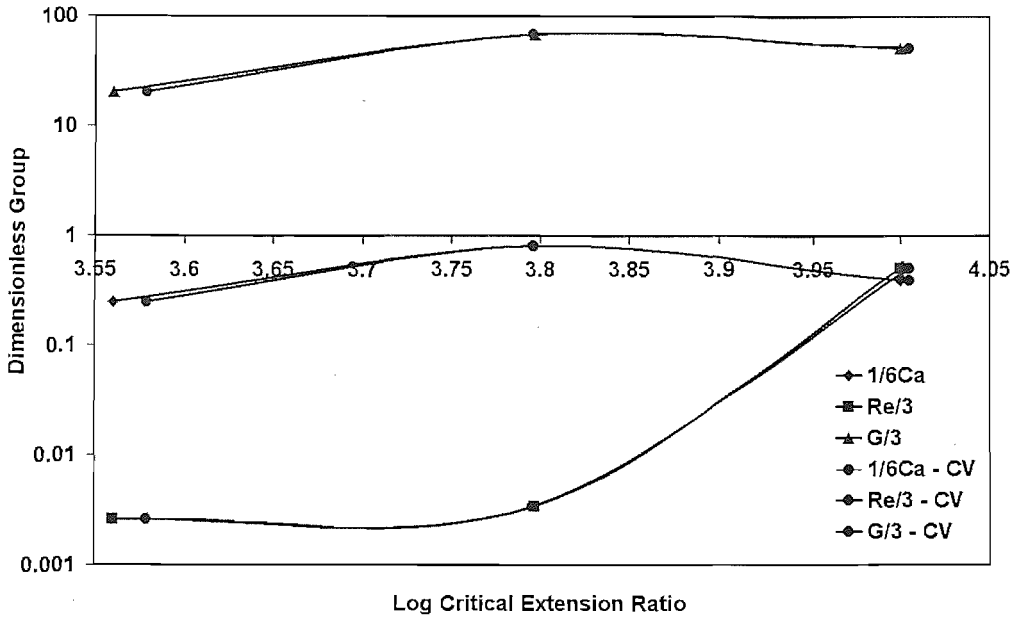

Figure 5.1: A comparison of predictions of critical draw–ratio made by the code for capillary drawing (denoted "CV") and those made by [32] and [33], where the extension ratio is W_d/W_f. The lines with circular symbols correspond to calculations using the capillary code. Other lines correspond to the calculations made by [32] and [33].

point at which an eigenvalue with a positive real part is found is called the critical draw–ratio (CDR), where the draw ratio is the ratio of the feed to draw speed.

As a check of the code we compare numerical calculations made in [32] and [33] for the case of a solid fibre with calculations made using the code established for the drawing of capillary tube (detailed in Appendix A). It was these comparisons that determined the 500×500 matrix size to be used for capillary calculations. The critical draw–ratio was found as a function of three key dimensionless groups as determined by [32] and [33], these being

$$\frac{1}{6Ca} = \frac{\gamma L}{6\mu_0 W h}, \qquad Re = \frac{\rho W L}{\mu_0}, \qquad G = \frac{\rho g L^2}{\mu_0 W}.$$

Remarkable agreement was achieved with the existing literature, as shown in Figure 5.1.

5.3.4 Numerical results for capillary tubes

Having successfully compared the predictions made by the finite difference code with those of Chang and Denn [32] we now consider the stability of capillary fibre drawing, as opposed that of solid fibres.

The parameter space to be explored is large since there are nine parameters available to change. They are W_d, W_f, h_{10}, h_{20}, γ, ρ, g, T (equivalent to setting the viscosity μ) and p_0. To find the critical draw ratio (critical W_d/W_f) we fix W_f and increase W_d until a positive real eigenvalue σ is found. Thus only eight of the available nine parameters will be modified. The methodology used in all cases to follow will be to fix all eight parameters, determine the critical draw ratio and then vary one incrementally, at each point determining the critical draw ratio. The results will then be plotted, illustrating how the critical draw ratio varies with the chosen parameter, and the results interpreted.

The viscosity law given in Chapter 3 was used for all of the following numerical examples and all parameter values assigned were chosen to represent values typically used experimentally.

Interesting cases were examined more closely having completed the above analysis. For example, we considered the stability of a thin–walled capillary tube as compared that of a thick–walled capillary tube.

Table 5.2 lists all cases that will be considered.

5.3.4.1 The effect of fibre inertia and gravity on stability

The fibre density was incrementally increased from zero and the critical draw–ratio determined at each point. It may be anticipated, through experience with the solid fibre case, that the effect of inertia on the stability of the draw will be negligible.

Table 5.2: Table summarizing cases considered for stability of capillary tube drawing. $p_0 = 0$ for all cases and "–" denotes a variable parameter.

Case	W_f	h_{10}	h_{20}	T	γ	ρ	g	Figure
1	2.6×10^{-5}	1.8×10^{-2}	2×10^{-2}	2100	0	–	0	5.2
2	2.6×10^{-5}	1.8×10^{-2}	2×10^{-2}	2100	0	–	9.81	5.2
3	2.6×10^{-5}	1.8×10^{-2}	2×10^{-2}	2100	–	0	0	5.3
4	2.6×10^{-5}	1.8×10^{-2}	2×10^{-2}	2100	–	1400	9.81	5.4
5	2.6×10^{-5}	1.8×10^{-2}	2×10^{-2}	2000	–	1400	9.81	5.5
6	2.6×10^{-5}	1.8×10^{-2}	2×10^{-2}	–	0.3	1400	9.81	5.6
7	2.6×10^{-5}	1.0×10^{-2}	2×10^{-2}	2050	–	0	0	5.7
8	2.6×10^{-5}	1.8×10^{-2}	2×10^{-2}	2050	–	0	0	5.7
9	2.6×10^{-5}	1.0×10^{-2}	2×10^{-2}	2050	0	–	0	5.8
10	2.6×10^{-5}	1.8×10^{-2}	2×10^{-2}	2050	0	–	0	5.8

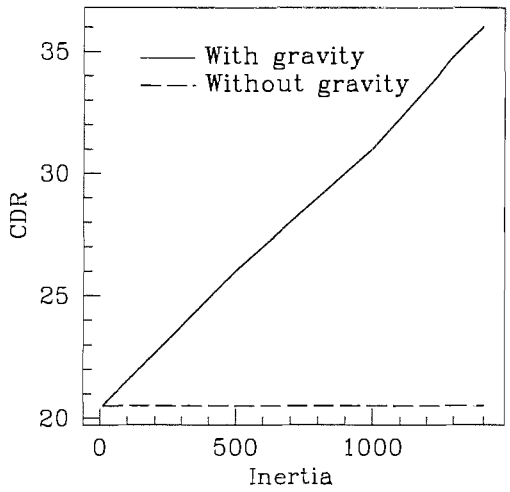

Figure 5.2: Graph to show the effects of both inertia (ρ) and gravity on the critical draw–ratio. (Case 1: $W_f = 2.6 \times 10^{-5}$, $h_{10} = 1.8 \times 10^{-2}$, $h_{20} = 2 \times 10^{-2}$, $T = 2100$, $\gamma = 0$, $\rho =$ variable, $g = 0$. Case 2: $W_f = 2.6 \times 10^{-5}$, $h_{10} = 1.8 \times 10^{-2}$, $h_{20} = 2 \times 10^{-2}$, $T = 2100$, $\gamma = 0$, $\rho =$ variable, $g = 9.81$.)

This is because in the case with no surface tension or hole overpressure, the physics becomes almost identical to the solid fibre limit. Other parameters were set as follows: $W_f = 2.6 \times 10^{-5}$m/s, $W_d =$ variable, $T = 2100$C, $h_{10} = 1.8 \times 10^{-2}$m, $h_{20} = 2.0 \times 10^{-2}$, $p_0 = 0$Pa, $\gamma = 0$N/m, $L = 3 \times 10^{-2}$m, $g = 9.81\text{ms}^{-2}$ and $\rho = 1400\text{kgm}^{-3}$. These values represent those typically used when drawing capillary tubes experimentally.

With gravity set to zero we find that the critical draw–ratio does not depend on inertia unless the feed speed is increased to ≈ 0.1m/s, in which case it is observed that the critical draw–ratio increases linearly with inertia. Also, at this higher feed speed but without gravity, the critical draw–ratio may be made independent of inertia by suitably reducing the temperature and hence increasing the viscosity. To make a useful comparison, consider the case of W_f fixed at $2.6 \times 10^{-5}\text{ms}^{-1}$. Results are shown in Figure 5.2 for the cases of $g = 0$ (Case 1, Table 5.2, where the slope of the line is small but non–zero) and $g = 9.81$m/s (Case 2, Table 5.2).

This behaviour may be understood when the boundary conditions are considered. The constant velocity boundary condition at $z = L$ may not be completely realistic. In the case of constant speed boundary conditions, whatever force is needed to create the required draw speed will automatically be provided by the fibre winder. It is possible to imagine that as the inertia increases, so will the critical draw–ratio. This may be because an initial perturbation is difficult to force into a regime where the system becomes unstable. Additionally, the effect of including gravity will intuitively be to increase the critical draw ratio.

5.3.4.2 The effect of surface tension on stability

Fitt *et al.* [15] state that when the boundary condition at $z = L$ is that the force and not the speed is prescribed, then some progress may be made asymptotically in determining the point at which h_1 drops to zero and the fibre collapses.

However, our stability analysis focuses on the event where the fibre feed speed, and not force, is prescribed. In this instance, several points may be made. First, that surface tension is expected to be destabilising in all cases, whatever the boundary conditions. The reasons for this are that surface tension will act to close a hole, and acts on two surfaces. One of these surfaces is at a significantly smaller radius, thus exacerbating the effect. Secondly, in the limit of small surface tension, an analytic solution of the equations becomes possible and demonstrates that hole closure is more sensitive to changes in feed speed than in draw speed, and that it is also sensitive to changes in viscosity. The degree of hole closure has a direct impact on the stability. Thus if the hole is small (for reasons suggested above), any perturbation may easily be fatal to fibre geometry, with the force of surface tension becoming increasingly important through its inverse dependence on the radius of the fibre. It is suggested that most positive eigenvalues correspond to hole–closure and not preform "explosion", because when oscillations in h_1 are $O(h)$, any hole will close and not reopen, which will clearly occur before oscillations are large enough to cause

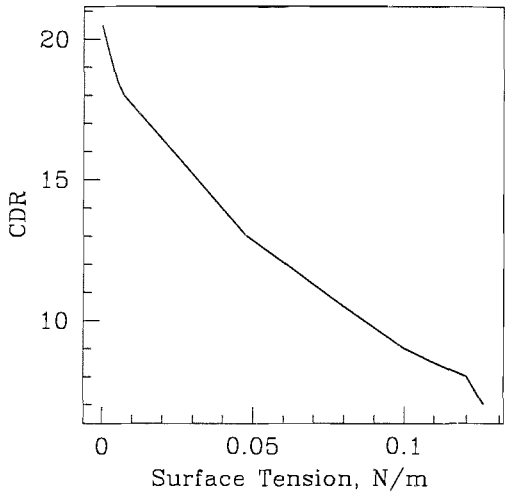

Figure 5.3: Graph to show the effects of surface tension on the critical draw–ratio with gravity excluded. (Case 3: $W_f = 2.6 \times 10^{-5}$, $h_{10} = 1.8 \times 10^{-2}$, $h_{20} = 2 \times 10^{-2}$, $T = 2100$, $\gamma =$ variable, $\rho = 0$, $g = 0$.)

preform explosion.

To examine the stability whilst including surface tension, we consider the case with inertia and gravity excluded. The temperature was set to 2100C and the feed speed set to $2.6 \times 10^{-5}\text{ms}^{-1}$ as before. The surface tension was incrementally increased, the critical draw–ratio being determined at each point. These findings (Case 3, Table 5.2) are illustrated in Figure 5.3.

We now include both inertia and gravity to allow the effect of surface tension on the critical draw–ratios to become evident in this more–realistic drawing regime. The inertia was set to 1400kgm^{-3} and gravity included. The results (Case 4, Table 5.2) are illustrated in the Figure 5.4.

Figures 5.3 and 5.4 demonstrate that surface tension is destabilising, and that the rate of change of critical draw ratio with changes in surface tension is non–linear. As expected, the presence of inertia and gravity help stave off fatal failure of the fibre.

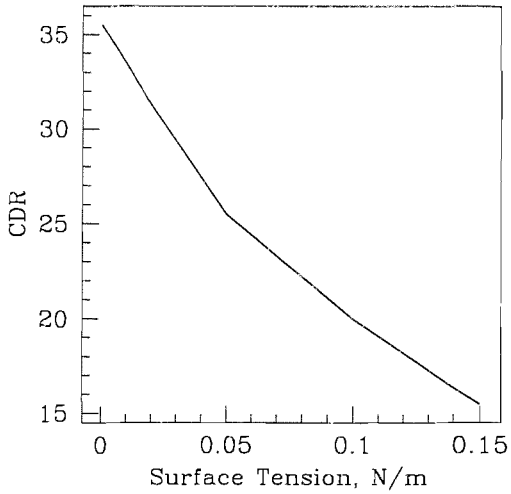

Figure 5.4: Graph to show the effects of surface tension on the critical draw–ratio with inertia and gravity included and $T = 2100$C. (Case 4: $W_f = 2.6 \times 10^{-5}$, $h_{10} = 1.8 \times 10^{-2}$, $h_{20} = 2 \times 10^{-2}$, $T = 2100$, $\gamma =$ variable, $\rho = 1400$, $g = 9.81$.)

Finally, it would be instructive to see a comparison of the effect of surface tension between capillaries of differing initial geometries, as it is these that will be varied in practice along with a combination of other parameters to ensure that the correct geometry of the final is achieved.

When the temperature is lowered to 2000C and hence the viscosity increased, the results of Figure 5.4 are modified and shown in Figure 5.5 (Case 5, Table 5.2).

The critical draw–ratio decreases for all surface tensions as the temperature is decreased, though it is not completely clear how the fibre tension (created by the fibre winder) is related to the phenomenon of critical draw–ratio. As the temperature is decreased the fibre tension (force required to draw fibre at the given draw speed) increases, but to separate this from other temperature–induced effects is nontrivial. Figure 5.6 shows the variation in critical draw ratio when temperature is altered, where $\gamma = 0.3$Nm (Case 6, Table 5.2). This value of surface tension coefficient corresponds to the best estimate for silica glass at typical furnace temperatures.

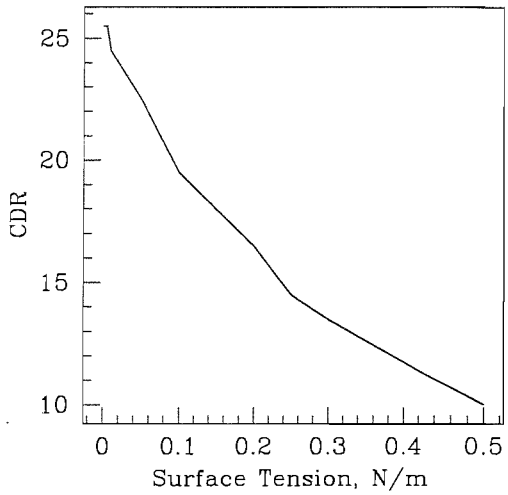

Figure 5.5: Graph to show the effects of surface tension on the critical draw–ratio with inertia and gravity included and T = 2000C. (Case 5: $W_f = 2.6 \times 10^{-5}$, $h_{10} = 1.8 \times 10^{-2}$, $h_{20} = 2 \times 10^{-2}$, $T = 2000$, $\gamma =$ variable, $\rho = 1400$, $g = 9.81$.)

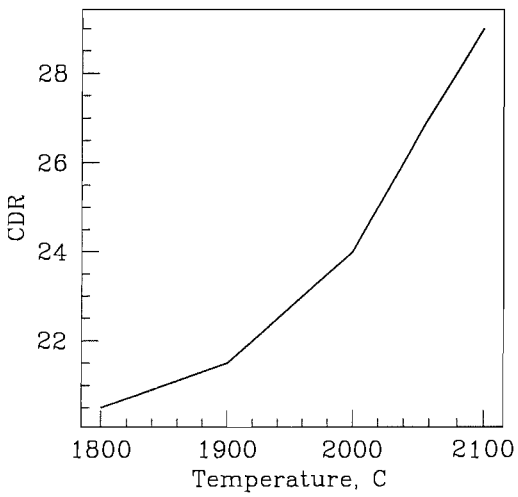

Figure 5.6: The effects of temperature on the critical draw–ratio with surface tension included. (Case 6: $W_f = 2.6 \times 10^{-5}$, $h_{10} = 1.8 \times 10^{-2}$, $h_{20} = 2 \times 10^{-2}$, $T =$ variable, $\gamma = 0.3$, $\rho = 1400$, $g = 9.81$.)

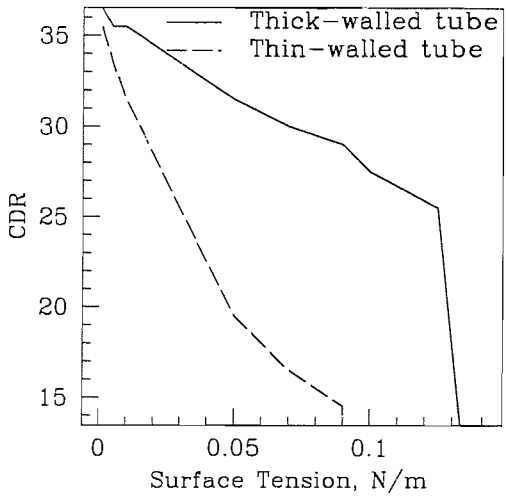

Figure 5.7: Graph to compare the effects of surface tension for different capillary geometries on the critical draw–ratio. (Case 7: $W_f = 2.6 \times 10^{-5}$, $h_{10} = 1.0 \times 10^{-2}$, $h_{20} = 2 \times 10^{-2}$, $T = 2050$, $\gamma =$ variable, $\rho = 0$, $g = 0$. Case 8: $W_f = 2.6 \times 10^{-5}$, $h_{10} = 1.8 \times 10^{-2}$, $h_{20} = 2 \times 10^{-2}$, $T = 2050$, $\gamma =$ variable, $\rho = 0$, $g = 0$.)

The results of the stability analysis on two different structures and at two different temperatures are now shown. One thick–walled capillary tube and one thin–walled capillary tube are simulated, with the following dimensions:

Thick–walled tube: $h_{10} = 1.0 \times 10^{-2}$, $h_{20} = 2.0 \times 10^{-2}$.
Thin–walled tube: $h_{10} = 1.8 \times 10^{-2}$, $h_{20} = 2.0 \times 10^{-2}$.

Figure 5.7 compares the effects of surface tension on the critical draw–ratio for the thick– (Case 7, Table 5.2) and thin–walled (Case 8, Table 5.2) tubes. Figure 5.8 compares the effects of inertia on the critical draw–ratio for the thick– (Case 9, Table 5.2) and thin–walled (Case 10, Table 5.2) tubes.

The fact that the thin–walled capillary tube is less stable than the thicker–walled capillary is by no means obvious, though there appear to be two competing effects here, the first being the wall thickness. It seems reasonable to suppose that a thin–

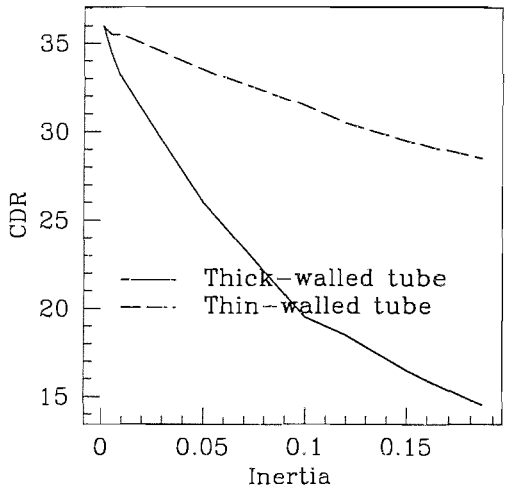

Figure 5.8: Graph to compare the effects of inertia for different capillary geometries on the critical draw–ratio. (Case 9: $W_f = 2.6\times10^{-5}$, $h_{10} = 1.0\times10^{-2}$, $h_{20} = 2\times10^{-2}$, $T = 2050$, $\gamma = 0$, $\rho =$ variable, $g = 0$. Case 10: $W_f = 2.6 \times 10^{-5}$, $h_{10} = 1.8 \times 10^{-2}$, $h_{20} = 2 \times 10^{-2}$, $T = 2050$, $\gamma = 0$, $\rho =$ variable, $g = 0$.)

walled capillary tube is less stable as a result of a number of competing factors. First, there will be less resistance to a change in the inner radius due to there being less mass between it and $r = h_2(z,t)$. Secondly, any such change in h_1 would have to be accompanied by a similar change in h_2 (in the case of h_1 increasing), in order to prevent the two radii from meeting ($h_1(z,t) = h_2(z,t)$ for any z or t) and the fibre collapsing. This seems to suggest that the thin–walled tube should prove less stable. The second of the competing factors is the effect of surface tension. It is clear that the effect of this on decreasing the critical draw–ratio should be greater with the thick–walled capillary (as demonstrated earlier). The outer radii are identical in both tubes, but the inner radius is smaller in the case of the thick–walled capillary, thus explaining its greater effect. The consideration of surface tension effects suggest that the thick–walled tube should prove the less stable. It is not intuitively clear which of the two effects is the more important, though the results inform that the former effect is dominant, at least in the regime of parameter space considered.

5.4 Conclusions

We have identified and investigated the effect of each parameter available for change on the stability of the drawing process for capillary tubes. However, it is important to be aware of the potential limitations of the model. The stability analysis of solid fibre drawing has been completed by many authors in the past, and all state that it is not possible to draw solid fibres stably with a draw–ratio of greater than about 20.2 (when excluding the effects of inertia, surface tension and gravity). This is not so in practice, where fibres may be drawn at many times this ratio.

There are several reasons suggested for this lack of consistency, some of which lie in the boundary conditions of fibre drawing. For example, we normally we specify the speed at which the fibre is drawn and not the force that is applied to draw it (at a largely constant speed). The effect of the difference between these boundary conditions is often nontrivial, and constant–speed boundary conditions are easier to work with. To illustrate how such a change in boundary conditions may affect the predicted critical draw–ratio it is noted that if the force alone is specified, then the fibre can be drawn at any draw–ratio imposed (see §5.2). Will a combination of constant speed and constant force boundary conditions lead to predictions that match experimental results? The accurate modelling of the cooling of the preform in the furnace is not a realistic task, and neither is accurately determining the temperature profile of a furnace. The non–constant temperature profile of the preform could affect the stability ratio in the same way as altering the boundary conditions.

Whilst this problem remains open, it is clear that the *trends* predicted theoretically correspond exactly with the trends in critical draw ratio observed experimentally (e.g. how the ratio varies with temperature, all other parameters remaining fixed), suggesting that such studies as these are, at worst, qualitatively correct.

5.4.1 Practical Results

In this Chapter we:

- have shown that both inertia and gravity act to stabilize the drawing process (see §5.3.4.1);
- have shown that surface tension destabilizes the drawing process (see §5.3.4.2);
- have shown that increasing the temperature (thus decreasing the glass viscosity) stabilizes the drawing process (see §5.3.4.2).

Chapter 6

The Rotation of Capillary Tubes: Numerical Analysis

6.1 Numerics of leading–order capillary drawing equations

Chapter 3 models the process of capillary drawing. Equations (3.53)–(3.56) with boundary conditions (3.58) were solved analytically in some limiting cases, but the full equations must be solved numerically to characterize parameter space and guide the manufacture process.

In this chapter we consider the effects of imparting a rotation to the preform, changing the size of the draw length, varying the surface tension, and altering the draw–down ratio (DDR). We consider the effects both for solid fibres and capillary tubes. All numerical calculations were performed by solving the final leading–order equations that describe the drawing of capillary tubes using the mathematical software Maple, which itself uses a standard set of library routines and invokes Runge–Kutta–Merson methods and Newton iteration in a shooting and matching technique, among

others.

6.1.1 Numerical calculations for the rotation of a solid fibre

The drawing conditions for the fibre simulations were as follows. We used $W_f = 2.6 \times 10^{-5}$, $W_d = 20W_f$, $h_0 = 1 \times 10^{-2}$, $\gamma = 3 \times 10^{-1}$, $p_0 = 0$, $T = 2000$, $L = 3 \times 10^{-2}$, and the viscosity law given in Chapter 3 with gravity and inertia included. We assume the glass used is Suprasil F300, a high purity commercially available silica glass. Also, a constant temperature drawing furnace was assumed (μ does not vary with z). These drawing conditions are not wholly realistic (for example in practice W_d is considerably more than $20W_f$), but have been chosen so as to allow the effects of rotation to be clearly seen.

The numerical calculations considered in this Chapter for solid fibre drawing are summarized in Table 6.1.

Figure 6.1 shows the effects of rotating a preform at the realistic rotation rate of 300rpm at $z = 0$ (no rotation at $z = L$) and compares the results with the case of no rotation. The upper curve (Case 1, Table 6.1) corresponds to the rotated preform and the lower curve (Case 2, Table 6.1) to the preform not rotated. The graph shows that, as one might expect, the effect of rotation is to increase the fibre radius along the entirety of the draw length as a result of the centripetal acceleration that the fluid experiences during its residence time in the furnace. The final dimensions of the fibre are fixed by mass conservation considerations and the angular frequency exhibits boundary layer behaviour close to $z = L$ as a result of the large DDR (see Chapter 3).

Figure 6.2 shows the effects of varying the draw length of the furnace, L. Typically furnaces have a draw length of a approximately 3cm (Case 4, Table 6.1), though Figure 6.2 compares this value with $L = 1.5$cm (Case 3, Table 6.1) and $L = 6$cm (Case 5, Table 6.1), where rotation has been included in all cases. The radii of

Table 6.1: Table summarizing parameter values considered for solid fibre drawing.

Case	W_f	W_d	h_0	T	γ	L
1	2.6×10^{-5}	5.2×10^{-4}	1×10^{-2}	2000	3×10^{-1}	3×10^{-2}
2	2.6×10^{-5}	5.2×10^{-4}	1×10^{-2}	2000	3×10^{-1}	3×10^{-2}
3	2.6×10^{-5}	5.2×10^{-4}	1×10^{-2}	2000	3×10^{-1}	1.5×10^{-2}
4	2.6×10^{-5}	5.2×10^{-4}	1×10^{-2}	2000	3×10^{-1}	3×10^{-2}
5	2.6×10^{-5}	5.2×10^{-4}	1×10^{-2}	2000	3×10^{-1}	6×10^{-2}
6	2.6×10^{-5}	5.2×10^{-4}	1×10^{-2}	2000	3×10^{-1}	1.5×10^{-2}
7	2.6×10^{-5}	1.04×10^{-3}	1×10^{-2}	2000	3×10^{-1}	1.5×10^{-2}
8	2.6×10^{-5}	5.2×10^{-4}	1×10^{-2}	2000	0	1.5×10^{-2}
9	2.6×10^{-5}	5.2×10^{-4}	1×10^{-2}	2000	3×10^{-1}	1.5×10^{-2}
10	2.6×10^{-5}	5.2×10^{-4}	1×10^{-2}	2000	9×10^{-1}	1.5×10^{-2}

Case	g	$B(0)$	Figure
1	9.81	300rpm	6.1
2	9.81	0rpm	6.1
3	9.81	300rpm	6.2
4	9.81	300rpm	6.2
5	9.81	300rpm	6.2
6	9.81	300rpm	6.3
7	9.81	300rpm	6.3
8	9.81	300rpm	6.4
9	9.81	300rpm	6.4
10	9.81	300rpm	6.4

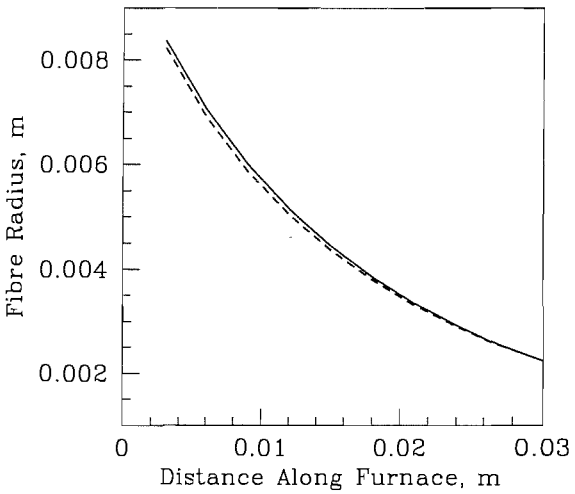

Figure 6.1: Graph to show the effects of rotation on solid fibre geometry. (Case 1 (Upper curve): $W_f = 2.6 \times 10^{-5}$, $W_d = 5.2 \times 10^{-4}$, $h_0 = 1 \times 10^{-2}$, $T = 2000$, $\gamma = 3 \times 10^{-1}$, $L = 3 \times 10^{-2}$, $p_0 = 0$, $g = 9.81$, $B(0) = 300$rpm. Case 2 (Lower curve): $W_f = 2.6 \times 10^{-5}$, $W_d = 5.2 \times 10^{-4}$, $h_0 = 1 \times 10^{-2}$, $T = 2000$, $\gamma = 3 \times 10^{-1}$, $L = 3 \times 10^{-2}$, $p_0 = 0$, $g = 9.81$, $B(0) = 0$rpm.)

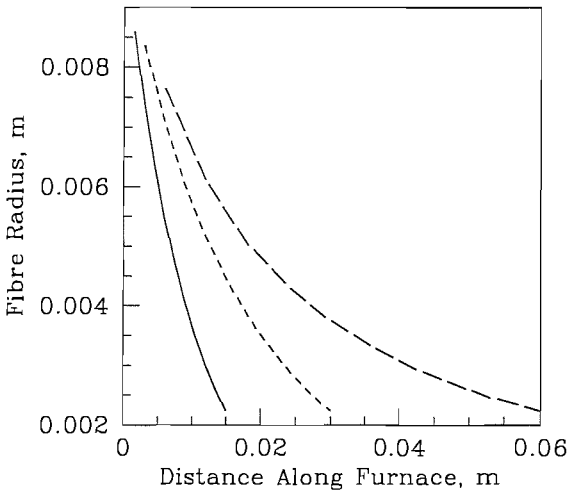

Figure 6.2: Graph to show the effects of varying the furnace length on solid fibre geometry. (Case 3 (Lower curve): $W_f = 2.6 \times 10^{-5}$, $W_d = 5.2 \times 10^{-4}$, $h_0 = 1 \times 10^{-2}$, $T = 2000$, $\gamma = 3 \times 10^{-1}$, $L = 1.5 \times 10^{-2}$, $p_0 = 0$, $g = 9.81$, $B(0) = 300$rpm. Case 4 (Middle curve): $W_f = 2.6 \times 10^{-5}$, $W_d = 5.2 \times 10^{-4}$, $h_0 = 1 \times 10^{-2}$, $T = 2000$, $\gamma = 3 \times 10^{-1}$, $L = 3 \times 10^{-2}$, $p_0 = 0$, $g = 9.81$, $B(0) = 300$rpm. Case 5 (Upper curve): $W_f = 2.6 \times 10^{-5}$, $W_d = 5.2 \times 10^{-4}$, $h_0 = 1 \times 10^{-2}$, $T = 2000$, $\gamma = 3 \times 10^{-1}$, $L = 6 \times 10^{-2}$, $p_0 = 0$, $g = 9.81$, $B(0) = 300$rpm.)

the fibre at both ends of the furnace are fixed by mass conservation considerations. The presence of surface tension might be expected to have a greater effect on the geometry for $L = 6$cm (Case 5, Table 6.1) than for $L = 1.5$cm (Case 3, Table 6.1) as a result of the increased time a fluid element spends in the furnace. However, Figure 6.2 demonstrates that typical values of surface tension are not large enough to have a significant impact. This suggests that the stability of the fibre draw will not be particularly sensitive to changes in L for typical values of surface tension, though the situation may change as longer furnace lengths are approached (see Chapter 5.4 for a stability analysis of the drawing process). Furnace lengths are fixed in practice, and do not vary greatly between furnaces.

Figure 6.3 shows the effects of increasing the DDR. Since this is accomplished by

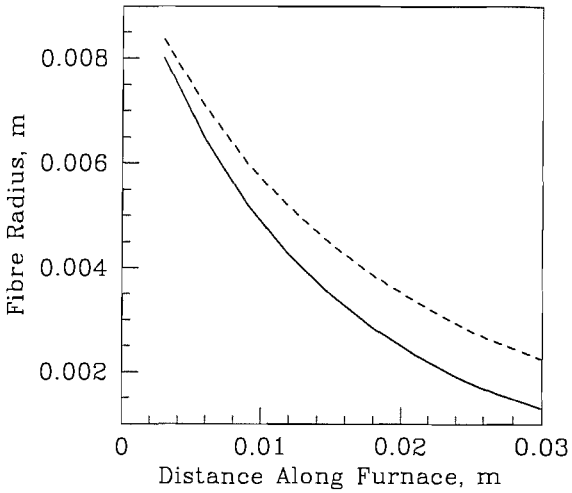

Figure 6.3: Graph to show the effects of varying the draw–down ratio on solid fibre geometry. (Case 6 (Upper curve): $W_f = 2.6 \times 10^{-5}$, $W_d = 5.2 \times 10^{-4}$, $h_0 = 1 \times 10^{-2}$, $T = 2000$, $\gamma = 3 \times 10^{-1}$, $L = 3 \times 10^{-2}$, $p_0 = 0$, $g = 9.81$, $B(0) = 300$rpm. Case 7 (Lower curve): $W_f = 2.6 \times 10^{-5}$, $W_d = 1.04 \times 10^{-3}$, $h_0 = 1 \times 10^{-2}$, $T = 2000$, $\gamma = 3 \times 10^{-1}$, $L = 3 \times 10^{-2}$, $p_0 = 0$, $g = 9.81$, $B(0) = 300$rpm.)

keeping the feed speed constant and increasing the draw speed from $20W_f$ (Case 6, Table 6.1) to $40W_f$ (Case 7, Table 6.1), the only significant effect will be to decrease the final dimension of the fibre as a result of mass conservation conditions. The lower curve (Case 7, Table 6.1) therefore corresponds to the larger DDR. Apart from the modification of final geometry, the form of the fibre geometry along the length is qualitatively similar in both cases.

Figure 6.4 shows the effects of varying the surface tension on solid fibre geometry. For a solid fibre draw the variations in geometry for realistic values of surface tension are small. Figure 6.4 shows three curves: the lower of the three (Case 8, Table 6.1) is the case with no surface tension. The middle curve (Case 9, Table 6.1) is the case of a typical surface tension value of $\gamma = 0.3$Nm. The upper curve (Case 10, Table 6.1) represents the case with 3 times as much surface tension as is realistic. Whilst the effect of this increase is small, it is clear that the effect is to increase the radius

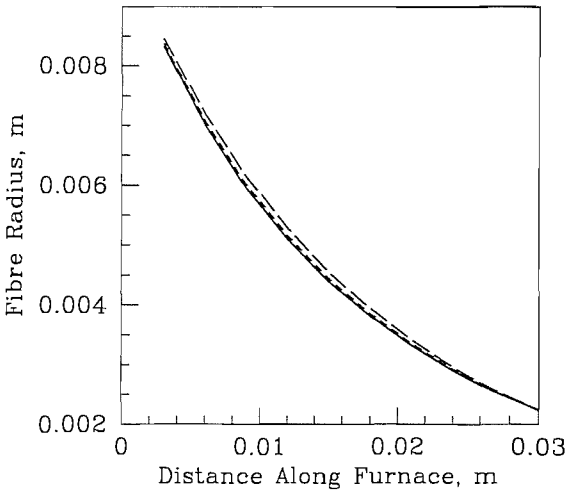

Figure 6.4: Graph to show the effects of varying the surface tension on solid fibre geometry. Case 8 (Lower curve): $W_f = 2.6 \times 10^{-5}$, $W_d = 5.2 \times 10^{-4}$, $h_0 = 1 \times 10^{-2}$, $T = 2000$, $\gamma = 0$, $L = 3 \times 10^{-2}$, $p_0 = 0$, $g = 9.81$, $B(0) = 300$rpm. Case 9 (Middle curve): $W_f = 2.6 \times 10^{-5}$, $W_d = 5.2 \times 10^{-4}$, $h_0 = 1 \times 10^{-2}$, $T = 2000$, $\gamma = 3 \times 10^{-1}$, $L = 3 \times 10^{-2}$, $p_0 = 0$, $g = 9.81$, $B(0) = 300$rpm. Case 10 (Upper curve): $W_f = 2.6 \times 10^{-5}$, $W_d = 5.2 \times 10^{-4}$, $h_0 = 1 \times 10^{-2}$, $T = 2000$, $\gamma = 9 \times 10^{-1}$, $L = 3 \times 10^{-2}$, $p_0 = 0$, $g = 9.81$, $B(0) = 300$rpm.)

of the fibre along the entirety of the draw length as already noted in Chapter 3. Though surface tension effects on solid fibre geometry are minimal, it is known that the presence of surface tension decreases the stability of the draw. This is discussed in Chapter 5.

The numerical results show that the effect of rotating solid fibres is to modify the radius of the preform at all points in the furnace except at $z = 0$ and $z = L$ in accordance with mass conservation considerations. However, the effects of rotating typical preforms at realistic rotation rates are not significant. Furthermore, it has been shown that fibre geometry is not sensitive to changes in any of the drawing parameters when the parameters are chosen to be typical of those used experimentally.

6.1.2 The capillary tube

The numerical calculations considered in this Chapter for capillary tube drawing are summarized in Table 6.2.

The drawing conditions simulated were the same as those for the solid fibre unless otherwise stated. The initial geometry of the tube was $h_{10} = 1.8$cm and $h_{20} = 2.0$cm. Each Figure in this section shows two curves. The lower of the two curves corresponds to the inner fibre radius h_1 and the upper curve corresponds to the outer fibre radius h_2.

Figure 6.5 shows a comparison between a rotated (Case 11, Table 6.2) and an unrotated (Case 12, Table 6.2) capillary tube drawn at $T = 1700$C with a modest 300rpm of rotation added at $z = 0$. It is clear that both inner and outer radii are increased throughout the length of the draw region when the preform is rotated (Case 11, Table 6.2) and that both rotated and unrotated preforms thin as the draw is completed, in order to approximately preserve the geometry ratio h_2/h_1. Surface tension prevents h_2/h_1 being preserved exactly as already discussed in Chapter 3. Whilst rotation has the effect of increasing h_1 and h_2 for the entire draw length, the effects at $z = L$ are much less significant. This may be understood from a consideration of the angular frequency profile, discussed in Chapter 3. For this reason preform rotation does not represent a sensible choice of mechanism for preventing hole collapse, since the rotation rates would have to be significant to effect the necessary change in h_1 at $z = L$. These numerical findings are supported by the discussion in Chapter 3. The geometrical effects of preform rotation are therefore not thought to be significant in terms of the final geometry, though any changes in the fibre geometry at any point in the draw length are known to affect the stability of the drawing process. Furthermore, as was shown in Chapter 4, the capillary tube may be used to model the behaviour of a particular class of holey fibres. When holey fibres are drawn, the manner in which the geometry varies with z may impact upon the microstructure. Furthermore, achievable rotation rates may significantly reduce unwanted Polariza-

Table 6.2: Table summarizing parameter values considered for capillary tube drawing.

Case	W_f	W_d	h_{10}	h_{20}	T	γ
11	2.6×10^{-5}	5.2×10^{-4}	1.8×10^{-2}	2.0×10^{-2}	1700	3×10^{-1}
12	2.6×10^{-5}	5.2×10^{-4}	1.8×10^{-2}	2.0×10^{-2}	1700	3×10^{-1}
13	2.6×10^{-5}	5.2×10^{-4}	1.8×10^{-2}	2.0×10^{-2}	2000	3×10^{-1}
14	2.6×10^{-5}	5.2×10^{-4}	1.8×10^{-2}	2.0×10^{-2}	2000	3×10^{-1}
15	2.6×10^{-5}	5.2×10^{-4}	1.8×10^{-2}	2.0×10^{-2}	2000	3×10^{-1}
16	2.6×10^{-5}	5.2×10^{-4}	1.8×10^{-2}	2.0×10^{-2}	2000	3×10^{-1}
17	2.6×10^{-5}	2.6×10^{-4}	1.8×10^{-2}	2.0×10^{-2}	2000	3×10^{-1}
18	2.6×10^{-5}	5.2×10^{-4}	1.8×10^{-2}	2.0×10^{-2}	2000	3×10^{-1}
19	2.6×10^{-5}	1.04×10^{-3}	1.8×10^{-2}	2.0×10^{-2}	2000	3×10^{-1}
20	2.6×10^{-5}	5.2×10^{-4}	1.8×10^{-2}	2.0×10^{-2}	2000	3×10^{-1}

Case	L	p_0	g	$B(0)$	Figure
11	3×10^{-2}	0	9.81	300rpm	6.5
12	3×10^{-2}	0	9.81	0rpm	6.5
13	3×10^{-2}	0	9.81	300rpm	6.6
14	3×10^{-2}	0	9.81	0rpm	6.6
15	1.5×10^{-2}	0	9.81	300rpm	6.7
16	3×10^{-2}	0	9.81	300rpm	6.7
17	3×10^{-2}	0	9.81	300rpm	6.8
18	3×10^{-2}	0	9.81	300rpm	6.8
19	3×10^{-2}	0	9.81	300rpm	6.9
20	3×10^{-2}	0	9.81	300rpm	6.9

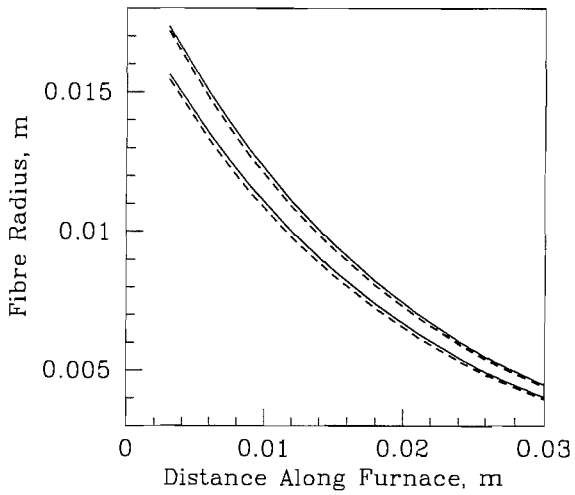

Figure 6.5: Graph to show the effects of preform rotation on capillary tube geometry at 1700C. (Case 11 (Solid curves): $W_f = 2.6\times10^{-5}$, $W_d = 5.2\times10^{-4}$, $h_{10} = 1.8\times10^{-2}$, $h_{20} = 2.0 \times 10^{-2}$, $T = 1700$, $\gamma = 3 \times 10^{-2}$, $L = 3 \times 10^{-2}$, $p_0 = 0$, $g = 9.81$, $B(0) = 300$rpm. Case 12 (Dashed curves): $W_f = 2.6 \times 10^{-5}$, $W_d = 5.2 \times 10^{-4}$, $h_{10} = 1.8 \times 10^{-2}$, $h_{20} = 2.0 \times 10^{-2}$, $T = 1700$, $\gamma = 3 \times 10^{-2}$, $L = 3 \times 10^{-2}$, $p_0 = 0$, $g = 9.81$, $B(0) = 0$rpm.)

tion Mode Dispersion in holey fibre drawing. For these reasons the effects of preform rotation on capillary tubes may yet prove to be significant.

Figure 6.6 shows the same comparison of rotated (Case 13, Table 6.2) and unrotated (Case 14, Table 6.2) preforms but for $T = 2000$C. As one might expect, the results are qualitatively similar, though the effects are more pronounced due to the decreased viscosity. Though this Figure suggests a large fractional change in final geometry, one must remember that this simulation has been carried out with a large capillary tube diameter in order to allow the effects to be clearly seen. Thus for typical capillary tube sizes preform rotation will not significantly impact the final geometry, though its effects may still be important for the reasons stated above.

Figure 6.7 shows, in the event that $T = 2000$C to create a system sensitive to any

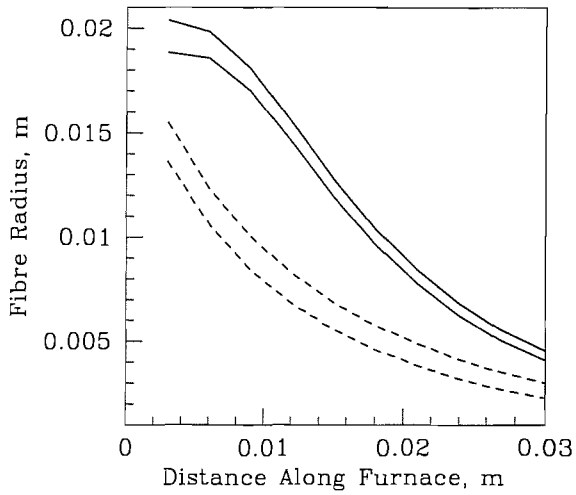

Figure 6.6: Graph to show effects of preform rotation on capillary tube geometry at 2000C. (Case 13 (Solid curves): $W_f = 2.6 \times 10^{-5}$, $W_d = 5.2 \times 10^{-4}$, $h_{10} = 1.8 \times 10^{-2}$, $h_{20} = 2.0 \times 10^{-2}$, $T = 2000$, $\gamma = 3 \times 10^{-2}$, $L = 3 \times 10^{-2}$, $p_0 = 0$, $g = 9.81$, $B(0) = 300$rpm. Case 14 (Dashed curves): $W_f = 2.6 \times 10^{-5}$, $W_d = 5.2 \times 10^{-4}$, $h_{10} = 1.8 \times 10^{-2}$, $h_{20} = 2.0 \times 10^{-2}$, $T = 2000$, $\gamma = 3 \times 10^{-2}$, $L = 3 \times 10^{-2}$, $p_0 = 0$, $g = 9.81$, $B(0) = 0$rpm.)

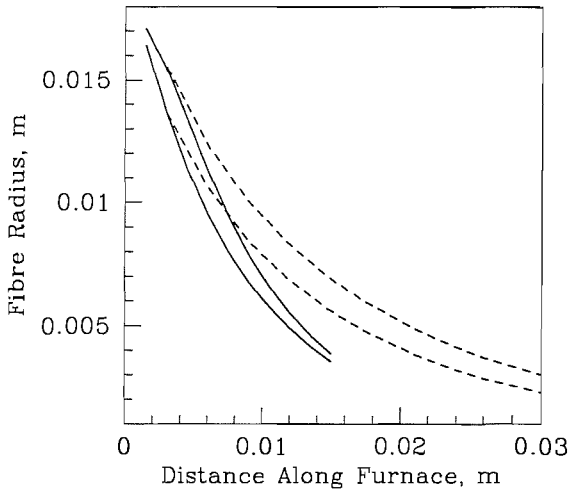

Figure 6.7: Graph to show effects of varying the furnace length on capillary tube geometry. (Case 15 (Solid curves): $W_f = 2.6 \times 10^{-5}$, $W_d = 5.2 \times 10^{-4}$, $h_{10} = 1.8 \times 10^{-2}$, $h_{20} = 2.0 \times 10^{-2}$, $T = 2000$, $\gamma = 3 \times 10^{-2}$, $L = 1.5 \times 10^{-2}$, $p_0 = 0$, $g = 9.81$, $B(0) = 300$rpm. Case 16 (Dashed curves): $W_f = 2.6 \times 10^{-5}$, $W_d = 5.2 \times 10^{-4}$, $h_{10} = 1.8 \times 10^{-2}$, $h_{20} = 2.0 \times 10^{-2}$, $T = 2000$, $\gamma = 3 \times 10^{-2}$, $L = 3 \times 10^{-2}$, $p_0 = 0$, $g = 9.81$, $B(0) = 300$rpm.)

changes in the rest of parameter space, the effect of decreasing the draw length with no rotation added. The value of L is halved from 3cm (Case 16, Table 6.2) to 1.5cm (Case 15, Table 6.2) and clearly the solid lines correspond to a draw length of 1.5cm and the dotted lines to a draw length of 3cm. No significant effect of this is apparent and we conclude, as in the case of the solid fibre simulation, that the draw length does little to affect the geometry of the final fibre (when compared with the effects of surface tension, for example) and hence cannot be used as a control parameter (this would only be possible in practice by using entirely different drawing towers).

Figures 6.8 and 6.9 compare the effects of a draw–down ratio of 20 with one of 10 (Cases 17 and 18, Table 6.2) and 40 (Cases 19 and 20, Table 6.2) respectively. As in the case of solid fibres, there appears to be no significant effect on the final fibre geometry that may be observed in terms of general numerical rules. For example,

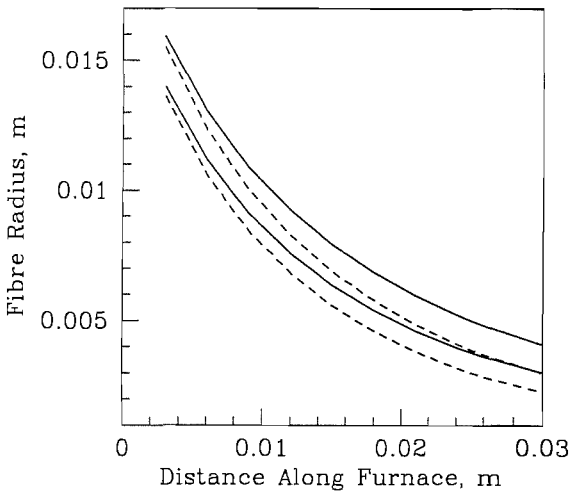

Figure 6.8: Graph to show effects of varying the draw–down ratio on capillary tube geometry. (Case 17 (Solid curves): $W_f = 2.6 \times 10^{-5}$, $W_d = 2.6 \times 10^{-4}$, $h_{10} = 1.8 \times 10^{-2}$, $h_{20} = 2.0 \times 10^{-2}$, $T = 2000$, $\gamma = 3 \times 10^{-2}$, $L = 3 \times 10^{-2}$, $p_0 = 0$, $g = 9.81$, $B(0) = 300$rpm. Case 18 (Dashed curves): $W_f = 2.6 \times 10^{-5}$, $W_d = 5.2 \times 10^{-4}$, $h_{10} = 1.8 \times 10^{-2}$, $h_{20} = 2.0 \times 10^{-2}$, $T = 2000$, $\gamma = 3 \times 10^{-2}$, $L = 3 \times 10^{-2}$, $p_0 = 0$, $g = 9.81$, $B(0) = 300$rpm.)

changing the DDR does indeed change both the final inner radius, outer radius, and their ratio. However, the presence of surface tension complicates matters and prevents a simple relationship being established from an observation of the numerical tendencies. The change in DDR remains the most used control parameter since it is easy to change experimentally and impacts most on the absolute geometry changes effected together with the final ratio h_2/h_1.

6.2 Tackling the problem of hole collapse

We now investigate the possible mechanisms for preventing hole collapse.

Since it is observed that hole closure only occurs when h_{10} is sufficiently small, we

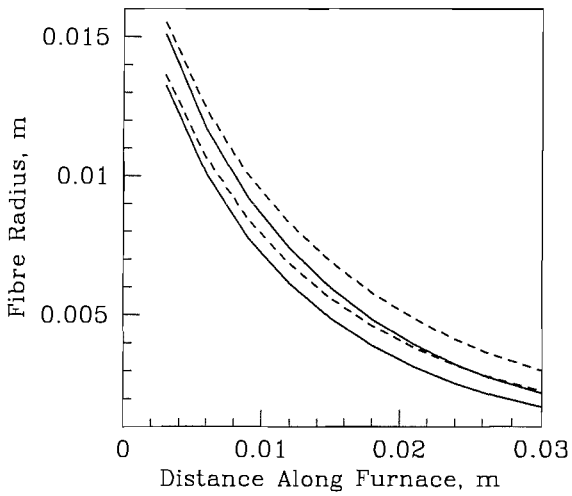

Figure 6.9: Graph to show effects of varying the draw–down ratio on capillary tube geometry. (Case 19 (Solid curves): $W_f = 2.6 \times 10^{-5}$, $W_d = 1.04 \times 10^{-3}$, $h_{10} = 1.8 \times 10^{-2}$, $h_{20} = 2.0 \times 10^{-2}$, $T = 2000$, $\gamma = 3 \times 10^{-2}$, $L = 3 \times 10^{-2}$, $p_0 = 0$, $g = 9.81$, $B(0) = 300$rpm. Case 20 (Dashed curves): $W_f = 2.6 \times 10^{-5}$, $W_d = 5.2 \times 10^{-4}$, $h_{10} = 1.8 \times 10^{-2}$, $h_{20} = 2.0 \times 10^{-2}$, $T = 2000$, $\gamma = 3 \times 10^{-2}$, $L = 3 \times 10^{-2}$, $p_0 = 0$, $g = 9.81$, $B(0) = 300$rpm.)

Table 6.3: Table showing minimum values of h_{10}.

Case	W_f	W_d	h_{10}	h_{20}	T	γ
21	2.5×10^{-4}	8.3×10^{-2}	3×10^{-4}	$1.5h_{10}$	1950	3×10^{-1}
22	2.5×10^{-4}	8.3×10^{-1}	2×10^{-4}	$1.5h_{10}$	1950	3×10^{-1}
23	2.5×10^{-4}	8.3×10^{-2}	1×10^{-3}	$1.5h_{10}$	2100	3×10^{-1}
24	2.5×10^{-4}	8.3×10^{-1}	7×10^{-4}	$1.5h_{10}$	2100	3×10^{-1}

Case	L	p_0	g	$B(0)$
21	3×10^{-2}	0	9.81	0
22	3×10^{-2}	0	9.81	0
23	3×10^{-2}	0	9.81	0
24	3×10^{-2}	0	9.81	0

shall consider how small h_{10} may be for a given set of drawing parameters before the hole in the capillary tube closes. Starting with no hole overpressure and no preform rotation, we determine how small h_{10} can be made for a given set of draw parameters without h_1 becoming negative at any point in the draw. When h_1 is negative, the hole has closed and the model is invalid. Hole closure is induced by surface tension as no hole closure occurs in its absence.

Table 6.3 gives the results of the minimum h_{10} possible for a variety of furnace temperatures and feed speeds.

Table 6.3 shows that whilst the differences in the smallest values of h_1 are marginal, larger draw speeds tend to decrease the final size of h_1 and a larger h_{10} will be required to counteract h_1 becoming negative at $z = L$. Higher draw temperatures (thus lower viscosities) allow surface tension to be more effective, since it is the balancing between surface tension and viscosity that largely determines the geometry.

We therefore discover that it is possible to draw fibres with small initial geometries at realistic temperatures and draw speeds. However, we should like to be able to draw smaller capillary tubes than currently possible. Part of the motivation for being able to draw capillary tubes with small holes is the potential application to full holey fibres.

Before we consider possible mechanisms we briefly analyse the effect of having a temperature profile in the furnace, since this is more realistic than the constant temperature profile assumed thus far.

It is observed that including a temperature profile does alter the minimum h_{10} possible for a given set of draw parameters. To give a qualitative demonstration of this, consider a draw furnace with a temperature profile that increases linearly from an initial minimum temperature at $z = 0$ to a maximum at $z = \frac{L}{2}$, and decreases to the same minimum at $z = L$. With a minimum temperature of 2000 and a maximum of 2100, the following points are notable. The final draw–ratio is found to be between that of the final draw–ratio obtained using a constant temperature of 2000, and that obtained using a constant temperature of 2100. This is also true of the final dimensions. At small values of z, we observe that both the inner and outer radii are larger in size than in either of the constant temperature cases. That is, larger than in the $T = 2000$ case, even, because further down the furnace the fluid has a lower viscosity, and so the effect of the force prescribed at $z = L$ on the upper part of the furnace to be reduced.

6.3 The effects of hole pressurization

We will now investigate the potential for pressurizing capillary tubes as a mechanism to prevent surface tension induced hole collapse.

Drawing small–holed fibres from preforms whose dimensions are small has beneficial implications for the ratio of final outer to inner radii, $(h_2/h_1)|_{z=L}$ and application in holey fibre technology. When the initial capillary tube has small dimensions surface tension tends to close the hole and final hole size is sensitive to changes in drawing parameters. On the other hand, preforms cannot be made arbitrarily large, since holey fibre preforms that are made from many packed capillaries cannot fit in the furnace if the overall radius is greater than a few centimetres.

It is possible that one way to achieve the small final dimensions whilst starting from a small capillary tube is to include an overpressure in the hole, preventing collapse brought about by surface tension and large draw speeds. Whilst pressurizing the hole will assist in preventing the capillary tube from closing at $z = L$, it will also cause the fibre radii to expand at $z = 0$. In extreme cases the fibre will "explode". This occurs because at large radii surface tension has little effect, whereas the effects of hole overpressure are unaltered. Before investigating hole collapse further we consider preform "explosion".

6.3.0.1 Preform "explosion"

As the overpressure applied for a given set of drawing parameters becomes too large, both the inner and outer radii tend to infinity: the preform "explodes". To determine the pressure at which this occurs, as predicted by Fitt *et al.* [15], we use the following parameter values and gradually increase the hole overpressure p_0 until the critical pressure is reached. The drawing parameters used correspond to typical values used experimentally. We set $W_f = 6.0 \times 10^{-5}$, $W_d = 4.0 \times 10^{-3}$, $h_{10} = 4.0 \times 10^{-3}$,

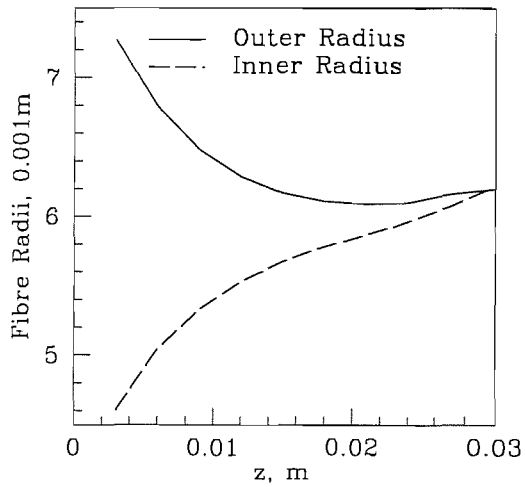

Figure 6.10: Graph to show h_1 and h_2 along the length of the drawing furnace at the limit of the numerical solutions, just before the fibre "explodes". (Parameter values: $W_f = 6.0 \times 10^{-5}$, $W_d = 4.0 \times 10^{-3}$, $h_{10} = 4.0 \times 10^{-3}$, $h_{20} = 8.0 \times 10^{-3}$, $T = 2100$, $\gamma = 1 \times 10^{-1}$, $L = 3 \times 10^{-2}$, $p_0 =$ variable, $g = 9.81$, $B(0) = 0$, $\rho = 2200$)

$h_{20} = 8.0 \times 10^{-3}$, $T = 2100$, $\gamma = 1 \times 10^{-1}$, $L = 3 \times 10^{-2}$, $p_0 =$ variable, $g = 9.81$, $B(0) = 0$, and $\rho = 2200$.

The graphs of h_1 and h_2 as a function of distance along the furnace z are shown in Figure 6.10.

To investigate how this maximum hole overpressure is affected by altering the capillary geometry we consider three preform geometries, and for each geometry plot the maximum hole overpressure as a function of temperature (tantamount to varying the viscosity). Other parameter values were chosen to be typical experimental parameters. We set $W_f = 2.6 \times 10^{-5}$, $W_d = 6.5 \times 10^{-4}$, $h_{10} =$ variable, $h_{20} =$ variable, $T = 2100$, $\gamma = 3 \times 10^{-1}$, $L = 3 \times 10^{-2}$, $p_0 =$ variable, $g = 9.81$, $B(0) = 0$, and $\rho = 2200$. The geometries and other parameters are summarized in Table 6.4.

It is clear from Cases 25–27, Table 6.4,shown in Figures 6.11–6.13 that, as the wall

Table 6.4: Table showing how capillary geometry affects maximum overpressure.

Case	W_f	W_d	h_{10}	h_{20}	T	γ
25	2.6×10^{-7}	6.5×10^{-4}	1×10^{-2}	2×10^{-2}	–	3×10^{-1}
26	2.6×10^{-7}	6.5×10^{-4}	2×10^{-2}	4×10^{-2}	–	3×10^{-1}
27	2.6×10^{-7}	6.5×10^{-4}	5×10^{-3}	1×10^{-2}	–	3×10^{-1}

Case	L	p_0	g	$B(0)$	ρ	Figure
25	3×10^{-2}	–	9.81	0	2200	6.11
26	3×10^{-2}	–	9.81	0	2200	6.12
27	3×10^{-2}	–	9.81	0	2200	6.13

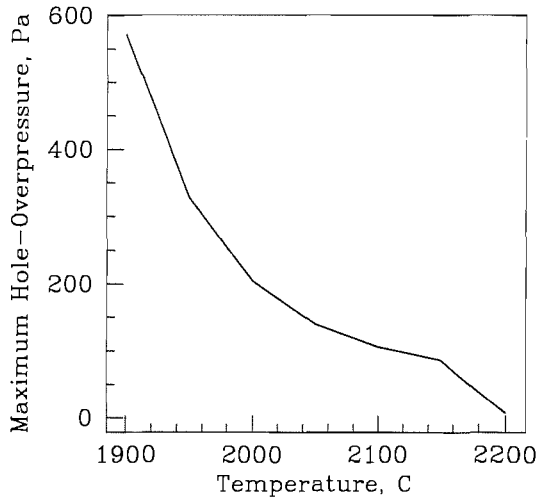

Figure 6.11: Graph to show the maximum hole overpressure as a function of temperature. (Case 25: $W_f = 2.6 \times 10^{-5}$, $W_d = 6.5 \times 10^{-4}$, $h_{10} = 1 \times 10^{-2}$, $h_{20} = 2 \times 10^{-2}$, T = variable, $\gamma = 3 \times 10^{-1}$, $L = 3 \times 10^{-2}$, p_0 = variable, $g = 9.81$, $B(0) = 0$, $\rho = 2200$.)

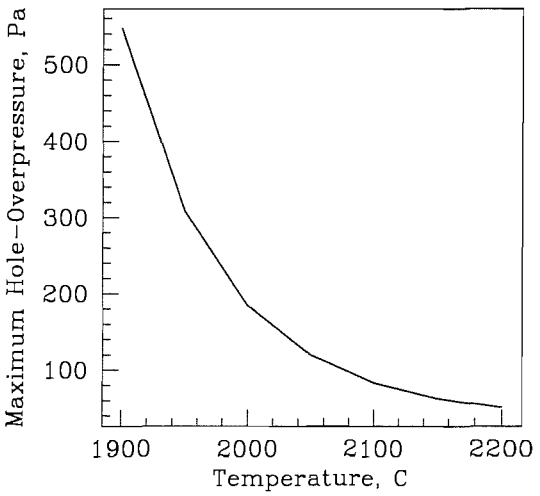

Figure 6.12: Graph to show the maximum hole overpressure as a function of temperature for Case 26. ($W_f = 2.6 \times 10^{-5}$, $W_d = 6.5 \times 10^{-4}$, $h_{10} = 2 \times 10^{-2}$, $h_{20} = 4 \times 10^{-2}$, T = variable, $\gamma = 3 \times 10^{-1}$, $L = 3 \times 10^{-2}$, p_0 = variable, $g = 9.81$, $B(0) = 0$, $\rho = 2200$.)

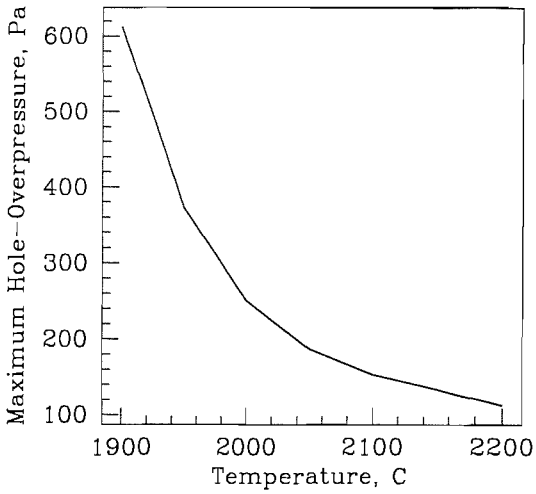

Figure 6.13: Graph to show the maximum hole overpressure as a function of temperature for Case 27. ($W_f = 2.6 \times 10^{-5}$, $W_d = 6.5 \times 10^{-4}$, $h_{10} = 5 \times 10^{-3}$, $h_{20} = 1 \times 10^{-2}$, T = variable, $\gamma = 3 \times 10^{-1}$, $L = 3 \times 10^{-2}$, p_0 = variable, $g = 9.81$, $B(0) = 0$, $\rho = 2200$.)

thickness and the dimensions of the preform are increased, the effects of surface tension are minimized. This has the effect of increasing the sensitivity of the resulting geometry to the quantity of overpressure applied.

6.3.1 Using overpressure to prevent hole collapse

Having studied preform explosion and established that hole overpressure may be used to prevent hole collapse, we now consider three separate cases, with differing furnace temperatures and feed speeds, and in each case determine how small the initial geometry can be made without the hole closing, whilst using an overpressure to prevent the closure. The results are shown in Table 6.5 and were obtained in the following manner. The overpressure was set to zero and h_{10} reduced until $h_1 = 0$ at $z = L$. The overpressure was then increased until the point of preform "explosion" was reached near $z = 0$. The initial inner radius was then reduced further until once

Table 6.5: Table to show minimum h_{10} with overpressure added.

Case	W_f	W_d	h_{10}	h_{20}	T	γ
28	8.3×10^{-1}	6.5×10^{-4}	4.0×10^{-5}	2×10^{-2}	1950	3×10^{-1}
29	8.3×10^{-1}	6.5×10^{-4}	2.2×10^{-4}	2×10^{-2}	2100	3×10^{-1}
30	8.3×10^{-2}	6.5×10^{-4}	2.5×10^{-4}	2×10^{-2}	2100	3×10^{-1}

Case	L	p_0	g	$B(0)$	ρ
28	3×10^{-2}	1.37×10^4	9.81	0	2200
29	3×10^{-2}	2.49×10^3	9.81	0	2200
30	3×10^{-2}	2.17×10^3	9.81	0	2200

again $h_1 = 0$ at $z = L$. The process was iterated until, for a given hole overpressure, the percentage reduction in h_{10} possible without hole closure was small.

As the initial inner radius decreases and the pressure increases, this iterative process becomes increasingly sensitive to the amount of hole overpressure. This is expected, as the minimum inner radius that overpressure will allow without h_1 and h_2 becoming unbounded, is being converged on. Additionally, the process is more sensitive to the amount of hole overpressure as the viscosity of the fluid is reduced by increasing the temperature.

The fact that it is observed that the above process is extremely sensitive to the amount of hole overpressure prescribed is discouraging. It is not at all clear that the

overpressure is constant, as it might vary along the length of the preform. Perhaps the pressure inside the capillary is a function of the length along the furnace, and this functional dependence is strong, therefore allowing the pressure sensitivity to be removed. Adding a pressure gradient to the problem would indeed be expected to reduce this sensitivity because if the pressure increases with z, the pressure at $z = 0$, which is the problematic region, could always be kept below the pressure that would cause the fibre radii to become unbounded, allowing overpressure to counteract the catastrophic effect of surface tension at $z = 0$. This is discussed in Chapter 3.

6.4 Rotation and pressure

We have seen in the preceding section that whilst pressurizing capillary tubes allows small holes to be manufactured more easily, the final geometry is still sensitive to changes in drawing parameters and to the amount of hole overpressure. We here investigate whether preform rotation might be used as an additional control mechanism. The ideal control mechanism will be one that produces a small effect on the final geometry when the parameter is altered, but where the parameter may assume a large range of values. This would ensure that the parameter may be used in a wide variety of drawing scenarios used in practice.

Assuming no temperature gradient, we will repeat the calculations performed in §6.3, while seeing how rapidly we may rotate the fibre without it exploding close to $z = 0$, since we observe this to occur numerically for reasons similar to those set out for overpressure induced explosion.

We reduce the pressure to below the critical values determined in §6.3, allowing the hole to close. At this point the geometry of the preform is not sensitive to changes in pressure. Preform rotation is then added until the hole is reopened and this value for $B(0)$ recorded. See 6.3 to see any effects on the minimum size of h_1 that this allows.

Table 6.6: Table to show results for smallest h_{10} with hole overpressure and rotation added.

Case	W_f	W_d	h_{10}	h_{20}	T	γ
31	8.3×10^{-1}	6.5×10^{-4}	4.0×10^{-5}	2×10^{-2}	1950	3×10^{-1}
32	8.3×10^{-1}	6.5×10^{-4}	2.2×10^{-4}	2×10^{-2}	2100	3×10^{-1}
33	8.3×10^{-2}	6.5×10^{-4}	2.5×10^{-4}	2×10^{-2}	2100	3×10^{-1}

Case	L	p_0	g	$B(0)_{max}$	ρ
31	3×10^{-2}	1.20×10^4	9.81	350rpm	2200
32	3×10^{-2}	2.35×10^3	9.81	900rpm	2200
33	3×10^{-2}	2.10×10^3	9.81	10rpm	2200

Rotation may not be used on its own to prevent a small hole from closing unless the preform has dimensions larger than those used in holey fibres. This is because the effects of preform rotation are more significant when the outer wall of the preform is far from the centreline. Using preforms with smaller dimensions would require rotation rates ($B(0) \approx 10^4$rpm) that are not currently achievable in practice.

The results in Table 6.6 demonstrate that whilst rotation alone may not be a useful mechanism to prevent hole collapse, it may in some cases be used to good effect when the capillary tube is already pressurized. The fact that preform rotation may need to be as large as $B(0) \approx 10^4$rpm to be used on its own suggests that changes in rotation rates of 10–100rpm will have little effect on preform geometry. This large parameter range corresponds precisely to the situation described above. With capillary tubes pressurized to their maximum value before explosion, rotation rates of 350–900rpm (Cases 31–33, Table 6.6) may be added without preform "explosion" occurring.

Case 31 represents a drawing scenario where rotation and pressure may be used together to prevent hole collapse. This is because a reduction in pressure to a value below the critical value (in practice going past this value "explodes" the preform and the draw must be started once again with a new preform) closes the hole but realistic rotation rates (350rpm) may be used to open the hole again. Similarly, Case 32 represents a drawing scenario where rotation and pressure may be used to prevent hole closure, but rotation rates much larger than 950rpm are not practical. Case 33 represents a drawing scenario where pressure and rotation may not realistically be used to prevent hole collapse. With hole overpressure reduced below the critical value allowing the hole to close, the results in Table 6.6 show that a rotation rate of 10rpm was necessary to open the hole, suggesting that geometry is overly sensitive to rotation rates in this regime.

6.5 Conclusions

The equations that govern the drawing of capillary tubes (3.53)–(3.56) with boundary conditions (3.58) were examined numerically and the results interpreted in a wholly practical and physical context. Specifically, the problem of hole collapse was examined, with pressure and rotation with pressure being considered to prevent the collapse. It was found both pressure and rotation may be used to prevent hole collapse, though for practical reasons a combination of the two is most effective. Ideally, a pressure *gradient* would be applied in the capillary tube (i.e. $p_0 = p_0(z)$), removing many of the problems encountered, such as the sensitivity of geometry to pressure and preform "explosion" that occurs in parts of the preform where h_1 and p_0 are large.

6.5.1 Practical Results

In this Chapter we:

- have shown that for a solid fibre, increasing the draw length increases the effects of preform rotation on fibre geometry (see §6.1.1);
- have shown that for a solid fibre, altering the draw–down–ratio does not significantly alter the effects of preform rotation on fibre geometry (see §6.1.1);
- established that preform rotation alone is not likely to prevent hole collapse in capillary tubes (see §6.1.2);
- have shown that increasing the furnace temperature (thus decreasing the glass viscosity) increases the effects of preform rotation on fibre geometry (see §6.1.2);
- have shown that using hole overpressure and preform rotation together is a possible mechanism for preventing hole collapse in capillary tubes (see §6.4).

Chapter 7

The Rotation of Capillary Tubes: Experimental Results and Discussion

7.1 Fibre predictions - full numerics

In previous Chapters we have developed a model for the rotation of capillary tubes and conducted lengthy numerical analysis of the resulting equations. In this Chapter we solve equations (3.53)–(3.56) with boundary conditions (3.58) numerically, and compare the results with data from experimental trials conducted at the Optoelectronics Research Centre.

Equations (3.53)–(3.56) with boundary conditions (3.58) were solved using standard numerical library routines available in the Maple package. However, as this software is not specifically aimed towards the numerical solution of ordinary differential equations, a more robust routine was required as the structure of the solution necessitates careful shooting to solve the boundary value problem at large rotation rates.

A Fortran 77 code was written that utilizes the NAG routine D02HAF. This routine solves two-point boundary value problems for a system of ordinary differential equations using a Runge–Kutta–Merson method and Newton iteration in a shooting and matching technique. For more details on the library routine see [70]. The Fortran code may be found in Appendix B.

7.1.1 The viscosity of silica glass

The viscosity and its variation with temperature of the Suprasil F300 silica glass used is unknown (this is proprietary information). The precise value of the surface tension of the glass is also unknown, along with possible variations with temperature. It has been assumed thus far that the drawing furnace has a constant temperature whereas in reality it is known to vary significantly. Whilst obtaining accurate data to remove all unknowns is unrealistic, a concerted effort was made to reduce the uncertainties. The author of [67], Professor R. H. Doremus, was contacted and upon his advice it was decided that the viscosity measurements carried out by Hetherington *et al.* [71] should be used to represent the viscosity of Suprasil F300 glass between 1000 and 1400, and that between 1400 and 2500 those of Urbain *et al.* [72] should be used. The viscosity is measured in Poise and the temperature, T, in Celsius. This puts the viscosity somewhere in-between that determined by Paek and Runk [73] and that determined by Bansal and Doremus [74], as shown in Figure 7.1. The experimentally measured viscosity laws are

$$1000\text{C} - 1400\text{C} \qquad \mu = 3.8 \times 10^{-13} \exp\left(\frac{712000}{(8.3145T + 2271.10567)}\right),$$

$$1400\text{C} - 2500\text{C} \qquad \mu = 5.8 \times 10^{-7} \exp\left(\frac{515400}{(8.3145T + 2271.10567)}\right).$$

For details on how these viscosities were measured, how the techniques varied with temperature and a general discussion of these results see [67].

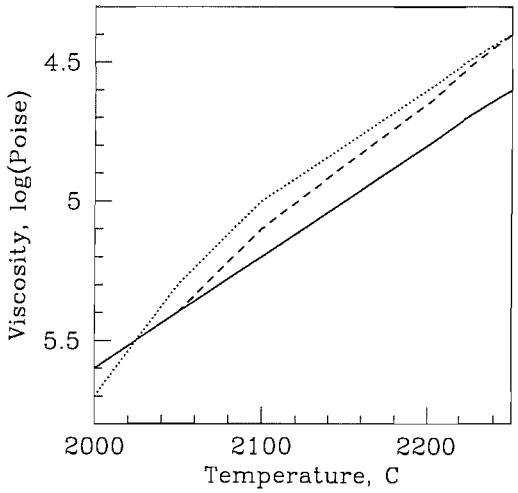

Figure 7.1: Graph comparing the viscosity laws given in the literature for the temperature range of interest. (Upper curve: Doremus [67]. Central curve: Urbain [72]. Lower curve: Paek and Runk [73].)

7.1.2 Measurement of the furnace temperature profile

The following section describes some of the efforts afforded the correct measurement of the temperature profile of the furnace used in the drawing experiments described below.

To obtain accurate numerical predictions for comparison with optical fibre drawing experiments conducted in the Optoelectronics Research Centre, we clearly require knowledge of the temperature distribution in the furnace.

Since in making our predictions we implicitly assume that the temperature of the glass is the same as that of the furnace at any point, it is possible to make measurements of the temperature of the furnace element by measuring the temperature in a glass preform as it traverses the length of the furnace.

This investigative experiment was conducted by Mr John R. Hayes of the Optoelec-

tronics Research Centre, assisted and overseen by myself.

A glass preform that was 10mm in diameter was chosen, since this is of a similar size to those used to manufacture holey fibres. The preform contained an air-hole into which a thermocouple was passed. The thermocouple reading is accurate to within 0.4C, and was calibrated against the ambient air temperature of the room.

Experiment showed that after the thermocouple makes contact with a solid object it achieves thermal equilibrium. If this were not the case it might be expected that the position of the maximum temperature in the furnace would change noticeably with a change in peak temperature (resulting from the time–delay in temperature measurement). This phenomenon was not observed and thus it is satisfactory to assume that the thermocouple readings taken are accurate.

The preform containing the thermocouple was passed into the furnace and slowly fed along the length of the furnace, which was held at three different temperatures in turn. The preform traversed the furnace at a speed of 5 mm/min and the claimed peak temperature of the furnace was set to 1300C, 1600C and 1760C respectively. The temperature readings of the furnace are correct to within 0.4C and the distance down the furnace may be assumed to be accurate to within 0.05mm. The reason that measurements were taken for temperatures outside the operating regime of fibre drawing (typically 1900–2100C) is that above 1700C the thermocouple first becomes inaccurate and then begins to melt.

When establishing the temperature profile of the furnace, two things are of paramount importance. The first is the shape of the furnace temperature profile and a knowledge of whether or not this shape depends on the peak temperature. The second is the difference between the claimed peak temperature of the furnace and the measured peak temperature. If it is established that the shape of the temperature profile is independent of peak temperature, then the correct temperature profile may be obtained from a knowledge of (a) the shape of the furnace temperature profile and (b) the relationship between peak temperature and the claimed peak temperature.

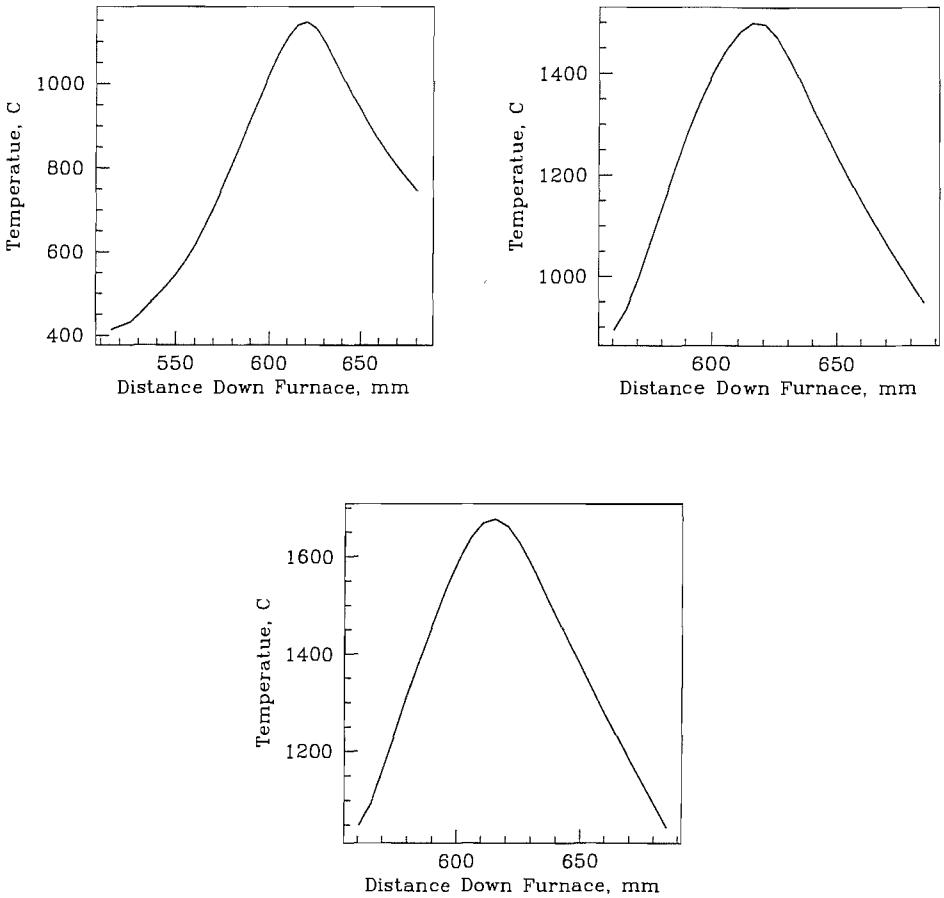

Figure 7.2: Temperature profiles of furnace taken at claimed peak temperature of 1300C, 1600C and 1760C respectively.

The graphs in Figure 7.2 show the data obtained. Temperature profiles of the drawing furnace taken at claimed peak temperatures of 1300C–1760C are displayed. Figure 7.3 shows a plot of the claimed peak temperature vs. the measured peak temperature, demonstrating the relative off-set of the temperature measurements as a function of temperature and also shows this relationship extrapolated to include the temperature range of interest. It is from this graph that the claimed peak temperature is converted into what we regard as a "real temperature" to be used in the numerical simulations of experimental draws. Figure 7.4 shows the superposition of the various temperature profiles taken, both in terms of their actual magnitude and also relative to some fixed maximum, in order to allow easy comparison of their relative shape to be made.

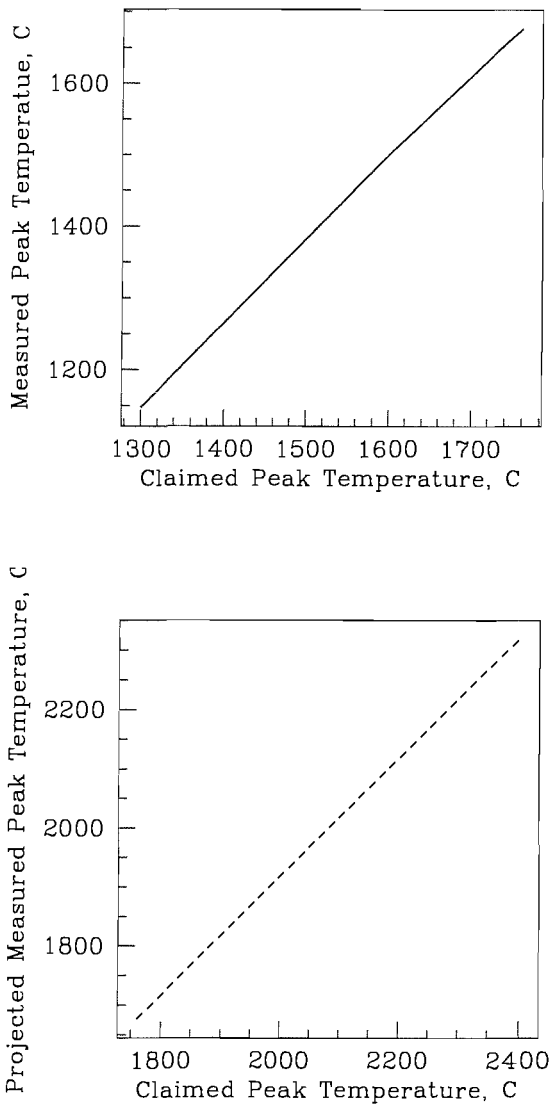

Figure 7.3: A comparison between claimed and measured peak temperatures of the furnace. (Upper diagram: actual values. Lower diagram: projected values.)

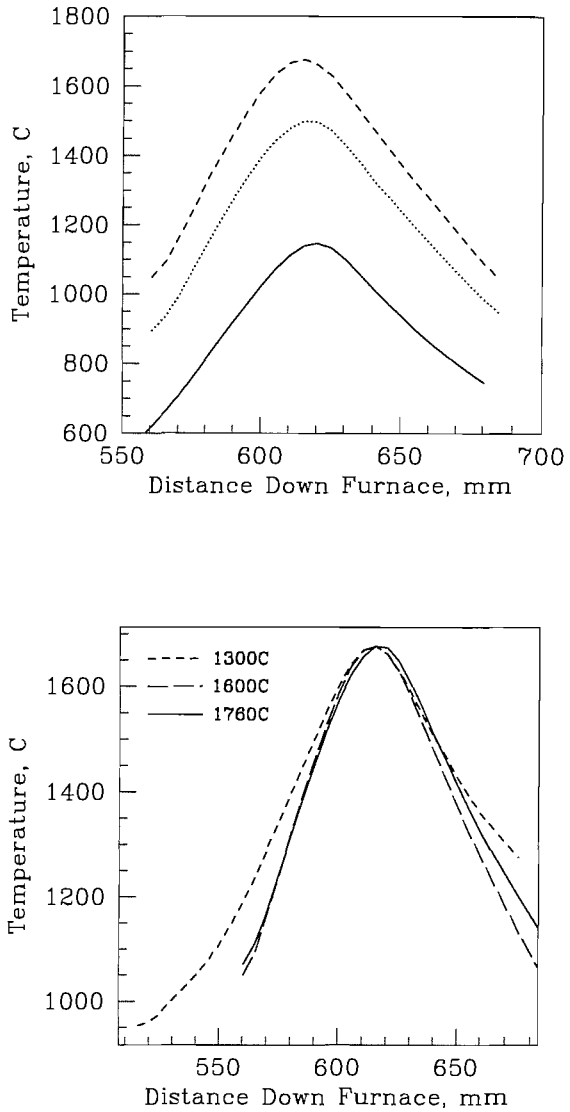

Figure 7.4: Graphs to allow the comparison of all three temperature profiles. (Upper diagram: actual values. Lower diagram: values shifted to allow comparison of shape.)

We observe that the peak temperature of the furnace does not represent the claimed peak temperature, being different by almost 150C in the case of the 1300C measurement. This temperature difference changes according to the magnitude of the peak temperature, and the trend shown has been extrapolated (see lower diagram, Figure 7.3) in order to predict the actual peak temperature from a knowledge of the claimed peak temperature for the temperature range of interest. The exact trend is critical as a result of the exponential temperature dependence of the viscosity. The extrapolation was carried out by assuming that the gradient of the line shown in the upper diagram of Figure 7.3 would continue to change with claimed peak temperature as it had over the three values of peak temperature measured. The implication is that at large enough peak temperatures, the claimed peak temperature will in fact be higher than the measured peak temperature. Whether this is reasonable or not is unclear, though any error is likely to be small over such small temperature ranges as those considered (approximately 200C).

One should not expect the peak temperature measured by the thermocouple to be the same as the temperature of the furnace for several reasons. First, the temperature of the furnace is set by varying the current to the element, which in turn is controlled by the temperature as measured by a pyrometer that reads the temperature of the outside of the element that heats the furnace. As such, the pyrometer might be expected to give a temperature that is greater than the true value of the furnace temperature. This fact was established experimentally for low temperatures.

If the thermocouple is not in thermal equilibrium with its surroundings then it is likely that the position of the maximum temperature will change as the peak temperature of the furnace changes. The fact that this was not seen to be the case suggests that the thermocouple was in constant thermal equilibrium with its surroundings.

We further note that the furnace temperature profile is asymmetric, though the reasons for this are unclear. The gas flows around the furnace might not be symmetrical, or the furnace element may not heat symmetrically, or both. Even though the pre-

form has been in the furnace for a considerable time before these reading are taken, the preform may still not be in thermal equilibrium. This would explain the observed asymmetry.

Since the shape of the furnace temperature profile does not vary greatly with peak temperature (see Figure 7.4), and the two profiles measured at larger temperatures agree well, we will assume this profile to be realistic irrespective of the peak temperature.

In conclusion, we now have a way to derive the peak temperature of the furnace from a knowledge of the claimed peak temperature. We also know that the shape of the furnace temperature profile does not change significantly with temperature, and know its basic form. Thus we know the temperature profile of the furnace at any chosen value of claimed peak temperature, as required. As a final point, we note that the experimental results of fibre pulls obtained below were carried out before the temperature profile of the furnace was measured. In-between these times the element that comprises the furnace was changed. Further experimental tests that compare draw–down dimensions before and after the furnace element replacement confirm that the new element does not significantly alter the results.

7.2 Experimental draws and prediction comparison

We now perform detailed numerical/experimental comparisons for capillary tubes. The predictions are made in the following way: experiments were carried out that considered a variety of drawing scenarios, the main aim being to rotate capillary tubes and compare their final geometries with those predicted by the mathematical model constructed. Predictions were made as to the final fibre geometry of these specific experiments, which in practice was achieved by assuming the aforementioned

viscosity model for Suprasil F300 silica glass. The density of the glass is known to be 2200kg/m^3, the acceleration due to gravity was taken to be 9.81m/s^2, leaving only the surface tension unspecified. To our best estimate the surface tension does not vary significantly with temperature, and is likely to be about 0.3N/m: see [14].

The results were obtained in the following way. The peak temperature was assumed to correspond to the temperature measured at the middle–point of the furnace, i.e. $z = L/2$. Ideally one would include the whole temperature profile of the furnace, with the correct peak temperature, and run the numerical code to obtain the final fibre geometries. However, the temperature in the upper portions of the furnace is below the softening point of the glass (approximately 1600C). Thus in this part of the furnace both fibre radii and downstream velocity are constant and all derivatives are zero. If the whole portion of glass in the furnace were to be modelled, solving the problem by shooting would therefore be extremely problematic. In consequence of this only the portion of the furnace that contains glass above the softening point is included in the numerical model. This is achieved numerically by setting the draw length L to be 2cm (a deliberate underestimate) and then gradually increasing value for L until the resulting fibre geometry remains constant on further change of L. At this point we may assume that the fibre geometry obtained is as accurate.

7.2.1 Results

All of the experimental results shown below were obtained in the Optoelectronics Research Centre. The experiments were conducted by Doctor Walter Belardi and overseen by myself. Some pictorial examples of typical resulting fibres are shown in Figures 7.5 and 7.6.

In the Tables to follow, notation used is defined as:
Pre-ID : Predicted Inner Diameter, μm
Pre-OD : Predicted Outer Diameter, μm

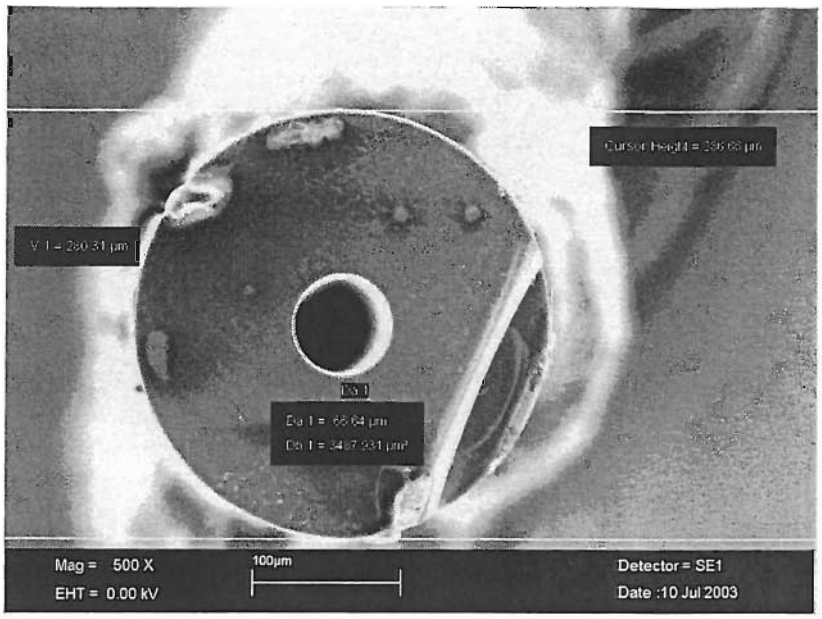

Figure 7.5: A magnified view of the cross–section of one of the fibres drawn without rotation.

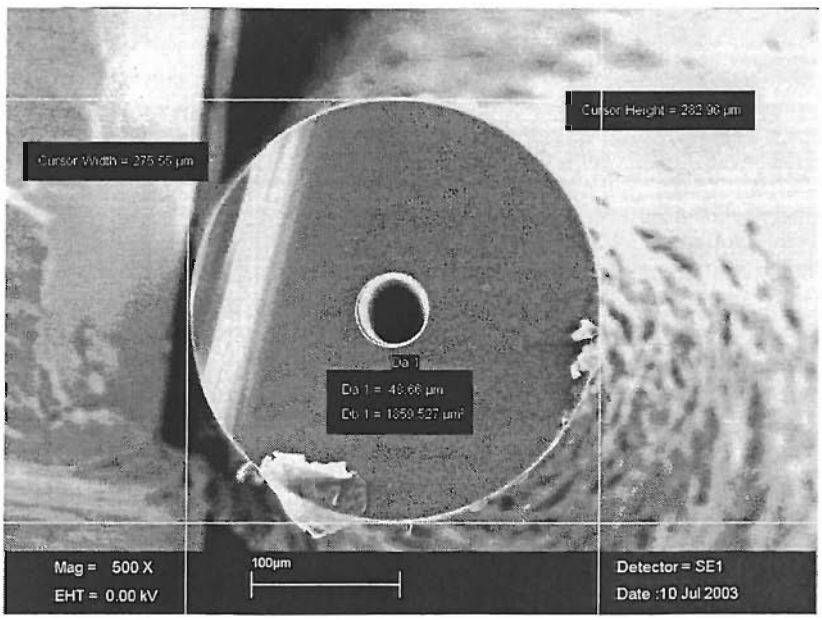

Figure 7.6: A magnified view of the cross–section of one of the fibres drawn whilst being rotated.

Exp-ID : Experimental Inner Diameter, μm

Exp-OD : Experimental Outer Diameter, μm

R : Rotation Rate, rad/s

Pre-d : Predicted spin pitch, cm (pitch of infinity indicates that the preform is not being rotated)

Exp-d : Experimental spin pitch, cm

Pre-AFF : Predicted Air Filling Fraction, defined as Pre-ID/Pre-OD

Exp-AFF : Experimental Air Filling Fraction, defined as Exp-ID/Exp-OD

We commence by drawing a solid fibre. This removes the complicating effects of surface tension, etc., and the dimensions of the resulting fibre are uniquely determined by the preform radius and the feed and draw speeds. This results from mass conservation considerations. Thus an estimate in the uncertainty in these quantities will be obtained by comparing experimental results with model predictions for solid fibre drawing.

Table 7.1 represents the drawing of a solid preform whose initial diameter was 20.6mm. The preform was drawn at a temperature of 2110C, with a feed speed set to 0.53mm/min and a draw speed set to 7.5m/min. The rotation rate was varied to obtain a measurement for d, the pitch, at a variety of rotation rates. Rotating the preform does not affect the geometry of the solid fibre.

The results in Table 7.1 give acceptable agreement between predicted and measured final geometry for all rotation rates. It is observed that the measured dimensions of the fibre are consistently less than those predicted, indicating an error in measurement of either the initial preform geometry, the feed speed or the draw speed. To see how sensitive $h|_{z=L}$ is to errors in the measurement of the various parameters we note that

$$h|_{z=L} = h_0 \exp\left(-\frac{\beta}{2}\right),$$

where

$$\beta = \ln\left(\frac{W_d}{W_f}\right).$$

Thus it is clear that a percentage error of ψ (where a negative ψ indicates an measured value below the actual value) in the measurement of h_0 produces an error of ψ percent in the predicted value of $h|_{z=L}$. A percentage error of ψ in the measurement of W_d gives a percentage error in $h|_{z=L}$ given by

$$10^2 \left(\frac{h(\psi)|_{z=L}}{h|_{z=L}} - 1 \right)$$
$$= 10^2 \left(\exp\left(-\frac{\chi}{2}\right) - 1 \right),$$

where

$$\chi = \ln\left(1 + 10^{-2}\psi\right).$$

Similarly, a percentage error of ψ in the measurement of W_d will give a percentage error of $10^2 \left(\exp\left(-\frac{\chi}{2}\right) - 1\right)$ in the value of $h|_{z=L}$. For the given values of h_0, W_f and W_d, 5% overestimate of h_0, W_f and W_d give errors of $+4\%$, -2.5% and $+2.5\%$ in $h|_{z=L}$ respectively. The possibility of fibre slippage on the drawing wheels suggests that the most likely source of error is in measurement of the drawing speed. To test this hypothesis we ran the experiment again with twice the original drawing speed. It is assumed that if the percentage error in $h|_{z=L}$ remains approximately constant then the error is elsewhere. On the other hand if the percentage error changes with W_d, and if the change is of the same order as the original percentage error, then W_d is assumed to be the likely source of the error.

Table 7.1 shows that as the preforms are rotated, the *measurements* of final geometry are unaltered. This demonstrates that the alignment of the preform in the furnace is acceptable and gives confidence in the experimental measurements of $h_1|_{z=L}$ when capillary tubes are spun at similar rotation rates.

Table 7.2 represents the same fibre being drawn as above under the same conditions except for the draw speed, which has here been increased from 7.5m/min to 15m/min. The percentage error in $h|_{z=L}$ decreased from $\approx 5\%$ to $\approx 2\%$, a change of the order of the original error. It is therefore supposed for the reasons given above, that discrepancies between the predicted and experimental values of $h|_{z=L}$ are attributable to an uncertainty in the experimental value of the draw speed W_d.

Table 7.1: Solid fibre results for $W_d = 7.5$m/min. (Experimental parameters: $h_0 = 1.03 \times 10^{-2}$, $W_f = 8.83 \times 10^{-6}$, $W_d = 1.25 \times 10^{-1}$ and $T = 2100$. Modelling parameters: $h_0 = 1.03 \times 10^{-2}$, $W_f = 8.83 \times 10^{-6}$, $W_d = 1.25 \times 10^{-1}$, $T = 2100$, $\gamma = 3 \times 10^{-1}$, $L = 3 \times 10^{-2}$ and $g = 9.81$.)

Pre-ID	Pre-OD	Exp-ID	Exp-OD	R	Pre-d	Exp-d
N/A	173.2	N/A	165	0	∞	∞
N/A	173.2	N/A	165	150	5	5
N/A	173.2	N/A	165	375	2	2
N/A	173.2	N/A	165	750	1	1

Table 7.2: Solid fibre results for $W_d = 15$m/min. (Experimental parameters: $h_0 = 1.03 \times 10^{-2}$, $W_f = 8.83 \times 10^{-6}$, $W_d = 2.50 \times 10^{-1}$ and $T = 2100$. Modelling parameters: $h_0 = 1.03 \times 10^{-2}$, $W_f = 8.83 \times 10^{-6}$, $W_d = 2.50 \times 10^{-1}$, $T = 2100$, $\gamma = 3 \times 10^{-1}$, $L = 3 \times 10^{-2}$ and $g = 9.81$.)

Pre-ID	Pre-OD	Exp-ID	Exp-OD	R	Pre-d	Exp-d
N/A	122.5	N/A	120	150	10	10
N/A	122.5	N/A	120	375	4	4
N/A	122.5	N/A	120	750	2	2

Table 7.3: Capillary tube results for a claimed peak temperature of $T = 2050$. (Experimental parameters: $h_{10} = 1.425 \times 10^{-3}$, $h_{20} = 4.975 \times 10^{-3}$, $W_f = 8.83 \times 10^{-5}$, $W_d = 1.00 \times 10^{-1}$ and $T = 2050$. Modelling parameters: $h_{10} = 1.425 \times 10^{-3}$, $h_{20} = 4.975 \times 10^{-3}$, $W_f = 8.83 \times 10^{-5}$, $W_d = 1.0 \times 10^{-1}$, $T = 2050$, $\gamma = 3 \times 10^{-1}$, $L = 3 \times 10^{-2}$ and $g = 9.81$.)

Pre-ID	Pre-OD	Exp-ID	Exp-OD	R	Pre-d	Exp-d	Pre-AFF	Exp-AFF
72.2	284.5	76.2	279	0	∞	∞	0.254	0.273
72.7	284.6	76.2	279	200	3	3	0.256	0.273
73.0	284.7	77.2	279	400	1.5	1.5	0.256	0.276
73.5	284.8	76.2	279	600	1	1	0.258	0.273
74.0	285.0	77.2	279	750	0.8	0.8	0.260	0.276
75.1	285.3	77.2	279	1000	0.6	0.6	0.263	0.276
76.5	285.6	77.2	279	1250	0.48	0.5	0.268	0.276
78.7	286.2	77.2	279	1500	0.4	0.4	0.275	0.276

The remainder of the Tables give results for the drawing of a capillary tube whose initial outer diameter was 9.95mm and whose initial inner diameter was 2.85mm. The feed speed is set to a constant 5mm/min and the draw speed is set to a constant 6m/min. The experiments listed in Table 7.3 were conducted at a claimed peak temperature of 2050C.

The results in Table 7.3 show perfect agreement between predicted spin–pitch and experimentally measured values. This is expected since in Chapter 3 it was shown that the spin–pitch depends only on the rotation rate and the draw speed. The agreement between predicted and experimental inner and outer diameters is far be-

Table 7.4: Capillary tube results for a claimed peak temperature of $T = 2100$. (Experimental parameters: $h_{10} = 1.425 \times 10^{-3}$, $h_{20} = 4.975 \times 10^{-3}$, $W_f = 8.83 \times 10^{-5}$, $W_d = 1.00 \times 10^{-1}$ and $T = 2100$. Modelling parameters: $h_{10} = 1.425 \times 10^{-3}$, $h_{20} = 4.975 \times 10^{-3}$, $W_f = 8.83 \times 10^{-5}$, $W_d = 1.0 \times 10^{-1}$, $T = 2100$, $\gamma = 3 \times 10^{-1}$, $L = 3 \times 10^{-2}$ and $g = 9.81$.)

Pre-ID	Pre-OD	Exp-ID	Exp-OD	R	Pre-AFF	Exp-AFF
62.1	282.1	59.8	279	0	0.220	0.214
67.4	283.3	70.95	279	1000	0.238	0.254
70.1	284.0	73.5	279	1200	0.247	0.263
74.2	285.0	76.0	279	1500	0.260	0.272
80.6	286.8	77.2	274	1800	0.281	0.281

yond what was expected, given the relative unknowns in the viscosity law and the temperature profile of the furnace. At low rotation rates the experimental values are consistently below the values predicted. This is consistent with the findings for solid fibres and the percentage differences are also similar. At large rotation rates the predicted values are sometimes smaller than those found experimentally. Given that this occurred when the rotation rate was larger than any rotation rate used in the solid preform experiments, and that the perfectly straight capillary tube preforms are difficult to manufacture, it is suggested that the alignment of the preform in the furnace gave rise to errors in the measurements taken in these cases.

The experiments listed in Table 7.4 were conducted at a claimed peak temperature of 2100C. The experiments listed in Table 7.5 were conducted at a claimed peak temperature of 2150C and those listed in Table 7.6 were conducted at a claimed peak temperature of 2200C.

Table 7.5: Capillary tube results for a claimed peak temperature of $T = 2150$. (Experimental parameters: $h_{10} = 1.425 \times 10^{-3}$, $h_{20} = 4.975 \times 10^{-3}$, $W_f = 8.83 \times 10^{-5}$, $W_d = 1.00 \times 10^{-1}$ and $T = 2150$. Modelling parameters: $h_{10} = 1.425 \times 10^{-3}$, $h_{20} = 4.975 \times 10^{-3}$, $W_f = 8.83 \times 10^{-5}$, $W_d = 1.0 \times 10^{-1}$, $T = 2150$, $\gamma = 3 \times 10^{-1}$, $L = 3 \times 10^{-2}$ and $g = 9.81$.)

Pre-ID	Pre-OD	Exp-ID	Exp-OD	R	Pre-AFF	Exp-AFF
44.5	278.8	57.3	274	0	0.160	0.209
47.1	279.2	64.74	274	400	0.169	0.236
52.5	280.2	74.4	279	800	0.187	0.266

Table 7.6: Capillary tube results for a claimed peak temperature of $T = 2200$. (Experimental parameters: $h_{10} = 1.425 \times 10^{-3}$, $h_{20} = 4.975 \times 10^{-3}$, $W_f = 8.83 \times 10^{-5}$, $W_d = 1.00 \times 10^{-1}$ and $T = 2200$. Modelling parameters: $h_{10} = 1.425 \times 10^{-3}$, $h_{20} = 4.975 \times 10^{-3}$, $W_f = 8.83 \times 10^{-5}$, $W_d = 1.0 \times 10^{-1}$, $T = 2200$, $\gamma = 3 \times 10^{-1}$, $L = 3 \times 10^{-2}$ and $g = 9.81$.)

Pre-ID	Pre-OD	Exp-ID	Exp-OD	R	Pre-AFF	Exp-AFF
14.1	275.6	14.94	263.9	0	0.051	0.056
14.6	275.8	14.94	268.9	200	0.052	0.055
15.1	275.9	14.94	268.9	400	0.055	0.055
16.7	275.7	17.43	268.9	600	0.061	0.064

7.3 Discussion

The results in Tables 7.4–7.6 once again give remarkably good agreement between predicted and experiment data, especially considering the fact that the viscosity law used represents our best estimate of the real viscosity, and the temperature profile and peak temperature were taken from experimental measurements of the furnace at much lower temperatures than those used to draw the fibres. The results in Tables 7.4–7.6 show that the identified trend of overestimating the values of outer fibre diameter and underestimating the inner diameter continues. Additionally, agreement once more becomes less accurate as preforms are spun at large rotation rates. As stated above, this disparity is thought to be a result of uncontrollable oscillations of the preform in the furnace.

7.3.1 The air filling fraction

The capillary tube experiments demonstrate a clear trend for the air filling fraction to increase when preforms are rotated, as shown in Tables 7.3–7.6. The air filling fraction h_1/h_2 is a parameter of crucial importance to experimentalists, and an understanding of how it is affected by preform spinning is desirable.

It is clear to see from the above results that at all temperatures the trend is for the air filling fraction to increase as the amount of rotation increases. Thus rotation may be used to increase the air filling fraction when simultaneously drawing and rotating capillary tubes.

The reason that the air filling fraction increases with increasing rotation rates may be stated as follows. As the preform is rotated the radius of both the inner and outer walls increases. Crucially, the inner wall will always experience a greater deformation than the outer wall as a result of the centrifugal forces (see Chapter 3, §3.6). Numerical calculations show that the difference between the expansion of

the inner and outer walls increases as the rotation rate increases.

It is possible to show that this leads to (a) the air filling fraction with rotation to be larger than the air filling fraction without rotation, and (b) an air filling fraction that increases with increasing B_0. To show this we assume that:

(i) the change in outer radius Δh_2 increases with increasing rotation rate;

(ii) the change in inner radius Δh_1 increases with increasing rotation rate;

(iii) the change in inner radius is greater than the change in outer radius, for any given B_0 (when compared to the case with no rotation);

(iv) the change in inner radius resulting from rotation increases with rotation rate at a rate greater than the rate of increase of the change in outer radius;

(v)

$$h_2 > 0, \;\; h_1 > 0, \;\; \Delta h_2 > 0, \;\; \Delta h_1 > 0 \text{ and } h_2 > h_1. \tag{7.1}$$

Assumptions (i) and (ii) may be expressed as

$$\Delta h_1 = f(B_0) > 0 \;\text{ and }\; \Delta h_2 = g(B_0) > 0 \tag{7.2}$$

respectively, where

$$\frac{\partial f(B_0)}{\partial B_0} \geq 0 \;\text{ and }\; \frac{\partial g(B_0)}{\partial B_0} \geq 0 \;\text{ for }\; B_0 \in [0, \infty]. \tag{7.3}$$

Assumption (iii), $\Delta h_1 > \Delta h_2$, may now be written as

$$f(B_0) - g(B_0) = k(B_0) > 0 \;\text{ for }\; B_0 \in [0, \infty]. \tag{7.4}$$

Assumption (iv) may be written as

$$\frac{\partial(\Delta h_1)}{\partial B_0} > \frac{\partial(\Delta h_2)}{\partial B_0}, \tag{7.5}$$

which, using (7.2), gives

$$\frac{\partial f(B_0)}{\partial B_0} - \frac{\partial g(B_0)}{\partial B_0} = m(B_0) \tag{7.6}$$

where

$$m(B_0) > 0 \text{ for } B_0 \in [0, \infty].$$

Assumptions (iii) and (v) give

$$\frac{h_2 \Delta h_1}{h_1} > \Delta h_2.$$

Adding h_2 to each side and rearranging gives

$$\frac{h_1 + \Delta h_1}{h_2 + \Delta h_2} > \frac{h_1}{h_2}. \tag{7.7}$$

The left hand side of (7.7) is the air filling fraction with rotation and the right hand side is the air filling fraction without rotation, thus proving (a).

In order to prove (b) we set

$$Q = \frac{h_1 + \Delta h_1}{h_2 + \Delta h_2} - \frac{h_1}{h_2}, \tag{7.8}$$

and must show that

$$\frac{\partial Q(B_0)}{\partial B_0} > 0 \text{ for } B_0 \in [0, \infty]. \tag{7.9}$$

We have that

$$\frac{\partial Q(B_0)}{\partial B_0} = \frac{1}{(h_2 + g(B_0))} \left[\frac{\partial f(B_0)}{\partial B_0} - \frac{\partial g(B_0)}{\partial B_0} \frac{(h_1 + f(B_0))}{(h_2 + g(B_0))} \right].$$

Using (7.1) and (7.4) gives

$$\frac{\partial Q(B_0)}{\partial B_0} > 0,$$

as required by (7.9) and thus proving (b).

7.3.1.1 The effects of surface tension on the air filling fraction

Since surface tension acts to decrease both fibre radii, but acts more on the inner radius, one might expect that the effects of surface tension will be to decrease the amount by which the air filling fraction increases as a result of the fibre being rotated.

Whether this effect increases or decreases as the size of B_0 increases depends on the relative difference between two things. On the one hand it will decrease because both fibre radii are increasing in magnitude as B_0 increases making the difference in effect of surface tension on each fibre radius less. On the other, it might be expected to decrease with increased B_0 as the fibre radii become closer in magnitude, decreasing this relative difference. The exact balance achieved quite possibly depends on the drawing conditions, though some law may hold independently of them. No further analysis will be undertaken here.

7.4 Conclusions

Numerical predictions were compared directly with experimental results, having carefully measured unknown quantities in the mathematical model including the temperature of the drawing furnace. Given the uncertainties in some of the parameters, the results compared remarkably well. Of particular interest to experimentalists is the air filling fraction. The effects of preform rotation on the air filling fraction were described and explained.

7.4.1 Practical Results

In this Chapter we:

- estimated the viscosity law for high–purity silica glass (see §7.1.1);
- determined the temperature profile in a drawing furnace and show how it varies with "peak temperature" (see §7.1.2);
- compared numerical predictions for the effects of rotation on solid fibres and capillary tubes with results obtained experimentally (see §7.2.1);

- have shown that preform rotation acts to increase the air–filling fraction for all rotation rates, and that the effect increases with increasing rotation rates (see §7.3.1).

Chapter 8

The "Cup–Handle" Problem

8.1 Introduction

Figure 8.3 shows a particular type of holey fibre made in the Optoelectronics Research Centre, known colloquially as a "cup–handle" fibre. It possesses novel and unique optical properties but various problems can occur during the manufacture of this fibre. In this Chapter the process of manufacture will be examined, and mathematical models constructed in order to address some of the problems that may arise.

Figures 8.1, 8.2, and 8.3 show the transverse cross–section of the preform, the cane, and final fibre respectively. The preform is extruded from a die such as the one shown in figure 8.5, and starts its life having a circular core with three struts attached. As the preform is drawn into a cane, the initially–circular core structure becomes more triangular (see Figure 8.2), though it still has sharp edges where the struts join the core of the cane. As the cane is drawn into fibre form these sharp edges vanish and an approximately triangular core is created, as shown in Figure 8.3.

Experimentalists require a fibre whose surface is smooth on a nanometre scale, and a smoothly–varying geometry is desirable. Furthermore, experimenters would like to

be able to predict and control the geometry of the fibre. Lastly, during the extrusion process (a process of preform manufacture) it is observed that certain undesirable geometrical features occur. If the mechanism that governs the observed behaviour of the cup–handle problem can be understood, then it may be possible whilst drawing the preforms, to remove some of the undesirable structure features (of preforms made with glass extrusion).

The struts (see Figure 8.4) thicken as they reach the core and outer–wall of the preform/fibre, and are found to be most thin at the central point in the strut. This affects the light propagation modes of the fibre and is highly undesirable. Ideally, experimentalists would like to be able to consistently, and with a variety of geometries, produce a final fibre with struts that are uniform along their length, and whose core is more circular than the one pictured.

In order to give some insight into how it may be possible to obtain such a fibre, the way in which the fluid flows in a cross–section of preform must be understood. For example, does the strut thicken at each end because it is somehow draining fluid from what was the core, and from the outer–wall, therein causing the core to become triangular? Is the reverse true, or is there some other mechanism? Is it possible to counteract these effects by altering the initial geometry, or some other property of the flow? If so, one must remember that whilst experimentalists are able to manufacture a wide range of preforms with, for example, more than three struts, optical properties of the fibre dictate that the strut–thickness should be less than 400nm and ideally about 200nm. Additionally, the strut length must be greater than 4μm in the final fibre.

The initial structure of the preform before drawing is shown in Figure 8.1. This preform is then drawn down (a process known as caning), resulting in a structure similar to that shown in Figure 8.2, which we call the cane. The cane is then inserted into a larger circular hollow tube and a vacuum applied to the outside of the cane, resulting in the cane expanding to attach itself to the outside wall of the tube. The

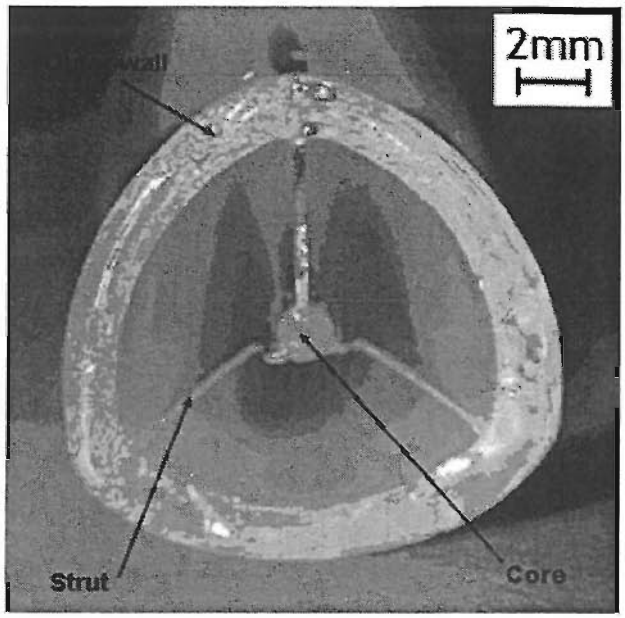

Figure 8.1: The structure of a cup–handle preform.

vacuum is applied as this new structure is being drawn, and once the cane has fused itself to the tube the final fibre is obtained, whose structure is similar to that shown in Figure 8.3.[1] The glass used varies, with some typical examples being those of lead silicate glass and bismuth oxide glass. For more information on fibres of this type see [68].

Figure 8.4 shows a schematic of the problem geometry. The z–axis is the direction in which the fibre is drawn, following the notation used throughout the thesis. The "strut", marked in Figure 8.4 as region 2, is assumed to be straight and have length $2l(z)$. The width of the strut, assumed the same throughout the strut, is $h(z)$. At the very bottom of the picture in Figure 8.4 is the core of the fibre. In between the core and the strut is a curved region, which we will assume has a constant radius of curvature, $a(z)$, and call region 1. This portion of the cross–section joins the core of the fibre to the strut. Similarly, at the extreme top of the picture shown in Figure 8.4 is the outer wall of the fibre. This is the thick portion of glass that surrounds the struts in Figure 8.2, for example. The curved region in between the

[1]Figures 8.1, 8.2 and 8.3 are courtesy of Doctor Heike Ebendorff-Heidepriem of the Centre of Expertise in Photonics, School of Chemistry and Physics, University of Adelaide, Australia.

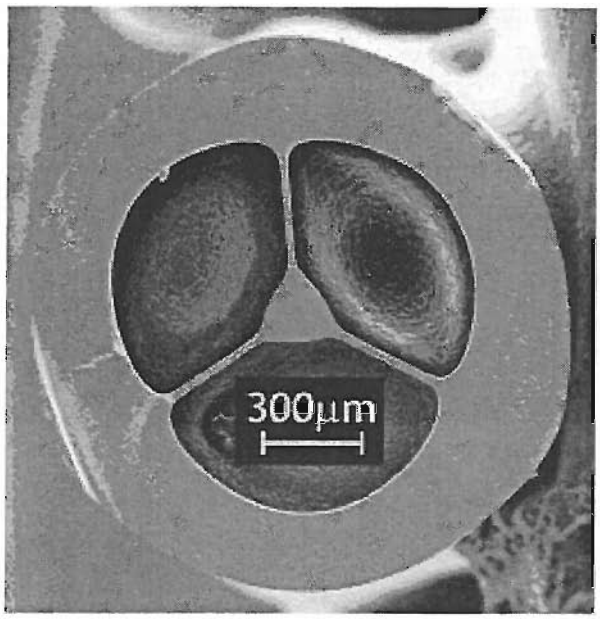

Figure 8.2: The structure of the cane.

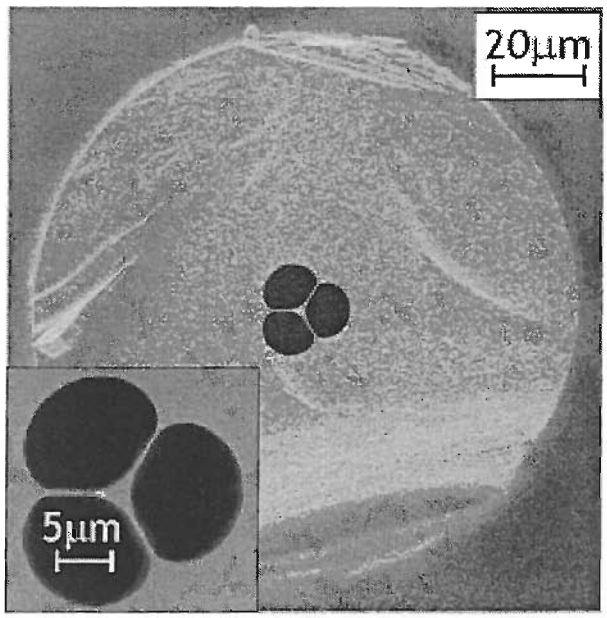

Figure 8.3: The geometry of the resulting fibre.

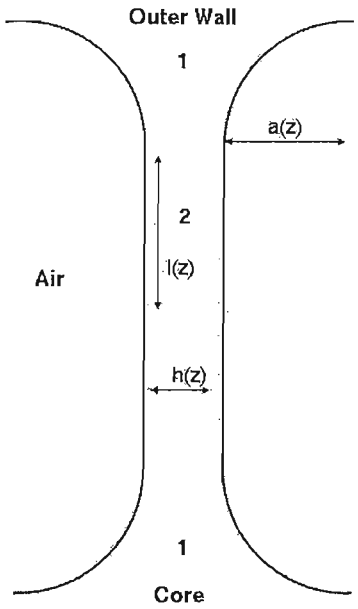

Figure 8.4: Schematic to show the region of interest, where the z axis points into the page. To be compared with Figures 8.1 and 8.2.

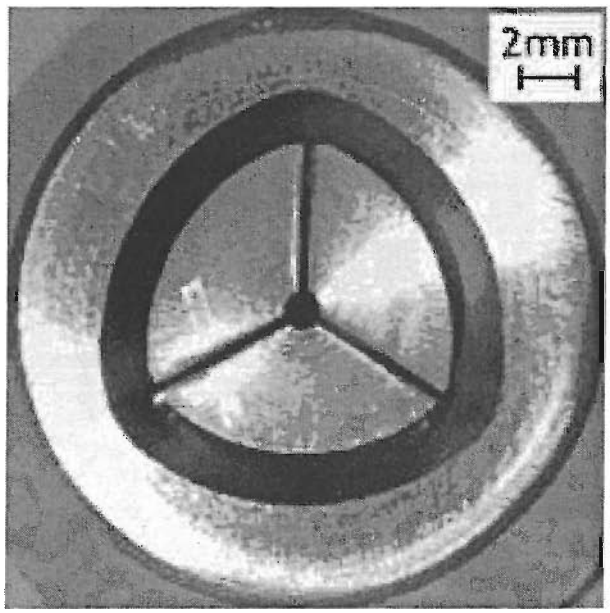

Figure 8.5: A transverse cross–section of the extrusion die.

strut and the outer wall is also assumed to have constant curvature $a(z)$, and thus is also denoted region 1. Thus the area of glass pictured in region 1 of Figure 8.4 has area $2a(z)^2 - \pi a(z)^2/2 + h(z)a(z)$, which we shall approximate by $\lambda a(z)^2$ where $\lambda = 2 - \pi/2$, so long as $h(z) \ll a(z)$.

It is clear that the portions of glass that form the struts joining the edge of the transverse cross–section to its centre thin dramatically during drawing. It is less clear from the Figures that coupled with this is a change in shape of the region that connects the struts to the outer regions, which at one end comprises the outer wall and at the other comprises the core. This will be described in terms of the change in the radius of curvature $1/a$ in the regions 1 (see Figure 8.4), whose curvature is assumed to be the same at each end of the strut, allowing no flow to occur between the core and the outer wall. Later this assumption will be relaxed as we consider asymmetries in the strut. Specifically, a difference in curvature at the two ends of the strut will be considered. To clarify, Figure 8.4 shows the model of a transverse cross–section that will be drawn in the direction of the perpendicular to the plane of the transverse cross–section (the z–axis).

8.2 The draining of the thin film of region 2

It is observed experimentally that as the preform is drawn into a fibre, region 2 becomes both thinner and shorter (relative to the geometry–preserving shrinkage of the outer wall) and region 1 becomes larger (the radius a increases, relative to the geometry preserving solution).

In order to try to predict the effects observed, the motion of the fluid in the part of the cross-section shown in Figure 8.4 will be considered. It is assumed that the outer wall of the preform is so thick in comparison with any section of glass within that its bending moment (related to the glass viscosity) is large enough not to be influenced by the evolution of glass within. A consequence of this is that this model

may only truly hold for the second stage of the drawing process, when the walls of the tube being drawn are relatively thick.

We further assume that the downstream fluid velocity is of the usual geometry-preserving form given by

$$\bar{w} = \bar{W}_f e^{\beta \bar{z}} \tag{8.1}$$

as in previous Chapters, where $\bar{z}$ has been non–dimensionalized with $z = L\bar{z}$ and overbars that denote non–dimensional quantities are henceforth dropped. Since the effects of surface tension and hole overpressure serve only to modify this solution slightly, this assumption for the form of w is probably justified. It is also assumed that the draw is geometry–preserving, as mentioned above. This means that whilst the radii may decrease as the fibre is drawn, the *shape* is unaltered (see Chapter 3 for a discussion of this). If surface tension was included in the model, the effects can be separated into two parts. First, the inner and the outer wall of the fibre will be affected by the surface tension that acts on the inner and outer surface of the wall. Secondly, the effects of surface tension acting on the struts of the preform will have an additional effect on the outer wall, "pulling" it in at the point that struts join the outer wall. This last effect is demonstrated by observing the change in geometry that takes place in drawing the preform shown in Figure 8.1 to produce that shown in Figure 8.2.

The consequence of ignoring the effects of surface tension is to produce a geometry preserving solution for the downstream fluid velocity w and fibre radius. Since a strut has a length equivalent to the inner radius, this strut length must also obey a geometry preserving solution. Thus it follows that

$$(l^2 w)_z = 0, \tag{8.2}$$

from which we deduce that

$$l = l_0 e^{-\frac{\beta z}{2}}, \tag{8.3}$$

where l_0 is approximately half the height of region 2 (thus ignoring the height of region 1 in Figure 8.4), which is a valid approximation so long as $a \ll l$.

It is worth noting that the assumptions of geometry–preserving solutions for w and l are not necessary for the modelling of this problem. Indeed, one could treat the outer wall structure as a capillary tube with surface tension acting, evolve the structure numerically to determine the manner in which its geometry and downstream fluid velocity change, and use these results in place of the geometry–preserving solutions assumed herein. The assumptions made mean that the model will only be valid when describing the second stage of fibre production in which the (circular) cane has already been formed from the preform and is drawn into final fibre. The previous stage of manufacture might be more accurately modelled by taking account of the effects of surface tension in the strut on the triangular outer–wall, since it seems likely that these forces are responsible for the macroscopic change of shape as the preform is drawn to a cane.

Fluid is permitted to flow between the regions 1 and 2, but not between regions 1 and the outer wall of the fibre. This seems reasonable because of viscous effects in the outer wall. We therefore construct two mass conservation equations governing the flow of fluid in region 1 and the flow in region 2 (see Figure 8.4). Since there is no net mass loss from the sum of these regions as the fibre is drawn along the z–axis, we know that the flux q from region 2 is the negative of the flux from region 1.

Mass conservation considerations therefore require that

$$(whl)_z = -q \tag{8.4}$$

and

$$(\lambda w a^2)_z = q, \tag{8.5}$$

where q is the mass flux leaving region 2 and entering region 1. To recap, the geometry of the strut is determined by the four variables w, l, h and a. w and l are known, and h and a may be determined by equations (8.4)–(8.5) above. However, in order to fully solve the problem, the variable q, which characterizes the flux mass between regions 1 and 2, must be determined.

The variable q was determined by Howell in [16] with reference to the drainage of a

two–dimensional bubble.[2] The interested reader is referred to [16] for further detail and a derivation of the expression for q. It transpires that we may describe the flow between regions 1 and 2 with q given by

$$q = \frac{8\gamma}{3\mu}\sqrt{\frac{h^3}{(l+a)a}}. \tag{8.6}$$

It is worth noting that this analysis will only hold so long as $a \ll l$. If it is not then the above analysis fails both because we may no longer make use of the thin film drainage parameter q and because it becomes unrealistic to approximate the area of region 1 by λa^2.

We now reduce the problem to a single equation in the unknown $a(z)$. Adding (8.4) and (8.5) we have

$$w(hl + \lambda a^2) = Q, \tag{8.7}$$

where Q is a constant of integration. Thus h may be written as

$$h = \frac{1}{l}\left(\frac{Q}{w} - \lambda a^2\right). \tag{8.8}$$

The constant Q is evaluated by applying the boundary conditions at $z = 0$, requiring $a = A$, $h = h_0$, $l = l_0$ and $w = W_f$. This gives

$$Q = W_f(h_0 l_0 + \lambda A^2). \tag{8.9}$$

Substituting (8.8) into expression (8.6) for q, and both of these into (8.5) gives

$$(\lambda w a^2)_z = \frac{C}{l\sqrt{la(l+a)}}\left(\frac{Q}{w} - \lambda a^2\right)^{3/2}, \tag{8.10}$$

which, making use of the fact that $a \ll l$, becomes

$$(\lambda w a^2)_z = \frac{C}{l^2\sqrt{a}}\left(\frac{Q}{w} - \lambda a^2\right)^{3/2}, \tag{8.11}$$

where here and henceforth

$$C = \frac{8\gamma}{3\mu}. \tag{8.12}$$

[2]Thanks are due to Doctor Peter D. Howell of the University of Oxford for suggesting this approach to the problem.

Equation (8.11) may be rewritten by making use of the form of w and l to give

$$(\lambda e^{\beta z} a^2)_z = \frac{D}{e^{-\beta z}\sqrt{a}} \left(\frac{(h_0 l_0 + \lambda A^2)}{e^{\beta z}} - \lambda a^2 \right)^{3/2}, \tag{8.13}$$

where $D = C/l_0^2$ and the explicit shape–preserving solutions for w and l given by (8.1)–(8.3) have been used. At this point other forms of w and l could be imposed, so as to allow for the effects of surface tension on the overall structure to be modelled. The complete problem to determine the evolution of the fibre therefore consists of solving (8.13) subject to $a(0) = A$.

From this result the functional dependence of a on z may in principle be derived. Experiments carried out at the Optoelectronics Research Centre show that $a|_{z=L} > A$. Physically this corresponds to the fact that the region 2 will shrink due to the standard drawing process (which results in the geometry–preserving solutions normally found in the absence of surface tension), but will thin further because of the drainage effect brought about by the introduction of regions 1, increasing the value of a from its initial value, A.

We will later go on to solve the equations that govern the behaviour of $a(z)$ numerically, but we first use equations (8.11) and (8.13) to determine some properties of the behaviour of $a(z)$.

8.2.1 Model analysis

First we note that a must not be zero, preventing a singularity from developing in the curvature. If a is zero then the analysis undertaken above fails for two reasons. First, the area of region 1 may not be approximated by λa^2. Secondly, the drainage parameter q develops a singularity.

The maximum value of a can be determined by considering the right hand side of

equation (8.13), which must be positive for all z, showing that

$$a \leq \frac{\sqrt{(h_0 l_0 + \lambda A^2)}}{\sqrt{\lambda} e^{\frac{\beta z}{2}}}. \tag{8.14}$$

Physically this results from equation (8.8), where a takes its maximum value by draining all fluid from the strut giving $h = 0$. The maximum value for a, clearly increases with increasing h_0, A_0 and l_0. This is because h_0 or l_0 increasing means an increased area of fluid in the strut to be drained into region 1, resulting in a larger value for $a|_{z=L}$. Similarly, as the value of a at $z = 0$ increases, the value of a at all further points will be increased with the addition of further fluid from region 2.

Whilst a must not be zero, it can approach zero. To determine the behaviour close to zero we may rewrite (8.13) as

$$\lambda a^{3/2} e^{2\beta z}(\beta a + 2a_z) = D\left(\frac{h_0 l_0 + \lambda A^2}{e^{\beta z}} - \lambda a^2\right)^{3/2}. \tag{8.15}$$

As $a \longrightarrow 0$ the right hand side of (8.15) remains finite and

$$\lambda a^{3/2} a_z \approx \frac{D}{2}\left(\frac{h_0 l_0 + \lambda A^2}{e^{\beta z}}\right)^{3/2}, \tag{8.16}$$

where $D = C/l_0^2$. This can be solved to give

$$a = \frac{1}{\lambda}\left(\frac{5D}{4}\left(\frac{h_0 l_0 + \lambda A^2}{e^{\beta z}}\right)^{3/2} z + E\right)^{2/5}, \tag{8.17}$$

where E is an arbitrary constant of integration. Setting $a(0) = 0$ gives

$$a = \frac{1}{\lambda}\left(\frac{5D}{4}\right)^{2/5}\left(\frac{h_0 l_0 + \lambda A^2}{e^{\beta z}}\right)^{3/5} z^{2/5}, \tag{8.18}$$

which shows that even if $a \longrightarrow 0$ for some z, it then rapidly increases with z. Physically this is because the curvature becomes large when a is small, resulting in a large drainage parameter q. The mass flux between the two regions and hence the rate of increase of the area a^2 is therefore large.

We have now stated that physically a must always be non–zero, and that if it is close to zero it rapidly increases with z. Does this means that a must always increase? To

answer this we return to equation (8.15). Since the right–hand side is everywhere positive we require

$$\beta a + 2a_z \geq 0, \tag{8.19}$$

where the equality holds for $D = 0$; for example when $\gamma = 0$ giving

$$a_z \geq -\frac{\beta a}{2}. \tag{8.20}$$

Equation (8.19) shows that a_z may be both positive and negative. Furthermore, differentiating (8.15) shows that a turning point in a exists if

$$D\left(\frac{h_0 l_0 + \lambda A^2}{e^{\beta z}} - \lambda a^2\right)^{3/2} = \lambda\beta a^{3/2} e^{2\beta z}, \tag{8.21}$$

which is clearly allowed. As an example, if $a_z = 0$ at $z = 0$ we must have that $\lambda\beta A^{3/2} = D(h_0 l_0)^{3/2}$.

8.2.2 Solutions to the equations

We have reduced the problem to one of determining a, through which h may be determined from (8.8). Though equation (8.10) cannot be solved directly, by setting $a = \phi(z)/\sqrt{w}$, (8.10) may be rewritten as

$$(\lambda\phi^2)_z = \frac{C}{l w^{5/4}\sqrt{l\phi(l+\phi)}}(Q - \lambda\phi^2)^{3/2}, \tag{8.22}$$

which is a separable equation from which a and thence h may be determined, fixing the geometry of the final fibre. Though the known z dependence of w will be used explicitly it should be remembered that any w may be substituted at this point, perhaps taking account of surface tension effects in order to improve the accuracy of this calculation.

Equation (8.22), with w given by (8.1), may be solved in closed form and its solution given in terms of elliptic integrals as

$$200 W_f^{5/4}\beta\lambda \exp\left(\frac{\beta z}{4}\right)\left(U\sqrt{\phi(0)}\,\phi - V\phi(0)\sqrt{\phi}\right) + 4CUV\lambda\sqrt{(\phi(0)\,\phi)}$$

$$\left(1-\exp\left(\frac{\beta z}{4}\right)\right)+100\sqrt{2\lambda}W_f^{5/4}\beta\exp\left(\frac{\beta z}{4}\right)\left(V\sqrt{\lambda\phi(0)^2-Q}\sqrt{\phi}\right.$$
$$\int_0^{\sqrt{\frac{\lambda\phi(0)-\sqrt{Q\lambda}}{\sqrt{Q\lambda}}}}\frac{1}{\sqrt{1-t^2}\sqrt{1-t^2/2}}\,dt-U\sqrt{\phi(0)}\sqrt{\lambda\phi^2-Q}$$
$$\left.\int_0^{\sqrt{\frac{\lambda\phi-\sqrt{Q\lambda}}{\sqrt{Q\lambda}}}}\frac{1}{\sqrt{1-t^2}\sqrt{1-t^2/2}}\,dt\right)\Big/\left(100UVW_f\beta\lambda\sqrt{\phi(0)}\,\phi\exp\left(\frac{\beta z}{4}\right)\right)=0, \quad (8.23)$$

where

$$U=\sqrt{Q-\lambda\phi(0)^2},\ \ V=\sqrt{Q-\lambda\phi^2},$$

and

$$\phi(0)=A\sqrt{W_f},\ \ \phi=a\sqrt{w}.$$

Whilst no useful closed form solution exists for a, equation (8.11) may be solved numerically but is found to be stiff. Thus we set $a=\tilde{a}(z)Ae^{-\beta z/2}$ and write $w=W_fe^{\beta z}$, $l=l_0e^{-\beta z/2}$. Equation (8.11) can then be written as

$$(\lambda\tilde{a}^2)_z=\frac{Ce^{-\beta z/4}}{l_0\sqrt{\tilde{a}Al_0(\tilde{a}A+l_0)}}\left(\frac{Q}{W_f}-\lambda\tilde{a}^2A^2\right)^{3/2}. \quad (8.24)$$

Setting

$$C=e^{\beta/4}\widetilde{C}$$

gives

$$(\lambda\tilde{a}^2)_z=\frac{\widetilde{C}e^{-\beta(z-1)/4}}{l_0W_fA^2\sqrt{\tilde{a}Al_0(\tilde{a}A+l_0)}}\left(h_0l_0+\lambda A^2(1-\tilde{a}^2)\right)^{3/2}, \quad (8.25)$$

which is numerically more simple to handle. Numerical calculations show that the solution for $\tilde{a}$ tends to a constant value along the majority of the draw length z if the strut is completely drained of its fluid. This means that the strut is being drawn in the geometry preserving way from the point along z at which h first becomes $h=0$.

If the drainage initially occurs more slowly (further along the draw length z), the rate at which drainage occurs is significantly reduced since the drainage parameter q scales with $h^{3/2}$, with h having its dimensions reduced further as a natural result of the usual draw–down process.

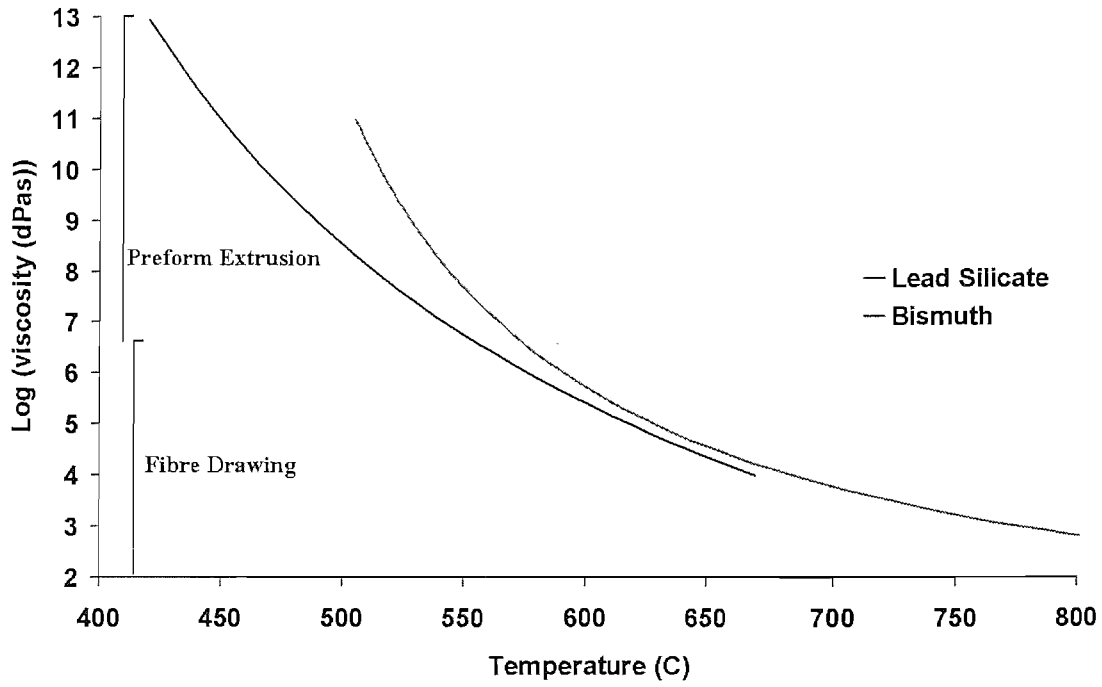

Figure 8.6: Graph to show viscosity curve of soft glasses used to manufacture this type of fibre. Data obtained by the Optoelectronics Research Centre, where the units dPa.s are deci–Pascal seconds.

8.2.3 Numerical examples

In this section we investigate the behaviour of the system by solving the governing equations numerically. This is accomplished by solving (8.25) to obtain a, and then using (8.8) to obtain h. Changes will be made in parameter values such as surface tension and the results compared to a control example. The parameters used in example numerical–tests are listed in Table 8.1, for which a of the control example is shown in Figure 8.7. All values are chosen to be able to demonstrate the necessary results clearly whilst being close to those that might be used experimentally. All values are given in SI units, and the values of glass viscosity assume that bismuth oxide glass is used, whose viscosity varies with temperature as shown in Figure 8.6.

Without the effects of surface tension a should take the form $a = e^{-\frac{\beta z}{2}}$ (i.e. de-

Table 8.1: Table to show parameters used in numerical examples.

Case	A	l_0	h_0	W_f	W_d
1	1.0×10^{-6}	2.0×10^{-2}	1.0×10^{-3}	2.5×10^{-5}	1.0×10^{-1}
2	1.0×10^{-6}	2.0×10^{-2}	1.0×10^{-3}	2.5×10^{-5}	1.0×10^{-1}
3	1.0×10^{-6}	2.0×10^{-2}	1.0×10^{-3}	2.5×10^{-5}	1.0×10^{-1}
4	1.0×10^{-6}	2.0×10^{-2}	1.0×10^{-3}	2.5×10^{-5}	1.0×10^{-1}
5	1.0×10^{-6}	2.0×10^{-2}	1.0×10^{-3}	2.5×10^{-5}	1.0×10^{-1}
6	1.0×10^{-3}	2.0×10^{-2}	1.0×10^{-3}	2.5×10^{-5}	1.0×10^{-1}

Case	γ	μ	Figure
1	3.0×10^{-1}	4.0×10^{4}	8.7
2	0.0	4.0×10^{4}	8.8
3	1.0×10^{1}	4.0×10^{4}	8.9
4	3.0×10^{-1}	4.0×10^{2}	8.11
5	3.0×10^{-1}	4.0×10^{6}	8.12
6	3.0×10^{-1}	4.0×10^{4}	8.13

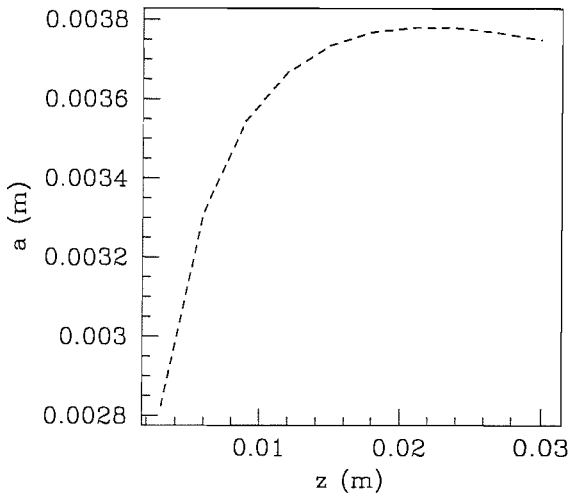

Figure 8.7: Graph to show a plotted as a function of z: control example. (Case 1: $A = 1.0 \times 10^{-6}$, $l_0 = 2.0 \times 10^{-2}$, $h_0 = 1.0 \times 10^{-3}$, $W_f = 2.5 \times 10^{-5}$, $W_d = 1.0 \times 10^{-1}$, $\gamma = 3.0 \times 10^{-1}$, $\mu = 4.0 \times 10^{4}$.)

crease in the usual geometry–preserving way). Therefore, any results for a should be compared with this standard result. The fact that Figure 8.7 (Case 1, Table 8.1) shows an increase in a and then a gradual decrease as z increases is expected, as the drainage effect is such as to increase a. However, as a is increased the drainage effect is reduced because the drainage parameter q decreases. Furthermore, the fibre has its dimensions drawn–down in the usual way as a result of the drawing process. These two effects compete at all times, balancing surface tension with viscosity. It is this competition that allows both a positive and negative gradient in a and therefore a turning point as shown earlier, the sign depending at all points along the draw length on the relative strength of the two effects.

The removal of surface tension, analogous to setting $D = 0$ in (8.15), should therefore produce an exponential decrease in a along the length of the draw furnace, L. This solution is plotted in Figure 8.8 (Case 2, Table 8.1).

Since surface tension is responsible for deviations from geometry–preserving solutions

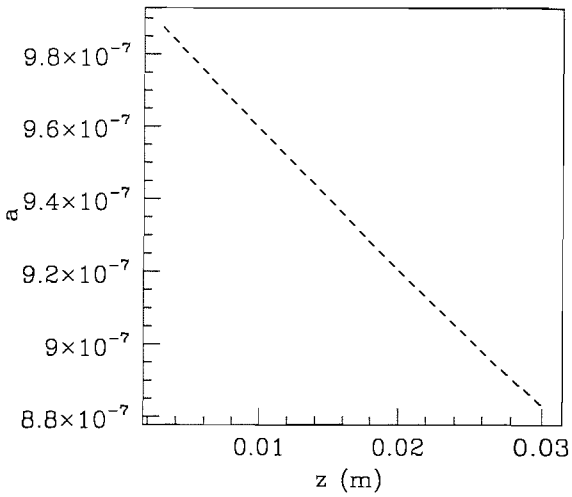

Figure 8.8: Graph to show a plotted as a function of z with the removal of surface tension. (Case 2: $A = 1.0 \times 10^{-6}$, $l_0 = 2.0 \times 10^{-2}$, $h_0 = 1.0 \times 10^{-3}$, $W_f = 2.5 \times 10^{-5}$, $W_d = 1.0 \times 10^{-1}$, $\gamma = 0.0$, $\mu = 4.0 \times 10^4$.)

in a, the effects of surface tension should in some way be related to the size of a, and it is expected that increasing the coefficient of surface tension will increase the value to which a increases before turning. Furthermore, this is expected to occur for smaller values of z as γ increases. These effects are shown in Figure 8.9 (Case 3, Table 8.1). Figure 8.10 is a schematic diagram that shows how the shape of the strut changes with z.

Viscosity acts to counter the effects of surface tension, so a decrease in the viscosity should give qualitatively similar results as those obtained by increasing the surface tension coefficient (compare Figure 8.9 with increased surface tension (Case 3, Table 8.1) and Figure 8.11 with reduced viscosity (Case 4, Table 8.1)). A large viscosity should give results similar to those obtained with no surface tension (compare Figure 8.8 (Case 2, Table 8.1) and Figure 8.12 (Case 5, Table 8.1)). The agreement between Figures 8.9 and 8.11 is good, whereas the agreement between Figures 8.8 and 8.12 is not. Since viscosity and surface tension only enter the problem through a single parameter C given by (8.12), this demonstrates the sensitivity of the drainage effect

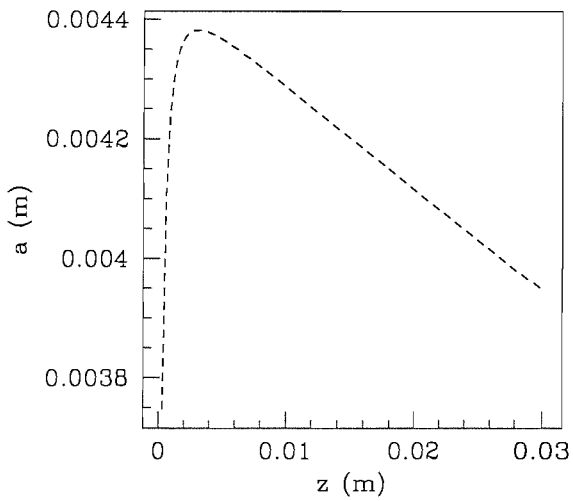

Figure 8.9: Graph to show a plotted as a function of z with an increased surface tension. (Case 3: $A = 1.0 \times 10^{-6}$, $l_0 = 2.0 \times 10^{-2}$, $h_0 = 1.0 \times 10^{-3}$, $W_f = 2.5 \times 10^{-5}$, $W_d = 1.0 \times 10^{-1}$, $\gamma = 1.0 \times 10^{1}$, $\mu = 4.0 \times 10^{4}$.)

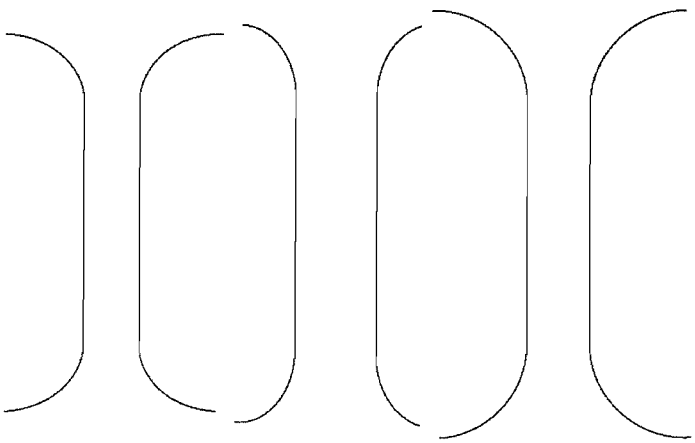

Figure 8.10: A schematic diagram showing how the shape of the strut changes with z. The leftmost diagram shows the strut near $z = 0$, the central diagram shows the strut close to $z = 0.1$ and the rightmost diagram shows the strut close to $z = L$.

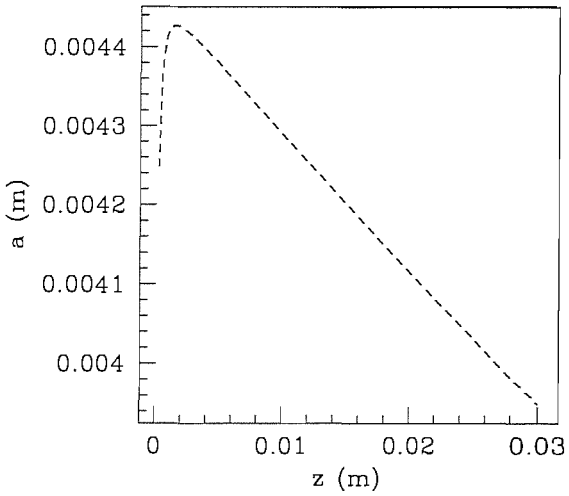

Figure 8.11: Graph to show a plotted as a function of z with decreased viscosity. (Case 4: $A = 1.0 \times 10^{-6}$, $l_0 = 2.0 \times 10^{-2}$, $h_0 = 1.0 \times 10^{-3}$, $W_f = 2.5 \times 10^{-5}$, $W_d = 1.0 \times 10^{-1}$, $\gamma = 3.0 \times 10^{-1}$, $\mu = 4.0 \times 10^{2}$.)

on the presence of surface tension of any strength. This is to be anticipated however as the radius of curvature a is extremely small, giving prominence to the effects of surface tension.

Given this result we should expect an increase in the initial radius of curvature A to cause the system to react more strongly than it would to an increase in viscosity or a decrease in surface tension. When A is increased by a factor of 10^3 the results shown in Figure 8.13 are obtained (Case 6, Table 8.1). As required, the system appears more sensitive to changes in initial geometry than to changes in viscosity or surface tension. It should be noted that in the last example, A was increased so as to be larger than the value of l_0, which makes the analysis unphysical. However, this was done in order to demonstrate clearly the effect of increasing A, and because the system behaves in a qualitatively similar manner whether A is within its allowed range or not, the choice of example parameters is valid.

In the preceding sections we have discussed the drainage mechanism in terms of its

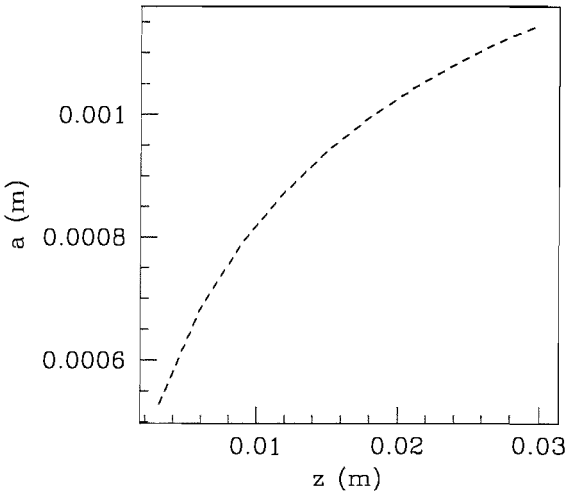

Figure 8.12: Graph to show a plotted as a function of z with increased viscosity. (Case 5: $A = 1.0 \times 10^{-6}$, $l_0 = 2.0 \times 10^{-2}$, $h_0 = 1.0 \times 10^{-3}$, $W_f = 2.5 \times 10^{-5}$, $W_d = 1.0 \times 10^{-1}$, $\gamma = 3.0 \times 10^{-1}$, $\mu = 4.0 \times 10^{6}$.)

resultant effect on a, but must remember that this change in a is coupled directly with a change in h, the two of which determine the structure of the final fibre produced (at $z = 1$).

8.3 Asymmetries in the geometry

To explore how sensitive the final geometry is to changes in the initial radius of curvature, A, the case where the initial curvature is different in the two regions marked 1 in Figure 8.4 is considered. Thus far the analysis has considered only one end of the strut, implicitly assuming that the half–way point between the two ends is essentially a fixed boundary.

An equation to describe the flow between the other end of the strut and region 2 must be derived in terms of a new drainage parameter that depends on the additional radius of curvature present in the problem. l is now assumed to cover the whole length

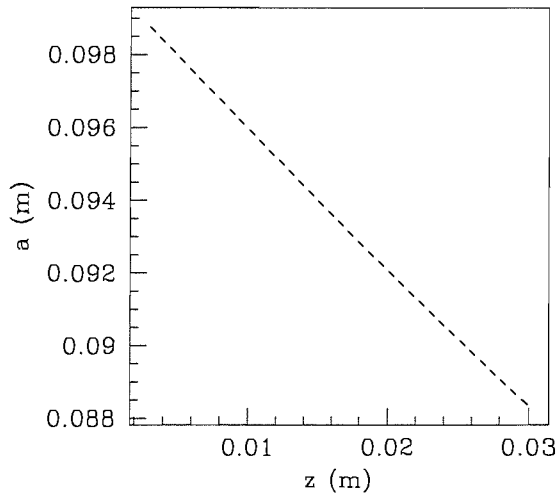

Figure 8.13: Graph to show a plotted as a function of z with increased initial radius of curvature, A. (Case 6: $A = 1.0 \times 10^{-3}$, $l_0 = 2.0 \times 10^{-2}$, $h_0 = 1.0 \times 10^{-3}$, $W_f = 2.5 \times 10^{-5}$, $W_d = 1.0 \times 10^{-1}$, $\gamma = 3.0 \times 10^{-1}$, $\mu = 4.0 \times 10^{4}$.)

of the strut as depicted in Figure 8.4 and the flow equations are modified to allow for the asymmetry by setting from region 2 so as to allow for this additional drainage. Thus we have

$$(w\lambda a^2)_z = q_1, \tag{8.26}$$

$$(w\lambda b^2)_z = q_2, \tag{8.27}$$

and

$$(whl)_z = -(q_1 + q_2) \tag{8.28}$$

where

$$q_1 = \frac{8\gamma}{3\mu}\sqrt{\frac{h^3}{(l+a)a}} \tag{8.29}$$

is the drainage parameter at one end of the strut and

$$q_2 = \frac{8\gamma}{3\mu}\sqrt{\frac{h^3}{(l+b)b}} \tag{8.30}$$

is the drainage parameter at the other end. b is the radius of curvature at the new end, whose value at $z = 0$ is $b = B$.

Adding (8.26), (8.27) and (8.28) gives

$$w\left(hl + \lambda(a^2 + b^2)\right) = Q. \tag{8.31}$$

Using the boundary conditions at $z = 0$ in (8.31) gives

$$Q = W_f\left(h_0 l_0 + \lambda(A^2 + B^2)\right).$$

As a simple check of the model, setting $A = B$ should return the same result as the one–ended strut model. To see this it must be realized that the value of l in the one–ended–strut model is half the value of l in the two–ended–strut model, giving the same value of h in both problems. Additionally, Q and $\lambda(A^2 + B^2)$ are also now twice their original values.

The two models will not produce *identical* results simply by setting $A = B$, as the drainage parameter also depends explicitly on l, which has now been doubled. Strictly speaking the value of l in the drainage parameter of the one–strut model should be set to $2l$ despite the fact that we are only modelling one end but the effect of not doing this is minimal.

Rearranging (8.31) for h gives

$$h = \frac{1}{l}\left(\frac{Q}{w} - \lambda(a^2 + b^2)\right), \tag{8.32}$$

which may be substituted into (8.26) and (8.27) giving two equations in a and b that must once again be solve numerically, from which the parameter of most interest, h, may be found.

The system behaves identically to the one–strut model as discussed in §8.2.1. A closed-form solution to this system of equations was not found though some numerical solutions are shown below to demonstrate the system's behaviour.

Table 8.2: Table to show parameters used in numerical examples.

Case	A	B	l_0	h_0	W_f
7	1.0×10^{-6}	1.0×10^{-5}	2.0×10^{-2}	1.0×10^{-3}	2.5×10^{-5}
8	1.0×10^{-6}	1.0×10^{-3}	2.0×10^{-2}	1.0×10^{-3}	2.5×10^{-5}
9	1.0×10^{-6}	1.0×10^{-3}	2.0×10^{-2}	1.0×10^{-3}	2.5×10^{-5}

Case	W_d	γ	μ	Figures
7	1.0×10^{-1}	3.0×10^{-1}	4.0×10^{4}	8.14, 8.15
8	1.0×10^{-1}	1.0×10^{-1}	4.0×10^{4}	8.16, 8.17
9	1.0×10^{-1}	1.0×10^{1}	4.0×10^{4}	8.18, 8.19

8.3.1 Numerical examples

Following the same procedure as for the one–strut model, a number of examples showing the difference between the a and b along the length of the draw are given. This illustrates how differences in A and B affect the final geometry.

The numerical values chosen for the parameters involved are shown in Table 8.2, and all values are given in S.I. units.

Figures 8.14 and 8.15 (Case 7, Table 8.2) show the results for both a and b respectively, where the difference in A and B was one order of magnitude. It is clear there is little effect on the geometry at any point along the z–axis. Even at high mag-

nification it is clear to see that the two radii of curvature have almost completely converged. This behaviour may be understood by noting that the drainage parameter is inversely proportional to the radius of curvature. Thus the two radii of curvature will always try to equalize.

In order to determine how far along z the two radii of curvature become equal, B is taken to be three orders of magnitude smaller than A, and the results plotted for a and b in Figures 8.16 and 8.17 respectively (Case 8, Table 8.2). The greater initial difference in A clearly show the curvatures equalizing as z increases.

To increase the disparity between the two drainage parameters the coefficient of surface tension is increased. This has the effect of equalizing a and b for smaller z than in the previous example. The same three orders of magnitude difference in A and B are retained to allow a direct comparison, and the results are shown in Figures 8.18 and 8.19 (Case 9, Table 8.2).

In conclusion, we expect that any differences that arise in the curvatures of the two ends of the strut have an insignificant impact on the final geometry of the fibre cross–section.

8.3.2 A constant curvature?

Thus far we have implicitly assumed that the initial curvature of regions 1 is constant throughout the region, which may or may not be the case depending on the initial geometry imposed by the experimenter. Regions 1 could be subdivided and a separate curvature attached to each subdivision. The flow between these two divisions could be modelled to determine what happens if there are differences in curvature within a region. However, any initial variation in the curvature in regions 1 will almost immediately reduce to zero as a result of the effects of surface tension. How rapidly this occurs and the value of curvature that results is not of interest though, so long as it occurs when $z \ll 1$. The examples above demonstrated that all differences in

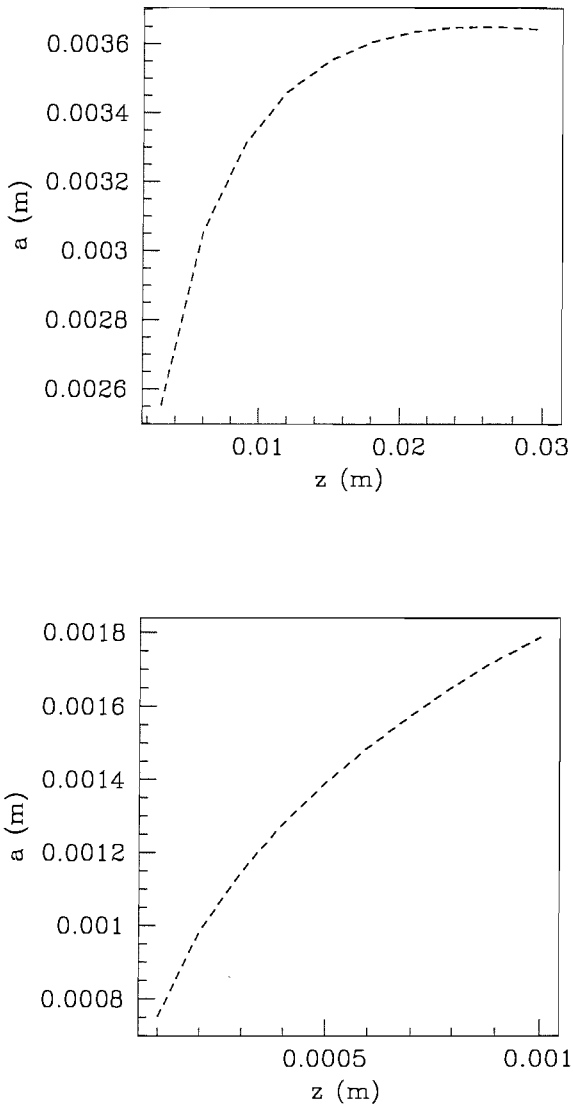

Figure 8.14: Graphs to show a plotted as a function of z. The upper diagram shows the full draw length $0 \leq z \leq 1$ and the lower shows more clearly what happens close to $z = 0$. (Case 7: $A = 1.0 \times 10^{-6}$, $B = 1.0 \times 10^{-5}$, $l_0 = 2.0 \times 10^{-2}$, $h_0 = 1.0 \times 10^{-3}$, $W_f = 2.5 \times 10^{-5}$, $W_d = 1.0 \times 10^{-1}$, $\gamma = 3.0 \times 10^{-1}$, $\mu = 4.0 \times 10^{4}$.)

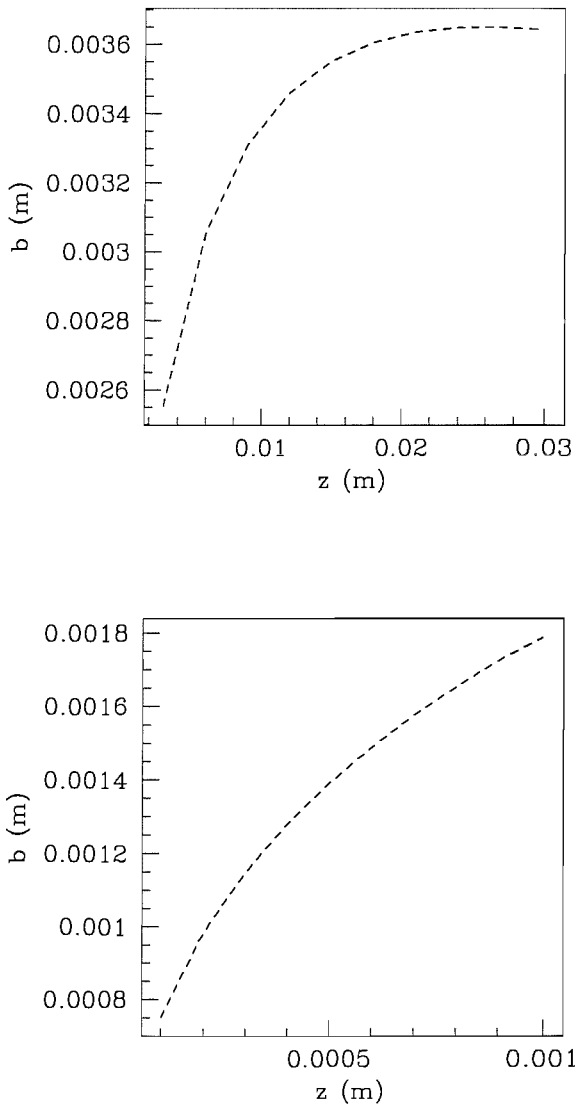

Figure 8.15: Graphs to show b plotted as a function of z. The upper diagram shows the full draw length $0 \leq z \leq 1$ and the lower shows more clearly what happens close to $z = 0$. (Case 7: $A = 1.0 \times 10^{-6}$, $B = 1.0 \times 10^{-5}$, $l_0 = 2.0 \times 10^{-2}$, $h_0 = 1.0 \times 10^{-3}$, $W_f = 2.5 \times 10^{-5}$, $W_d = 1.0 \times 10^{-1}$, $\gamma = 3.0 \times 10^{-1}$, $\mu = 4.0 \times 10^{4}$.)

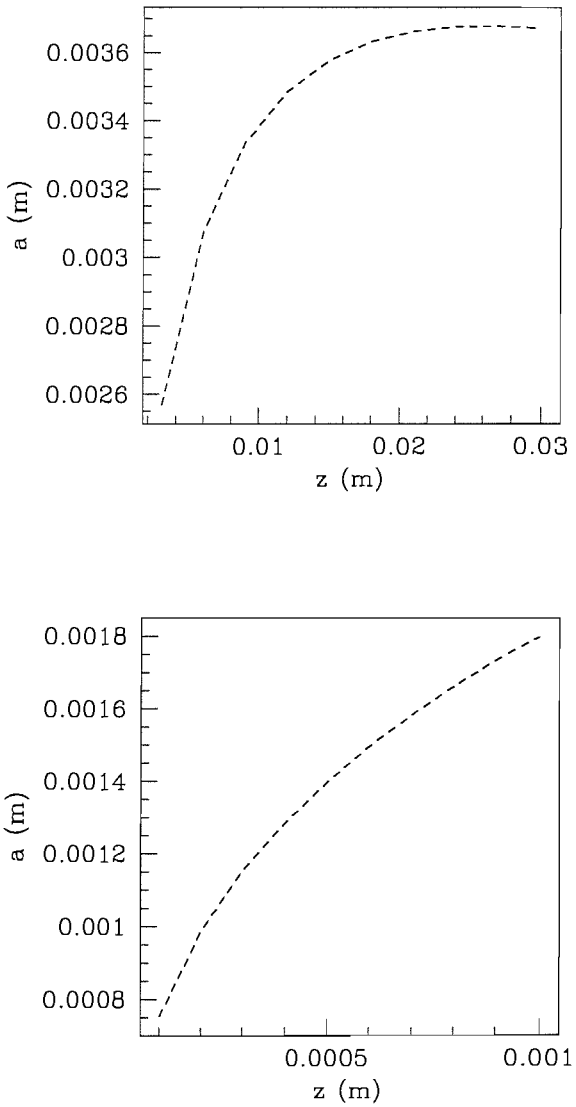

Figure 8.16: Graphs to show a plotted as a function of z. The upper diagram shows the full draw length $0 \leq z \leq 1$ and the lower shows more clearly what happens close to $z = 0$. (Case 8: $A = 1.0 \times 10^{-6}$, $B = 1.0 \times 10^{-3}$, $l_0 = 2.0 \times 10^{-2}$, $h_0 = 1.0 \times 10^{-3}$, $W_f = 2.5 \times 10^{-5}$, $W_d^{'} = 1.0 \times 10^{-1}$, $\gamma = 1.0 \times 10^{-1}$, $\mu = 4.0 \times 10^{4}$.)

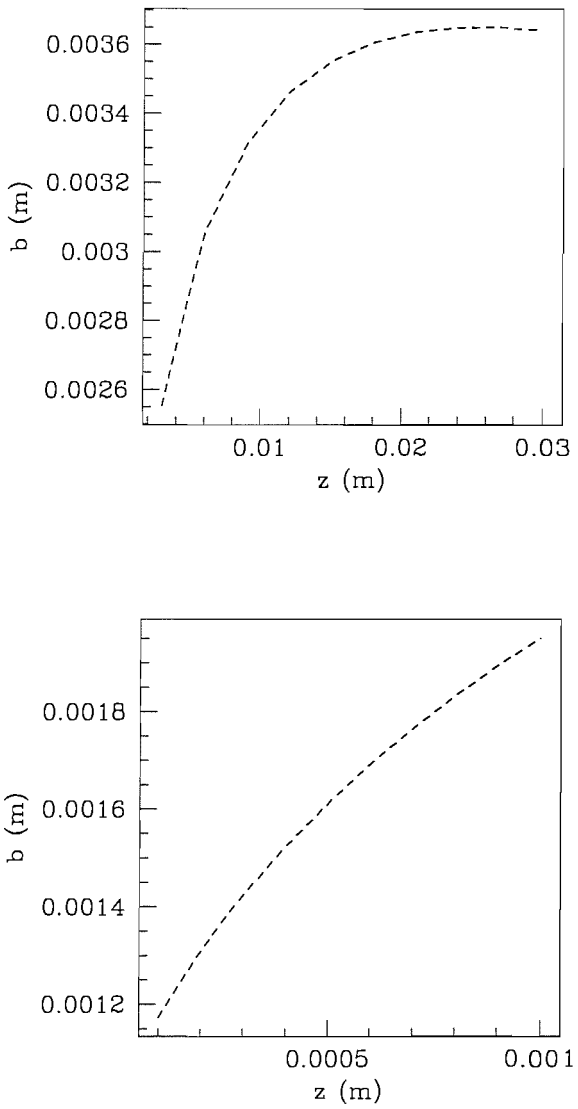

Figure 8.17: Graphs to show b plotted as a function of z. The upper diagram shows the full draw length $0 \leq z \leq 1$ and the lower shows more clearly what happens close to $z = 0$. (Case 8: $A = 1.0 \times 10^{-6}$, $B = 1.0 \times 10^{-3}$, $l_0 = 2.0 \times 10^{-2}$, $h_0 = 1.0 \times 10^{-3}$, $W_f = 2.5 \times 10^{-5}$, $W_d = 1.0 \times 10^{-1}$, $\gamma = 1.0 \times 10^{-1}$, $\mu = 4.0 \times 10^{4}$.)

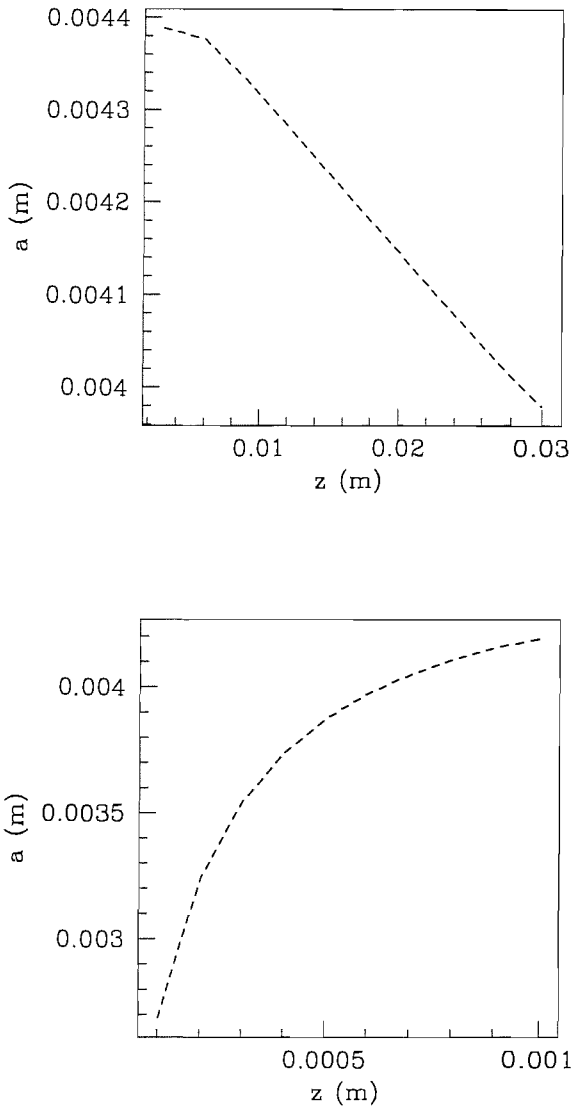

Figure 8.18: Graphs to show a plotted as a function of z. The upper diagram shows the full draw length $0 \leq z \leq 1$ and the lower shows more clearly what happens close to $z = 0$. (Case 9: $A = 1.0 \times 10^{-6}$, $B = 1.0 \times 10^{-3}$, $l_0 = 2.0 \times 10^{-2}$, $h_0 = 1.0 \times 10^{-3}$, $W_f = 2.5 \times 10^{-5}$, $W_d = 1.0 \times 10^{-1}$, $\gamma = 1.0 \times 10^{1}$, $\mu = 4.0 \times 10^{4}$.)

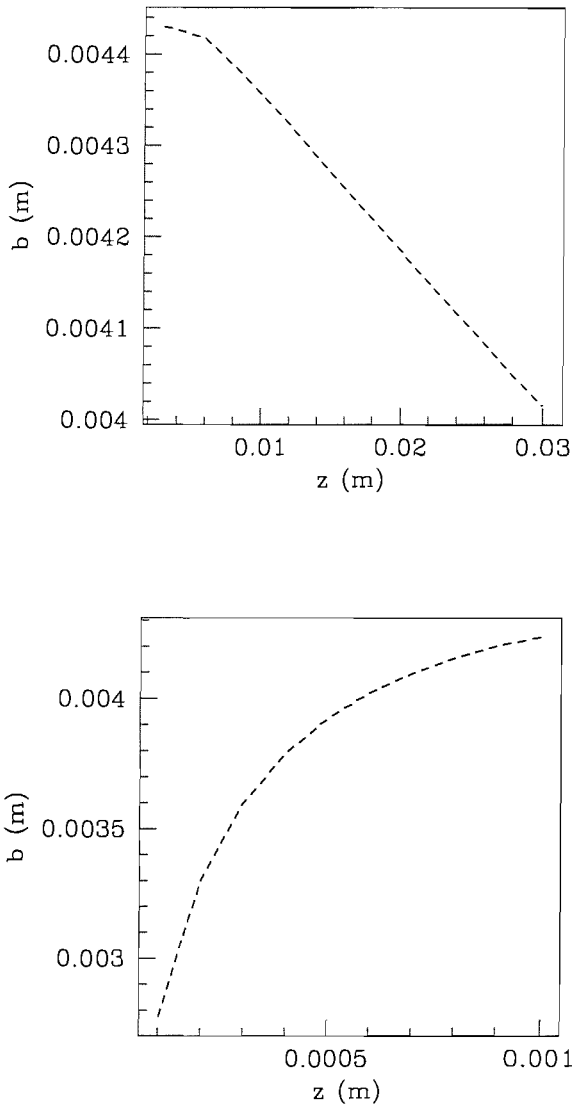

Figure 8.19: Graphs to show b plotted as a function of z. The upper diagram shows the full draw length $0 \leq z \leq 1$ and the lower shows more clearly what happens close to $z = 0$. (Case 9: $A = 1.0 \times 10^{-6}$, $B = 1.0 \times 10^{-3}$, $l_0 = 2.0 \times 10^{-2}$, $h_0 = 1.0 \times 10^{-3}$, $W_f = 2.5 \times 10^{-5}$, $W_d = 1.0 \times 10^{-1}$, $\gamma = 1.0 \times 10^{1}$, $\mu = 4.0 \times 10^{4}$.)

curvature between the two strut–ends will rapidly reduce to zero, and there is no physical reason to suggest that this will not be the case when considering variations of curvature within a region. Unfortunately it is not practical to test this hypothesis experimentally as the radii of curvature are extremely small and it is not practically possible to impose a variation of curvature within a region. However, should such differences of curvature within a region make a measurable difference to the structure of the final fibre, then the values of $a|_{z=1}$ and $h|_{z=1}$ found experimentally will surely differ from those predicted (where the curvature within a region remains constant).

Numerical calculations that consider changes in curvature between the two ends in the two–strut model show that at $z = L$ the two curvatures are almost identical (they are almost the value of the final curvature that would result if both of the two ends started with the same curvature). Also, the final value of h is almost identical to the value that would result from the two ends having the same curvature at $z = 0$. This deviation that may be measured by $\frac{h_{fd}-h_f}{h_f}$, where h_{fd} is the final h with a different initial curvature at each end and h_f is the final h for equal initial curvatures. In all numerical examples given, this number always represented a change of less than a few percent change in h.

8.3.3 Modifications to the model

The mechanism that governs the movement of fluid within a transverse cross–section has been established, and it is now possible to make comparisons between experimental data and theoretical predictions.

It is clear from Figures 8.1, 8.2 and 8.3 that l decreases as a function of z much more than the geometry–preserving solutions supposes. Since the effects of surface tension along this strut must surely be of secondary importance given the thickness of the outer–wall, the following explanations seems reasonable. As a increases, region 1 'absorbs' fluid from the strut so that at $z = L$, whilst the increase in volume of

the fluid that is bounded by a has been drained from the strut , it has not all come from the *thinning* of the strut. It seems likely that some of the fluid comes from the *reduction in length* of the strut. Otherwise put, to an extent the observed reduction in h beyond a geometry preserving reduction, is a side–effect of the change in the core shape.

The model could be refined to quantify this effect, but since the region bounded by a encompasses only a small fraction (typically about 2/10) of what was once a part of the strut, it may be ignored without significantly affecting results. The model could be modified by calculating the final strut–thickness and length $h|_{z=L}$ and $l|_{z=L}$ as before, but then decreasing l by an empirical factor of 8/10 and increasing h accordingly, giving

$$h_N|_{z=L} = \frac{10}{8} h|_{z=L}. \tag{8.33}$$

Such an approximation might be expected to be first–order correct but we note that a more sophisticated model would take account of the fact that q depends on h.

8.3.4 Comparisons with experiment

Experimental data was obtained in order to make comparisons between the predictions of the model above, and experiment. However, it was found that the resolution of the pictures of cross–sections of the fibre was insufficiently high to enable comparison. For this reason we investigate the necessary accuracy with with data must be obtain in order use the model to make quantitative predictions.

It is important to know how accurately experimental data must be known to be able to evaluate the model experimentally. The preforms used to make "cup–handle" fibres are difficult to manufacture and their precise geometry is not easily controlled. Imperfections in the geometry of the preform and cane make it difficult to assign accurate numbers to parameters such as the strut thickness. The suggested criterion is that an error in data taken must produce no more than a 20% change in either

$h|_{z=1}$ or $a|_{z=1}$. It is not necessarily the case that a 20% error in a will also produce a 20% error in h. An error in a corresponding to an $X\%$ increase in its value (errors that result in a value less than the true value of a are represented by a negative quantity) gives an error in h of $Y\%$, where

$$Y = \frac{10^2(Q - \lambda X^2 a^2 w)}{Q - \lambda a^2 w}.$$

In practice the effect of varying the parameters on $a|_{z=1}$ is minimal, because the initial size of a, h and l dictate that h will be much more sensitive to changes in the initial parameters.

In order to determine how accurately each of the experimental parameters must be measured , a control experiment that results in a given $a|_{z=L}$ and $l|_{z=L}$ will be used. Each parameter will then be varied in turn until it produces a 20% error in $h|_{z=1}$, or an error greater than 20% of the difference between the geometry–preserving solution, h_{GP}, and the control experiment solution with drainage accounted for. Whichever of these two errors is smaller will be taken to give the maximum allowable error in the parameter being varied.

The possible acceptable ranges in h to be considered are thus

$$8 \times 10^{-1} h < h_P < 1.2h \tag{8.34}$$

and

$$(1.2h - 2 \times 10^{-1} h_{GP}) < h_P < (1.2h + 2 \times 10^{-1} h_{GP}), \tag{8.35}$$

where h_P is the value of h produced by calculating the effect of varying the size of a parameter. It is usually the case that (8.34) is a smaller range than (8.35) because the drainage parameter is often large, and strongly influences the final value of h. Thus equation (8.35) will be disregarded from now on.

The above method is only approximate, since it is unclear how a combination of errors in parameters will affect the model, and parameter space is too large to scan for all possible combinations. It might be the case that if two parameters are known

Table 8.3: Table to show control experiment parameter values and results.

Quantity (S.I Units)	Value at $z = 0$	Value at $z = L$
a	1.00×10^{-4}	1.91×10^{-6}
h	4.17×10^{-5}	2.62×10^{-8}
l	3.33×10^{-4}	–
W_d	3.20×10^{-1}	–
W_f	5.00×10^{-5}	–
μ	5.00×10^{5}	5.00×10^{5}
γ	1.00×10^{-1}	1.00×10^{-1}
z	0	3.00×10^{-2}

only to within the maximum tolerance of each separate parameter, that the model predicts values of $h|_{z=L}$ and $a|_{z=L}$ that are more than 20% different from the control example. It is assumed herein that the model does not react to such errors in a highly non–linear manner, and that any deviation from the 20% value is not significant.

The control experiment has realistic parameters values shown in Table 8.3, together with the results. To recap, each of the parameters available for change in the model are varied in turn until they produced both a 20% increase and a 20% decrease in the value of h; whichever occurs sooner. $h(0)$ was permitted to vary between 5.00×10^{-8} and 5.00×10^{-4}m as in this case the range produced by (8.34) was much smaller than (8.35), in agreement with the previous suggestion. Table 8.4 shows the error allowed in each of h, a and l, both as a percentage and in absolute terms. The quantity most appropriate will depend on the relative size of the geometry and the drainage parameter, thus discretion must be employed.

Table 8.4: Table to show maximum allowed errors in parameters.

Quantity (SI Units)	Percentage error	Absolute error
A	50	5×10^{-5}
h_0	50	2×10^{-5}
l_0	17	5×10^{-1}
W_d	156	5×10^{-2}
W_f	14	7.5×10^{-6}
μ	20	1.0×10^{5}
L	17	5.0×10^{-1}

The maximum allowed error in surface tension γ is not included since it only appears in the drainage parameter as a ratio between surface tension and viscosity, and the effects of its variance may thus be seen through the effects of a change in the viscosity.

The variable h has been shown to be sensitive to changes in each of the draw parameters, but this sensitivity may depend upon the size of the parameters in the control experiment. Further calculations show that this is not the case, though it is possible that exceptions can be found. For example, by altering the viscosity to $\mu = 10^6$Pas, the change of sensitivity of the system is dramatic. This change in viscosity corresponds to a viscosity an order of magnitude greater than that used in the previous examples, and represents only a small change in glass temperature (see Figure 8.6). The change in the viscosity causes the drainage parameter to decrease to almost zero, giving a value of h only 2% less than a geometry–preserving value, $h_{GP} = h_0 e^{-\beta/2}$. The system thus reacts extremely slowly to changes in draw parameters.

In conclusion, the accuracy with which it is necessary to know the various parameters in the model such as the draw speed and viscosity, depend wholly on the values of the parameters themselves. Further numerical calculations suggest that the size of the drainage parameter is an approximate measure of how accurately one must know the value of a given parameter. The maximum errors given in Table 8.4 should therefore be used to determine the difference in accuracy required for each of h, a and l, either in percentage or absolute terms depending on which of the two measurements of error is considered appropriate. However, when the value of q changes from that used in Table 8.4, at least one of these accuracies must be re–calculated. For example, if the drainage parameter is extremely small and calculations show that the allowed error in W_f is 28%, then the error allowed in μ may be assumed to be 40%.

8.4 Conclusions

In this Chapter we have developed a mathematical model capable of explaining and quantifying the geometrical changes that take place when drawing a "cup–handle" fibre. The model was extended to include the effects of an asymmetric strut and other complexities. Numerical calculations were undertaken to verify that the model behaved as it should, and suggestions were made as to how one may best compare the model with experimental results.

It may be that difficulties in obtaining data accurate enough to enable quantitative comparison with experiment are not possible to overcome. In this case the model will remain largely phenomenological, providing physical insight into the mechanism that produces the observed changes in geometry of the fibre during drawing.

8.4.1 Practical Results

In this Chapter we:

- explained the effect that gives rise to the strut thinning (see §8.2);
- have shown that minor asymmetries in preform geometry are removed as a natural consequence of drawing the fibre (see §8.3);
- described the accuracy with which experimental parameters (in particular the geometry of the preform) must be known in order to make useful comparison between experimental results and the model developed here (see §8.3.4).

Chapter 9

Pressurizing Capillary Tubes

9.1 Introduction

We have previously discussed pressurizing capillary tubes in order to counteract the effects of surface tension. We have modelled the effects of applying an overpressure (constant in time and space) to a capillary tube, and the effects of applying a pressure gradient to a capillary tube. In this Chapter we will consider pressurization in more detail.

In practice pressurization is often achieved *not* by directly applying an overpressure to the hole of the capillary tube, but instead by sealing the tube before drawing it. The drawn fibre is seen to have an inner–diameter that gradually increases with time as the draw proceeds, before later decreasing. In this Chapter we consider the effects of this particular method of hole pressurization, where a capillary tube is sealed and then drawn.

We now clarify the exact experimental procedure before modelling the problem. Our aim is to predict the inner fibre radius and the overpressure as a function of time. We shall then compare predictions made by the model to the results of experiments

conducted at the Optoelectronic Research Centre, University of Southampton, UK. The reason for the need to consider this problem is that, for example, if one wished to simultaneously spin preforms and pressurize them, practical limitations would require the tube to be sealed to achieve pressurization: applying an overpressure to the tube directly is not possible in this case.

9.1.1 Experimental procedure

A capillary tube is first sealed at one end and is significantly longer than the furnace, with as much as 50cm of tube protruding from the top of the furnace (see Figure 9.1). The tube is placed in the furnace with the sealed end at the top. The furnace is then heated to the "drop temperature" of the glass. At this point the portion of the tube in the furnace is at approximately the same temperature as the furnace. The portion of tube outside of the furnace is significantly cooler, but has a temperature significantly higher than air (as a result of radiative heating). Conduction and radiation are both significant sources of heating and therefore the temperature of the tube above the furnace can only be approximated.

As the air in the tube heats up it expands, and an amount of air to be determined exits at the bottom of the furnace (because the bottom of the tube is still open to approximately–atmospheric pressure). The tube is then pulled as normal and thins rapidly, initially closing under the effects of surface tension (this is a transient effect and this part of the manufacture process is called "the initial drop") before a stable fibre diameter is then reached (steady–state drawing conditions are obtained). The volume of glass and gas lost from the tube by the initial part of the pull, which serves to close the hole, is not significant and will be assumed negligible. To summarize, the preform open at one end (and the enclosed gas at atmospheric pressure) is heated in the furnace until thermal equilibrium is established. The preform is then pulled, and the bottom end becomes sealed (at approximately atmospheric pressure). The pressure and inner and outer fibre radius then evolve with time according to the

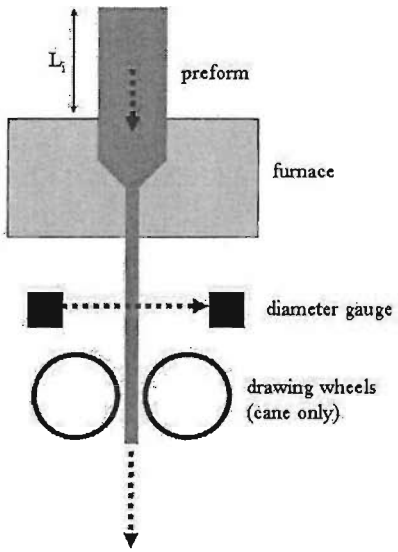

Figure 9.1: Schematic of experimental set–up. A capillary tube is sealed at the top, left open at the bottom, and passed slowly into the furnace. As the preform melts and is drawn, the tube initially closes under the action of surface tension. A quasi–steady state is the reached and the fibre is drawn, where the capillary tube radius and pressure vary slowly with time.

model that we shall describe.

The pull will never reach an exact steady–state (only a quasi–steady state) because air is being removed from the capillary tube at the end of the furnace, thus decreasing the ratio of the mass of glass to air. Furthermore, as the fibre is gradually drawn the capillary tube is lowered into the furnace, increasing the ratio of the mass of glass to air and increasing the average temperature of the air in the tube. These effects combine to give a continually changing pressure inside the capillary tube, and in consequence, the dimensions of the drawn fibre (at $z = L$) will vary with time. Since this is a common practice and pressure is a possible control mechanism for manufacturing fibres with extremely small (perhaps as small as 30 nanometres) holes, we wish to model the change in fibre geometry with time.

9.1.2 Modelling assumptions

(i) The mass of glass and gas lost in the initial drop is negligible and will be ignored.

(ii) The temperature of the glass is approximated for the large region outside the furnace.

(iii) The air is assumed to be in thermal equilibrium with the glass throughout.

(iv) The temperature profile of the glass is assumed to (a) vary linearly with distance and (b) not to depend on time.

(v) Whilst the temperature of the glass varies inside the furnace, the viscosity of the glass will be assumed constant in this region (numerical calculations confirm that allowing for the correct variable viscosity does not significantly alter the results for fibre geometry produced, whilst including a variable viscosity introduces numerical difficulties).

9.2 Mathematical modelling

We start by considering the equations that govern the isothermal drawing of capillary tubes. These are (see Chapter 3 for an explanation of the notation used)

$$\rho(h_2^2 - h_1^2)(w_{0t} + w_0 w_{0z} - g) = \left(3\mu(h_2^2 - h_1^2)w_{0z} + \gamma(h_1 + h_2)\right)_z, \tag{9.1}$$

$$(h_1^2)_t + (h_1^2 w_0)_z = \frac{h_1 h_2(2p_0 h_1 h_2 - 2\gamma(h_1 + h_2))}{2\mu(h_2^2 - h_1^2)}, \tag{9.2}$$

$$(h_2^2)_t + (h_2^2 w_0)_z = \frac{h_1 h_2(2p_0 h_1 h_2 - 2\gamma(h_1 + h_2))}{2\mu(h_2^2 - h_1^2)}. \tag{9.3}$$

We consider the steady–state version of these equations, ignoring the effects of gravity, the inertial–force term and those of surface tension and rotation. Equations (9.1)–(9.3) become

$$\left((h_2^2 - h_1^2)w_{0z}\right)_z = 0, \tag{9.4}$$

$$(h_1^2 w_0)_z = \frac{h_1^2 h_2^2 p_0}{\mu(h_2^2 - h_1^2)}, \tag{9.5}$$

$$(h_2^2 w_0)_z = \frac{h_1^2 h_2^2 p_0}{\mu(h_2^2 - h_1^2)}, \tag{9.6}$$

and may be solved in closed–form by eliminating $(h_2^2 - h_1^2)$ and solving for w_0. We are then left with equations for h_2 and h_1. Since it is the volume of air enclosed within the capillary tube with which we are principally concerned, it is helpful to know the steady–state value of h_1 as a function of overpressure, given by

$$h_1 = h_{10}\sqrt{\frac{(h_{20}^2 - h_{10}^2)\exp\left(-\frac{\left(\mu\beta^2 W_f z e^{\beta z/L} + p_0 L^2\right)e^{-\beta z/L}}{\mu\beta W_f L}\right)}{h_{20}^2 \exp\left(-\frac{p_0 L}{\mu\beta W_f}\right) - h_{10}^2 \exp\left(-\frac{p_0 L e^{-\beta z/L}}{\mu\beta W_f}\right)}}, \tag{9.7}$$

where h_{10} and W_f are the usual initial and boundary conditions for h_1 and w_0.

Equation (9.7) gives h_1 in terms of p_0. We will now derive a model that describes the drawing process of sealed capillary tubes. The model will relate $h_1(L,t)$ and $p_0(t)$. Setting $p_0 = p_0(t)$ in (9.7) and using the solution for $h_1(t)$ in the model derived will allow the model to be solved for $p_0(t)$. We then make use of (9.7) once more to determine the time-dependent solution $h_1(L,t)$.

The temperature $T(z)$ is known within the furnace but must be estimated for the remainder of the capillary tube (the part that protrudes from the top of the furnace). The top of the capillary tube is at $z = -L_i$ for $t = 0$ and moves with speed W_f.

We assume that the air inside the capillary tube is an ideal gas obeying the ideal–gas law given by

$$p = \rho RT, \tag{9.8}$$

where R is the universal gas constant. We assume that $p = p(t)$ as the speed of sound in air is large compared with the rate at which the volume of gas changes, allowing us to ignore changes in pressure from one portion of the capillary to the next.

The total mass of air inside the capillary tube is given by

$$\int_{-z_{min}}^{0} \pi h_{10}^2 \, \rho(z,t) \, dz + \int_0^L \pi h_1(z,t)^2 \rho(z,t) \, dz + \int_0^t \pi h_1(L,t')^2 \, \rho(L,t') \, W_d \, dt', \tag{9.9}$$

where $z_{min} = L_i - W_f t$ denotes the top of the capillary tube. The first term in equation (9.9) represents the mass of gas in the part of the preform above the furnace. The second term represents the mass of gas in the furnace. The third term accounts for the mass of gas that "leaves the system" and becomes trapped in the fibre. This is determined by the density of gas, the preform velocity at $z = L$ and the final fibre radius.

Since the total mass of gas remains constant we may differentiate this expression and set it equal to zero. Differentiating and substituting for $\rho(z,t)$ from the ideal gas law (9.8) gives

$$\frac{\partial}{\partial t}\left[\int_{-z_{min}}^{0} \pi h_{10}^2 \frac{p(t)}{RT(z)} \, dz + \int_0^L \pi h_1(z,t)^2 \frac{p(t)}{RT(z)} \, dz\right] + \pi h_1(L,t)^2 \, \frac{p(t)}{RT(L)} W_d = 0, \tag{9.10}$$

which, on writing $p(t) = p_0(t) + p_a$ where p_a denotes atmospheric pressure, gives

$$\frac{\partial}{\partial t}\left[h_{10}^2 \int_{-z_{min}}^{0} \frac{(p_0(t)+p_a)}{T(z)} \, dz + \int_0^L \frac{h_1(z,t)^2 (p_0(t)+p_a)}{T(z)} \, dz\right] +$$

$$h_1(L,t)^2 \, \frac{(p_0(t)+p_a)}{T(L)} W_d = 0. \tag{9.11}$$

Substituting in the expression (9.7) for $h_1(z,t)$ gives an equation for $p(t)$ that must be solved in order to determine $p_0(t)$. Equation (9.7) may then be used to determine the manner in which $h_1|_{z=L}$ varies with time. Since (9.7) was obtained by solving (9.1)–(9.3) and assuming a steady–state process, the methodology employed here assumes that the timescales in (9.1)–(9.3) are much smaller than than the timescale for the change of $p_0(t)$ and $h_1(L,t)$ in equation (9.11); equivalent to a quasi–steady analysis. We find that

$$\frac{\partial}{\partial t}\left\{h_{10}^2\int_{-z_{min}}^{0}\frac{(p_0(t)+p_a)}{T(z)}\,dz+\int_0^L\left(\frac{h_{10}^2(h_{20}^2-h_{10}^2)\exp\left(-\frac{\left(\mu\beta^2W_f z e^{\beta z/L}+p_0(t)L^2\right)e^{-\beta z/L}}{\mu\beta W_f L}\right)}{h_{20}^2\exp\left(-\frac{p_0(t)L}{\mu\beta W_f}\right)-h_{10}^2\exp\left(-\frac{p_0(t)Le^{-\beta z/L}}{\mu\beta W_f}\right)}\right)\right.$$

$$\left.\frac{(p_0(t)+p_a)}{T(z)}\,dz\right\}+\left(\frac{h_{10}^2(h_{20}^2-h_{10}^2)\exp\left(-\frac{\left(\mu\beta^2W_fLe^{\beta}+p_0(t)L^2\right)e^{-\beta}}{\mu\beta W_f L}\right)}{h_{20}^2\exp\left(-\frac{p_0(t)L}{\mu\beta W_f}\right)-h_{10}^2\exp\left(-\frac{p_0(t)Le^{-\beta}}{\mu\beta W_f}\right)}\right)\frac{(p_0(t)+p_a)}{T(L)}W_d=0. \tag{9.12}$$

An inspection of (9.11) reveals that the second term will always be much smaller than the first because $T(z'') > T(z')$ where $-z_{min} < z' < 0$ and $0 < z'' < L$, and $h_1(z)/h_{10} \ll 1$ when $0 < z \leq L$. Furthermore, since z_{min} is always much smaller than L (the capillary tube is never quite pushed fully into the furnace in practice), we may ignore the second term since it is always less than a factor of $L/z_{min} \ll 1$ smaller than the first. This leaves us with the following equation to solve for p_0:

$$h_{10}^2\frac{\partial}{\partial t}\int_{-z_{min}}^{0}\frac{(p_0(t)+p_a)}{T(z)}\,dz+h_1(L,t)^2\,\frac{(p_0(t)+p_a)}{T(L)}W_d=0. \tag{9.13}$$

The function $T(z)$ is assumed to be

$$T(z)=T_{max}-\frac{(T_{min}-T_{max})z}{L_i}, \tag{9.14}$$

where T_{min} and T_{max} are the temperature at the top of the capillary tube at the start of the experiment and temperature in the furnace respectively. Finally, for the viscosity of Suprasil F300 glass we have used

$$\mu=5.8\times10^{-8}\exp\left(\frac{515400}{8.3145(T_{max}-273)+2271.10567}\right),$$

where T is now given in units of C and the viscosity in units of Poise. (Assumption (iv) is employed here, where the glass is assumed to have a viscosity determined by the maximum temperature in the furnace, whereas the air in the glass has a temperature that varies for all $z \in [-z_{min}, L]$.)

When (9.14) is used in (9.13) and the resulting equation simplified, we arrive at a first–order non–linear ordinary differential equation for $p(t)$ that is not possible to solve in closed form in general, and must be solved numerically. Having determined $p(t)$, $h_1(L,t)$ may be found from (9.7).

9.3 Comparison with experimental results

Experiments were conducted at the Optoelectronics Research Centre, and here we summarize the results by directly comparing one set of results chosen at random with numerical predictions made by the above model.

The initial dimensions of the capillary tube were chosen so that the effects of surface tension could be minimized (i.e. a large h_{10} and h_{20} were chosen). A temperature distribution for the glass was determined by assuming that the temperature difference between the top of the preform and that of the glass in the furnace was 640C, with the furnace temperature being at $T_{max} = 1840$C, giving $T_{min} = 1200$C. The preform extended above the furnace with $L_i = 0.8m$. Other experimental parameters were $W_f = 1.5$mm/min, $W_d = 15$m/min, $h_{20} = 1.25$cm and $h_{10} = 0.95$cm.

Numerical simulations that calculate $p_0(t)$ from (9.13) were performed using the parameter values given above. From this data (9.7) was used to compute the inner radius h_1 at $z = L$ as a function of time. Numerical results for both $h_1(t)$ and $p_0(t)$ are shown in Figure 9.2.

Experimental data for $h_1(t)$ and $p_0(t)$ is shown in Figure 9.3. In both cases a splines

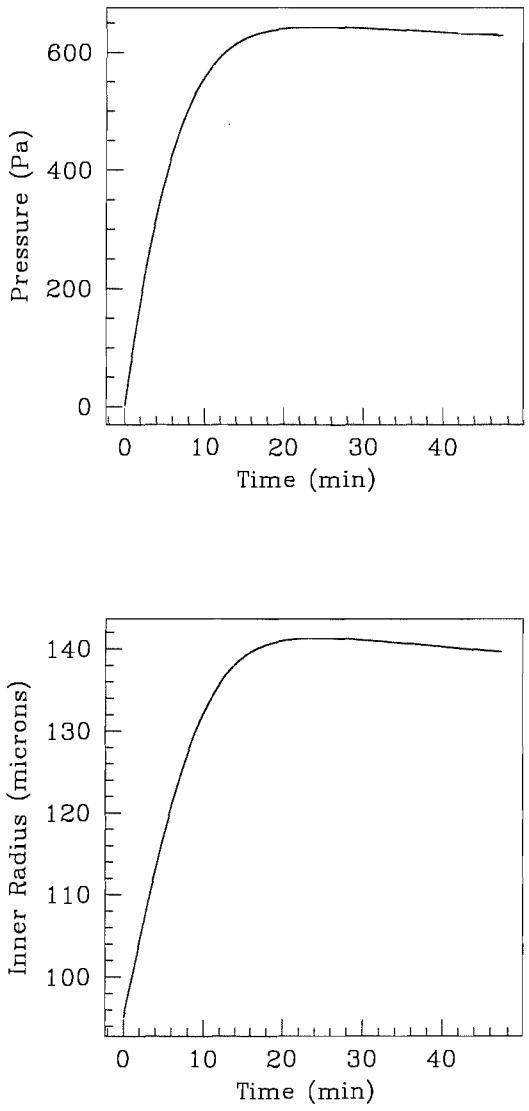

Figure 9.2: Graphs to show the numerical results for $h_1(L,t)$ and $p_0(t)$. (Parameter values: $W_f = 2.5 \times 10^{-5}$, $W_d = 2.5 \times 10^{-1}$, $h_{20} = 1.25 \times 10^{-2}$, $h_{10} = 9.50 \times 10^{-3}$, $L_i = 8 \times 10^{-1}$, $T_{max} = 1840$, $T_{min} = 1200$.)

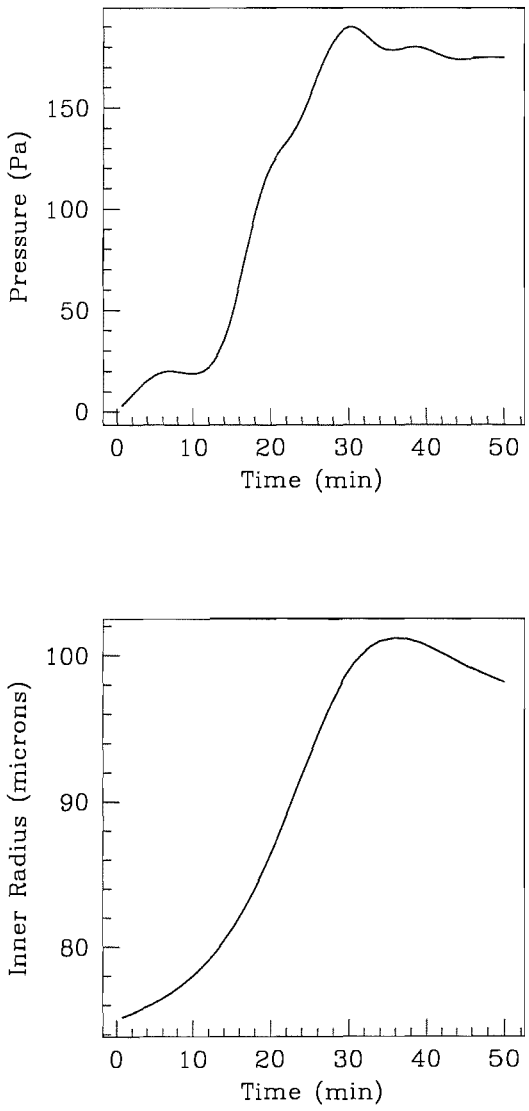

Figure 9.3: Graphs to show the experimental results for $h_1(L,t)$ and $p_0(t)$. (Parameter values: $W_f = 2.5 \times 10^{-5}$, $W_d = 2.5 \times 10^{-1}$, $h_{20} = 1.25 \times 10^{-2}$, $h_{10} = 9.50 \times 10^{-3}$, $L_i = 8 \times 10^{-1}$, $T_{max} = 1840$, $T_{min} = 1200$.)

fit has been applied to the data. Given the fact that the temperature distribution of the capillary tube outside of the furnace has been estimated rather crudely and that the effects of surface tension have been ignored in this model, the experimental results compare favourably with numerical predictions. Both the form of the pressure curve and that for the inner fibre–radius are qualitatively correct, though there is a significant difference between the magnitude of pressure values, which in turn gives rise to disparity in values of $h_1(t)$.

A possible explanation for this difference relates directly to the fact that the effects of surface tension have been ignored in our model. Were we to include surface tension, $h_1(t)$ would be everywhere reduced in size. Since this would mean that $h_1|_{z=L}$ would be reduced, after time t one would find more gas above $z = L$ for a given reduction in size of preform (mass of glass) above $z = L$.

The rate at which the pressure increases as the fibre is drawn depends on a balance of two effects. (i) As the preform is lowered into the furnace, the gas within heats up, thus increasing the overpressure. (ii) As the fibre is drawn, gas leaving "the system" at the bottom of the furnace becomes trapped in the fibre. This has the effect of counteracting the effect of the mechanism (i) and reducing the preform overpressure. To give an illustrative example of the feedback mechanism in place, consider that if surface tension were to completely close the hole (this does not happen in practice precisely because of this feedback mechanism) then glass but no air, would leave the furnace at $z = L$. As the preform is continually lowered into the furnace, the volume of air within the furnace region remains constant, whilst the volume of glass decreases (the length of the tube decreases). Consequently, the overpressure increases indefinitely with time until it is large enough to overcome the effects of surface tension at $z = L$. At this point a hole opens once more and equilibrium is eventually established between hole size and overpressure.

The shape of the graphs in Figures 9.2 and 9.3 may therefore be interpreted in the following way. At the start of the drawing process much of the preform is above

the furnace at a lower temperature than the furnace. As the fibre is drawn and the preform lowered into the furnace, the dominant effect is that of an increased average temperature for the air inside the preform, giving rise to both an increased overpressure (see equation (9.7)) and an increased fibre radius. However, as time proceeds, the increase in average temperature, per unit length of preform lowered into the furnace, reduces. This allows the effect of air removal at $z = L$ to dominate, and the pressure begins to decrease, as does the fibre radius (see equation (9.7)).

9.3.1 The effects of neglecting surface tension

The model assumes no surface tension and since the ratio of glass volume to air volume leaving the furnace per second is

$$\left(\frac{h_2^2 - h_1^2}{h_1^2}\right)|_{z=L} = \left(\frac{h_{20}e^{-\frac{\beta}{2}} + \frac{\gamma L e^{-\beta}\left((3h_{10}-h_{20})\left(1-e^{\frac{\beta}{2}}\right)+h_{10}e^{\frac{\beta}{2}}\left(e^{-\frac{\beta}{2}}-1\right)\right)}{3\beta W_f(h_{20}^2-h_{10}^2)}}{h_{10}e^{-\frac{\beta}{2}} + \frac{\gamma L e^{-\beta}\left((3h_{20}-h_{20})\left(1-e^{\frac{\beta}{2}}\right)+h_{10}e^{\frac{\beta}{2}}\left(e^{-\frac{\beta}{2}}-1\right)\right)}{3\beta W_f(h_{20}^2-h_{10}^2)}}\right)^2 - 1, \quad (9.15)$$

we find that

$$\left(\frac{h_2^2 - h_1^2}{h_1^2}\right)|_{z=L} = \frac{h_{20}^2 - h_{10}^2}{h_{10}^2} \quad (9.16)$$

when surface tension is disregarded.

If the difference between (9.15) where surface tension is included and (9.16) where $\gamma = 0$, is greater than zero, then less mass will leave when surface tension effects are accounted for, and vice versa. Consequently the hole overpressure is expected to be larger at any given time when the effects of surface tension are included if

$$\left(\frac{h_2^2 - h_1^2}{h_1^2}\right)|_{z=L} - \frac{h_{20}^2 - h_{10}^2}{h_{10}^2} > 0, \quad (9.17)$$

or equivalently when

$$\frac{h_{20}e^{-\frac{\beta}{2}} + \frac{\gamma L e^{-\beta}\left((3h_{10}-h_{20})\left(1-e^{\frac{\beta}{2}}\right)+h_{10}e^{\frac{\beta}{2}}\left(e^{-\frac{\beta}{2}}-1\right)\right)}{3\beta W_f(h_{20}^2-h_{10}^2)}}{h_{10}e^{-\frac{\beta}{2}} + \frac{\gamma L e^{-\beta}\left((3h_{20}-h_{20})\left(1-e^{\frac{\beta}{2}}\right)+h_{10}e^{\frac{\beta}{2}}\left(e^{-\frac{\beta}{2}}-1\right)\right)}{3\beta W_f(h_{20}^2-h_{10}^2)}} > 0. \quad (9.18)$$

Setting $W_f = 1.5\text{mm/min}$, $W_d = 15\text{m/min}$, $h_{20} = 1.25\text{cm}$, $h_{10} = 0.95\text{cm}$ and using the given viscosity law and temperature distribution, (9.18) gives a value of 0.04. This suggests that we should expect to observe a larger pressure and smaller value of $h_1|_{z=L}$ than our model predicts. This is not observed experimentally and it is therefore expected that the estimate of the temperature profile for the air in the capillary tube outside of the furnace is inadequate, though direct measurement of the temperature profile is currently not possible.

9.4 Conclusions

A model was developed to describe the time–fluctuating pressure and fibre geometry observed when sealed capillary tubes are drawn to fibre form. Numerical solutions to the equations compared favourably with experimental data, especially given the large uncertainties in quantities such as the temperature profile of the preform above the furnace. It is anticipated that once the uncertainties in experimental quantities are reduced, this model will provide an accurate tool for developing a method to control the size of extremely small holes (as a result of the feedback mechanism between hole size and hole overpressure).

Chapter 10

Two–Phase Flow

10.1 Introduction

In Chapter 3 we developed a model for the drawing and rotation of capillary tubes. The aim in this Chapter is to construct a model capable of describing the process of the manufacture of microstructured optical fibres made from a preform that contains a large number of holes. To accomplish this, we will take a "two–phase flow" approach that involves determining average properties of the equations. We will limit ourselves to the case where an axisymmetric geometry is present in the preform. Analytic solutions to the governing equations are obtained for certain limiting cases, and a numerical analysis of the full equations is undertaken.

10.2 Mathematical modelling

Our aim is to develop a mathematical model for the process of capillary drawing that is capable of including the effects of the presence of an array of pressurized, infinitely–long cylindrical bubbles (or holes) in a transverse cross–section, surface

tension, gravity and inertia. For simplicity we will ignore the effects of preform rotation here, though the modelling could easily be developed to include this. The model will be derived by averaging the effects of the presence of the bubbles in a cross–section of the fibre, allowing equations to be derived that describe the averaged behaviour of the holes. The model will examine the limit where there is a large number of small holes or a small number of large holes, and will be able to predict the average hole size and distribution of holes at any point in a cross–section of the fluid. We begin with the Navier-Stokes equations, using cylindrical coordinates. Averages in two–phase flow are often first taken over realizations (initial conditions) and then over cross–sections. However, whilst the bubbles in a cross–section of a fibre will be described by a distribution, the experiment is expected to be reproducible. For this reason the averaging process here takes place in a preform cross–section.

In the equations that follow, we label the bubbles so that i denotes the "bubble number", t denotes time, z measures the distance along the axis of a capillary, and r denotes distance normal to this central axis. A schematic diagram of the geometry of the capillary is shown in Figure 10.1. The flow is assumed to be axisymmetric and is therefore independent of the azimuthal angle θ (although a velocity could be permitted to exist in that direction if the effects of preform rotation were included). All t, z and r subscripts denote differentiation, and the velocity $\boldsymbol{q}$ of the molten glass is denoted by $\boldsymbol{q} = w\boldsymbol{e}_z + u\boldsymbol{e}_r + v\boldsymbol{e}_\theta$, where $\boldsymbol{e}_z$, $\boldsymbol{e}_r$ and $\boldsymbol{e}_\theta$ are unit vectors in the z, r and θ directions respectively. Here we consider only the case where there is no azimuthal fluid velocity; that is $v \equiv 0$. To a first approximation the temperature of the furnace and thus of the glass, is constant throughout. Therefore initially the viscosity is assumed constant throughout the glass and the energy equation need not be considered.

The fluid pressure is denoted by p, the pressure of gas inside an individual bubble i is denoted by p_i and g is the acceleration due to gravity. The total number of bubbles (holes), density, dynamic viscosity and surface tension are denoted by D, ρ, μ and γ respectively.

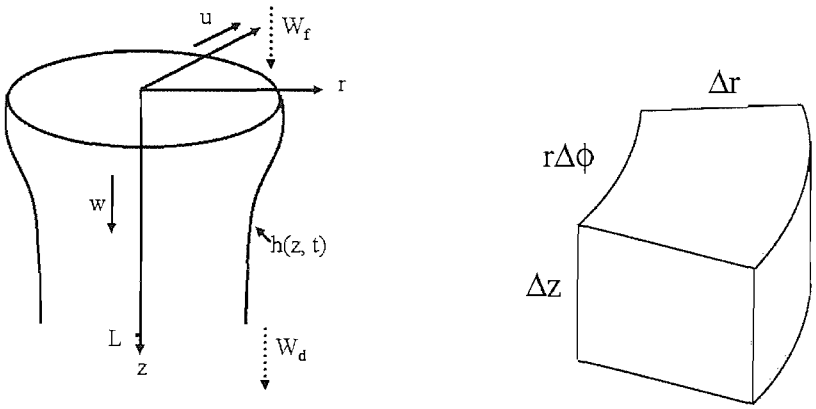

Figure 10.1: Problem geometry and a fluid element.

To derive an averaged model it will be necessary to describe the local fluid velocity in the region immediately surrounding a bubble. The drawing of holey fibres involves a highly extensional flow, where the effects of this extension and those of surface tension dominate the characteristics of the flow. For this reason, in §10.2.3 below, we use u_i to denote the radial velocity of the fluid on the boundary of the bubble labelled i of radius a_i that would result if the bubble were left to close in an infinite fluid, under the action of the effects of surface tension and an extensional flow characterised by the downstream fluid velocity gradient w_z. We therefore ignore the effects of the fibre free surface (the outer edge of the fibre) and of the presence of the other holes on the evolution of a single bubble. The exact form of u_i will be clarified later in the Chapter.

10.2.1 Momentum conservation

The governing momentum equations for the macroscopic flow are (see [59])

$$\rho(w_t + uw_r + ww_z) = -p_z + \frac{\mu}{r}(rw_r)_r + 2\mu w_{zz} + \frac{\mu}{r}(ru_z)_r + \rho g, \quad (10.1)$$

$$\rho\left(u_t + uu_r + wu_z\right) = -p_r + \mu\left(\frac{1}{r}(ru)_r\right)_r + \mu u_{zz}, \quad (10.2)$$

$$p_\theta = 0, \quad (10.3)$$

and p is therefore a function of r, z and t only.

We denote the preform radius of the capillary by $r = h(z,t)$. Equations (10.1)–(10.3) thus apply in the region $0 \leq z \leq L$, $0 \leq r \leq h$, for $0 \leq t \leq \infty$, and must be solved subject to suitable boundary and initial conditions, which will be considered presently. The feed and draw speeds are, as usual, denoted by W_f and W_d respectively and the ambient pressure in the air surrounding the fibre is denoted by p_a.

Note that we have yet to derive a continuity equation, which is modified from the standard single–component fluid from as a result of the presence of the many bubbles in a cross–section. This equation will involve a and n (where a is the averaged bubble radius and n is the averaged number density of bubbles, the number of bubbles per m^2 in a cross–section). Thus a and n will also have to be determined. We must also derive global boundary conditions for the free surface $r = h(z,t)$.

10.2.2 Derivation of the continuity equation

We commence by deriving a continuity equation for the case of many bubbles in a cross–section by considering a "continuum of bubbles". By this we mean that the fluid detects the presence of the many bubbles through their effect averaged in the cross–section. This will give an equation that holds locally. As a check, we will rederive the continuity equation for the case of a discrete set of bubbles, and integrate the result over an area that is small compared to the area of a cross–section, but large compared to the average bubble area and separation, and show that this derivation agrees with the former. This second approach ensures that the averaged effect of the bubbles is determined without the local flow being dominated by non–local effects. Given the size of a cross–section (typically a few centimetres) and the number of bubbles therein (typically a few hundred), in practice our procedure is equivalent to averaging over the area of approximately ten bubbles.

We start by considering an isolated fluid element similar to the one shown in Figure

10.1. If there were no bubbles in a cross–section, mass conservation would require that

$$w(r\Delta\phi\Delta r) - (w + w_z\Delta z)r\Delta r\Delta\phi + u(r\Delta\phi\Delta z) - (u + u_r\Delta r)\left[(r + \Delta r)\Delta\phi\Delta z\right] = 0. \tag{10.4}$$

Taking the limit $\Delta r \to 0$, $\Delta\phi \to 0$, $\Delta z \to 0$ and rearranging would give the usual continuity equation

$$\frac{1}{r}(ru)_r + w_z = 0, \tag{10.5}$$

as required. This intuitive derivation using (10.4) allows for the effect of the presence of bubbles to be clearly identified. The presence of the bubbles changes the terms containing r in (10.5), the effect of which is to reduce the area of fluid on any face of the volume element. Explicitly, mass conservation requires that the $(r\Delta\phi\Delta r)$ term in (10.5) becomes

$$r\Delta\phi\Delta r \Longrightarrow r\Delta r\Delta\phi - \pi r\Delta r\Delta\phi a^2 n, \tag{10.6}$$

where $\Longrightarrow$ indicates the effect of adding bubbles, n denotes the number of bubbles in a preform cross–section, and $r\Delta r\Delta\phi\pi a^2 n$ is the volume of the bubbles within the element under consideration. Similarly, other terms in (10.4) are altered according to

$$r\Delta r\Delta\phi \Longrightarrow r\Delta r\Delta\phi - \pi r\Delta r\Delta\phi(n + n_z\Delta z)(a^2 + (a^2)_z\Delta z) \tag{10.7}$$

$$r\Delta\phi\Delta z \Longrightarrow r\Delta\phi\Delta z - \pi a^2 n r\Delta\phi\Delta z \tag{10.8}$$

$$(r + \Delta r)\Delta\phi\Delta z \Longrightarrow (r + \Delta r)\Delta\phi\Delta z - \pi(a^2 + (a^2)_r\Delta r)(n + n_r\Delta r) \times (r + \Delta r)\Delta\phi\Delta z. \tag{10.9}$$

Using (10.6) and (10.7)–(10.9) in (10.4) gives

$$\begin{aligned} &w(r\Delta r\Delta\phi - \pi r\Delta r\Delta\phi a^2 n) - (w + w_z\Delta z)(r\Delta r\Delta\phi - \pi r\Delta r\Delta\phi(n + n_z\Delta z) \\ &(a^2 - (a^2)_z\Delta z)) + u(r\Delta\phi\Delta z - \pi r\Delta\phi\Delta z a^2 n) - (u + u_r\Delta r)[(r + \Delta r)\Delta\phi\Delta z \\ &- \pi(a^2 + (a^2)_r\Delta r)(n + n_r\Delta r)(r + \Delta r)\Delta\phi\Delta z] = 0. \end{aligned} \tag{10.10}$$

Expanding, dividing through by $r\Delta r\Delta\phi\Delta z$ and taking the limit $\Delta r \to 0$, $\Delta\phi \to 0$,

$\Delta z \to 0$, upon rearranging gives

$$\frac{u}{r} - 2\pi w a a_z n - \pi w a^2 n_z - \pi w_z a^2 n + w_z + u_r - \pi u a^2 n_r - \pi u_r a^2 n - 2\pi u a a_r n - \frac{\pi u a^2 n}{r} = 0,$$

which may be recast to give

$$\frac{1}{r}\left(ru(1-\pi a^2 n)\right)_r + w_z = \pi (w a^2 n)_z. \tag{10.11}$$

This is the new continuity equation. To convince ourselves that it takes the correct form we may consider the case where $w = w(z)$, $a = a(z)$ and $n = n(z)$ only. We solve (10.11) for u to give

$$u = \frac{r[\pi (w a^2 n)_z - w_z]}{2(1 - \pi a^2 n)}. \tag{10.12}$$

The kinematic boundary condition in steady–state is $u = w h_z$ at $r = h(z)$. This, together with the result for u from (10.12) give,

$$(h^2 w)_z = \pi (w h^2 a^2 n)_z. \tag{10.13}$$

Equation (10.13) is precisely as one might expect since in a steady–state cross–section the mass flux in the z–direction is

$$\frac{\partial}{\partial z}(w \times \text{ area of glass}) = 0 \tag{10.14}$$

where

$$\text{area of glass} = \text{total area} - \text{area of bubbles} = \pi h^2 - \pi h^2 n \pi a^2. \tag{10.15}$$

Using (10.15) in (10.14) gives

$$(h^2 w)_z = \pi (w h^2 a^2 n)_z, \tag{10.16}$$

which is identical to (10.11), as required.

We have not yet considered the case of discrete bubbles, so we repeat the same process as before but this time require that

$$r\Delta\phi\Delta r \Longrightarrow r\Delta r\Delta\phi - \pi r \Delta r \Delta\phi \sum_{i=1}^{D} a_i^2 \delta(z - z_i)\delta(\phi - \phi_i)\delta(r - r_i)$$

$$\times \frac{\sum_{i=1}^{D}(\int_{\Omega_i} dA)\delta(z-z_i)\delta(\phi-\phi_i)\delta(r-r_i)}{N_{\Omega_i}},$$

where we sum over all bubbles positioned at $z = z_i$, $\phi = \phi_i$ and $r = r_i$, where Ω_i is the area of approximately ten bubbles (the number of bubbles that correspond to the area needed to match to the far–field flow, as discussed above) at the point $\mathbf{x}_i$, D is the total number of bubbles in a cross–section and N_{Ω_i} is the number of bubbles in an area Ω_i. In the continuum limit the sums may be replaced by integrals and we therefore find that

$$\frac{\sum_{i=1}^{D}(\int_{\Omega_i} dA)\delta(z-z_i)\delta(\phi-\phi_i)\delta(r-r_i)}{N_{\Omega_i}} \Longrightarrow n(r,z)$$

and

$$\sum_{i=1}^{D} \pi a_i^2 \delta(z-z_i)\delta(\phi-\phi_i)\delta(r-r_i) \Longrightarrow a(r,z)a(r,z),$$

giving finally that

$$r\Delta r\Delta\phi \Longrightarrow r\Delta r\Delta\phi - \pi r\Delta r\Delta\phi a^2 n,$$

which is identical to equation (10.6) as required for consistency of the two approaches.

For the remainder of this Chapter, for simplicity, we shall write the continuity equation (10.11) as

$$\frac{1}{r}(ru\alpha)_r = -(\alpha w)_z, \tag{10.17}$$

where $\alpha = 1 - \pi a^2 n$.

10.2.3 Local fluid flow around a bubble

The model is not yet closed as (10.17) involves a and n. To determine these, we now consider a single bubble and determine the form of the flow field in the cross–sectional plane surrounding the bubble. We consider a single, infinitely–long cylindrical bubble in a purely–extensional flow under the action of surface tension γ. This represents the local flow problem surrounding a single bubble (situated anywhere with the cross–section of a preform). Conservation of mass requires

$$\frac{1}{r}(ru_i)_r + w_z = 0,$$

which may be integrated when w is a function of z alone, as is the case on the local–scale considered here, giving

$$u_i = -\frac{rw_z}{2} + \frac{\phi(z,t)}{r}.$$

The integration constant $\phi(z,t)$ is determined by applying the condition that the fluid velocity must equal the rate of change of the bubble's radius with respect to time (following a fluid particle on the surface of the bubble) when $r = a_i$, the radius of the bubble. Thus setting $u_i = \dot{a}_i$ on $r = a_i$ gives

$$\phi(z,t) = a_i\dot{a}_i,$$

where $\dot{a}_i$ is the bubble surface velocity following a bubble in the fluid flow, which may be expressed as

$$\dot{a}_i = \frac{D(a_i)}{Dt} = \frac{\partial a_i}{\partial t} + \mathbf{q}.\nabla a_i = a_{it} + wa_{iz} + ua_{ir},$$

where $\mathbf{q} = u(r,z)\mathbf{e_r} + w(r,z)\mathbf{e_z}$.

The local flow field is therefore given by

$$u_i = -\frac{rw_z}{2} + \frac{a_i(a_{it} + wa_{iz} + ua_{ir})}{r} + \frac{w_z a_i^2}{2r}. \tag{10.18}$$

In §10.2.5 below, we will use the form of the local flow field together with a stress balance on the surface of a single bubble to derive an equation for the fluid pressure. Before doing this, however, we determine n.

10.2.4 The evolution equation for the bubble number density

The final property of the system that we have not taken account of is the bubble number density, n, which is directly related through the problem geometry to the

number of bubbles in a transverse cross–section and hence in the final drawn fibre. The number density n (dimensions m^{-2}) is the number of bubbles per unit area of cross–section, averaged over a region of approximately ten bubbles. We assume that bubbles remain open (i.e. that surface tension does not completely close them) and that bubbles do not coalesce. This is tantamount to requiring a conservation of the number of bubbles.

In order to derive an equation that enforces the condition of "conservation of bubbles" we consider a ring of infinitesimal thickness $dr(t)$ in a transverse cross–section. The ring has area J given by

$$J = 2\pi r(t) dr(t). \tag{10.19}$$

As the fibre is drawn down the ring is translated in z, and expands or contracts (in r) according to the radial velocity of the fluid at its inner and outer edge. The rate of change of area is given by

$$\frac{dJ(t)}{dt} = 2\pi \left(\frac{dr(t)}{dt} dr(t) + r(t) \frac{d\left(dr(t)\right)}{dt} dr(t) \right), \tag{10.20}$$

where $\frac{dr(t)}{dt} dr(t)$ denotes the change of the inner radius, previously at $r(t)$, and $r(t) \frac{d(dr(t))}{dt} dr(t)$ denotes the change in difference between outer and inner radii, previously $dr(t)$. We may use the relations

$$\frac{dr(t)}{dt} = u,$$

and

$$\frac{d\left(dr(t)\right)}{dt} = \frac{du}{dr} dr,$$

to rewrite (10.20) as

$$\frac{dJ(t)}{dt} = 2\pi \left(u dr(t) + r(t) \frac{du}{dr} dr \right). \tag{10.21}$$

The statement that the number of bubbles within area J remains constant following the element may be expressed as

$$Jn = G, \tag{10.22}$$

where n is the bubble number density and G is a constant. Taking the convective derivative of equation (10.22) gives

$$n\frac{dJ}{dt} + J\frac{Dn}{Dt} = 0, \tag{10.23}$$

where

$$\frac{Dn}{Dt} = n_t + un_r + wn_z. \tag{10.24}$$

Substituting (10.24) into (10.23) and rearranging gives

$$\frac{n}{r}(ru)_r + (n_t + un_r + wn_z) = 0. \tag{10.25}$$

As an example of a possible solution of equation (10.25), we consider the steady–state case where $h(z,t) = h_0 \exp\left(-\frac{\beta z}{2}\right)$, $w = W_f e^{(\beta z)}$ and we have the boundary condition $n(0,r,t) = N_0$. Equation (10.25) may now be solved in closed–form to give

$$n(z,r,t) = N_0 \exp(\beta z),$$

which may be interpreted as stating that as the preform thins, the number *density* (the number of bubbles per unit area of cross–section) must increase accordingly in order that the number of bubbles remains the same. We thus see that, as expected, the distribution of bubbles in a cross–section remains the same when a geometry–preserving solution for w is assumed.

10.2.5 Stress balance on the surface of a single bubble

In order to relate the local flow field to the macroscopic properties of the fluid we conduct a stress balance on the surface on a single bubble using result (10.25) above. A local stress balance on the surface of a bubble i, where $(i = 1, 2, ...D)$, gives

$$p_i + \frac{\gamma}{a_i} - p = 2\mu u_{ir}|_{r=a_i}. \tag{10.26}$$

Using the result for u_i from equation (10.18), (10.26) becomes

$$p_i + \frac{\gamma}{a_i} - p = 2\mu\left(w_z + \frac{a_{it} + wa_{iz} + ua_{ir}}{a_i}\right). \tag{10.27}$$

The next step is to transform equation (10.27) from one that accounts for a discrete set of bubbles to one that accounts for a continuum of infinitely–long cylindrical bubbles with an area number density of bubbles, $n = n(z, r, t)$ and a bubble radius $a = a(z, r, t)$. To do this we integrate (10.27) over the area of approximately ten bubbles in order that the equations are global and depend on the averaged bubble number density and bubble radius at a given point in the fluid.

Equation (10.27) thus becomes

$$p_H + \frac{\gamma}{a} - p = 2\mu \left(w_z + \frac{a_t + w a_z + u a_r}{a} \right), \tag{10.28}$$

where p_H denotes the pressure inside the bubbles and in general is a function of position in the fluid and time. However, we will assume that it is the same pressure in every bubble for all time without any loss of generality. We also assume that the pressure within a single bubble does not vary with r, z or t. This restriction may therefore be relaxed at any stage.

10.2.6 Non–dimensionalization, asymptotic analysis and boundary conditions

Our model now consists of five equations (10.1)–(10.2), (10.17), (10.27) and (10.28) for the five unknowns w, u, p, a and n. The equations are

$$\rho(w_t + u w_r + w w_z) = -p_z + \frac{\mu}{r}(r w_r)_r + 2\mu w_{zz} + \frac{\mu}{r}(r u_z)_r + \rho g, \tag{10.29}$$

$$\rho\left(u_t + u u_r + w u_z\right) = -p_r + \mu \left(\frac{1}{r}(ru)_r \right)_r + \mu u_{zz}, \tag{10.30}$$

$$\frac{1}{r}(ru\alpha)_r = -(\alpha w)_z, \tag{10.31}$$

$$\frac{n}{r}(ru)_r + (n_t + u n_r + w n_z) = 0, \tag{10.32}$$

$$p_H - p + \frac{\gamma}{a} = 2\mu \left(w_z + \frac{a_t + w a_z + u a_r}{a} \right), \tag{10.33}$$

where $\alpha = 1 - \pi a^2 n$.

It is not entirely clear what the boundary conditions for equations (10.29)–(10.33) are, but more modelling is to be done and the initial and boundary conditions include

$$\begin{aligned} w(0,t) &= W_f, \\ w(1,t) &= W_d, \\ h(0,t) &= h_0, \\ a(0,r,t) &= A_0(r), \\ n(0,r,t) &= N_0(r), \end{aligned}$$

for $t \geq 0$.

We will presently non–dimensionalize the equations and make simplifying assumptions by taking advantage of the problem geometry. However, we note that equations (10.29)–(10.33) were derived without any such assumptions. The only assumption beyond the usual assumptions of continuum fluid dynamics was of the smoothness of the functions and first derivatives of a and n.

It is now appropriate to non–dimensionalize (10.29)–(10.33) to take advantage of the small parameters present, henceforth allowing dominant terms to become evident. To non–dimensionalize we set

$$z = L\bar{z}, \quad r = h_0\bar{r},$$

$$h = h_0\bar{h}, \quad \mu = \mu_0\bar{\mu},$$

$$p = (\mu_0 W/L)\bar{p}, \quad w = W\bar{w},$$

$$u = (hW/L)\bar{u}, \quad a = A\bar{a},$$

$$n = N\bar{n}, \quad \gamma = \mu_0 W\epsilon^2\bar{\gamma},$$

$$t = (L/W)\bar{t},$$

where an overbar denotes a non–dimensional quantity and the surface tension coefficient γ was chosen in the same way as in Chapter 3, §3.5. We only need model the region encompassed by the hot–zone of the drawing furnace, since the fluid solidifies

rapidly and is therefore everywhere else assumed to be solid. Here L denotes a typical hot–zone length in the fibre drawing furnace, h denotes a typical drawn capillary size, W denotes a typical draw speed, A denotes a typical bubble radius and N and μ_0 denote a typical bubble number density and typical glass viscosity respectively.

As mentioned above, we wish to allow for the possibility of controlling hole size by internal hole pressurization. The normal stress boundary conditions will thus include both the surface tension coefficient γ and the fibre hole pressure p_H. If we define the non–dimensional fibre hole pressure by $p_H = (\mu_0 W/L)\bar{p}_H$, it is clear that we must further write

$$\bar{p}_H = \frac{\bar{p}_a}{\epsilon^2} + \bar{p}_b, \tag{10.34}$$

where $\bar{p}_b$ is the non–dimensional hole overpressure and $\bar{p}_a$ denotes the non–dimensional ambient pressure, defined in the obvious way by

$$p_a = (\mu_0 W/L)\bar{p}_a.$$

This scaling reflects the fact that, unless the fibre hole pressure is within $O(\epsilon^2)$ of the ambient pressure, the capillary will either collapse immediately or "explode" [14]. Equation (10.34) therefore already gives a useful estimate of the size of hole inflation pressure that is required to prevent collapse.

Upon application of these non–dimensionalizations the equations become

$$\epsilon^2 Re\,(\bar{w}_{\bar{t}} + \bar{u}\bar{w}_{\bar{r}} + \bar{w}\bar{w}_{\bar{z}}) = -\epsilon^2\bar{p}_{\bar{z}} + \frac{\bar{\mu}}{\bar{r}}(\bar{r}\bar{w}_{\bar{r}})_{\bar{r}} + \epsilon^2 2\bar{\mu}\bar{w}_{\bar{z}\bar{z}} + \frac{\epsilon^2\bar{\mu}}{\bar{r}}(\bar{r}\bar{u}_{\bar{z}})_{\bar{r}} + \frac{\epsilon^2 Re}{Fr}, \tag{10.35}$$

$$\epsilon^2 Re\,(\bar{u}_{\bar{t}} + \bar{u}\bar{u}_{\bar{r}} + \bar{w}\bar{u}_{\bar{z}}) = -\bar{p}_{\bar{r}} + \bar{\mu}\left(\frac{1}{\bar{r}}(\bar{r}\bar{u})_{\bar{r}}\right)_{\bar{r}} + \epsilon^2\bar{\mu}\bar{u}_{\bar{z}\bar{z}}, \tag{10.36}$$

$$\frac{1}{\bar{r}}(\bar{r}\bar{u}(1 - \pi A^2 N\bar{a}^2\bar{n}))_{\bar{r}} = -\left((1 - \pi A^2 N\bar{a}^2\bar{n})\bar{w}\right)_{\bar{z}}, \tag{10.37}$$

$$\frac{\bar{n}}{\bar{r}}(\bar{r}\bar{u})_{\bar{r}} + (\bar{n}_{\bar{t}} + \bar{u}\bar{n}_{\bar{r}} + \bar{w}\bar{n}_{\bar{z}}) = 0, \tag{10.38}$$

$$\bar{p}_b - \bar{P} + \frac{\epsilon}{\psi}\frac{\bar{\gamma}}{\bar{a}} = 2\bar{\mu}\left(\bar{w}_{\bar{z}} + \frac{\bar{a}_{\bar{t}} + \bar{w}\bar{a}_{\bar{z}} + \bar{u}\bar{a}_{\bar{r}}}{\bar{a}}\right), \tag{10.39}$$

where the key non–dimensional parameters in the problem are given by

$$\epsilon = \frac{h}{L}, \quad Re = \frac{\rho W L}{\mu_0}, \quad Fr = \frac{W^2}{gL}, \quad \psi = \frac{A}{h_0}.$$

We note at this stage that in all cases of interest $h_0 \ll L$ (the largest values of ϵ tend to occur for capillaries where L is of order cm and h of order mm. For optical fibres ϵ is smaller still). We thence assume that the small parameter in the problem is ϵ, where $\epsilon \ll 1$. The leading–order equations in ϵ are now satisfied by the obvious *ansätze*, as we seek solutions in the form of expansions in powers of the small parameter ϵ. We set

$$\begin{aligned}
\bar{w} &= \bar{w}_0(\bar{z},\bar{t}) + \epsilon^2 \bar{w}_1(\bar{z},\bar{r},\bar{t}) + \ldots\ldots, \\
\bar{u} &= \bar{u}_0(\bar{z},\bar{r},\bar{t}) + \epsilon^2 \bar{u}_1(\bar{z},\bar{r},\bar{t}) + \ldots\ldots, \\
\bar{p} &= \frac{\bar{p}_a}{\epsilon^2} + \bar{P}(\bar{z},\bar{r},\bar{t}) + \ldots\ldots, \\
\bar{a} &= \bar{a}_0(\bar{z},\bar{r},\bar{t}) + \epsilon^2 \bar{a}_1(\bar{z},\bar{r},\bar{t}) + \ldots\ldots, \\
\bar{n} &= \bar{n}_0(\bar{z},\bar{r},\bar{t}) + \epsilon^2 \bar{n}_1(\bar{z},\bar{r},\bar{t}) + \ldots\ldots
\end{aligned}$$

To first order in ϵ the $\bar{z}$-momentum equation (10.35) becomes

$$Re\,(\bar{w}_{0\bar{t}} + \bar{w}_0\bar{w}_{0\bar{z}}) + \bar{P}_{\bar{z}} - \frac{Re}{Fr} - 2\bar{\mu}\bar{w}_{0\bar{z}\bar{z}} + \frac{\bar{\mu}}{\bar{r}}(\bar{r}\bar{u}_{\bar{z}})_{\bar{r}} = \frac{\bar{\mu}}{\bar{r}}(\bar{r}\bar{w}_{1\bar{r}})_{\bar{r}}, \tag{10.40}$$

and the $\bar{r}$–momentum equation (10.36) yields $\bar{P}_{\bar{r}} = 0$ so that $\bar{P}$ is a function of $\bar{z}$ and $\bar{t}$ alone.

Ignoring terms $O(\epsilon^y)$ where $(y \geq 2)$, equations (10.37)–(10.39) become

$$\frac{1}{\bar{r}}(\bar{r}\bar{u}_0(1 - \pi A^2 N \bar{a}_0^2 \bar{n}_0))_{\bar{r}} = -\left((1 - \pi A^2 N \bar{a}_0^2 \bar{n}_0)\bar{w}_0\right)_{\bar{z}}, \tag{10.41}$$

$$\frac{\bar{n}_0}{\bar{r}}(\bar{r}\bar{u}_0)_{\bar{r}} + (\bar{n}_{0\bar{t}} + \bar{u}_0\bar{n}_{0\bar{r}} + \bar{w}_0\bar{n}_{0\bar{z}}) = 0, \tag{10.42}$$

$$\bar{p}_b - \bar{P} + \frac{\epsilon}{\psi}\frac{\bar{\gamma}}{\bar{a}_0} = 2\bar{\mu}\left(\bar{w}_{0\bar{z}} + \frac{\bar{a}_{0\bar{t}} + \bar{w}_0\bar{a}_{0\bar{z}} + \bar{u}_0\bar{a}_{0\bar{r}}}{\bar{a}_0}\right). \tag{10.43}$$

The surface tension term in equation (10.43) is included because ψ can be as small as ϵ, as will become clear.

It is now appropriate to consider the boundary conditions for the flow. The kinematic boundary condition is

$$\bar{u}_0 = \bar{h}_{\bar{t}} + \bar{w}_0\bar{h}_{\bar{z}} \quad \text{at} \quad \bar{r} = \bar{h}. \tag{10.44}$$

The normal stress boundary conditions may now be applied. The stress tensor $\mathcal{T}$ is given by

$$\mathcal{T} = \begin{pmatrix} (\frac{\mu_0 W}{L})(-\bar{p} + 2\bar{\mu}\bar{w}_{\bar{z}}) & (\frac{\mu_0 W}{L})(\bar{\mu}\epsilon\bar{u}_{\bar{z}} + \frac{\bar{\mu}\bar{w}_{\bar{r}}}{\epsilon}) \\ (\frac{\mu_0 W}{L})(\bar{\mu}\epsilon\bar{u}_{\bar{z}} + \frac{\bar{\mu}\bar{w}_{\bar{r}}}{\epsilon}) & (\frac{\mu_0 W}{L})(-\bar{p} + 2\bar{\mu}\bar{u}_{\bar{r}}) \end{pmatrix}.$$

If we denote the dimensionless unit outward-pointing normal to $\bar{r} = \bar{h}$ by $\hat{\boldsymbol{n}}$, then the normal stress conditions are

$$-\hat{\boldsymbol{n}}^T \mathcal{T} \hat{\boldsymbol{n}} - \frac{\epsilon\bar{\gamma}\mu_0 W}{\bar{h}L} = \frac{\bar{p}_a \mu_0 W}{L\epsilon^2} \text{ at } \bar{r} = \bar{h}. \tag{10.45}$$

We assume that the tangential stress on both of the fibre boundaries is zero (for rotation rates used in typical research–grade drawing towers this is realistic and so rotation may be included at a later stage without affecting the validity of this boundary condition), giving

$$\hat{\boldsymbol{t}}^T \mathcal{T} \hat{\boldsymbol{n}} = 0,$$

where $\hat{\boldsymbol{t}}$ is the unit tangent vector.

To complete the specification of the boundary conditions, the normal and tangential stress conditions may now be expanded according to the *ansätze* for $\bar{w}$, $\bar{u}$ and $\bar{p}$. With

$$\hat{\boldsymbol{n}}^T = \frac{(-1)}{\sqrt{1+\epsilon^2\bar{h}_{\bar{z}}^2}}(\epsilon\bar{h}_{\bar{z}}, -1), \quad \hat{\boldsymbol{t}}^T = \frac{(-1)}{\sqrt{1+\epsilon^2\bar{h}_{\bar{z}}^2}}(1, \epsilon\bar{h}_{\bar{z}}),$$

we find that

$$\begin{aligned} \frac{\epsilon\bar{\gamma}}{\bar{h}} - \bar{P} + 2\bar{\mu}\bar{u}_{0\bar{r}} &= 0 \quad \text{at } \bar{r} = \bar{h}, \\ 2\bar{h}_{\bar{z}}(\bar{w}_{0\bar{z}} - \bar{u}_{0\bar{r}}) - \bar{u}_{0\bar{z}} &= \bar{w}_{1\bar{r}} \quad \text{at } \bar{r} = \bar{h}. \end{aligned}$$

10.2.7 Deriving a closed system

It is now possible to derive a closed system of leading order equations that govern the drawing of holey fibres. Dropping overbars, we now have four equations in six

unknowns (w_0, w_1, u_0, a_0, n_0, P), and three boundary conditions given by

$$Re\,(w_{0t} + w_0 w_{0z}) + P_z - \frac{Re}{Fr} - 2\mu w_{0zz} - \frac{\mu}{r}(r u_{0z})_r = \frac{\mu}{r}(r w_{1r})_r, \tag{10.46}$$

$$\frac{1}{r}(r u_0 \alpha)_r = -(\alpha w_0)_z, \tag{10.47}$$

$$\frac{n_0}{r}\,(r u_0)_r + (n_{0t} + u_0 n_{0r} + w_0 n_{0z}) = 0, \tag{10.48}$$

$$p_b - P + \frac{\epsilon}{\psi}\frac{\gamma}{a_0} = 2\mu\left(w_{0z} + \frac{a_{0t} + w_0 a_{0z} + u_0 a_{0r}}{a_0}\right), \tag{10.49}$$

where $\alpha = 1 - \delta$, $\delta = \pi A^2 N a_0^2 n_0$ and

$$\frac{\epsilon\gamma}{h} - P + 2\mu u_{0r} = 0 \quad \text{at } r = h, \tag{10.50}$$

$$2h_z(w_{0z} - u_{0r}) - u_{0z} = w_{1r} \quad \text{at } r = h, \tag{10.51}$$

$$h_t + w_0 h_z = u_0 \quad \text{at } r = h. \tag{10.52}$$

(i) Solving (10.47) for u_0 gives

$$u_0 = -r\frac{(\alpha w_0)_z}{2\alpha}, \tag{10.53}$$

and the stress boundary–condition (10.50) on $r = h$ gives

$$P = \frac{\epsilon\gamma}{h} - \frac{\mu(\alpha w_0)_z}{\alpha}. \tag{10.54}$$

Equations (10.53)–(10.54) may be used in (10.46), which may then be integrated over a preform cross–section from $r = 0$ to $r = h(z)$. Now (10.51) gives,

$$w_{1r}|_{r=h} = h_z\left(2w_{0z} + \frac{(\alpha w_0)_z}{\alpha}\right) + \frac{h}{2}\left(\frac{(\alpha w_0)_z}{\alpha}\right)_z. \tag{10.55}$$

Using this, (10.46) may be reduced to

$$Reh^2\left(w_{0t} + w_0 w_{0z} - \frac{1}{Fr}\right) = \left(2\mu h^2 w_{0z} + h^2\frac{\mu(\alpha w_0)_z}{\alpha} + \epsilon\gamma h\right)_z. \tag{10.56}$$

(ii) Using the stress balance on a single bubble (10.49) and the result (10.54) for P in (10.49) gives

$$2\mu\,(a_{0t} + (w_0 a_0)_z) = r a_{0r}\frac{\mu(\alpha w_0)_z}{\alpha} + a_0\left(\frac{\mu(\alpha w_0)_z}{\alpha} + P_b\right) - \epsilon\gamma\left(\frac{1}{\psi} + \frac{a_0}{h}\right). \tag{10.57}$$

(iii) Using the equation of continuity (10.47) together with the kinematic boundary–condition (10.52) we have that

$$\alpha(h^2)_t + (h^2\alpha w_0)_z = 0. \tag{10.58}$$

(iv) The equation for the conservation of the number of bubbles in a cross–section (10.48) is rewritten using (10.53) to give

$$\frac{n_0}{\alpha}(\alpha w_0)_z = \left(n_{0t} + w_0 n_{0z} - r n_{0r}\frac{(\alpha w_0)_z}{2\alpha}\right), \tag{10.59}$$

where we have made use of (10.58) to allow differentiation with respect to r.

When $\delta \to 0$ we recover equations (3.59)–(3.61) in Chapter 3, §3.5, with $h_1 = 0$, which are the solid fibre equations as expected.

10.2.8 Summary of equations and boundary conditions

The closed system is represented by four partial differential leading order equations in the four unknowns $w_0(z,t)$, $h(z,t)$, $a_0(z,r,t)$ and $n_0(z,r,t)$. The equations are

$$Reh^2\left(w_{0t} + w_0 w_{0z} - \frac{1}{Fr}\right) = \left(2\mu h^2 w_{0z} + h^2\frac{\mu(\alpha w_0)_z}{\alpha} + \epsilon\gamma h\right)_z, \tag{10.60}$$

$$2\mu\left(a_{0t} + (w_0 a_0)_z\right) = r a_{0r}\frac{\mu(\alpha w_0)_z}{\alpha} + a_0\left(\frac{\mu(\alpha w_0)_z}{\alpha} + P_b\right) - \epsilon\gamma\left(\frac{1}{\psi} + \frac{a_0}{h}\right), \tag{10.61}$$

$$\alpha(h^2)_t + (h^2\alpha w_0)_z = 0, \tag{10.62}$$

$$\frac{n_0}{\alpha}(\alpha w_0)_z = \left(n_{0t} + w_0 n_{0z} - r n_{0r}\frac{(\alpha w_0)_z}{2\alpha}\right). \tag{10.63}$$

Equation (10.60) may be considered an equation for w_0, equation (10.61) as an equation for the evolution of a_0, equation (10.62) an equation for h, and equation (10.63) an equation for n_0. We note that equations (10.60)–(10.61) depend only on (z,t) and equations (10.62)–(10.63) depend on (z,r,t). To show this we note that, for example, in equation (10.60) the term $h^2\frac{\mu(\alpha w_0)_z}{\alpha}$ may be rewritten using (10.62)

as $-[(h^2)_t + 2hh_z w]$, which depends on (z,t) only. Similarly, in equation (10.62) the term $(h^2 \alpha w_0)_z$ may be rewritten using (10.60) such that it depends on (z,t) only.

For the unsteady problem the initial and boundary conditions are not clear. However, we shall only consider steady–state problems and in this case the initial and boundary conditions for equations (10.60)–(10.63) are given by

$$\begin{aligned} w_0(0,t) &= W_f, \\ w_0(1,t) &= W_d, \\ h(0,t) &= h_0, \\ a_0(0,r,t) &= A_0(r), \\ n_0(0,r,t) &= N_0(r), \end{aligned}$$

for $t \geq 0$.

These are the key equations in this Chapter, which we shall go on to solve numerically in §10.5.1. First though, we examine some interesting limiting cases.

10.3 Analytic and numerical analysis

There are many interesting asymptotic limits that we could investigate, but here we focus solely on the limit where $\delta \ll 1$, which corresponds to a limit where only a small fraction of the cross–section is air, the bulk of it being glass. Since $\delta = \pi A^2 N a_0^2 n_0$, this condition may be satisfied by having an extremely small number density (few bubbles per unit area of cross–section), or by having many bubbles but of small radius. In this limit one would expect that the fluid flow is unaffected by the presence of the bubbles. This is evidenced by the fact that a_0 and n_0 decouple from the equation for w_0 (10.60) and from the equation for h_0 (10.62), leaving an equation for a_0 (10.61) and an equation (10.63) for n_0 that may thus be solved separately from the flow problem of determining w_0 and h.

In the limit $\delta \to 0$ equations (10.60)–(10.63) become

$$Reh^2\left(w_{0t} + w_0 w_{0z} - \frac{1}{Fr}\right) = \left(2\mu h^2 w_{0z} + \mu h^2 w_{0z} + \epsilon\gamma h\right)_z, \tag{10.64}$$

$$2\mu\left(a_{0t} + (w_0 a_0)_z\right) = r\mu a_{0r} w_{0z} + a_0\left(\mu w_{0z} + P_b\right) - \epsilon\gamma\left(\frac{1}{\psi} + \frac{a_0}{h}\right), \tag{10.65}$$

$$(h^2)_t + (h^2 w_0)_z = 0, \tag{10.66}$$

$$n_0 w_{0z} = \left(n_{0t} + w_0 n_{0z} - r n_{0r}\frac{w_{0z}}{2}\right). \tag{10.67}$$

Since in the limit $\delta \ll 1$ the evolution equations for a_0 and n_0 decouple from the flow problem we expect that if the initial conditions for a_0 and n_0 are independent of r, that the solutions for $a_0(z, r, t)$ and $n_0(z, r, t)$ prove to be independent of r. We may confirm this for the case of no surface tension γ, internal bubble pressure P_b, Reynolds number Re and for steady–draws by solving the equations (10.64)–(10.67) in closed form. This gives

$$\begin{aligned} w_0 &= W_f e^{(\beta z)} \\ h &= h_0 e^{-\left(\frac{\beta z}{2}\right)} \\ a_0 &= F_1\left(r e^{\frac{\beta z}{2}}\right) e^{-\frac{\beta z}{2}} \\ n_0 &= F_2\left(r e^{\frac{\beta z}{2}}\right) e^{\beta z} \end{aligned}$$

Applying boundary conditions that assert no radial dependence of a_0 or n_0 at $z = 0$ ensures that no radial dependence develops later in the draw (for $z \neq 0$). We therefore set $a_0(0) = A_0$ and $n_0(0) = N_0$ to obtain leading–order solutions of

$$\begin{aligned} a_0 &= A_0 e^{-\frac{\beta z}{2}} \\ n_0 &= N_0 e^{\beta z}. \end{aligned}$$

For all cases where the boundary conditions for a_0 and n_0 do not include an r dependence, these will be the leading–order solutions to the equations; a result that will be used in the following analysis.

10.3.1 The effects of surface tension

Including the effect of surface tension but ignoring those of gravity, inertia, hole overpressure and taking $\delta \to 0$, allows us to assume a perturbation solution for the variables by writing, dropping subscripts in the governing equations,

$$w = w_0(z) + \gamma w_1(z), \tag{10.68}$$

$$h = h_0(z) + \gamma h_1(z), \tag{10.69}$$

$$a = a_0(z) + \gamma a_1(r, z), \tag{10.70}$$

$$n = n_0(z) + \gamma n_1(r, z). \tag{10.71}$$

Substituting these into equations (10.64)–(10.67) and equating terms of similar power in ϵ allows us to solve for w, h, and a in closed–form but not for n. Applying boundary conditions $w_1(0) = 0$, $w_1(1) = 0$ and $h_0(0) = 0$ gives

$$w_1 = \frac{2}{3\beta h_0} e^{\frac{\beta z}{2}} \left(1 + e^{\frac{\beta z}{2}} \left(z\left(1 - e^{-\frac{\beta}{2}}\right) - 1\right)\right) \tag{10.72}$$

$$h_1 = \frac{1}{3W_f\beta} \left(1 - e^{-\frac{\beta z}{2}} + z\left(1 - e^{-\frac{\beta}{2}}\right)\right). \tag{10.73}$$

The solution for a_1 is given in terms of a general function $F\left(re^{-\frac{\beta z}{2}}\right)$, which is determined by noting that $a_1(0, r) \equiv 0$, requiring that

$$F(r) = -\frac{2\psi A_0 + 3h_0}{3h_0 W_f \psi \beta}.$$

Thus

$$a_1 = \frac{e^{-\frac{\beta z}{2}}}{3h_0 W_f \beta \psi} \left((2\psi A_0 + 3h_0)e^{-\frac{\beta z}{2}} + A_0 \psi z \left(e^{-\frac{\beta}{2}} - 1\right) - (2\psi A_0 + 3h_0)\right). \tag{10.74}$$

The exact form of the solution for a_1 varies with parameter values, but an example if given in Figure 10.2 below where we have set $A_0 = 1$, $W_f = 0.1$, $W_d = 1$, $h_0 = 1$ and $\psi = 1$. It may be seen that a_1 is negative for all values of z, but that towards the end of the draw its value starts to increase. This is a result of the fact that the effects of surface tension on the solution for h_1 is to cause h_1 to be everywhere positive but that surface tension still acts to close individual holes and thus locally decrease the value of a from its unperturbed value. Of course, whilst a_1 remains everywhere negative, a remains positive for all z as seen in Figure 10.2.

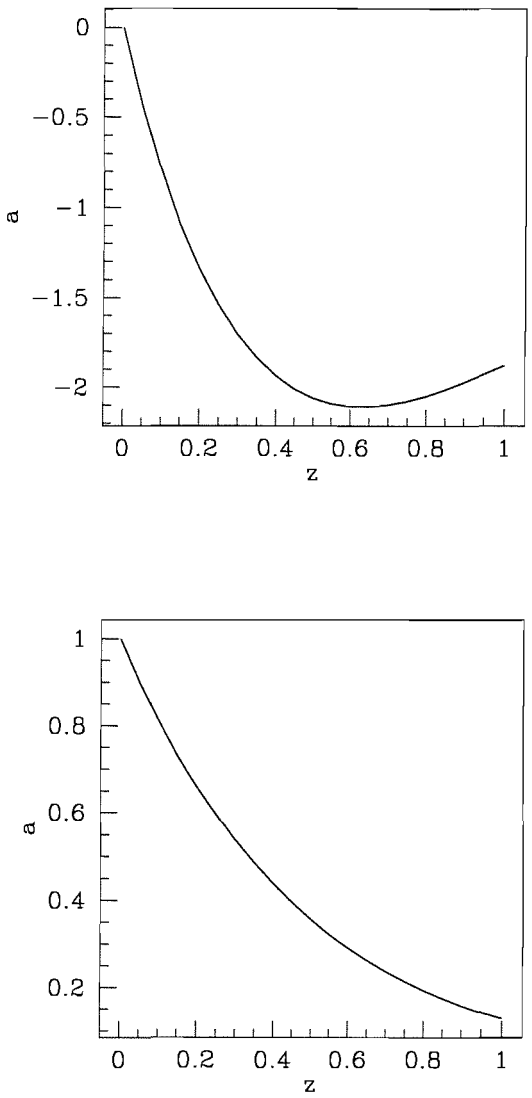

Figure 10.2: Top: the solution for a_1 and bottom: the solution for a.

10.4 Variable viscosity

We have assumed that the temperature in the furnace is constant, allowing us to suppose that the viscosity does not vary with position. However, in reality there is often some variation in temperature and thus viscosity, which we will now account for by rederiving the equations that determine the evolution of bubble size and distribution and allowing a variation in viscosity. First the viscosity of the glass does vary from place to place and time to time, but secondly it may turn out to be a useful tool in controlling, for example, the radial distribution of hole size.

We commence by assuming a viscosity distribution whose z and r component parts are separable by setting

$$\mu(r,z) = \mu'(r) + \mu''(z) + \mu_0, \tag{10.75}$$

where μ_0 is a constant (note that primes do *not* denote differentiation). The equation of continuity (10.47) may be solved to give

$$u = -r\frac{(\alpha w)_z}{2\alpha}, \tag{10.76}$$

which may be used in the z–momentum equation (10.46) to give

$$Re\left(w_t + ww_z - \frac{1}{Fr}\right) + P_z - 2(\mu w_z) - \frac{1}{r}(\mu r u_z)_r = \frac{1}{r}(\mu r w_{1r})_r, \tag{10.77}$$

together with stress boundary–condition (10.50) to give

$$Re\left(w_t + ww_z - \frac{1}{Fr}\right) - \frac{\epsilon\gamma h_z}{h^2} - \left(\mu\frac{(\alpha w)_z}{\alpha}\right) - 2(\mu w_z)_z + \mu\left(\frac{(\alpha w)_z}{\alpha}\right)_z$$
$$+ r\mu_r\left(\frac{(\alpha w)_z}{2\alpha}\right)_z = \frac{1}{r}(\mu r w_{1r})_r, \tag{10.78}$$

where we have here and henceforth dropped all zero subscripts.

The first–order stress boundary–condition (10.51) may then be used in equation (10.78) together with (10.75), and integrated from $r = 0$ to $r = h(z,t)$ to give

$$Reh^2\left(w_t + ww_z - \frac{1}{Fr}\right) - \epsilon\gamma h_z - 2\left(\frac{(\alpha w)_z}{\alpha}\right)\left(\int_0^{h(z,t)} r\mu''(z)_z\, dr\right.$$

$$+ (\mu'(r) + \mu''(z) + \mu_0)hh_z\Big) + \left(\frac{(\alpha w)_z}{\alpha}\right)_z \left(\int_0^{h(z,t)} r^2\mu'(r)_r\, dr - (\mu'(r) + \mu''(z)$$
$$+ \mu_0)h^2\Big) - 4w_{zz}\int_0^{h(z,t)} r\mu'(r)\, dr - 2(\mu'(r) + \mu''(z) + \mu_0)w_{zz}h^2$$
$$- 4w_z\int_0^{h(z,t)} r\mu''(z)_z\, dr - 4(\mu'(r) + \mu''(z) + \mu_0)hh_z w_z = 0. \tag{10.79}$$

The three other equations that govern the case of variable viscosity, namely (10.61)–(10.63), remain unchanged by allowing for variable viscosity.

10.4.1 Summary of equations and boundary conditions allowing for a variable viscosity

The closed system that allows for variable viscosity is represented by four partial differential leading order equations in the four unknowns $w(z,t)$, $h(z,t)$, $a(z,r,t)$ and $n(z,r,t)$. The equations are

$$Reh^2\left(w_t + ww_z - \frac{1}{Fr}\right) - \epsilon\gamma h_z - 2\left(\frac{(\alpha w)_z}{\alpha}\right)\left(\int_0^{h(z,t)} r\mu''(z)_z\, dr$$
$$+ (\mu'(r) + \mu''(z) + \mu_0)hh_z\Big) + \left(\frac{(\alpha w)_z}{\alpha}\right)_z \left(\int_0^{h(z,t)} r^2\mu'(r)_r\, dr - (\mu'(r) + \mu''(z)$$
$$+ \mu_0)h^2\Big) - 4w_{zz}\int_0^{h(z,t)} r\mu'(r)\, dr - 2(\mu'(r) + \mu''(z) + \mu_0)w_{zz}h^2$$
$$- 4w_z\int_0^{h(z,t)} r\mu''(z)_z\, dr - 4(\mu'(r) + \mu''(z) + \mu_0)hh_z w_z = 0, \tag{10.80}$$
$$2\mu\left(a_{0t} + (w_0 a_0)_z\right) = ra_{0r}\frac{\mu(\alpha w_0)_z}{\alpha} + a_0\left(\frac{\mu(\alpha w_0)_z}{\alpha} + P_b\right)$$
$$- \epsilon\gamma\left(\frac{1}{\psi} + \frac{a_0}{h}\right), \tag{10.81}$$
$$\alpha(h^2)_t + (h^2\alpha w_0)_z = 0, \tag{10.82}$$
$$\frac{n}{\alpha}(\alpha w)_z = \left(n_t + wn_z - rn_r\frac{(\alpha w)_z}{2\alpha}\right). \tag{10.83}$$

The initial and boundary conditions for these equations are

$$\begin{aligned} w(0,t) &= W_f, \\ w(1,t) &= W_d, \\ h(0,t) &= h_0, \\ a(0,r,t) &= A_0(r), \\ n(0,r,t) &= N_0(r), \end{aligned}$$

for $t \geq 0$.

We note that by setting $\mu'(r) = 0$ and $\mu''(z) = 0$, (10.80) reduces to (10.60), as required. At this point we assume that $\mu(r,z)$ has the form $\mu(r,z) = fz + gr + \mu_0$. This is reasonable since a consideration of heat transfer processes suggests that the viscosity is likely to decrease with increasing radius, and vary along the length of the furnace such that having been in the furnace for longer, glass positioned at large z has a higher temperature.

Using this in (10.80) gives

$$\begin{aligned} Reh^2\left(w_t + ww_z + \frac{1}{Fr}\right) = \left(2w_z h^2\left(\frac{2gh}{3} + fz + \mu_0\right)\right. \\ \left. + \frac{(\alpha w)_z}{\alpha} h^2\left(\frac{2gh}{3} + fz + \mu_0\right) + \epsilon\gamma h\right)_z. \end{aligned} \tag{10.84}$$

Setting, for example, $g = 0$ allows equations (10.84) and (10.81)–(10.83) to be solved in closed form with boundary conditions $h(0) = h_0$, $w(0) = W_f$, $w(1) = W_d$, $a(r,z) = A_0 R(r)$ and $n(r,z) = N_0 R'(r)$ to give

$$h = h_0 \mu_0^{\left(-\frac{\beta}{2\chi_1}\right)} (fz + \mu_0)^{\left(\frac{\beta}{2\chi_1}\right)}, \tag{10.85}$$

$$w = W_f \exp\left(\frac{\beta\chi_2}{\chi_1}\right)(fz + \mu_0)^{\left(-\frac{\beta}{\chi_1}\right)}, \tag{10.86}$$

$$a = A_0 R\left(r\beta^{-\frac{\chi_2 fz}{2\chi_1}}\right)\beta^{\left(-\frac{\chi_2 fz}{\chi_1}\right)}, \tag{10.87}$$

$$n = N_0 R'\left(r\beta^{-\frac{\chi_2 fz}{2\chi_1}}\right)\beta^{\left(-\frac{\chi_2 fz}{\chi_1}\right)}, \tag{10.88}$$

where

$$\chi_1 = \ln\left(\frac{f + \mu_0}{\mu_0}\right),$$

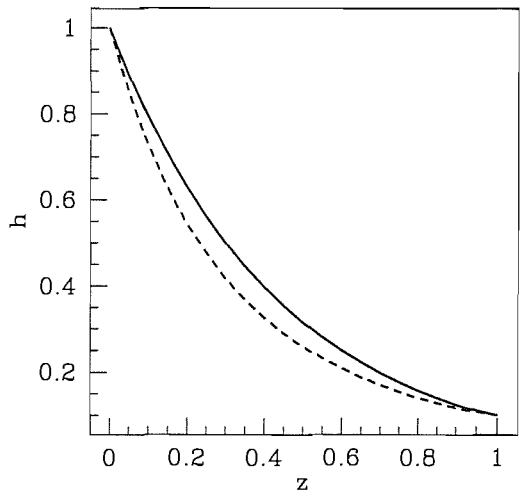

Figure 10.3: Graph to show variable–viscosity solution for h, where $W_f = 10^{-2}$, $W_d = 1$, $h_0 = 1$, $A_0 = 1$, $f = 1$ (lower curve) and $f = 0$ (upper curve).

$$\chi_2 = \ln(\mu_0).$$

Setting $W_f = 10^{-2}$, $W_d = 1$, $h_0 = 1$, $A_0 = 1$, $\delta = 0$, $Re = 0$, $\gamma = 0$, $P_b = 0$, $g = 0$, and $f = 1$, $f = 0$, gives the solutions shown in Figures 10.3-10.5. Figure 10.3 shows solutions for h with $f = 0$ and $f = 1$, where it is clear to see that the effects of including a variable viscosity (resulting from furnace temperature that varies with z) are to decrease the value of h for all z. Figure 10.4 shows solutions for w with $f = 0$ and $f = 1$, where because of the effect on h described above, we see that w is increased for all z. Finally, Figure 10.5 shows solutions for a with $f = 0$ and $f = 1$. The effect on a is more pronounced than for h or w.

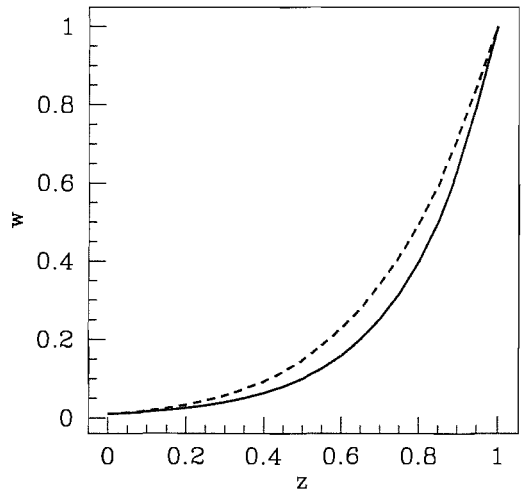

Figure 10.4: Graph to show variable–viscosity solution for w, where $W_f = 10^{-2}$, $W_d = 1$, $h_0 = 1$, $A_0 = 1$, $f = 1$ (upper curve) and $f = 0$ (lower curve).

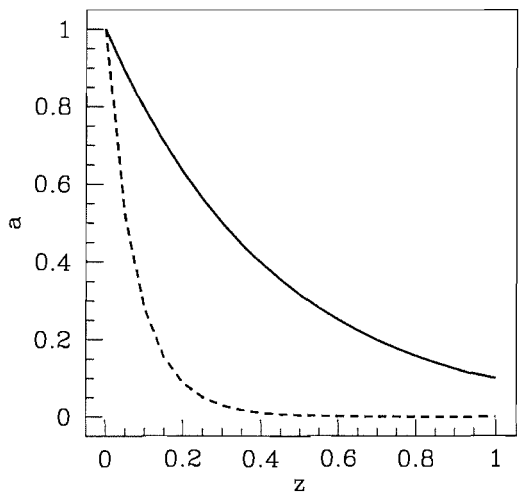

Figure 10.5: Graph to show variable–viscosity solution for a, where $W_f = 10^{-2}$, $W_d = 1$, $h_0 = 1$, $A_0 = 1$, $f = 1$ (lower curve) and $f = 0$ (upper curve).

Table 10.1: Table summarizing parameter values considered for two–phase flow solutions.

Case	W_f	W_d	h_0	A_0	δ	Re	μ	γ	P_b	g	Figure
1	1.0×10^{-1}	1.0	1.0	1.0	0.0	0.0	1.0	0.0	0.0	0.0	10.6
2	1.0×10^{-1}	1.0	1.0	1.0	0.1	0.0	1.0	0.0	0.0	0.0	10.7
3	1.0×10^{-1}	1.0	1.0	1.0	0.0	0.0	1.0	3×10^{-1}	0.0	0.0	10.8
4	1.0×10^{-1}	1.0	1.0	1.0	0.1	0.0	1.0	3×10^{-1}	0.0	0.0	10.9
5	1.0×10^{-1}	1.0	1.0	1.0	0.0	0.0	1.0	1.0	0.0	0.0	10.10
6	1.0×10^{-1}	1.0	1.0	1.0	0.1	0.0	1.0	1.0	0.0	0.0	10.11

10.5 Numerical solutions

10.5.1 Numerics

There are three principal objectives of the following numerical study. First, we wish to solve the full equations (10.60)–(10.63) and compare solutions for w, h, a and n under a variety of conditions in order to check that the solutions to the equations behave as one might expect. Throughout the following numerical solutions we set $W_f = 1.0 \times 10^{-1}$, $W_d = 1.0$, $h_0 = 1.0$, $A_0 = 1.0$, $Re = 0.0$, $\mu = 1.0$, $P_b = 0.0$, $g = 0.0$, scaled n so that its maximum value was $n_{max} \approx 1$ and considered only the steady versions of (10.60)–(10.63). We confine the study to cases where there is no radial variation in either a or n at $z = 0$, which reduces the equations (10.60)–(10.63) to a system of ordinary differential equations. Table 10.1 summarizes the chosen parameter values for the cases considered.

Figure 10.6 shows solutions for h, a and n obtained by setting $\gamma = 0$ and $\delta = 0$ (Case 1, Table 10.1). If one increases the value of δ to $\delta = 0.1$ whilst keeping $\gamma = 0$ (Case 2,

Table 10.1), tantamount to ignoring surface tension but having a significant density of holes in a cross–section, one might expect that the non–dimensional solution for all variables would remain the same. This behaviour is observed in Figure 10.7. However, one would expect variation in the solutions when surface tension is added, and would also expect variation in the solutions between the $\delta = 0$ and $\delta = 0.1$ cases where surface tension is included in both.

Figure 10.8 shows solutions for $\gamma = 0.3$ and $\delta = 0$ (Case 3, Table 10.1). The effect of surface tension on the value of a is to cause it to reduce in size for all z as one would expect. To be consistent with previous findings one would expect the effect of surface tension on the radius of the fibre h would be to increase it for $0 < z < 1$. As shown in Figure 10.8 however, the change in h is minimal. This makes sense because one would expect that for small surface tension the effect on holes would be far more dramatic than the the effect in the macroscopic radius of the fibre. The solution for n has hardly changed from the previous two cases considered as one would expect. Since n measures the number density of holes in a fibre cross–section but the macroscopic size of the fibre has not significantly changed, the fact that the holes themselves have become smaller should not be expected to impact the size of n.

Figure 10.9 shows solutions of the equations for $\gamma = 0.3$ and $\delta = 0.1$ (Case 4, Table 10.1). It is not possible to anticipate the exact form of the solution for a in this case, though we note that a is expected to be smaller for all z than for the $\gamma = 0$ case. The solution for h shows that h is slightly smaller for all z than in any of the previous three cases. This is because to leading–order one would expect to find a and n coupled to the equation for h (the z–momentum equation and/or the kinematic boundary–condition). Another way of saying this is the mass lost from a cross–section with such a large density of holes is no longer insignificant to the solution for h. The solution for n may now be understood in terms of the solutions for h and a. Because a and h are smaller for all z, the number density of holes in a cross–section is expected to increase, as is clearly the case in Figure 10.9.

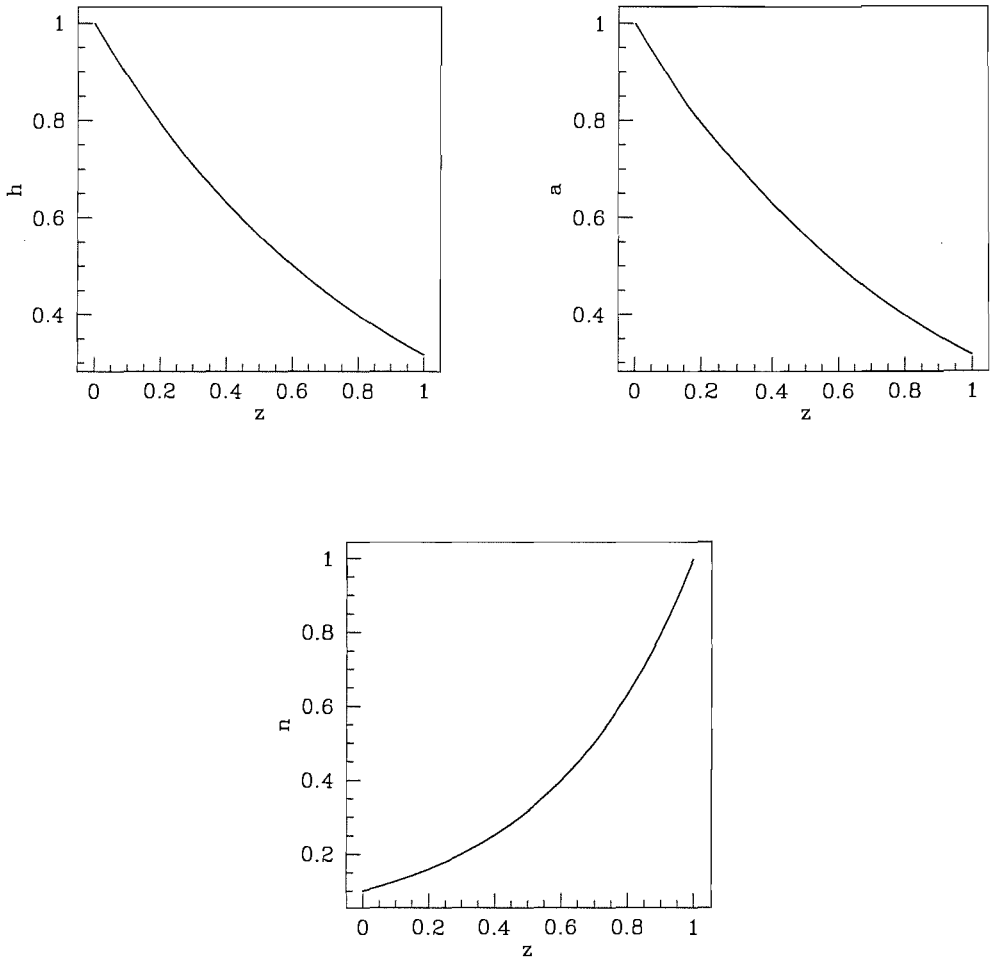

Figure 10.6: Graph to show $\delta = 0$ and $\gamma = 0$ solution for h, a and n. (Case 1: $W_f = 1.0 \times 10^{-1}$, $W_d = 1.0$, $h_0 = 1.0$, $A_0 = 1.0$, $\delta = 0.0$, $Re = 0.0$, $\mu = 1.0$, $\gamma = 0.0$, $P_b = 0.0$, $g = 0.0$.)

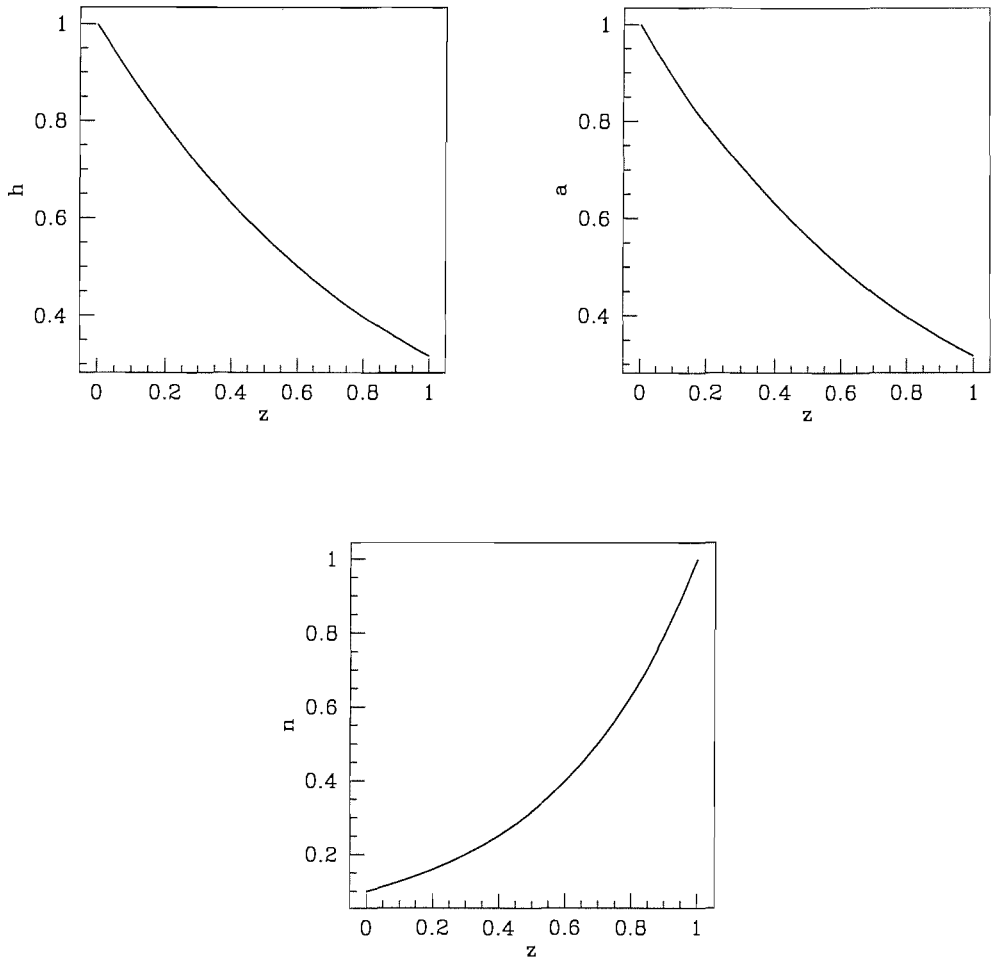

Figure 10.7: Graph to show $\delta = 0.1$ and $\gamma = 0$ solution for h, a and n. (Case 2: $W_f = 1.0 \times 10^{-1}$, $W_d = 1.0$, $h_0 = 1.0$, $A_0 = 1.0$, $\delta = 0.1$, $Re = 0.0$, $\mu = 1.0$, $\gamma = 0.0$, $P_b = 0.0$, $g = 0.0$.)

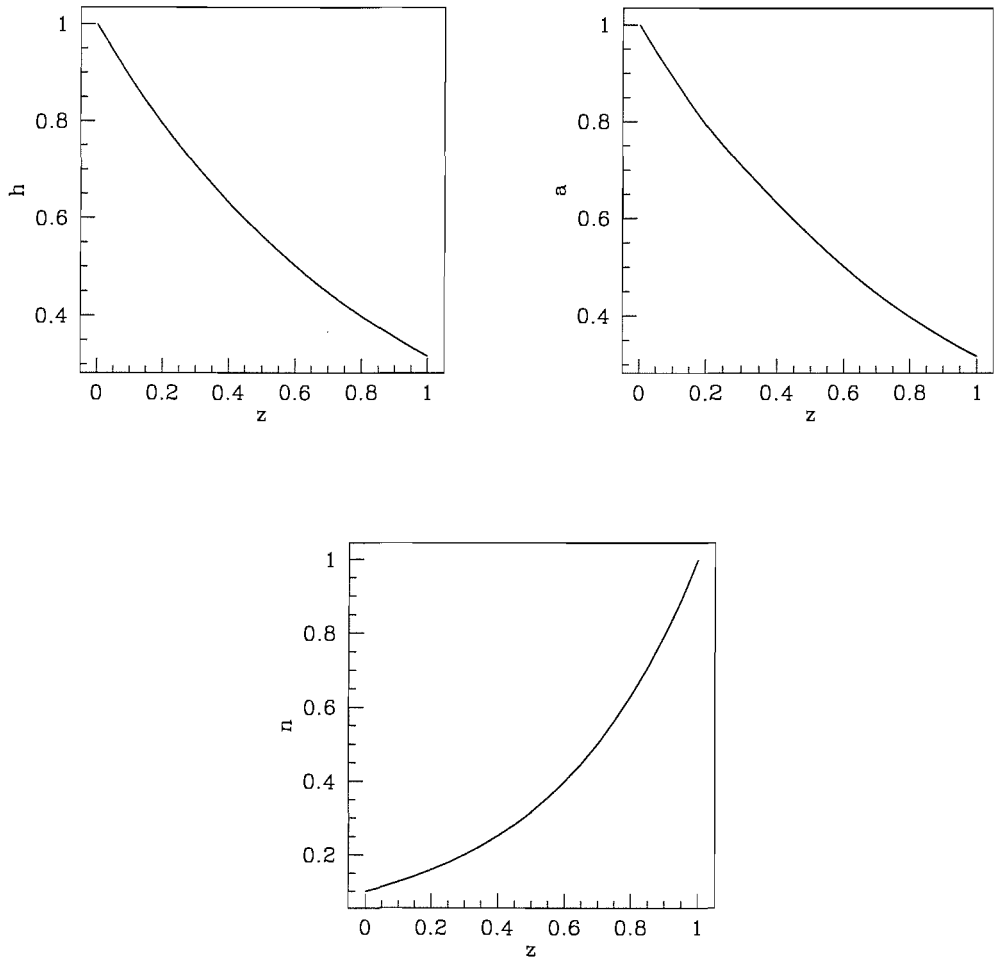

Figure 10.8: Graph to show $\delta = 0$ and $\gamma = 0.3$ solution for h, a and n. (Case 3: $W_f = 1.0 \times 10^{-1}$, $W_d = 1.0$, $h_0 = 1.0$, $A_0 = 1.0$, $\delta = 0.0$, $Re = 0.0$, $\mu = 1.0$, $\gamma = 3 \times 10^{-1}$, $P_b = 0.0$, $g = 0.0$.)

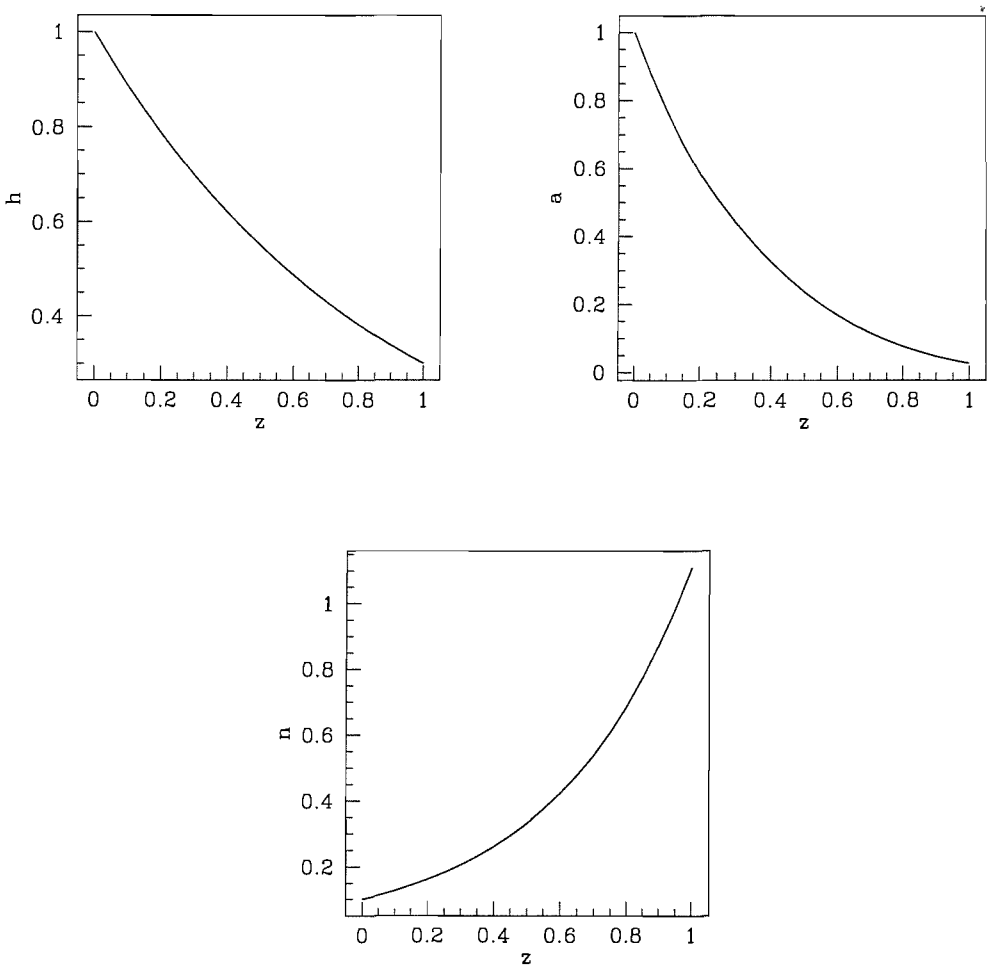

Figure 10.9: Graph to show $\delta = 0.1$ and $\gamma = 0.3$ solution for h, a and n. (Case 4: $W_f = 1.0 \times 10^{-1}$, $W_d = 1.0$, $h_0 = 1.0$, $A_0 = 1.0$, $\delta = 0.1$, $Re = 0.0$, $\mu = 1.0$, $\gamma = 3 \times 10^{-1}$, $P_b = 0.0$, $g = 0.0$.)

10.5.2 The effects of surface tension

In §10.3.1 we obtained perturbation solutions (equations (10.68)–(10.71)) for w_1, h_1 and a_1, though closed a closed form solution for n_1 was not obtained. We now examine these first–order solutions to the equations where surface tension is the small perturbing parameter, solving numerically for n_1, for two cases: (i) where $\delta = 0$ and (ii) where $\delta = 0.1$. Figure 10.10 shows the first–order solutions for h, w, a and n for the $\delta = 0$ case (Case 5, Table 10.1). We note that the effects of surface tension are to (i) increase h for all z, except where mass conservation (remembering that $\delta = 0$) requires the first–order term to drop to zero; (ii) decrease w for $0 < z < 1$ consistent with (i) and mass conservation; (iii) decrease a for all z whilst allowing it to increase (but remain negative) for large z as a result of the behaviour seen for w; and (iv) decrease n for all z as a result of the behaviour for h and the fact that $\delta = 0$.

Figure 10.11 shows the $O(\gamma)$ solutions to the equations for the $\delta = 0.1$ case (Case 6, Table 10.1), where we note that w and h behave similarly to the $\delta = 0$ solutions, though h is slightly smaller for all z. As a direct result of this, a behaves similarly to the $\delta = 0$ solutions but n does not. Changes in n are larger than changes in h, and are such as to decrease n for small z and then increase it for larger values. The change in behaviour for n may be understood in terms of h decreasing for small z and increasing for larger z values in accordance with (10.63). The reason that the magnitude of the changes in n are considerably larger than the changes in h at $z = 1$ may be obtained by setting $h = h_0 + \gamma h_1$, $n = n_0 + \gamma n_1$ and making use of the leading–order solutions for h_0 and n_0. To leading order this gives

$$n_1|_{z=1} = -\frac{2h_1|_{z=1}}{\sqrt{N_0}},$$

where $n(0) = N_0$. Since in Figures 10.10–10.11, $N_0 = 1 \times 10^{-1}$ (scaled so that $N_0|_{z=1} = O(1)$), we expect $n_1|_{z=1} \gg h_1|_{z=1}$ as observed.

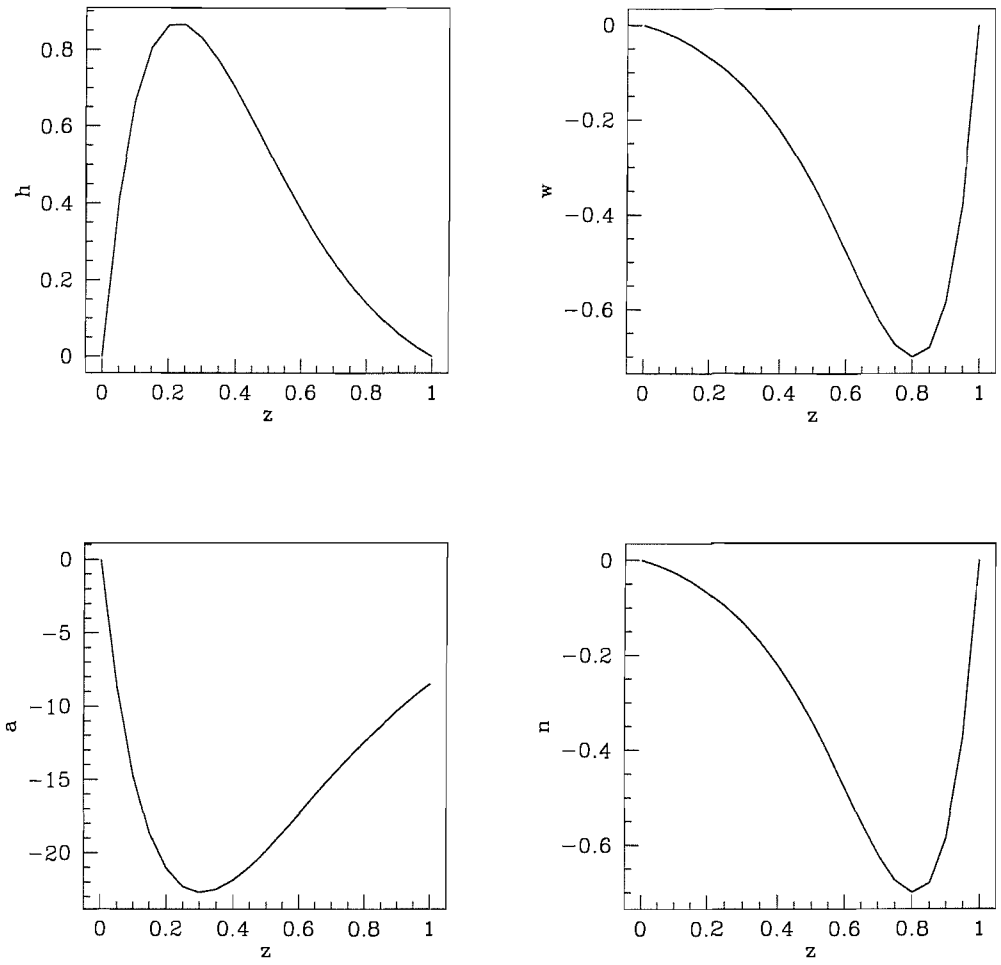

Figure 10.10: Graph to show first–order (perturbation) solutions for h, w, a and n. (Case 5: $W_f = 1.0 \times 10^{-1}$, $W_d = 1.0$, $h_0 = 1.0$, $A_0 = 1.0$, $\delta = 0.0$, $Re = 0.0$, $\mu = 1.0$, $\gamma = 1 \times 10^{-1}$, $P_b = 0.0$, $g = 0.0$, $\epsilon = 1 \times 10^{-1}$, $\psi = 1 \times 10^{-1}$, $N_0 = 1 \times 10^{-1}$.)

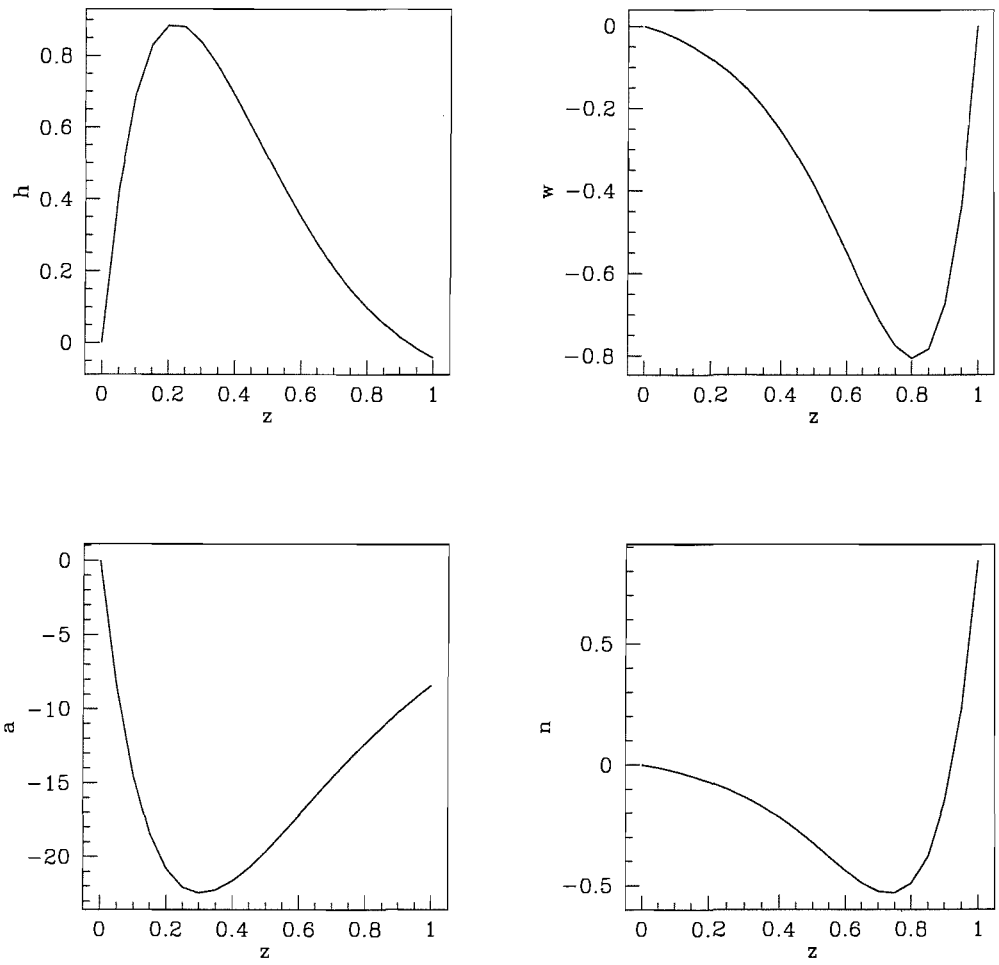

Figure 10.11: Graph to show first–order solution for h with $\delta \neq 0$. (Case 6: $W_f = 1.0 \times 10^{-1}$, $W_d = 1.0$, $h_0 = 1.0$, $A_0 = 1.0$, $\delta = 0.1$, $Re = 0.0$, $\mu = 1.0$, $\gamma = 1 \times 10^{-1}$, $P_b = 0.0$, $g = 0.0$, $\epsilon = 1 \times 10^{-1}$, $\psi = 1 \times 10^{-1}$, $N_0 = 1 \times 10^{-1}$.)

10.6 Conclusions

As an intermediate step between modelling a capillary tube and modelling the full holey fibre problem, a two–phase flow model was derived (see equations (10.60)–(10.63) for constant viscosity model and equations (10.80)–(10.83) for variable viscosity model). Analytical solutions to the model were found using asymptotic analysis and these results compared with numerical results of the full equations. Where analytical solutions were not found interesting cases were considered, the equations were solved numerically and the results interpreted.

10.6.1 Practical Results

In this Chapter we:

- described the effects of a the furnace temperature profile on the average hole size and hole density in final fibre (see §10.4.1);
- have shown that when the preform air fraction is large, the effects of surface tension on holey fibres are to reduce the average hole size but not to alter the macroscopic fibre geometry or the density of holes in the final fibre (see §10.5.1);
- have shown that when the preform air fraction is small, the effects of surface tension on holey fibres are to reduce the average hole size, reduce the macroscopic fibre geometry, and increase the density of holes in the final fibre (see §10.5.1).

Chapter 11

Full Holey Fibre Problem

11.1 Introduction

In general we wish to be able to predict the evolution of a preform whose cross–section takes an arbitrary form. The preform will often lack symmetry and rarely be axisymmetric. It will include many holes whose size and shape will vary from place to place. The centre–line of the preform will typically evolve as it is drawn and it is expected that the effects of surface tension will be critical in this process. A schematic diagram of a possible preform cross–section is shown in Figure 11.1.

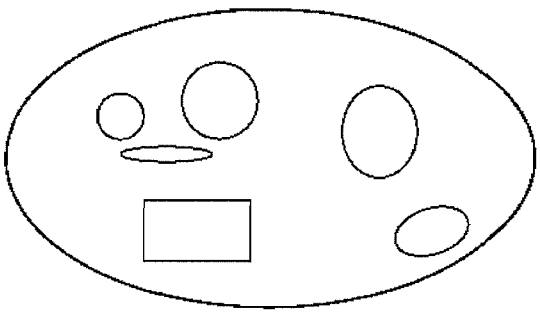

Figure 11.1: Possible preform cross–section.

We considered the drawing of optical fibres with an arbitrary number of holes. A number of assumptions are made. First we assume that the preform is slender, so that its radius is always much less than its length. This introduces a small parameter into the problem. We assume that the preform centreline remains almost straight, in a sense that will be later clarified. We assume that the preform may be twisted as it is pulled and assume that the glass viscosity may vary, but only along the length of the preform. Finally we assume that the density of glass is constant.

11.2 Mathematical modelling

The flow is governed by the variable–viscosity Navier–Stokes equations

$$\begin{aligned} \rho[\mathbf{q}_t + (\mathbf{q}.\nabla)\mathbf{q}] &= -\nabla p + \frac{\partial}{\partial x_j}\left(\mu \frac{\partial q_i}{\partial x_j}\right) + \rho \mathbf{g}, \\ \nabla.\mathbf{q} &= 0, \end{aligned} \tag{11.1}$$

written in Cartesian coordinates (x, y, z) and the preform velocity $\mathbf{q}$ is given by (u, v, w), time is denoted by t, ρ denotes density, p denotes pressure, μ denotes dynamic viscosity and $\mathbf{g}$ is the gravitational acceleration vector. The Navier–Stokes equations are to be applied in the region between the internal and external boundaries of the preform. We assume that the fibre is pulled in the direction of the z–axis (though as mentioned above, the centreline may, in general, not remain straight).

In addition to the Navier–Stokes equations we must prescribe suitable initial and boundary conditions. We assume that the cross–section of the preform is as shown in Figure 11.1 and that the outer surface of the preform is given by

$$H_0(x, y, z, t) = 0,$$

while the inner holes are defined by

$$H_i(x, y, z, t) = 0, \quad (i = 1, 2, ..., N),$$

where N may be as many as a few hundred. We note that, according to this definition, each H_i $(i = 0, 1, ..., N)$ describes a simple closed curve and the total surface of the

preform is given by

$$H = \bigcup_{i=0}^{N} H_i.$$

It should be appreciated that N may decrease from its value at $z = 0$, owing to the effects of surface tension. Also, for simplicity, we shall adopt the convention that the H_i are defined so that the gradient of each H_i gives the correct outward–pointing normal (pointing from the preform material to the air). Thus for a circular preform with radius a we choose $H_0 = x^2 + y^2 - a^2$ rather than -1 times this, but for an internal preform hole with radius a we choose $H_1 = a^2 - x^2 - y^2$.

We now consider the kinematic and dynamic boundary conditions for the preform. Denoting the stress tensor by $\mathcal{T}$ we have

$$\mathcal{T} = \begin{pmatrix} -p + 2\mu w_z & \mu(w_y + v_z) & \mu(w_x + u_z) \\ \mu(w_y + v_z) & -p + 2\mu v_y & \mu(v_x + u_y) \\ \mu(w_x + u_z) & \mu(v_x + u_y) & -p + 2\mu u_x \end{pmatrix}.$$

The required kinematic boundary conditions are

$$H_{it} + (\mathbf{q}.\nabla)H_i = 0 \quad \text{on} \quad H_i = 0 \quad (i = 0, 1, ..., N).$$

The dynamic boundary conditions assert that the applied stress is continuous at each of the preform surfaces. We therefore have that

$$\mathcal{T}_{ij}\hat{n}_{0j} = -\gamma\kappa\hat{n}_{0i} - p_a\hat{n}_{0i} \quad \text{on} \quad H_0 = 0$$

and

$$\mathcal{T}_{ij}\hat{n}_{kj} = -\gamma\kappa\hat{n}_{ki} - p_h\hat{n}_{ki} \quad \text{on} \quad H_k = 0 \quad (k = 1, 2, ..., N),$$

where $\hat{n}_k$ is the unit normal to the surface H_k (directed so that it always points away from the preform material) and, as described above, is therefore given by $\hat{n}_k = \nabla H_k/|H_k|$, γ is the surface tension coefficient, κ is the mean curvature of the preform (see Appendix C for details), p_a is the pressure outside the preform and p_h

is the pressure inside of the holes. Note that in experiments, it tends to be possible to maintain the holes at a constant pressure. Since the holes are vented, p_h tends to be constant in both space and time. Hole pressures that vary from hole to hole and/or increase owing to the compressibility of air as a hole shrinks, may also be incorporated into the model if required. Note also that the above conditions assume that none of the preform surfaces experience a tangential force (because of viscous drag, for example). This could also be easily included if required.

We will normally concern ourselves with steady–flow problems; if the full unsteady problem is solved then of course initial conditions will also be required.

As far as conditions at the two ends of the preform are concerned, we shall assume that both ends of the preform are fixed rigidly to end plates. Thus

$$\mathbf{q} = \mathbf{q}_f \quad \text{at} \quad x = s_f(t) \tag{11.2}$$

and

$$\mathbf{q} = \mathbf{q}_d \quad \text{at} \quad x = s_d(t), \tag{11.3}$$

where the subscripts f and d denote the feed and draw ends respectively. We note that the conditions (11.2) and (11.3) allow for twist to be imposed on the preform during the drawing process; something that is of practical relevance in the manufacture of holey fibres. It is worth noting that the alternative problem specification of assuming that the downstream tension is known may also be formulated in an obvious way: unlike simpler models of the preform problem, however, assuming that the tension is known does not lead to an appreciably simpler problem.

We now non–dimensionalize the problem and denote a typical draw–length and preform radius by L and h respectively, and then define the key small parameter in the problem as

$$\epsilon = \frac{h}{L}.$$

A suitable non–dimensionalization is given by setting $z = L\bar{z}$, $y = \epsilon L\bar{y}$, $x = \epsilon L\bar{x}$, $w = W\bar{w}$, $v = W\epsilon\bar{v}$, $u = W\epsilon\bar{u}$, $t = (L/W)\bar{t}$, $\mu = \mu_0\bar{\mu}$ and $p = (\mu_0 W/L)\bar{p}$ where bars

denote non–dimensional variables and W is a typical draw speed and μ_0 a typical value of the viscosity. With these scalings the Navier–Stokes equations become (on dropping the bars for convenience)

$$\begin{aligned}
\epsilon^2 Re[w_t + ww_z + vw_y + uw_x] &= -\epsilon^2 p_z + \epsilon^2(\mu w_z)_z + \mu w_{yy} + \mu w_{xx} + \epsilon^2 St, \\
\epsilon^2 Re[v_t + wv_z + vv_y + uv_x] &= -p_y + \epsilon^2(\mu v_z)_z + \mu v_{yy} + \mu v_{xx}, \\
\epsilon^2 Re[u_t + wu_z + vu_y + uu_x] &= -p_z + \epsilon^2(\mu u_z)_z + \mu u_{yy} + \mu u_{xx}, \\
w_z + v_y + u_x &= 0,
\end{aligned}$$

where the Reynolds number, capillary and Stokes numbers (the key physical parameters in the problem) are defined respectively by

$$Re = \frac{\rho W L}{\mu_0}, \quad Ca = \frac{\mu_0 W}{\gamma}, \quad St = \frac{\rho L^2 g}{\mu_0 W}.$$

The free surface kinematic conditions become

$$H_{it} + wH_{iz} + vH_{iy} + uH_{iz} = 0 \quad \text{on} \quad H_i = 0 \quad (i = 0, 1, ..., N).$$

For the scaled dynamic surface conditions the normal vector is required. The normal to $H_i = 0$ $(i = 0, 1, ..., N)$ in scaled variables is given by

$$\hat{\mathbf{n}}_\mathbf{i} = \frac{1}{\sqrt{\epsilon^2 H_{iz}^2 + H_{ix}^2 + H_{iy}^2}} \begin{pmatrix} \epsilon^2 H_{iz} \\ H_{iy} \\ H_{ix} \end{pmatrix}.$$

We also assume (see Appendix C for details) that the mean curvature of the preform has an asymptotic expansion of the form

$$\kappa = \frac{1}{L}\left(\frac{1}{\epsilon}\kappa_0 + \epsilon\kappa_1 + ...\right),$$

where κ_0 and κ_1 involve derivatives of H_i. Before we can continue and evaluate the surface dynamic boundary conditions, we must decide the order of magnitude of the surface tension and the internal hole pressurization. As far as the surface tension is concerned, a number of different cases may be considered. When γ satisfies

$$\epsilon^3 Ca = O(1),$$

it transpires that the surface tension does not enter into the problem to leading order. A general solution may be determined to the cross–flow equations, and a second–order mixed elliptic/hyperbolic partial differential equation may be derived that governs the motion of the centreline of the preform. An equation for the rotation of the preform may also be derived. We do not pursue this case further here as clearly in the parameter regime of interest for holey fibre manufacture, the role of surface tension is crucial and must therefore enter the problem to leading order. Thus we consider the case where

$$\epsilon Ca = O(1),$$

so that the relevant scaling consists of setting $\gamma = \epsilon\mu_0 W\gamma^*$. We also scale the ambient hole pressures using

$$p_a = \frac{\mu_0 W}{L}p_a^*, \quad p_h = \frac{\mu_0 W}{L}p_h^*;$$

a result that suggests that the hole pressure should have an order of magnitude of $\mu_0 W/L$ to be of any use in the manufacturing process: if it is maintained at a level lower than this, then it can have no influence, while if it is an order of magnitude higher, the fibre will immediately "explode". This is the same as the conclusion reached in Chapter 3.

The scaled stress tensor is now

$$\mathcal{T} = \frac{\mu_0 W}{L}\begin{pmatrix} -p + 2\mu w_z & \mu(w_y/\epsilon + \epsilon v_z) & \mu(w_x/\epsilon + \epsilon u_z) \\ \mu(w_y/\epsilon + \epsilon v_z) & -p + 2\mu v_y & \mu(v_x + u_y) \\ \mu(w_x/\epsilon + \epsilon u_z) & \mu(v_x + u_y) & -p + 2\mu u_x \end{pmatrix}$$

and the dynamic boundary conditions are thus

$$\begin{pmatrix} -p + 2\mu w_z & \mu(w_y/\epsilon + \epsilon v_z) & \mu(w_x/\epsilon + \epsilon u_z) \\ \mu(w_y/\epsilon + \epsilon v_z) & -p + 2\mu v_y & \mu(v_x + u_y) \\ \mu(w_x/\epsilon + \epsilon u_z) & \mu(v_x + u_y) & -p + 2\mu u_x \end{pmatrix}\begin{pmatrix} \epsilon^2 H_{0z} \\ H_{0y} \\ H_{0x} \end{pmatrix}$$

$$= \left[-\epsilon\gamma^*\left(\frac{\kappa_0}{\epsilon} + \epsilon\kappa_1\right) - p_a^*\right]\begin{pmatrix} \epsilon^2 H_{0z} \\ H_{0y} \\ H_{0x} \end{pmatrix}$$

on $H_0 = 0$ and

$$\begin{pmatrix} -p + 2\mu w_z & \mu(w_y/\epsilon + \epsilon v_z) & \mu(w_x/\epsilon + \epsilon u_z) \\ \mu(w_y/\epsilon + \epsilon v_z) & -p + 2\mu v_y & \mu(v_x + u_y) \\ \mu(w_x/\epsilon + \epsilon u_z) & \mu(v_x + u_y) & -p + 2\mu u_x \end{pmatrix} \begin{pmatrix} \epsilon^2 H_{iz} \\ H_{iy} \\ H_{ix} \end{pmatrix}$$

$$= \left[\epsilon\gamma^* \left(\frac{\kappa_0}{\epsilon} + \epsilon\kappa_1\right) - p_h^*\right] \begin{pmatrix} \epsilon^2 H_{iz} \\ H_{iy} \\ H_{ix} \end{pmatrix}$$

on $H_i = 0$ $(i = 1, 2, ..., N)$.

The next stage is to assume regular power–series perturbations in the small parameter ϵ^2 for the dependent variables in the problem by setting

$$\begin{aligned} w &= w_0 + \epsilon^2 w_1 + \epsilon^4 w_2 + \dots, \\ v &= v_0 + \epsilon^2 v_1 + \epsilon^4 v_2 + \dots, \\ u &= u_0 + \epsilon^2 u_1 + \epsilon^4 u_2 + \dots, \\ p &= p_a^* + p_0 + \epsilon^2 p_1 + \epsilon^4 p_2 + \dots, \end{aligned}$$

and insert these expansions into the equations and boundary conditions. Although not all of the following equations will be used, for completeness and to aid any future works, we give each of the leading order and next order equations.

The leading order Navier–Stokes equations are

$$0 = w_{0yy} + w_{0xx}, \tag{11.4}$$

$$0 = -p_{0y} + \mu v_{0yy} + \mu v_{0xx}, \tag{11.5}$$

$$0 = -p_{0x} + \mu u_{0yy} + \mu u_{0xx}, \tag{11.6}$$

$$0 = w_{0z} + v_{0y} + u_{0x}. \tag{11.7}$$

The leading order kinematic boundary condition is

$$0 = H_{it} + w_0 H_{iz} + v_0 H_{iy} + u_0 H_{ix} \text{ on } H_i = 0 \quad (i = 0, 1, ..., N). \tag{11.8}$$

Leading order dynamic boundary conditions on $H_0 = 0$ are

$$0 = w_{0y}H_{0y} + w_{0x}H_{0x}, \tag{11.9}$$

$$-\gamma^*\kappa_0 H_{0y} = \mu w_{0y}H_{0z} + (-p_0 + 2\mu v_{0y})H_{0y} + \mu(v_{0x} + u_{0y})H_{0x}, \tag{11.10}$$

$$-\gamma^*\kappa_0 H_{0x} = \mu w_{0x}H_{0z} + \mu(v_{0x} + u_{0y})H_{0y} + (-p_0 + 2\mu u_{0x})H_{0x}, \tag{11.11}$$

where κ_0 denotes the leading–order term in the expansion for the mean curvature.

The leading order dynamic boundary conditions on $H_i = 0$ $(i = 0, 1, ..., N)$ are

$$0 = w_{0y}H_{iy} + w_{0x}H_{ix}, \tag{11.12}$$

$$\gamma^*\kappa_0 H_{iy} + (p_a^* - p_h^*)H_{iy} = \mu w_{0y}H_{iz} + (-p_0 + 2\mu v_{0y})H_{iy} + \mu(v_{0x} + u_{0y})H_{ix}, \tag{11.13}$$

$$\gamma^*\kappa_0 H_{ix}(p_a^* - p_h^*)H_{ix} = \mu w_{0x}H_{iz} + \mu(v_{0x} + u_{0y})H_{iy} + (-p_0 + 2\mu u_{0x})H_{ix}, \tag{11.14}$$

where p_h denotes the non–dimensionalized hole overpressure (the pressure above the ambient).

The $O(\epsilon^2)$ Navier–Stokes equations are

$$Re(w_{0t} + w_0 w_{0z} + v_0 w_{0y} + u_0 w_{0x}) = St - p_{0z} + (\mu w_{0z})_z + \mu w_{1yy} + \mu w_{1xx}, \tag{11.15}$$

$$Re(v_{0t} + w_0 v_{0z} + v_0 v_{0y} + u_0 v_{0x}) = -p_{1y} + (\mu v_{0z})_z + \mu v_{1yy} + \mu v_{1xx}, \tag{11.16}$$

$$Re(u_{0t} + w_0 u_{0z} + v_0 u_{0y} + u_0 u_{0x}) = -p_{1x} + (\mu u_{0z})_z + \mu u_{1yy} + \mu u_{1xx}, \tag{11.17}$$

$$0 = w_{1z} + v_{1y} + u_{1x}. \tag{11.18}$$

The $O(\epsilon^2)$ kinematic boundary condition is

$$0 = w_1 H_{iz} + v_1 H_{iy} + u_1 H_{ix} \text{ on } H_i = 0 \quad (i = 0, 1, ..., N) \tag{11.19}$$

and the $O(\epsilon^2)$ dynamic boundary conditions on $H_0 = 0$ are

$$\begin{aligned} 0 &= (-p_0 + 2\mu w_{0z} + \gamma^* K_0) H_{0z} + \mu(w_{1y} + v_{0z}) H_{0y} + \mu(w_{1x} \\ &\quad + u_{0z}) H_{0x}, \qquad (11.20) \\ 0 &= \mu(w_{1y} + v_{0z}) H_{0z} + (-p_1 + 2\mu v_{1y} + \gamma^* K_1) H_{0y} + \mu(u_{1y} \\ &\quad + v_{1x}) H_{0x}, \qquad (11.21) \\ 0 &= \mu(w_{1x} + u_{0z}) H_{0z} + \mu(u_{1y} + v_{1x}) H_{0y} \\ &\quad + (-p_1 + 2\mu u_{1x} + \gamma K_1) H_{0x}. \qquad (11.22) \end{aligned}$$

Finally, the $O(\epsilon^2)$ dynamic boundary conditions on $H_i = 0$ $(i = 1, 2, ..., N)$ are

$$\begin{aligned} 0 &= (-p_0 + 2\mu w_{0z} - \gamma^* K_0 + p_h^* - p_a^*) H_{iz} + \mu(w_{1y} + v_{0z}) H_{iy} \\ &\quad + \mu(w_{1x} + u_{0z}) H_{ix}, \qquad (11.23) \\ 0 &= \mu(w_{1y} + v_{0z}) H_{iz} + (-p_1 + 2\mu v_{1y} - \gamma^* K_1) H_{iy} \\ &\quad + \mu(v_{1y} + v_{1x}) H_{ix}, \qquad (11.24) \\ 0 &= \mu(w_{1x} + u_{0z}) H_{iz} + \mu(v_{1y} + v_{1x}) H_{iy} + (-p_1 + 2\mu v_{1x} \\ &\quad - \gamma^* K_1) H_{ix}. \qquad (11.25) \end{aligned}$$

11.3 Solving the equations

To solve the governing equations and boundary conditions (11.4)–(11.25), we first note that (11.4), (11.9) and (11.12) imply that

$$\nabla^2 w_0 = 0$$

with

$$\frac{\partial w_0}{\partial n} = 0$$

on $H_i = 0$ $(i = 1, 2, ..., N)$, where here and henceforth we adopt the notation that ∇^2 denotes the Laplacian operator in the (x, y)–plane and n denotes the outward–pointing normal. Thus w_0 must be constant in x and y and we conclude that

$$w = w_0(z).$$

We may now write (11.5) and (11.6) as

$$0 = (-p_0 + \mu v_{0y})_y + (\mu v_{0x})_x + (\mu v_{0y})_y - (\mu v_{0y})_y, \tag{11.26}$$

$$0 = (\mu u_{0y})_y + (-p_0 + \mu u_{0x})_x + (\mu u_{0x})_x - (\mu u_{0x})_x \tag{11.27}$$

and thus

$$0 = (-p_0 + 2\mu v_{0y})_y + (\mu v_{0x})_x - (\mu v_{0y})_y, \tag{11.28}$$

$$0 = (\mu u_{0y})_y - (\mu u_{0x})_x + (-p_0 + 2\mu u_{0x})_x. \tag{11.29}$$

Since w_0 is a function of z alone, differentiating the leading order continuity equation (11.7) with respect to x and y yields

$$0 = v_{0yx} + u_{0xx}, \tag{11.30}$$

$$0 = v_{0yy} + u_{0yx}, \tag{11.31}$$

and this allows (11.28) and (11.29) to be written as

$$0 = (-p_0 + 2\mu v_{0y})_y + (\mu v_{0x} + \mu u_{0y})_x, \tag{11.32}$$

$$0 = (\mu v_{0x} + \mu u_{0y})_y + (-p_0 + 2\mu u_{0x})_x. \tag{11.33}$$

If we now define

$$\tau_{11} = -p_0 + 2\mu v_{0y}, \tag{11.34}$$

$$\tau_{12} = \mu(v_{0x} + u_{0y}), \tag{11.35}$$

$$\tau_{22} = -p_0 + 2\mu u_{0x}, \tag{11.36}$$

then equations (11.34)–(11.35) are

$$0 = (\tau_{11})_y + (\tau_{12})_x, \tag{11.37}$$

$$0 = (\tau_{12})_y + (\tau_{22})_x. \tag{11.38}$$

Since both of these equations are in divergence form, there exist stream functions A and B with

$$\tau_{11} = A_x, \quad \tau_{12} = -A_y,$$

$$\tau_{12} = B_x, \quad \tau_{22} = -B_y.$$

Thus $B_x = -A_y$, $A_y + B_x = 0$ and therefore an Airy stress function ψ exists with

$$\tau_{11} = \psi_{xx}, \quad \tau_{12} = -\psi_{yx}, \quad \tau_{22} = \psi_{yy}. \tag{11.39}$$

We now note that by differentiating and adding (11.5) and (11.6), we conclude that

$$\nabla^2 p = \mu(v_{0yyy} + v_{0xxy} + u_{0yyx} + u_{0xxx}). \tag{11.40}$$

By differentiating the continuity equation (11.7) and using the fact that w_0 is a function of z alone, we find that the right hand side of (11.40) is zero and thus

$$\nabla^2 p_0 = 0. \tag{11.41}$$

Now from the definitions of ψ (11.39) we have

$$\nabla^4 \psi = \tau_{11xx} - \tau_{12yx} + \tau_{22yy}. \tag{11.42}$$

Thus

$$\nabla^4 \psi = -\nabla^2 p_0 + 2\mu(v_{0yxx} - v_{0yxx} - u_{0yyx} + u_{0yyx}) = 0, \tag{11.43}$$

and ψ satisfies the biharmonic equation

$$\nabla^4 \psi = 0. \tag{11.44}$$

11.3.1 The reduction to fibre and capillary drawing models

To solve the many–holes full holey fibre problem, one must solve the biharmonic equation in the domain of a preform cross–section. However, it is not at all obvious what boundary conditions should be used on the boundaries of the many holes (a constant value of ψ and its normal derivative must be specified).

It is clear that when the preform is solid and circular with no holes, that $\psi = 0$ and $\frac{\partial \psi}{\partial n} = 0$ on $H_0 = 0$ are the required boundary conditions since there are no sources or sinks of fluid in a cross–section. To show how this gives rise to the familiar equation of continuity we solve the biharmonic equation in cylindrical coordinates to give

$$\psi = A + Br^2 + Cr^2 \log(r) + D \log(r),$$

where A, B, C and D are arbitrary constants of integration. Applying the boundary conditions $\psi = 0$ and $\frac{\partial \psi}{\partial n} = 0$ on $H_0 = 0$, gives $A = B = C = D = 0$ and thus $\psi \equiv 0$. From this we deduce using (11.39) that $\tau_{11} = \tau_{12} = \tau_{22} = 0$.

Using the results in (11.34), (11.36) and making use of (11.7) we see that

$$v_{0y} = \frac{1}{4\mu}(\psi_{xx} - \psi_{yy}) - \frac{w_{0z}}{2}$$

giving

$$v_0 = F(z, x) - \frac{y w_{0z}}{2}, \tag{11.45}$$

and

$$u_{0x} = \frac{1}{4\mu}(\psi_{yy} - \psi_{xx}) - \frac{w_{0z}}{2}$$

giving

$$u_0 = G(z, y) - \frac{x w_{0z}}{2}, \tag{11.46}$$

where $F(z, x)$ and $G(z, y)$ are arbitrary constants of integration. To determine the constant that arise when integrating u_x and v_y, rigid body translations and rotations must be carefully considered, corresponding to motion of the centreline and the angular momentum of fluid about that centreline. In this trivial case where the centreline is stationary and the preform is not rotating, we find that $F(z, x) = G(z, y) = 0$.

For a solid preform with a circular preform we have $H_0 = x^2 + y^2 - h(z)^2 = 0$, where $h(z)$ is the profile of the outer preform radius. Using this and the results (11.45) and (11.46) together in (11.8) yields

$$2w_0 h h_z + y^2 w_{0z} + x^2 w_{0z} = 0,$$

which reduces to

$$(h^2 w)_z = 0.$$

This is in agreement with the result in Chapter 3.

11.4 Conclusions

We have shown that it is a relatively trivial matter to derive the mass–conservation equation for a solid fibre. It is also possible to derive equations of momentum conservation. However, things become rapidly complicated with the inclusion of effects such as surface tension. When attempting to solve the biharmonic equation in order to describe the manufacture of a capillary tube, it is unclear what constants and other boundary conditions should be chosen for ψ on each of the two surfaces. Preforms with multiple holes are even more challenging and it is not currently known how to solve the problem in such cases, where once again, the problem lies in specifying the boundary conditions for ψ on the surfaces of the holes.

It is therefore proposed that the cross–flow problem is solved directly in such cases as these, though we do not attempt such a lengthy numerical problem in this study.

Chapter 12

Conclusions and Future Work

12.1 Conclusions

A model that describes the drawing and rotation of capillary tubes was developed in Chapter 3, and the model was solved for some interesting limiting cases in §3.7). The model was solved numerically to determine the effects on the fibre dimensions of preform rotation (see Chapter 6), which results in the reduction or removal of fibre birefringence. It was discovered that a sub–mm spin pitch (see §3.7.1.1) could be achieved for holey fibres that fall into two categories (see Chapter 4). It was shown that the manufacture of one type of fibre must be broken into two stages and that in this case preform rotation may not be used as a method to control the resulting fibre geometry (see §4.5.1). For the second fibre type it was shown that care must be taken to preserve the microstructured region of the fibre, having broken the manufacture into two stages and used the second stage to prescribe the fibre geometry (see §4.5.2). The two–stage process also allows fibres to be drawn at higher temperatures, producing fibres of superior strength. The model has successfully predicted the outcome of rotation experiments on holey fibres and will be used as a guide in future attempts.

A stability analysis for drawing capillary tubes was conducted in Chapter 5), furthering previous studies on the stability of drawing solid optical fibres with and without surface tension. We included the effects of gravity (see §5.3.4.1), inertia (see §5.3.4.1), surface tension (see §5.3.4.2) and hole overpressure. The model agreed well with previous studies, shown in §5.3.3. We identified and investigated the role of each separate parameter available for change when drawing capillary tubes, in terms its effect on the stability of the drawing process. However, this model and all previous studies show that it is not possible draw fibres with a draw–ratio of greater than 20.2. This is not the case in practice, where fibres may be drawn at many times this ratio. Some possible reasons for this discrepancy were suggested (see §5.4) and the problem remains open.

A lengthy numerical analysis for the rotation of capillary tubes was conducted in Chapter 7, with numerical results compared to analytical solutions to the equations as well as to experiments. Excellent agreement was achieved in both cases. The Optoelectronics Research Centre regularly uses the numerical code to predict and guide experimental studies.

The "cup–handle" fibre was modelled in Chapter 8, and analytic solutions to the equations obtained in §8.2.2. The hitherto unexplained drainage phenomenon was understood (see §8.2) and suggestions were made as to how accurate experimental data must be in order to facilitate useful comparison with the model developed (see §8.3.4).

In Chapters 3 and 7 it was shown that preform rotation alone is unlikely to provide a mechanism to prevent surface tension induced hole collapse, but that applying a hole overpressure and rotating the preform simultaneously, is a possible solution to this problem. For practical reasons directly applying an overpressure is not possible whilst spinning preforms. A possible solution to this problem is to allow the preform to "self pressurize" by sealing on end before drawing. In Chapter 9 we develop a model to describe the time evolution of pressure and fibre geometry, and make

predictions that compare favourably with experimental results.

As an intermediate step between modelling a capillary tube and modelling the full holey fibre problem, a two–phase flow model was derived in Chapter 10. This model allows us to predict how the drawing of an optical fibre from a preform influences the size and distribution of an array of holes present in the preform, based on the averaged properties of the fluid. To a large extent the model must be solved numerically, though some limiting cases were studied where closed–form solutions were found and physical insight into the behaviour of the model was obtained (see §10.3). It is seen that in the limit that the total bubble area is small, by which we mean the sum of the areas of separate bubbles is small, the presence of the bubbles does not affect the macroscopic flow parameters such as the shape of the preform, characterized by the preform radius $h(z,t)$. The bubbles follow the flow that would have resulted in their absence and have their size determined by the balance of forces on their boundaries.

Where this limiting case does not exist we learn that the presence of the bubbles affects the large–scale flow in a way that may be understood analytically in some restricted cases. A more thorough numerical investigation was undertaken, a concise exposition of which is detailed in §10.5.1.

The model was extended to allow for a viscosity that varies in space and time (see §10.4). This is the model that will correspond most closely with reality and a next step would be to further investigate the solutions to this model both analytically and numerically, and to compare the solutions with experimental results.

The ultimate goal of this thesis was to derive a model that describes the manufacture of arbitrary holey fibres. Such a model was derived in Chapter 11, and we have shown that it is trivial to derive the mass–conservation equation for a solid fibre (see §11.3.1). It is also possible to derive equations of momentum conservation. However, things become complex with the inclusion of effects such as surface tension as it is unclear what the boundary conditions for the flow are. Preforms with multiple holes are even more challenging and it is not currently known how to solve the problem in

such cases. It is therefore proposed that the cross–flow problem is solved directly in such cases as these, though this is not attempted in this study.

12.2 Future work

12.2.1 Fibre manufacture

There are outstanding issues in the modelling of fibre manufacture, most notably the inability to predict the fibre geometry that results from preforms of arbitrary cross–section. However, the cross–flow model has been derived and may be solved numerically. Analytic solutions to the model will not be possible except for the most trivial geometries. It remains possible to solve the problem using the biharmonic equation (see Chapter 11), but some closure–difficulties persist.

12.2.2 Preform manufacture

To date, most studies have focused on silica technology, and the exploration of microstructured fibres made from non–silica (i.e. not pure silica) glasses is largely unexplored. Non–silica, often described as compound or *soft* glasses, promise the development of a host of new optical fibres and operational regimes because they offer properties that cannot be provided by silica, including new transmission wavelengths and highly-variable amounts of nonlinearity.

The fibres are manufactured by heating a macroscopic structured–preform and drawing it down to fibre form as for silica holey fibres, which has been the main focus of this study. However, preform manufacture which is the most labour intensive part of fibre manufacture and is an area that lies largely unexplored to this point in time.

In practice, it is often the case that a particular set of optical properties are desired from a fibre. These optical-properties are translated into geometric properties that the fibre produced must possess. From here, experience, intuition and previous mathematical modelling work is used to determine the type of preform that must be manufactured to obtain such a fibre.

Preforms for optical fibres may be manufactured in many ways, depending on whether silica glass or *soft* glass is used. Soft glass preform manufacture with a low softening point allow for preforms to be manufactured by glass extrusion, significantly increasing the number of possible structures. These preforms are made either by the stacking method or by glass extrusion (see Figure 12.1).

There are advantages and disadvantages of both stacking and extrusion, but glass extrusion has some crucial advantages and the stacking method, disadvantages. First, the stacking method has the problem of surface quality of capillary tubes that are stacked many times. Secondly, the number of thermal cycles that the glasses pass through is important, with fewer cycles reducing the chance of seeding and, or, growing crystals. This degrades the performance of the fibres. When preforms are made by stacking, glass must be melted to make capillary tubes, melted again to create the canes, which may then be melted once again to produce the preform. With glass extrusion though, the glass is melted only once and the preform made directly, thus reducing the number of thermal cycles to one. Thirdly, the manufacture via stacking is time consuming and therefore costly.

A foremost advantage of extrusion over the traditional preform manufacture-route is that many different structures are possible since holes are not restricted to hexagonal arrangements or to circular shapes. Furthermore, once the extrusion process has been optimised in terms of die geometry and other parameters such as glass feeding-speed, the process may be automated, giving a consistent and reproducible preform geometry. It is the range of preform structures available through extrusion, the reproducibility, possibilities for automation, and reduction in the number of thermal

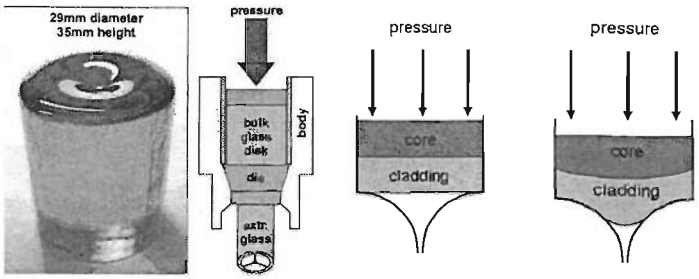

Figure 12.1: (Left 2) A bismuth glass billet used in glass extrusion and the extrusion set-up. (Right 2) Two glass billets at the start of the extrusion process. During extrusion, the upper glass flows into the lower.

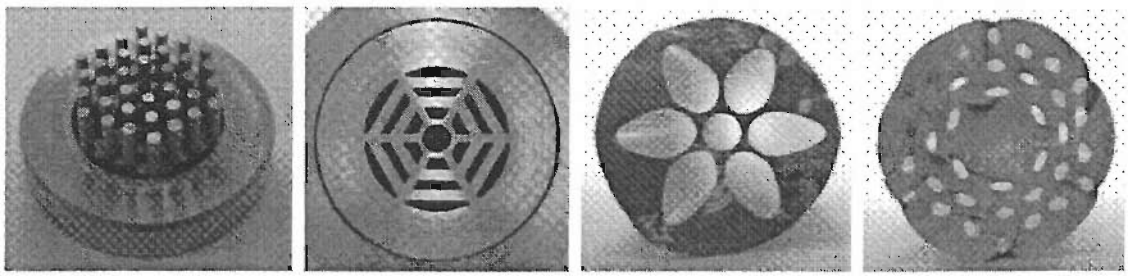

Figure 12.2: (Left 2) Multiple-hole extrusion dies. (Right 2) Preform cross-sections showing the complex structures now possible. Pictures courtesy of Professor Tanya M. Monro.

cycles, that makes glass extrusion the exciting and preferred method of preform production. Preliminary experimental results are promising, with up to 36 holes possible in a single preform extrusion as shown in Figure 12.2. However, progress is limited by a lack of understanding of the exact fluid flows that occur within the die, and thus on the die geometry best employed.

Mathematical modelling of this process is desperately needed and will further current understanding and facilitate future progress in die design.

To date little work has been done on the mathematical modelling of glass extrusion except in terms of the phenomenon of die–swell [13]. Die swell is the increase in cross–sectional area of fluid as the fluid exits the die. Its occurrence results from the non–uniform fluid velocity profile at the die exit. However, the usual no–slip conditions on the surfaces of the die must be carefully considered. It is crucial with

glass extrusion to have an accurate picture of the conditions that must be applied to the inner surfaces of the die, since this will dramatically affect the mechanical pressure in the fluid, the stress at the boundaries, the local temperature, and thus the likelihood of glass crystallisation. If crystals form in the glass, its quality is dramatically reduced, thus motivating the need to minimise the extrusion pressure and temperature.

It is desirable to develop a set of predictive tools that allow the experimenter, who requires a fibre of a particular geometry, to manufacture the corresponding preform that is able to be drawn into the correct fibre. It is necessary to determine the limit to the number of features (complexity) and feature–size ratios that may be achieved via an improved understanding or improvement of the flow behaviours. This must be done whilst minimising the number of heat cycles that the glass has gone through, the peak stress in the extrusion process, and the effects of die swell and preform bending that occur as preforms exit the die. All of this is amenable to mathematical analysis, which would increase the quality of the final fibre and, ultimately, allow a new range of fibres to be manufactured.

Appendix A

Stability Code

The following is the complete stability code discussed and demonstrated in Chapter 5. In the code below where

$$\begin{aligned} h1x &= h_1(z), \\ h2x &= h_2(z), \\ u1x &= w_0(z), \\ U(x) &= w_2(z), \\ H1(x) &= h_{12}(z), \\ H2(x) &= h_{22}(z). \end{aligned}$$

```
restart:
AA:=35:
BB:=AA:
CC:=AA:
u0:=Uf*exp(beta*x/L)*U(x):
h1:=h10*exp(-beta*x/(2*L))*H1(x):
h2:=h20*exp(-beta*x/(2*L))*H2(x):
```

```
beta:=log(Ud/Uf):
rat:=20:
g:=0:
p0:=0.0:
rho:=500:
gammy:=0.0:
Ud:=rat*Uf:
Uf:=2.6E-05:
h10:=0.018:
h20:=0.020:
L:=0.03:
Tmin:=2638:
Tmax:=Tmin:
xtm:=0.01:

mea(x):=.1*10^(-6.24+26900/(((x*(Tmax-Tmin)/xtm)+Tmin)+273)):
meb(x):=.1*10^(-6.24+26900/(((x-L)*((Tmin-Tmax)/(L-xtm))+Tmin)+273)):
dmdx1:=diff(mea(x),x):
dmdx2:=diff(meb(x),x):
dmdx:=x->piecewise(x<=xtm, dmdx1, x>xtm, dmdx2):
temp:=x->piecewise (x<=xtm, x*(Tmax-Tmin)/xtm+Tmin, x>xtm, (x-L)
*((Tmin-Tmax)/(L-xtm))+Tmin):

me:=0.1*(10^(-6.24 + 26900/(temp(x)+273))):

eq1:=me*(h2^2-h1^2)*(diff(h1^2, t)+diff(u0*h1^2, x))-p0*h1^2*h2^2
+gammy*h1*h2*(h1+h2)=0:

eq2:=me*(h2^2-h1^2)*(diff(h2^2, t)+diff(u0*h2^2, x))-p0*h1^2*h2^2
+gammy*h1*h2*(h1+h2)=0:
```

```
eq3:=rho*(h2^2-h1^2)*(diff(u0, t)+diff(u0,x)*u0 - g) -(3*(h2^2-h1^2)
*diff(u0,x)*dmdx(x)+3*me*diff((h2^2-h1^2)*diff(u0,x),x)+gammy
*diff((h2+h1),x))=0:

sys:= eq1, eq2, eq3:
bound:=U(0)=1, U(L)=1, H1(0)=1, H2(0)=1:
infolevel[dsolve]:=4:
ans:=dsolve ({sys, bound}, numeric, output=listprocedure):

a:= eval(H1(x), ans):
b:= eval(H2(x), ans):
c:= eval(U(x), ans):
d:= eval(diff(U(x),x), ans):

h1x:=h10*exp(-beta*x/(2*L))*a(x):
h2x:=h20*exp(-beta*x/(2*L))*b(x):
u1x:=Uf*exp(beta*x/L)*c(x):
dudx:=Uf*exp(beta*x/L)*(beta/L*c(x)+d(x)):
dh1dx:=(((p0*h1x^2*h2x^2-gammy*h1x*h2x*(h1x+h2x))
/(me*(h2x^2-h1x^2)))-dudx*h1x^2)/(2*h1x*u1x):
dh2dx:=(((p0*h1x^2*h2x^2-gammy*h1x*h2x*(h1x+h2x))
/(me*(h2x^2-h1x^2)))-dudx*h2x^2)/(2*h2x*u1x):
d2udx2:=(rho*(h2x^2-h1x^2)*(dudx*u1x-g)-3*(h2x^2-h1x^2)*dudx*dmdx(x)
-3*me*dudx*(2*h2x*dh2dx-2*h1x*dh1dx)-gammy*(dh1dx+dh2dx))
/(3*me*(h2x^2-h1x^2)):

n:=AA:
N:=BB:
M:=CC:
aa:=array(1..n+N+M+6,1..1):
```

```
x:=m*L/(n+1):
for m from 0 to n do

aa[m+1,1]:=gammy*h2x*(2*H1(m)*h1x+h1x*H2(m)+h2x*H1(m)+2*h2x*H2(m))
-2*p0*h2x^2*h1x*(H2(m)+H1(m))+me*(-h1x^3*u1x*(U(m+1)-U(m-1))/(2*L
/(n+1))-2*h1x^3*u1x*(H1(m+1)-H1(m-1))/(2*L/(n+1))-h1x^3*dudx*U(m)
-4*h1x^3*dudx*H1(m)-2*h1x^3*H1(m)*sigma-8*h1x^2*u1x*dh1dx*H1(m)
-2*h1x^2*u1x*dh1dx*U(m)+h1x*h2x^2*u1x*(U(m+1)-U(m-1))/(2*L/(n+1))
+2*h1x*h2x^2*u1x*(H1(m+1)-H1(m-1))/(2*L/(n+1))+2*h1x*h2x^2*H1(m)
*sigma+2*h1x*h2x^2*dudx*H1(m)+h1x*h2x^2*dudx*U(m)+2*h1x*h2x^2*H2(m)
*dudx+2*h2x^2*u1x*dh1dx*U(m)+4*h2x^2*u1x*dh1dx*H1(m)+4*h2x^2*H2(m)
*u1x*dh1dx): od:

unassign('m'):
x:=(m-n-2)*L/(n+1):
for m from (n+2) to (n+N+2) do

aa[m+1,1]:=-p0*2*h1x^2*h2x*(H2(m)+H1(m))+gammy*(h1x*(2*h1x*H1(m)
+h1x*H2(m)+2*H2(m)*h2x+h2x*H1(m)))+me*(2*h2x^3*H2(m)*sigma+4*h2x^3
*dudx*H2(m)+h2x^3*u1x*(U(m+1)-U(m-1))/(2*L/(n+1))+2*h2x^3*u1x*
(H2(m+1)-H2(m-1))/(2*L/(n+1))+h2x^3*dudx*U(m)+8*h2x^2*u1x*dh2dx*H2(m)
+2*h2x^2*u1x*dh2dx*U(m)-2*h2x*h1x^2*H2(m)*sigma-2*h2x*h1x^2*dudx
*H2(m)-h2x*h1x^2*dudx*U(m)-2*h2x*h1x^2*u1x*(H2(m+1)-H2(m-1))/(2
*L/(n+1))-2*h2x*h1x^2*H1(m)*dudx-h2x*h1x^2*u1x*(U(m+1)-U(m-1))
/(2*L/(n+1))-4*h1x^2*u1x*dh2dx*H2(m)-4*h1x^2*H1(m)*u1x*dh2dx
-2*h1x^2*u1x*dh2dx*U(m)): od:

unassign('m'):
x:=(m-n-N-4)*L/(n+1):
for m from (n+N+4) to (n+N+M+4) do
```

```
aa[m+1,1]:=gammy*(-H1(m)*dh1dx-H2(m)*dh2dx-h1x*(H1(m+1)-H1(m-1))
/(2*L/(n+1))-h2x*(H2(m+1)-H2(m-1))/(2*L/(n+1)))+me*(-6*h2x^2*dudx
*(U(m+1)-U(m-1))/(2*L/(n+1))-6*h2x^2*(H2(m+1)-H2(m-1))/(2*L/(n+1))
*dudx-3*h2x^2*d2udx2*U(m)+6*h1x^2*H1(m)*d2udx2+6*h1x^2*(H1(m+1)
-H1(m-1))/(2*L/(n+1))*dudx+3*h1x^2*d2udx2*U(m)+6*h1x^2*dudx*(U(m+1)
-U(m-1))/(2*L/(n+1))-12*h2x*dh2dx*H2(m)*dudx+6*h1x*dh1dx*dudx*U(m)
-6*h2x*dh2dx*u1x*(U(m+1)-U(m-1))/(2*L/(n+1))+6*h1x*dh1dx*u1x*(U(m+1)
-U(m-1))/(2*L/(n+1))+12*h1x*dh1dx*H1(m)*dudx-6*h2x*dh2dx*dudx*U(m)
-3*h2x^2*u1x*(U(m+1)-2*U(m)+U(m-1))/(L/(n+1))^2-6*h2x^2*H2(m)*d2udx2
+3*h1x^2*u1x*(U(m+1)-2*U(m)+U(m-1))/(L/(n+1))^2)+rho*(h2x^2*u1x^2
*(U(m+1)-U(m-1))/(2*L/(n+1))-2*h2x^2*H2(m)*g+2*h2x^2*H2(m)*u1x
*dudx-2*h1x^2*u1x*dudx*U(m)-2*h1x^2*H1(m)*u1x*dudx+h2x^2*u1x*U(m)
*sigma+2*h2x^2*u1x*dudx*U(m)-h1x^2*u1x*U(m)*sigma+2*h1x^2*H1(m)*g
-h1x^2*u1x^2*(U(m+1)-U(m-1))/(2*L/(n+1)))-6*dmdx(x)*h2x^2*H2(m)*dudx
-3*dmdx(x)*h2x^2*dudx*U(m)-3*dmdx(x)*h2x^2*u1x*(U(m+1)-U(m-1))/(2*L
/(n+1))+3*dmdx(x)*h1x^2*dudx*U(m)+3*dmdx(x)*h1x^2*u1x*(U(m+1)-U(m-1))
/(2*L/(n+1))+6*dmdx(x)*h1x^2*H1(m)*dudx: od:

f:=array(1..n+N+M+6,1..n+N+M+6):
aa[1,1]:=sigma*H1(0):
aa[n+3,1]:=sigma*H2(n+2):
aa[n+N+5,1]:=sigma*U(n+N+4):
aa[n+N+M+6,1]:=sigma*U(n+N+M+5):

unassign('m'):
x:=L:
for m from (n+1) to (n+1) do

aa[n+2,1]:=gammy*h2x*(2*H1(m)*h1x+h1x*H2(m)+h2x*H1(m)+2*h2x*H2(m))
-2*p0*h2x^2*h1x*(H2(m)+H1(m))+me*(-h1x^3*u1x*(U(m)-U(m-1))/(L/(n+1))
-2*h1x^3*u1x*(H1(m)-H1(m-1))/(L/(n+1))-h1x^3*dudx*U(m)-4*h1x^3*dudx
```

```
*H1(m)-2*h1x^3*H1(m)*sigma-8*h1x^2*u1x*dh1dx*H1(m)-2*h1x^2*u1x*dh1dx
*U(m)+h1x*h2x^2*u1x*(U(m)-U(m-1))/(L/(n+1))+2*h1x*h2x^2*u1x*(H1(m)
-H1(m-1))/(L/(n+1))+2*h1x*h2x^2*H1(m)*sigma+2*h1x*h2x^2*dudx*H1(m)
+h1x*h2x^2*dudx*U(m)+2*h1x*h2x^2*H2(m)*dudx+2*h2x^2*u1x*dh1dx*U(m)
+4*h2x^2*u1x*dh1dx*H1(m)+4*h2x^2*H2(m)*u1x*dh1dx):
od:

unassign('m'):
x:=L:
for m from (n+N+3) to (n+N+3) do
aa[n+N+4,1]:=-p0*2*h1x^2*h2x*(H2(m)+H1(m))+gammy*(h1x*(2*h1x*H1(m)
+h1x*H2(m)+2*H2(m)*h2x+h2x*H1(m)))+me*(2*h2x^3*H2(m)*sigma+4*h2x^3
*dudx*H2(m)+h2x^3*u1x*(U(m)-U(m-1))/(L/(n+1))+2*h2x^3*u1x*(H2(m)
-H2(m-1))/(L/(n+1))+h2x^3*dudx*U(m)+8*h2x^2*u1x*dh2dx*H2(m)+2*h2x^2
*u1x*dh2dx*U(m)-2*h2x*h1x^2*H2(m)*sigma-2*h2x*h1x^2*dudx*H2(m)-h2x
*h1x^2*dudx*U(m)-2*h2x*h1x^2*u1x*(H2(m)-H2(m-1))/(L/(n+1))-2*h2x
*h1x^2*H1(m)*dudx-h2x*h1x^2*u1x*(U(m)-U(m-1))/(L/(n+1))-4*h1x^2
*u1x*dh2dx*H2(m)-4*h1x^2*H1(m)*u1x*dh2dx-2*h1x^2*u1x*dh2dx*U(m)):
od:

for j from 1 to (n+2) do for p from 1 to (n+2) do
f[j,p]:=coeff(aa[j,1],U(p-1))
od od:

for j from 1 to (n+2) do for p from 1 to (n+2) do
f[j,n+2+p]:=coeff(aa[j,1],H1(p-1))
od od:

for j from 1 to (n+2) do for p from 1 to (n+2) do
f[j,n+N+4+p]:=coeff(aa[j,1],H2(p-1))
od od:
```

```
for j from (n+3) to (n+N+4) do for p from 1 to (n+2) do
f[j,p]:=coeff(aa[j,1],U(n+2+p-1))
od od:

for j from (n+3) to (n+N+4) do for p from 1 to (n+2) do
f[j,n+2+p]:=coeff(aa[j,1],H1(n+2+p-1))
od od:

for j from (n+3) to (n+N+4) do for p from 1 to (n+2) do
f[j,n+n+4+p]:=coeff(aa[j,1],H2(n+2+p-1))
od od:

for j from (n+N+5) to (n+N+M+6) do for p from 1 to (n+2) do
f[j,p]:=coeff(aa[j,1],U(n+N+4+p-1))
od od:

for j from (n+N+5) to (n+N+M+6) do for p from 1 to (n+2) do
f[j,n+2+p]:=coeff(aa[j,1],H1(n+N+4+p-1))
od\, od:

for j from (n+N+5) to (n+N+M+6) do for p from 1 to (n+2) do
f[j,n+N+4+p]:=coeff(aa[j,1],H2(n+N+4+p-1))
od od:

for m from 1 to (n+N+M+6) do for j from 1 to (n+N+M+6) do
gurk:=coeff(f[m,j],sigma,1):
if gurk>0 then for g from 1 to (n+N+M+6) do
f[m,g]:=-f[m,g]/gurk:
od: end if: od: od:
```

```
g:=array(1...n+N+M+6,1..n+N+M+6):

for m from 1 to (n+N+M+6) do for j from 1 to (n+N+M+6) do
if coeff(f[m,j],sigma,1)<0 then for h from 1 to (n+N+M+6) do
g[j,h]:=f[m,h]:
od:
else f[m,j]:=f[m,j]:
end if: od: od:

sigma:=0:
for t from 1 to (AA+BB+CC+6) do for r from 1 to (AA+BB+CC+6) do
g[t,r]:=evalf(g[t,r])
od od:

sol:=array(1...12):
with(linalg):
sol:=eigenvalues(g):

b:=array(1..1):
sol:=[sol]:
sol:=convert(sol,array):

for j from 1 to (AA+BB+CC+6) do for m from 1 to (AA+BB+CC+5) do
if Re(sol[m])>Re(sol[m+1]) then b[1]:=sol[m]:
sol[m]:=sol[m+1]:
sol[m+1]:=b[1]:
end if: od: od:
sol();
```

Appendix B

Rotation Code

The following is the Fortran 77 code described and used in Chapter 7. It calls the NAG routine D02HAF, described in [70]. Comments are included throughout to aid the reader's understanding.

```
PROGRAM FIBRE
IMPLICIT REAL*8 (A-H,O-Z)
PARAMETER(M1=11)
REAL*8 W(6,46),SOLN(6,M1)
REAL*8 U(6,2),V(6,2)
COMMON/CA1/UFEED,UDRAW,HINNER,HOUTER,BFEED,BDRAW,
POP,ST,ELL,RHO,TMAX,TOL,G,STB,FR,S,RE,EMO,TE(26)
EXTERNAL FCN
C
This code calculates properties of a fibre that has been drawn by
rotating an annular preform (capillary tube), by solving the boundary
value problem arising from the slender body asymptotic analysis
carried out by C.J. Voyce, A.D. Fitt and T.M. Monro.  It uses a NAG
routine to solve the equations as a first--order system boundary
```

```
value problem that is presented in non--dimensional variables.
C
OPEN(12,FILE='furnace4.dat', STATUS='OLD')
DO I=1,26
   READ (12,*) POS,TP
   TE(I)=TP
END DO
CLOSE(12)

WRITE (6,*) '****************************'
WRITE (6,*) '****** PROGRAM FIBRE *******'
WRITE (6,*) '****************************'

UFEED  = 8.333333333333333D-05
UDRAW  = 0.1D00
        HINNER = 0.001425D00
        HOUTER = 0.004975D00
BFEED  = 0.00D+00
BDRAW  = 0.00D+00
POP    = 0.000D+00
ST     = 0.300D00
        ELL    = 3.0D-02
  RHO    = 2200.000D0
        TC     = 2100D00
TOL    = 1.000D-6
G      = 9.810D00
EMO    = 39316D+00

C The non-dimensional numbers that scale system of equations.
RE=RHO*UDRAW*ELL/EMO
S=HOUTER*BFEED/UDRAW
```

```
FR=UDRAW*UDRAW/G/ELL
STB=ST*ELL/EMO/UDRAW/HOUTER
TMAX=1.11D0*TC-345.5D0

        CALL SETDATA

C  Known B.C.s are Y1(0), Y2(0), Y3(0), Y3(ELL), Y5(0), Y5(ELL)

U(1,1) = HINNER/HOUTER
U(2,1) = 1
        U(3,1) = UFEED/UDRAW
        U(3,2) = 1
U(5,1) = 1
U(5,2) = 0

V(1,1) = 0.0D0
V(2,1) = 0.0D0
        V(3,1) = 0.0D0
        V(3,2) = 0.0D0
V(5,1) = 0.0D0
V(5,2) = 0.0D0

C  Unknown B.C.s

U(1,2) = 0.1D0          !DSQRT((HOUTER*HOUTER-HINNER*HINNER)/
C     &                         (HOUTER*HOUTER/HINNER/HINNER
- 1.0D0)*UFEED/UDRAW)
U(2,2) = 0.2D0            !    HOUTER/HINNER*U(1,2)
U(4,1) = 0.001D00             !    UFEED*dlog(udraw/ufeed)
        write (6,*) 'Enter udash(0) (Try 0.1)'
        read (5,*) U(4,1)
```

```
U(4,2) = 1.0D00              !    Udraw*dlog(udraw/ufeed)
U(6,1) = 0.0d00
U(6,2) = 0.0d00                   !   -BFEED/(ELL/20)

V(1,2) = 1.0D0
V(2,2) = 1.0D0
V(4,1) = 1.0D0
V(4,2) = 1.0D0
V(6,1) = 1.0D0
V(6,2) = 1.0D0

        IW = 46
A = 0.0D0
B = 1.00D0
        N = 6
        IFAIL = 110

CALL D02HAF(U,V,N,A,B,TOL,FCN,SOLN,M1,W,IW,IFAIL)

WRITE (6,*) '   x          h1              h2',
     &              '             u0              B ,'
        DO K = 1,M1
WRITE (6,765) ell*dfloat(k-1)/dfloat(m1-1),HOUTER*SOLN(1,K),
HOUTER*SOLN(2,K),
     &                UDRAW*SOLN(3,K),BFEED*SOLN(5,K)
        END DO
        WRITE (6,*) 'FINAL O/D = ',2.0D0*1D+06*HOUTER*SOLN(2,M1)
        WRITE (6,*) 'FINAL I/D = ',2.0D0*1D+06*HOUTER*SOLN(1,M1)
WRITE (6,*) 'FINAL N-O/R = ',SOLN(2,M1)
  WRITE (6,*) 'FINAL N-I/R = ',SOLN(1,M1)
WRITE (6,*) 'INIT UDASH = ',SOLN(4,1)
```

```
WRITE (6,*) 'FINAL UDASH = ',SOLN(4,M1)
WRITE (6,*) 'U(1,2) = ',SOLN(1,M1)
WRITE (6,*) 'U(2,2) = ',SOLN(2,M1)
WRITE (6,*) 'MASS CONS. TOP =',UFEED*(-HINNER*HINNER
        +HOUTER*HOUTER)
WRITE (6,*) 'MASS CONS. BOT =',UDRAW*(HOUTER*HOUTER
        *SOLN(2,M1)*
     &  SOLN(2,M1)-HOUTER*HOUTER*SOLN(1,M1)
        *SOLN(1,M1))

 765 FORMAT(1X,F6.3,4(1X,D14.7))
STOP
END

SUBROUTINE FCN(X,Y,F)
IMPLICIT REAL*8 (A-H,O-Z)
        REAL*8 Y(6),F(6)
COMMON/CA1/UFEED,UDRAW,HINNER,HOUTER,BFEED,BDRAW,POP,
        ST,ELL,RHO,TMAX,TOL,G,STB,FR,S,RE,EMO,TE(26)

EMUDASH = EMUPRIME(X,TE)*DTDX(X,TE)
F(1) = (2.0D0*POP*Y(1)*Y(2)*Y(2) - 2.0D0*STB*Y(2)*(Y(1)+Y(2))
+ RE*S*S*Y(1)*Y(2)*Y(2)*Y(5)*Y(5)*(Y(2)*Y(2)-Y(1)*Y(1)))/
     &          (4.0D0*Y(3)*EMU(X,TE)*(Y(2)*Y(2)-Y(1)*Y(1))) - 0.5D0*
     &          Y(1)*Y(4)/Y(3)
F(2) = (2.0D0*POP*Y(1)*Y(1)*Y(2) - 2.0D0*STB*Y(1)*(Y(1)+Y(2))+
     &          RE*S*S*Y(1)*Y(2)*Y(1)*Y(5)*Y(5)*(Y(2)*Y(2)-Y(1)*Y(1)))
     &          /(4.0D0*Y(3)*EMU(X,TE)*(Y(2)*Y(2)-Y(1)*Y(1))) - 0.5D0
     &          *Y(2)*Y(4)/Y(3)
F(3) = Y(4)
        SQ = (Y(2)*Y(2) - Y(1)*Y(1))
```

```
SQQ = (Y(2)*Y(2)*Y(2)*Y(2) - Y(1)*Y(1)*Y(1)*Y(1))
TT1 = RE/3.0D0/EMU(X,TE)*(Y(3)*Y(4) - 1.00D0/FR)
TT2 = - EMUDASH*Y(4)/EMU(X,TE)
TT3 = - 2.0D0*Y(4)*(F(2)*Y(2) - F(1)*Y(1))/SQ
TT4 = - STB*(F(1)+F(2))/3.0D0/EMU(X,TE)/SQ
TT5 = - RE*S*S*Y(5)*Y(6)*(Y(1)*Y(1)+Y(2)*Y(2))/6.0D0
     &        /EMU(X,TE)
TT6 = - RE*S*S*Y(5)*Y(5)*(F(2)*Y(2)*Y(2)*Y(2)-F(1)*Y(1)*Y(1)
     &        *Y(1))/3.0D0/EMU(X,TE)/SQ
F(4) = (TT1 + TT2 + TT3 + TT4 + TT5 + TT6)
F(5) = Y(6)
TT7 = (2.0D0*Y(5)*RE*Y(3) - 4.0D0*EMU(X,TE)*Y(6))*
     &        (Y(2)*Y(2)*Y(2)*F(2) - Y(1)*Y(1)*Y(1)*F(1))/EMU(X,TE)
     &       /SQQ
TT8 = RE*RE*S*S*Y(5)*Y(5)*Y(5)*Y(1)*Y(1)*Y(2)*Y(2)/2.0D0/
     &        EMU(X,TE)/EMU(X,TE)/(Y(1)*Y(1)+Y(2)*Y(2))
TT9 = -RE*STB*Y(1)*Y(2)*Y(5)*(Y(1) + Y(2))/EMU(X,TE)/
        EMU(X,TE)/SQQ
F(6) = Y(6)/EMU(X,TE)*(RE*Y(3) - EMUDASH) + RE*POP*Y(1)*Y(1)
        *Y(2)*
     &         Y(2)*Y(5)/EMU(X,TE)/EMU(X,TE)/SQQ + TT7 + TT8 + TT9
RETURN
END

REAL*8 FUNCTION EMU(X,TE)
IMPLICIT REAL*8 (A-H,O-Z)
COMMON/CA1/UFEED,UDRAW,HINNER,HOUTER,BFEED,BDRAW,POP,
        ST,ELL,RHO,TMAX,TOL,G,STB,FR,S,RE,EMO
REAL*8 X,TE(26),C
C=3D0
C An old viscosity law used to check the model.
```

```
C EMU = (0.1D0*(10.0D0**(-6.24D0 + 2.69D04/(TEMP(X,TE)
     &  +273.0D0))))
        /EMO
EMU = C*0.58D-7*EXP(515400D0/(8.3145D0*TEMP(X,TE)
     &  +2271.105675D0))
     &  /EMO
RETURN
END

REAL*8 FUNCTION TEMP(X,TE)
IMPLICIT REAL*8 (A-H,O-Z)
COMMON/CA1/UFEED,UDRAW,HINNER,HOUTER,BFEED,BDRAW,POP,
        ST,ELL,RHO,TMAX,TOL,G,STB,FR,S,RE,EMO
REAL*8 X,TE(26), J
J=1D0
DELTA=J*0.0054D0
XM=0.0594D0
C       The temperature profile: to be taken from furnace.dat.
k=int((X*ELL+XM-ELL/2D0)/DELTA
IF ((X*ELL+XM-ELL/2D0-DELTA*k) .GT. 0D0) THEN
   TEMP=TMAX - 1676.9D0 + (TE((k+1)*J+1)-(1D0-(X*ELL+XM-ELL/2D0
-DELTA*k)/DELTA)*(TE((k+1)*J+1)-TE(k*J+1)))
ELSE IF ((X*ELL+XM-ELL/2D0-DELTA*k) .LT. 0D0) THEN
   TEMP=TMAX - 1676.9D0 + (TE(k*J+1)-(1D0-(X*ELL+XM-ELL/2D0
-DELTA*(k-1))/DELTA)*(TE(k*J+1)-TE((k-1)*J+1)))
ELSE
   TEMP=TMAX - 1676.9D0 + TE(k*J+1)
END IF
RETURN
END
```

```
REAL*8 FUNCTION DTDX(X,TE)
IMPLICIT REAL*8 (A-H,O-Z)
COMMON/CA1/UFEED,UDRAW,HINNER,HOUTER,BFEED,BDRAW,POP,
      ST,ELL,RHO,TMAX,TOL,G,STB,FR,S,RE,EMO

REAL*8 X,TE(26),DELTA,DELTA2,DEL,XM,TEMP
       XM=0.0594D0
C      The derivative of $T$ with respect to $X$, the variable
C      that represents $z$ in our analysis.
DELTA2=0.04D0
DTDX=(TEMP((X+DELTA2),TE)-TEMP((X-DELTA2),TE))/DELTA2/2D0
RETURN
END

REAL*8 FUNCTION EMUPRIME(X,TE)
IMPLICIT REAL*8 (A-H,O-Z)
COMMON/CA1/UFEED,UDRAW,HINNER,HOUTER,BFEED,BDRAW,POP,
       ST,ELL,RHO,TMAX,TOL,G,STB,FR,S,RE,EMO
C      The derivative of $\mu$ with respect to $T$.
REAL*8 X,TE(26),DELTA,DELTA2,DEL,C
C=3D0
C EMUPRIME below belongs to the old viscosity law that was
C      used to check the model.
C EMUPRIME = (-2690.0D0*DLOG(10.0D0)*(10.0D0**(-6.24D0 + 2.69D04/
C     &             (TEMP(X,TE)+273.0D0)))/(TEMP(X,TE)+273.0D0)
C     &             /(TEMP(X,TE)+273.0D0))/EMO
EMUPRIME = (-C*0.58D-7*515400D0*8.3145D0)*EXP(515400D0/(8.3145
     &             D0*TEMP(X,TE)+2271.105675D0))/(8.3145D0*TEMP(
     &             X,TE) + 2271.105675D0)/(8.3145D0*TEMP(X,TE)
     &             +2271.105675D0)
     &             /EMO
```

```
RETURN
END

SUBROUTINE SETDATA
IMPLICIT REAL*8 (A-H,O-Z)
COMMON/CA1/UFEED,UDRAW,HINNER,HOUTER,BFEED,BDRAW,POP,
        ST,ELL,RHO,TMAX,TOL,G,STB,FR,S,RE,EMO,TE(1084)

200     WRITE (6,*)
        WRITE (6,*)
WRITE (6,*) ' CURRENT PARAMETERS (ALL IN SI!) SET AT:'
WRITE (6,*) '---------------------------------------'
        WRITE (6,*) '*'
        WRITE (6,10) UFEED
        WRITE (6,11) UDRAW
WRITE (6,12) HINNER
WRITE (6,13) HOUTER
WRITE (6,14) BFEED
WRITE (6,15) BDRAW
WRITE (6,16) POP
WRITE (6,17) ST
WRITE (6,18) ELL
WRITE (6,19) RHO
WRITE (6,20) TC
WRITE (6,21) TOL
WRITE (6,22) G
WRITE (6,23) EMO
        WRITE (6,*) '*'
WRITE (6,*) '---------------------------------------'
        WRITE (6,*)
```

```
100 WRITE(6,*) 'TYPE 1 TO PROCEED, 2 TO CHANGE DATA  '
READ (5,*) IPR
IF ((IPR-1)*(IPR-2) .NE. 0) WRITE (6,*) 'TYPE 1 OR 2 PLEASE'
IF ((IPR-1)*(IPR-2) .NE. 0) GOTO 100

        IF (IPR .EQ. 2) THEN
WRITE (6,*) 'SELECT ITEM (1-14) TO CHANGE '
        READ (5,*) IITEM
        IF (IITEM .EQ. 1) WRITE (6,*) 'NEW FEED SPEED = '
        IF (IITEM .EQ. 1) READ (5,*) UFEED
        IF (IITEM .EQ. 2) WRITE (6,*) 'NEW DRAW SPEED = '
        IF (IITEM .EQ. 2) READ (5,*) UDRAW
        IF (IITEM .EQ. 3) WRITE (6,*) 'NEW INNER RADIUS = '
        IF (IITEM .EQ. 3) READ (5,*) HINNER
        IF (IITEM .EQ. 4) WRITE (6,*) 'NEW OUTER RADIUS = '
        IF (IITEM .EQ. 4) READ (5,*) HOUTER
        IF (IITEM .EQ. 5) WRITE (6,*) 'NEW ROTATION RATE = '
        IF (IITEM .EQ. 5) READ (5,*) BFEED
        IF (IITEM .EQ. 6) WRITE (6,*) 'NEW ROTATION END RATE = '
        IF (IITEM .EQ. 6) READ (5,*) BDRAW
        IF (IITEM .EQ. 7) WRITE (6,*) 'NEW HOLE PRESSURE = '
        IF (IITEM .EQ. 7) READ (5,*) POP
        IF (IITEM .EQ. 8) WRITE (6,*) 'NEW SURFACE TENSION = '
        IF (IITEM .EQ. 8) READ (5,*) ST
        IF (IITEM .EQ. 9) WRITE (6,*) 'NEW DRAW LENGTH = '
        IF (IITEM .EQ. 9) READ (5,*) ELL
        IF (IITEM .EQ. 10) WRITE (6,*) 'NEW FIBRE DENSITY = '
        IF (IITEM .EQ. 10) READ (5,*) RHO
        IF (IITEM .EQ. 11) WRITE (6,*) 'NEW MAX CLAIMED
        TEMPERATURE = '
        IF (IITEM .EQ. 11) READ (5,*) TC
```

```
        IF (IITEM .EQ. 12) WRITE (6,*) 'NEW TOLERANCE = '
        IF (IITEM .EQ. 12) READ (5,*) TOL
        IF (IITEM .EQ. 13) WRITE (6,*) 'GRAVITATIONAL
        ACCELERATION = '
        IF (IITEM .EQ. 13) READ (5,*) G
IF (IITEM .EQ. 14) WRITE (6,*) 'MAX VISCOSITY = '
IF (IITEM .EQ. 14) READ (5,*) EMO

GOTO 200
END IF

10 FORMAT(1X,'* 1.  FEED SPEED           = ',E14.7)
11 FORMAT(1X,'* 2.  DRAW SPEED           = ',E14.7)
12 FORMAT(1X,'* 3.  INIT INNER RADIUS    = ',E14.7)
13 FORMAT(1X,'* 4.  INIT OUTER RADIUS    = ',E14.7)
14 FORMAT(1X,'* 5.  INIT ROT RATE        = ',E14.7)
15 FORMAT(1X,'* 6.  FINAL ROT RATE       = ',E14.7)
16 FORMAT(1X,'* 7.  HOLE OVERPRESSURE    = ',E14.7)
17 FORMAT(1X,'* 8.  SURFACE TENSION      = ',E14.7)
18 FORMAT(1X,'* 9.  DRAW LENGTH          = ',E14.7)
19 FORMAT(1X,'* 10.  FIBRE DENSITY        = ',E14.7)
20 FORMAT(1X,'* 11.  CLAIMED DRAW TEMPERATURE     = ',E14.7)
21 FORMAT(1X,'* 12. TOLERANCE FOR CALCS  = ',E14.7)
22 FORMAT(1X,'* 13. GRAV ACCLN           = ',E14.7)
23 FORMAT(1X,'* 14. MAXIMUM VISCOSITY    = ',E14.7)

RETURN
END
```

Appendix C

Mean Curvature in Three Dimensions

The analysis of the full holey fibre problem suggests that it may be necessary to proceed to second order in the mean curvature. For completeness, we therefore give the relevant formulae in this appendix. For a suitably smooth surface in three–space given by

$$H(z, x, y, t) = 0,$$

we follow the standard procedure and define coefficients a, b and c by

$$\det \begin{pmatrix} H_{zz} - \lambda & H_{xy} & H_{zx} & H_z \\ H_{zy} & H_{yy} - \lambda & H_{yx} & H_y \\ H_{zx} & H_y & H_{xx} - \lambda & H_x \\ H_z & H_y & H_x & 0 \end{pmatrix} = a + b\lambda + c\lambda^2.$$

The mean curvature is then given by

$$\kappa_m = \frac{b/c}{\sqrt{H_z^2 + H_x^2 + H_y^2}},$$

where a factor of 2 has been omitted from the bottom of this expression: as usual,

we actually require twice the classical definition of the mean curvature so that

$$\kappa_m = -\Big(H_{zz}(H_x^2+H_y^2)+H_{yy}(H_z^2+H_x^2)+H_{xx}(H_z^2+H_y^2)-2H_{zy}H_zH_y$$
$$-2H_{zx}H_zH_z-2H_{yx}H_yH_x\Big)/\left(\sqrt{H_z^2+H_x^2+H_y^2}\right).$$

In order to derive an expression for the fibre mean curvature that will be useful in the analysis, we now scale z with L and H, y and x with ϵL. On expanding for small ϵ this yields

$$\kappa_m = \frac{1}{L}\left(\frac{\kappa_0}{\epsilon}+\epsilon\kappa_1+\ldots\right),$$

where

$$\kappa_0 = \frac{H_y^2H_{xx}+H_x^2H_{yy}-2H_{xy}H_xH_y}{(H_x^2+H_y^2)^{3/2}},$$

and

$$\kappa_1 = \frac{A+B+C}{2(H_x^2+H_y^2)^{3/2}},$$

where

$$A = H_z^2H_y^2H_{xx}+H_z^2H_x^2H_{yy}-2H_{zz}(H_y^4+H_x^4),$$

$$B = -2H_z^2H_y^2H_{yy}-2H_z^2H_x^2H_{xx}-6H_z^2H_yH_xH_{yx},$$

and

$$C = 4H_{zy}(H_zH_yH_x^2+H_y^3)+4H_{zx}(H_zH_xH_y^2+H_zH_x^3)-4H_{zz}H_x^2H_y^2.$$

Appendix D

Transport Theorems for a Holey Fibre

In order to be able to derive global mass, momentum and angular momentum conservation laws, it is necessary to integrate over the cross–sectional area of the fibre. To allow us to do this, it is necessary to establish transport theorems. The proofs are elementary and will not be given. We assume that $\phi(z, y, x, t)$ is twice continuously–differentiable function and also that each of the closed curves H_i $(i = 0, 1, ..., N)$ is smooth. We also adopt the convention that the signs of the H_i are chosen so that taking the gradient gives a normal direction that points away from the fibre. We also assume that the total cross–sectional area of the fibre at any position z and at any time t is given by $A(z, t)$. The relevant transport theorems are then

$$\begin{aligned}
\frac{\partial}{\partial t}\int\int_A \phi\, dx\, dy &= \int\int_A \phi_t\, dx\, dy - \sum_{k=0}^{N} \oint_{\partial H_k} \frac{H_{kt}\phi\, ds}{(H_{kx}^2 + H_{ky}^2)^{1/2}}, \\
\frac{\partial}{\partial z}\int\int_A \phi\, dx\, dy &= \int\int_A \phi_z\, dx\, dy - \sum_{k=0}^{N} \oint_{\partial H_k} \frac{H_{kz}\phi\, ds}{(H_{kx}^2 + H_{ky}^2)^{1/2}}, \\
\int\int_A \phi_x\, dx\, dy &= \sum_{k=0}^{N} \oint_{\partial H_k} \frac{x(H_{kx}\phi_x + H_{ky}\phi_y)\, ds}{(H_{kx}^2 + H_{ky}^2)^{1/2}} - \int\int_A x(\phi_{xx} + \phi_{yy})\, dx\, dy, \\
\int\int_A \phi_y\, dx\, dy &= \sum_{k=0}^{N} \oint_{\partial H_k} \frac{y(H_{kx}\phi_x + H_{ky}\phi_y)\, ds}{(H_{kx}^2 + H_{ky}^2)^{1/2}} - \int\int_A y(\phi_{xx} + \phi_{yy})\, dx\, dy.
\end{aligned}$$

Appendix E

Glossary

Achromatic: refracting light without dispersing it into its constituent wavelengths.

Canes: see Stacking.

Chromatic dispersion: chromatic dispersion is a broadening of an input signal, which occurs as the signal travels the length of a fibre. It is typically made up of two separate dispersion effects; material dispersion and waveguide dispersion. Material dispersion results from different wavelengths of light seeing different refractive indices. Waveguide dispersion occurs because within a cross–section of fibre, different wavelengths will be confined to the core by different amounts. For example, large wavelength light will tend to have a significant portion of its optical power in the cladding of the fibre. Since in the cladding the refractive index is different to the refractive index of the core, dispersion results. In general material dispersion is the dominant effect.

Double crucible: see Figure 2.4. The molten core glass is placed in the inner crucible. The molten cladding glass is placed in the outer crucible. The two glasses come together at the base of the outer crucible and a fibre is drawn. Step-index fibres and graded-index fibres may be drawn with this method.

Extrusion: typically, two glass disks are placed on top of one another in a metal die. The glass is then heated until it softens, at which point pressure is applied to the upper of the two glass disks, forcing both glasses through the die and causing the top disk to "flow into" the bottom disk. The glass that has left the die then cools and solidifies, producing the preform.

Fibre: the structure resulting from having drawn a preform in a fibre drawing furnace.

Fibre drawing: the act of taking a fibre preform, placing it into a fibre drawing furnace at high temperature and then stretching it out into fibre form.

Modified Chemical Vapour Deposition (MCVD): a glass tube is taken and passed over a lathe and rotated. Chemicals are passed into the tube during this process and extremely fine particles of germanosilicate or phosphosilicate glass are deposited on the inside of the tube. A travelling lathe moving along the tube causes a chemical reaction to take place and then fuses the deposited material to the inside wall of the tube. The preform is deposited layer–by–layer, starting first with the cladding layers and followed by the core layers. Varying the mixture of chemicals changes the refractive index of the glass. When the deposition is complete, the tube is collapsed (drawn down in a fibre drawing furnace as one would the final preform) at approximately 2000C, into a preform of the purest silica with a core of a different composition and hence refractive index, creating the final preform. This preform is then placed in a drawing furnace and drawn down into the fibre form.

Microstructured fibre, holey fibre, photonic crystal fibre: fibre that contains a periodic structure in the transverse cross–section of the fibre. This periodic structure may comprise holes or, sometimes, other glasses or polymers. The arrangement of the holes will depend specifically on the intended optical properties of the fibre.

Nonlinear effects: typically light waves or photons transmitted through a fibre have little interaction with each other, and are not changed by their passage through the

fibre (except for absorption and scattering). However, there are exceptions arising from the interactions between light waves and the material transmitting them, which may affect optical signals. These processes are generally termed nonlinear because their strength typically depends on the square (or some higher power) of intensity. This means that nonlinear effects are weak at low powers, but may become much stronger when light reaches high intensities. This may occur either when the power is increased or when it is concentrated in a small area, such as the core of an optical fibre. Nonlinear optical devices have become common in some optical applications, such as to convert the output of lasers to shorter wavelengths by doubling the frequency (which halves the wavelength). Most nonlinear devices use exotic materials not present in fibreoptic systems, wherein nonlinear effects are much stronger than in glass. The nonlinearities in optical fibres are small, but they accumulate as light passes through many kilometres of fibre.

Photonic bandgap fibre: in a photonic bandgap fibre, light is guided due to the photonic bandgap effect, which is analogous to an electronic bandgap for electrons in semiconductors. The microstructure prohibits the propagation of certain wavelengths of light through the cladding. Since photonic bandgap guidance does not rely on the rod in tube method of manufacture (see **Rod in tube**), the core may either be made from glass or air, and the modes are confined to that region. The surrounding structure looks much the same as a regular holey fibre, though the positioning of the holes in the surrounding structure is crucial to exploit the photonic bandgap effect.

Preform: a glass rod ready to be drawn into fibre form. It may be made in a variety of ways but once the preform is obtained, either in the case of holey fibres or in the case of traditional solid glass fibres, the fibre is ready to be drawn directly from the preform structure.

Silica glass: Corning SMF28 high–purity silica glass is referred to in this thesis. More generally, oxygen (O_2) and silicon tetrachloride ($SiCl_4$) react to make silica (SiO_2). This pure silica is then doped with other chemicals, such as boron oxide

(B_2O_3), germanium dioxide (GeO_2) and phosphorus pentoxide (P_2O_5), which are used to modify the refractive index of the glass.

Rod in tube: a method of preform manufacture where a rod of core glass is placed inside a tube of cladding glass. The end of this assembly is heated; both glasses are softened and a fibre is drawn. The core rod has typically a 30 mm diameter. The core glass and the cladding glass must have similar softening temperatures and other mechanical properties. This method is relatively straightforward to exact but one must be careful not to introduce impurities onto the surface between the core and the cladding. For this reason it is now a little–used technique.

Soft glass: glasses that soften at much lower temperatures than silica (typically < 1000C).

Stacking: an array of capillary tubes are stacked together inside a larger capillary tube. This structure is then heated and drawn into canes, a process known as caning. These canes are then attached to the inside wall of a capillary tube (not yet drawn) and this structure drawn down to create the final preform with the necessary density of holes.

Third–order dispersion: the propagation constant β is defined as $\beta = n(\omega)\omega/c$, where c is the speed of light in vacuum, ω is the frequency of light and n is the refractive index. Third–order dispersion is defined as $\partial^2\beta/\partial\omega^2$, and is important when generating extremely short pulses.

'W' fibres: the most simple structure capable of producing low dispersion over a wide range of wavelengths is known as a 'W' fibre, so called because of the shape of the refractive–index profile in a cross–section of the fibre. On passing from the edge of the fibre to the core, the refractive index steps down and then up to a large value.

Weak stability analysis: a weak (linear) stability analysis assumes that any growth in perturbations introduced into a system is small. If the perturbations are small then

the effect of nonlinear terms is negligible and the resulting equations are simplified. If the perturbations derived from this analysis become large then the analysis breaks down and a weakly-nonlinear analysis must be completed, including the effect of non–linear terms in the governing equations.

Bibliography

[1] J.C. Knight, T.A. Birks, P.St.J. Russell, and D.M. Atkin. All–silica single–mode optical fiber with photonic crystal cladding. *Optics Letters*, 21(19):1457–1549, 1996.

[2] L.F. Mollenauer, R.H. Stolen, and J.P. Gordon. Experimental observation of picosecond pulse narrowing and solitons in optical fibers. *Physical Review Letters*, 45(13):1095–1098, 1980.

[3] T.M. Monro, D.J. Richardson, N.G.R. Broderick, and P.J. Bennett. Holey optical fibers: An efficient modal model. *Journal of Lightwave Technology*, 17(6):1093–1102, 1999.

[4] T.M. Monro, D.J. Richardson, and P.J. Bennett. Developing holey fibres for evanescent field devices. *Electron Letters*, 35(14):1188–1189, 1999.

[5] R.S. Ranka and A.J. Stentz. Optical properties of high-delta air-silica microstructure optical fibers. *Optics Letters*, 25(11):796–798, 2000.

[6] D.J. Richardson, K. Furusawa, H. Ebendorff-Heidepriem, P. Petropoulos, V. Finazzi, J.C. Baggett, W. Belardi, T.A. Kogure, J.H. Lee, Z. Yusoff, J. Nilsson, Y. Jeong, J.K. Sahu, and T.M. Monro. Practical applications of holey optical fibers. In *Optical Fiber Communication Conference, 2004*, volume 2, 2004.

[7] J.C. Baggett, T.M. Monro, J. Furusawa, V. Finazzi, and D.J. Richardson. Understanding bending losses in holey optical fibers. *Optical Communications*, 227(4–6):317–335, 2003.

[8] K. Kuriki, O. Shapria, S.D. Hart, G. Benoit, Y. Kurkik, J.F. Viens, M. Bayindir, J.D. Jonnopoulos, and Y. Fink. Hollow multilayer photonic bandgap fibers for nir applications. *Optics Express*, 12(8):1510–1517, 2004.

[9] X. Feng, T.M. Monro, P. Petropoulos, V. Finazzi, and D. Hewak. Solid microstructured optical fiber. *Optics Express*, 11(18):2225–2230, 2003.

[10] D.A. Nolan and M.-J. Li. Fibers with low polarization-mode dispersion. *Journal of Lightwave Technology*, 22(4):1066–1077, 2004.

[11] H. Ebendorff-Heidepriem, K. Furusawa, D.J. Richardson, and T.M. Monro. Fundamentals and applications of silica and non-silica holey fibers. In *Photonics West 2004*, 2004.

[12] M.A. van Eijkelenborg *et al.* Recent progress in microstructured polymer optical fibre fabrication and characterisation. *Optical Fiber Technology*, 9:199–209, 2003.

[13] H.-J. Mayer, Chr. Stiehi, and E. Roeder. Applying the finite-element method to determine the die-swell phenomenon during the extrusion of glass rods with non-circular cross-sections. *Journal of Materials Processing Technology*, 70:145–150, 1997.

[14] A.D. Fitt, K. Furusawa, T.M. Monro, C.P. Please, and D.J. Richardson. The mathematical modelling of capillary drawing for holey fibre manufacture. *Journal of Engineering Mathematics*, 43(2–4):201–227, 2002.

[15] A.D. Fitt, K. Furusawa, T.M. Monro, and C.P. Please. Modelling the fabrication of hollow fibers: capillary drawing. *Journal of Lightwave Technology*, 19(12):1924–31, 2001.

[16] P.D. Howell. The draining of a two-dimensional bubble. *Journal of Engineering Mathematics*, 35:251–272, 1999.

[17] J.C. Knight, R.F. Birks, P. Cregan, P. St. J. Russell, and J.P. de Sandro. Large mode area photonic crystal fiber. *Electron Letters*, 34(13):1347–1348, 1998.

[18] M. Key, I.G. Hughes, W. Rooijakkers, B.E. Sauer, E.A. Hinds, D.J. Richardson, and P.G. Kazansky. Propagation of cold atoms along a miniature magnetic guide. *Physics Review Letters*, 84(7):1371–1373, 2000.

[19] T.M. Monro, D.J. Richardson, and N.G.R. Broderick. Efficient modelling of holey fibers. In *Proceedings of the Optical Fiber Communication Conference, 1999*, page FG3, February 21–26 1999.

[20] A. Ferrando, E. Silvestre, J.J. Miret, and P. Andres. Nearly zero ultra-flattened dispersion in photonic crystal fibers. *Optics Letters*, 25(11):790–792, 2000.

[21] Jesper Laegsgaard, Anders Bjarklev, and Stig E. Barkou Libori. Chromatic dispersion in photonic crystal fibers: fast and accurate scheme for calculation. *Journal of the Optical Society of America B*, 20(3):443–448, 2003.

[22] Dimitre G. Ouzounov, Christopher J. Hensley, and Alexander J. Gaeta. Soliton pulse compression in photonic band–gap fibers. *Optics Express*, 12(16):6153–6159, 2005.

[23] C. Billet, John M. Mudley, N. Joly, and J.C. Knight. Intermediate asymptotic evolution and photonic bandgap fiber compression of optical similaritons around 1550 nm. *Optics Express*, 13(9):3236–3241, 2005.

[24] M.R. Matovich and J.R.A. Pearson. Spinning a molten threadline. steady–state isothermal viscous flows. *Industrial and Engineering Chemistry Fundamentals*, 8(3):512–520, 1969.

[25] J.R.A. Pearson and M.A. Matovich. Spinning a molten threadline. stability. *Industrial and Engineering Chemistry Fundamentals*, 8(4):605–609, 1969.

[26] Y.T. Shah and J.R.A. Pearson. On the stability of nonisothermal fiber spinning. *Industrial and Engineering Chemistry Fundamentals*, 11(2):145–149, 1972.

[27] A.L. Yarin, P. Gospodinov, and V.I. Ronssinov. Stability loss and sensitivity in hollow fiber drawing. *Physics of Fluids*, 6:1454–1463, 1994.

[28] J.A. Burgman. Liquid glass jets in the forming of continuous fibers. *Glass Technology*, 11:110–116, 1970.

[29] L.R. Glicksmann. The cooling of optical fibres. *Glass Technology*, 9:131–138, 1968.

[30] G. Manfre. Forces acting in the continuous drawing of glass fibres. *Glass Technology*, 10:99–106, 1997.

[31] M. Hucker, I. Bond, A. Foreman, and J. Hudd. Optimization of hollow glass fibers and their composites. *Adv. Comp. Lett.*, 8:181–189, 1999.

[32] Chang J.C., M.M. Denn, and F.T. Geyling. Effects of inertia, surface tension, and gravity on the stability of isothermal drawing of newtonian fluids. *Industrial and Engineering Chemistry Fundamentals*, 20(2):147–149, 1981.

[33] W.W. Schultz and S.H. Davis. Effects of boundary conditions on the stability of slender viscous fibers. *Journal of Applied Mechanics*, 106:1–5, 1984.

[34] J.C. Chang and M.M. Denn. An experimental study of isothermal spinning of a newtonian and viscoelastic liquid. *Non-Newtonian Fluid Mechanics*, 5:369–385, 1979.

[35] G.J. Donnelly and C.B. Weinberger. Stability of isothermal fiber spinning of a newtonian fluid. *Industrial and Engineering Chemistry Fundamentals*, 14(4):334–337, 1975.

[36] R.G. D'Andrea and C.B. Weinberger. Effects of surface tension and gravity forces in determining the stability of isothermal fiber spinning. *AIChE Journal*, 22:923–925, 1976.

[37] S. Senchenko and T. Bohr. The shape and stability of a viscous thread. *arXiv.org*, physics(0402130), 2004.

[38] F.T. Geyling and G.M. Homsy. Extensional instabilities of the glass fiber drawing process. *Glass Technology*, 21:95–102, 1980.

[39] F.T. Geyling. Basic fluid dynamic considerations in the drawing of optical fibres. *Bell System Technical Journal*, 55:1011–1056, 1976.

[40] J.N. Dewynne, P.D. Howell, and P. Wilmott. Slender viscous fibres with inertia and gravity. *Quarterly Journal of Mechanics and Applied Mathematics*, 47:541–555, 1994.

[41] J.N. Dewynne, J.R. Ockendon, and P. Wilmott. On a mathematical model for fibre tapering. *SIAM Journal of Applied Mathematics*, 49(4):983–990, 1989.

[42] J.I. Ramos. Asymptotic analysis of compound liquid jets at low Reynolds numbers. *Applied Mathematics and Computation*, 100(2–3):223–240, 1999.

[43] J.I. Ramos. Drawing of annular liquid jets at low Reynolds numbers. *Computational and Theoretical Polymer Science*, 11(6):429–443, 2001.

[44] J.I. Ramos. Compound liquid jets at low Reynolds numbers. *Polymer*, 43:2889–2896, 2002.

[45] P. Godpodinov and A.L. Yarin. Draw resonance of optical microcapillaries in non–isothermal drawing. *International Journal of Multiphase Flow*, 23:967–976, 1997.

[46] S.E. Rosenberg, H. Papamichael, and I.N. Miaoulis. A two-dimensional analysis of the viscous problem of a glass preform during the optical fiber drawing process. *Glass Technology*, 35:260–264, 1994.

[47] Z. Yin and Y. Jaluria. Thermal transport and flow in high-speed optical fiber drawing. *Journal of Heat Transfer*, 120:916–930, 1998.

[48] T.M. Monro, K. Furusawa, J.H. Lee, Price, J.H.V., Z. Yusoff, J.C. Baggett, and D.J. Richardson. Advances in holey fibers. In *Proceedings of SPIE*, volume 4974, pages 83–95, 2003.

[49] P.D. Howell. *Extensional thin layer flows*. PhD thesis, Oxford Centre for Industrial and Applied Mathematics, Mathematical Institute, University of Oxford, 24-29 St. Giles', Oxford, OX1 3LB, U.K., 1997.

[50] C.J. Voyce, A.D. Fitt, and T.M. Monro. Mathematical modelling of the drawing of spun capillary tubes. In A. Buikis, R. Ciegis, and A.D. Fitt, editors, *Progress in Industrial Mathematics at ECMI 2002*, pages 387–391. Berlin: Springer-Verlag, 2004.

[51] C.J. Voyce, A.D. Fitt, and T.M. Monro. The mathematical modelling of the rotation of capillary tubes. Submitted to the Journal of Engineering Mathematics, May 2005.

[52] J.P. Gordon and H. Kogelnik. PMD fundamentals: Polarization mode dispersion in optical fibers. In *Proceedings of the National Academy of Science of the United States of America*, volume 97(9), pages 4541–4550, 2000.

[53] A. Ortigosa-Blanch, J.C. Knight, W.J. Wadsworth, J. Arriaga, B.J. Mangan, T.A. Birks, and St. J. Russell. Highly birefringent photonic crystal fibers. *Optics Letters*, 25(18):1325–1327, 2000.

[54] A.J. Barlow, J.J. Ramskov-Hansen, and D.N. Payne. Birefringence and polarization mode-dispersion in spun single-mode fibers. *Applied Optics*, 20(17):2962–2967, 1981.

[55] M.J. Li and D.A. Nolan. Fiber spin-profile designs for producing fibers with low polarization mode dispersion. *Optics Letters*, 23(21):1659–1661, 1998.

[56] A.C. Hart Jr., R.G. Huff, and K.L. Walker. Method of making a fiber having low polarization mode dispersion due to a permanent spin., 1994. U.S. patent 5, 298, 047.

[57] R.E. Schuh, X. Shan, and A. Shamim Siddiqui. Polarization mode dispersion in spun fibers with difference linear birefringence and spinning parameters. *Journal of Lightwave Technology*, 16(9):1583–1588, 1998.

[58] M. Fuochi, J.R. Hayes, K. Furusawa, W. Belardi, J.C. Baggett, T.M. Monro, and D.J. Richardson. Polarization mode dispersion reduction in spun large mode area silica holey fibres. *Optics Express*, 12(9):1972–1977, 2004.

[59] R.B. Bird, W.E. Stewart, and E.N. Lightfoot. *Transport Phenomena.*, pages 83–89. Wiley, 1960.

[60] Andrea Galtarossa, Luca Palmieri, Anna Pizzinat, Giacomo Roba, and Davide Sarchi. Ultra low PMD fibers for long–haul high–capacity systems. In *Proceedings of the Optical Fiber Communication Conference, 2001*, pages ThA8–1, Match 15–21 2001.

[61] Andrea Galtarossa, Luca Palmieri, and Anna Pizzinat. Optimized spinning desigm for lw PMD fibers: An analytical approach. *Journal of Lightwave Technology*, 19(10):1502–1512, 2001.

[62] U.C. Paek. Free drawing and polymer coating of silica glass optical fibers. *ASME Journal of Heat Transfer*, 121(4):774–789, 1999.

[63] P.K.A. Wai, Kath, W.L., Menyuk, C.R., and J.W. Zhang. Nonlinear polarization–mode dispersion in optical fibers with randomly varying birefringence. *Journal of the Optical Society of America B*, 14(11):2967–2979, 1997.

[64] N.A. Mortensen and J.R. Folkenberg. Low–loss criterion and effective area considerations for photonic crystal fibres. *Journal of Optics A: Pure Applied Optics*, 5(3):163–167, 2003.

[65] Christopher J. Voyce, Alistair D. Fitt, and Tanya M. Monro. Mathematical model of the spinning of microstructured fibres. *Optics Express*, 12(23):5810–5820, 2004.

[66] J.R. Hayes. Personal Communication, 2003. Optoelectronics Research Centre, University of Southampton, University Road, Southampton, SO17 1BJ, U.K.

[67] R.H. Doremus. Viscosity of silica. *Journal of Applied Physics*, 92(12):7619–7629, 2002.

[68] P. Petropoulos, H. Ebendorff-Heidepriem, V. Finazzi, R.C. Moore, K. Frampton, D.J. Richardson, and T.M. Monro. Highly nonlinear and anomalously dispersive lead silicate glass holey fibers. *Optics Express*, 11(26):3568–3573, 2003.